An Experimental Study of Artificial Isotropic Chiral Media at Microwave Frequencies

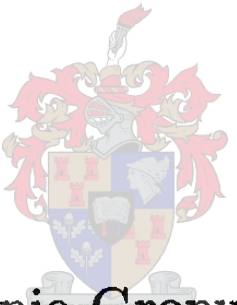

Anthonie Gronum Smith

Dissertation presented for the Degree of Doctor of Philosophy in Engineering at the University of Stellenbosch.

Promoter: Prof. J. H. Cloete
August 1994

Declaration

I, the undersigned, declare that the work contained in this thesis is my own original work, and has not previously in its entirety or in part been submitted at any other University for a degree.

A. G. Smith

Date: 23/11/1994

Dedicated to Kowie-Marié, my wife

Acknowledgements

I would like to express my sincere gratitude to everyone who assisted and supported me in completion of this thesis, and the following persons in particular:

Prof. John H. Cloete who initiated my interest in electromagnetics and who through his constant enthusiasm always inspired me. I thank him for his assistance and for arranging the funds to complete this study. I am most thankful to him for his influence on my ability to solve problems and my perception of science in general.

Dr. Scott Kuehl for the endless hours he spent preparing of the chiral samples. I am very grateful to Wessel Croukamp and Tom Coates for the design and manufacture of the free-space measurement system.

Keith Palmer for his general assistance with measurements and theoretical work during the years of my research. I would also like to thank my fellow students, Danie le Roux, Marius du Plessis, Pierre Steyn and Isak Theron, who often helped me with basic problems and the use of software, and Kevin Williams for proofreading this thesis.

Special thanks to my friend, Frans Meyer, for his interrest in my subject and the numerous discussions we had on science and life in general.

AMS Polymers (Pty) Ltd and Clive Pink in particular, without whose funding this research project would not have been possible.

I am grateful to my parents who provided me with a good education.

Finally I would like to express my deepest gratitude to my wife, Kowie-Marié, for her love, support and encouragement.

Opsomming

Kunsmatige kirale media kan gemaak word deur metaalhelikse lukraak te oriënteer in 'n niekirale (bv. diëlektriese) medium. Die mikrogolfeienskappe van kirale media kan toegeskryf word aan die anti-simmetrie van dié mikroskopiese insluitings. 'n Voorwerp word as kiraal beskryf indien dit nie deur translasie of rotasie op die spieëlbeeld daarvan gepas kan word nie. Die menslike hand is 'n goeie voorbeeld van so 'n kirale struktuur.

Die elektromagnetise eienskappe van 'n kunsmatige kirale medium kan beskryf word deur 'n addisionele (tot μ en ϵ) samestellingsparameter, die kiraliteitsparameter ξ. Kirale media het verskeie ongewone eienskappe waarvan optiese aktiwiteit waarskynlik die prominentste is. Optiese aktiwiteit beskryf die verskynsel waar die polarisasierigting van 'n lineêr-gepolariseerde golf geroteer word terwyl dit deur 'n kirale medium beweeg. 'n Direkte verband bestaan tussen dié rotasie en die kiraliteitsparameter.

Die weerkaats- en transmissiekoëffisiënte van 'n kirale plaat is bekend in terme van die samestellingsparameters (μ, ϵ en ξ) en die dikte van die plaat. In die tesis word 'n stel inversievergelykings afgelei wat gebruik kan word om die samestellingsparameters van 'n kirale medium te bepaal vanuit die gemete weerkaats- en transmissiekoëffisiënte, S_{11}, S_{21x} en S_{21y}. (S_{21y} is die kruis-gepolariseerde komponent van die transmissiekoëffisiënt wat 'n aanduiding van die rotasie gee.)

'n Analise word gedoen op die akkuraatheid waarmee metings uitgevoer kan word. Dit word gedoen deur gebruik te maak van die eerste orde parsiële afgeleide van die inversievergelykings. 'n Sensitiwiteitsanalise van die inversievergelykings word gedoen en in 'n analitiese vorm aangebied. Dié vorm maak dit moontlik om die bydrae van elke meetfout in S_{11}, S_{21x} en S_{21y} tot die totale meetfout in μ, ϵ en ξ te bepaal. 'n Statistiese metode (wortel gemiddelde kwadraat) word gebruik om die verwagte foutwaardes in die gemete samestellingsparameters te bepaal.

Verskeie kunsmatige kirale media word gemeet en 'n analise word gedoen op die akkuraatheid waarmee elk gemeet is. Die onakkuraatheid van die inversiemetode vir plate met lae verliese en wat veelvoude van 'n halwe golflengte dik is, word getoon deur middel van 'n sensitiwiteitsanalise.

Die vryeruimte meetstelsel (11-17 GHz) wat gebruik word om die weerkaats- en transmissiekoëffisiënte te meet, word breedvoerig bespreek. Die gemete stralingspatrone van die gefokusseerde lens antennes word vergelyk met teoreties bepaalde waardes. 'n Vryeruimte kalibrasietegniek word ontwikkel en die gemete dispersie in die fokusgebied word daarby ingesluit. Die resultate, soos verkry van verskillende kalibrasiestandaarde, word vergelyk en in verband gebring met die tegniek van kalibrasie-met-minimum-sensitiwiteit.

Ten slotte word die moontlike gebruik van kunsmatige kirale media as mikrogolfabsorbeerders ondersoek.

Abstract

An artificial chiral medium can be made by embedding metal helices (chiral or handed structures) with random orientation inside an achiral host medium. The electromagnetic behaviour of such artificial chiral media can be explained by an additional (to μ and ϵ) constitutive parameter, the chirality parameter ξ. Chiral media have certain special properties of which optical activity is the most prominent. Optical activity is the term used to describe the rotation of the polarization plane of a linearly polarized wave as it travels through a chiral medium. The chirality parameter is directly linked with this rotation.

The reflection and the transmission coefficients from a chiral slab are well known in terms of the constitutive parameters and the thickness of the sample. In the thesis a set of inversion equations are derived that can be used to determine the constitutive parameters (μ, ϵ, ξ) of a chiral medium from the measured S-parameters S_{11}, S_{21x} and S_{21y} (i.e. the reflection and co- and cross-polarized transmission coefficients respectively).

An accuracy analysis of the measurement method is made. This is done by using the first order partial derivatives of the inversion equations. A sensitivity analysis is done on the inversion equations and the results are in an analytical form. This makes it possible to determine the contribution of each of the measurement errors to the total expected error. A statistical root mean square method is used to predict the expected error in the measured constitutive parameters.

Several artificial chiral samples are measured and an accuracy analysis done on the measurements. The inaccuracy of the method of inversion for low loss samples that are multiples of half a wavelength thick is illustrated by example and explained by the sensitivity analysis.

The free-space system (11-17 GHz) used to measure the S-parameters is described in detail. The radiation patterns of the focused lens antennas are measured and compared to those obtained from two theoretical models. A free-space calibration procedure is developed and the dispersion in the focal region of the antennas incorporated into it. The results from different combinations of calibration standards are compared and related to the idea of minimum sensitivity calibration.

The possible use of an artificial chiral medium as a microwave absorber is also discussed.

Contents

List of Figures

List of Tables

Chapter 1

Introduction

1.1 The Scope of this Research

An enormous amount of research has recently been done on artificial chiral media at microwave frequencies. This activity was inspired through theoretical analysis which suggested that chiral media can be utilized in a number of novel applications. These applications have been made feasible by an additional constitutive parameter, the chirality parameter, that characterizes chiral media.

It is known that optically active media consist of handed asymmetric (chiral) inclusions. Media whose "optical activity" is observable at microwave frequencies can be made by embedding chiral structures in an achiral host medium. A composite medium of this type is referred to as an artificial chiral medium. Several of these chiral materials have been made by different researchers using helices as the chiral inclusions (see Table 9.1). The initial measurements on artificial chiral media were only of the rotation characteristics. To make further investigations into the characteristics of artificial chiral media it became necessary to measure their constitutive parameters. These measurements can be used to test some of the theories that have been developed on the interaction of the chiral inclusions with electromagnetic waves. The measured constitutive parameters can also be used to determine the feasibility of some of the applications that have been proposed for such media.

In this thesis an inversion method is presented to determine the constitutive parameters of chiral media from the measured scattering parameters of a chiral slab. The accuracy with which any measurement is made is important and should be known. A sensitivity analysis is used to determine the errors in the measured constitutive parameters, based on the first order partial derivatives of the inversion equations. With the measurement technique theoretically established the next step is to develop a system that can measure the scattering parameters of a chiral slab.

A free-space measurement system was developed to determine the reflection and transmission coefficients of a chiral sample, placed at the focus of two lens antennas facing each other. Since there are no commercially available calibration procedures for such a free-space system it was necessary to develop one. To do this the radiation characteristics of the antennas had to be determined because in both the calibration procedure and the inversion theory the characteristics of a plane wave is assumed. The accuracy with which the S-parameters can be measured by the calibrated free-space system has to be determined. This was done to calculate the errors in the measured

constitutive parameters.

Having established the accuracy of the free-space system and the inversion equations the characteristics of various artificial chiral media were investigated by experiment.

1.2 Original Contribution

Judging by information published in the current literature the thesis makes an original contribution in the following areas.

1. The *inversion equations* to obtain the constitutive parameters from the scattering parameters of a chiral slab.
2. A *sensitivity analysis* of the inversion equations. Although several measured results of the constitutive parameters of artificial chiral have been reported, little or no information is given on the accuracy of the measurements. The sensitivity analysis of the inversion equations make it possible to determine the expected errors in the measured constitutive parameters of chiral media. Because the sensitivity analysis is in an analytical form, it is possible to determine the contribution of each of the measurement errors to the total error of each of the complex constitutive parameters. The sensitivity analysis can also be used for the measurement of achiral (dielectric or magnetic) media.
3. The free-space system concept is not original. However, the experimental study of the fields of the lens antennas and the subsequent incorporation of the *dispersion* in the focal region into the calibration standards is original.
4. The *free-space calibration method* should also make a contribution to research on the calibration of similar systems.
5. The idea of *minimum sensitivity calibration* is investigated.
6. The *expected errors* in the scattering parameters of this system are determined.
7. A *parametric study* of chiral media as a function of helix density adds to the sparse body of published data.

In general it can be said that this thesis contributes to the measurement, with known accuracy, of artificial chiral media.

1.3 Overview of Thesis

A short introduction to chiral media and the characteristics of the waves inside such media is given in Chapter 2. The scattering parameters from a chiral slab are also given in this chapter. These scattering parameters are inverted in Chapter 3. The inversion equations are used to determine the constitutive parameters of a chiral slab. The different constitutive relations that are commonly used to describe chiral media are summarized in Appendix A.

The choice of a free-space measurement system to determine the reflection and transmission coefficients of a chiral slab is motivated in Chapter 4. This chapter also contains general information on the system used for this research, while Appendix C contains more detail. The radiation characteristics of the focused antennas are comprehensively investigated in Chapter 5. This knowledge is essential in the calibration of the setup.

In Chapter 6 a free-space calibration method is developed. The dispersion in the focal region of the antennas is incorporated in the specification of the calibration standards, and the effect of multiple reflections is investigated and solved by time domain gating.

The expected errors in the measured scattering parameters are determined in Chapter 7. A method to determine the errors in the measured constitutive parameters is given in Chapter 8.

The fabrication of several artificial chiral media and the measured results from these media are discussed in Chapter 9 and Appendix F.

The absorption characteristics of artificial chiral media are discussed in Chapter 10. Also shown in this chapter are measurements of the absorption of the artificial chiral media.

General conclusions on the thesis are made in Chapter 11.

The *Glossary of Symbols* at the end of the thesis should be useful to relocate the definitions of unfamiliar symbols and mathematical notation.

The harmonic time convention is $\exp(-i\omega t)$ and will be used throughout the thesis. All the measured values for permittivity ($\epsilon = \epsilon_r \epsilon_0$) and permeability ($\mu = \mu_r \mu_0$) are presented in their normalized form but the subscript r is not explicitly written. The chirality parameter ξ is not normalized.

Chapter 2

Chiral Media

> Our eye-beams twisted, and did thread
> Our eyes upon one double string;
> So to intergraft our hands, as yet
> Was all the means to make us one;
> And pictures in our eyes to get
> Was all our propagation.
>
> –John Donne *The Ecstasy* (1633)

2.1 Introduction

A chiral medium is intrinsically handed[1], due to the right- or left-handed asymmetry of its microscopic constituents. This property gives the wave equations two eigensolutions, a left circularly polarized (LCP) and a right circularly polarized (RCP) wave which propagate at different velocities. This property will cause the plane of polarization of a linearly polarized wave that is incident upon a chiral medium to be rotated when it emerges at the other side of a chiral medium. This phenomenon is called optical activity [1, 2].

It is important to distinguish between composite media where the chiral inclusions are randomly oriented i.e. *biisotropic* chiral media and composite media where the chiral inclusions are oriented in a crystalline way, called *bianistropic* media. The emphasis of this thesis will be on artificial biisotropic chiral media in the microwave region.

The influence of the chiral structure in nature has been discussed in several papers [3, 4, 5] and books [6].

[1] Chirality is a geometric term used to describe the lack of symmetry (or handedness) of an object.

2.2 Natural Chiral Media

The historical development of the study of chiral media at optical frequencies has been discussed in many articles [1, 2, 4, 7, 8, 9, 10, 11] and will be reviewed briefly. In 1811 Arago and in 1812 Biot discovered that polarized light is rotated if it is shone through certain biological and mineral substances such as quartz and sugar. This phenomenon is called optical activity because of its discovery in the optical spectrum. Fresnel conjectured in 1822 that a linearly polarized wave is divided into two circularly polarized waves, LCP and RCP, with different phase velocities if it is traveling along the optic axis of a crystal of quartz, resulting in the rotation of the polarization plane of the wave.

Pasteur showed through experiments with tartaric acid that optical activity is found in media that contain handed objects and that the direction of rotation depends on the handedness of the inclusions of the medium. Silverman [12, 13] proposed a method and performed measurements to detect chiral asymmetry in light, specularly reflected from a naturally optically active medium.

2.3 Artificial Chiral Media

Natural chiral media apparently do not exhibit measurable optical activity at microwave frequencies and have to be made artificially. Research into the crystalline nature of optically active media (at optical frequencies) led to the first *artificial*[2] chiral media. In 1920 and 1922 Lindman [14, 15, 16] published results of experiments done earlier[3] in which he made an artificial chiral medium by embedding copper helices (wire length 9 cm, diameter of helix 10 mm, 2.5 turns per helix, both left- and right-handed) in cotton balls and then positioned these in a cardboard box with random orientations. Lindman studied the rotation characteristics (frequencies 1 to 3 GHz) of the medium, and compared the results to the Drude model of frequency dependency of the rotation. The model was inadequate as it predicted infinite rotation at the helix resonance frequency and was later extended by Natanson [16] to include a damping term to give zero rotation at the resonant frequency.

Similar experiments by Tinoco and Freeman [17] and by Winkler [18] followed, who studied the rotation characteristics of different artificial chiral media at microwave frequencies. Several works have been published that give a more comprehensive overview on the historical development of artificial chiral media [7, 10, 19]. It appears that since 1960 very few measurements were done on artificial chiral media at microwave frequencies. It was only fairly recently that the research group at the Pennsylvania State University reinstated interest in the manufacturing and measurement of artificial chiral media [19, 20, 21]. Since then several researchers have made and measured the properties of artificial chiral media. The experiments that have been done on artificial chiral media are summarized in Table 9.1 of Chapter 9.

All of the above mentioned artificial chiral media exhibit the same phenomena at microwave frequencies as observed with natural chiral media at optical frequencies. These special phenomena of chiral media are summarized in Table 2.1.

[2]Described as "artificial chiral media" since they are man-made for use at microwave frequencies.
[3]Actually the first article by Lindman on this subject appeared six years earlier, in 1914 [16].

Definition	Physical Description
Circular birefringence	Different wave numbers for left and right circularly polarized waves.
Optical activity which is a result of circular birefringence	Rotation of the polarization plane of a linearly polarized wave as it travels through a chiral medium.
Circular dichroism	Differential absorption of left and right circularly polarized waves.
Rotatory dispersion	Frequency dependence of the angle of rotation with optical activity.
Cotton effect	The change in sign of the rotation angle. Occurs in artificial chiral media at the helix resonance frequency.

Table 2.1: Physical phenomena observed in chiral media.

The interest in artificial chiral media has been raised because of several claims for the use of such media for special applications in microwave engineering which exploit the unique characteristics of chiral media. Some of the novel applications proposed for chiral media are the following:

1. Chiro-waveguides [22, 23, 24, 25, 26], a waveguide filled with a chiral medium.
2. Conductor-backed Tellegen[4] slab as twist polarizers [28].
3. Chirodome [29, 30], a radome made from a chiral medium.
4. Chirolens [31], a lens of an antenna made from chiral medium.
5. Chiral patch antennas [32, 33, 34, 35], using a chiral medium substrate.
6. Chiral absorbers [36, 37, 38, 39, 40, 41, 42, 43].
7. Chiral coaxial line [44].

Some of the theoretical analyses of these applications use values for the constitutive parameters that were conveniently chosen to illustrate the principles involved. This might be misleading since it is not known whether such values for the constitutive parameters are physically attainable. It is therefore not surprising that much of the research is directed to the prediction measurement of these parameters. The theoretical models that are developed are then also tested against actual measurements of the constitutive parameters [45, 46, 47].

The possibility that artificial chiral media might make better microwave absorbers than their achiral counterparts has generated considerable interest. The suggestion to use chiral media as microwave absorbers was made by Varadan *et al.* [36] and

[4]The Tellegen parameter, χ, was introduced to account for the nonreciprocity of biisotropic media [27].

Jaggard and Engheta, (*Chirosorb*^{TM} [37] and *Chiroshield* [39]). However, very little experimental work has been done in support of this idea and research is continuing in this field [10, 20, 48, 49, 50, 51, 52]. The use of chiral media as microwave absorbing materials will be discussed in more detail in Chapter 10.

2.4 Constitutive Relations

A chiral medium responds with both magnetic and electric polarization if excited by either electric or magnetic fields. This "coupling" is a function of the microscopic chiral inclusions [53]. It is thus the geometry and the currents induced in such a handed object that is responsible for the coupling between the electric and magnetic fields of a chiral medium.

A chiral medium is a special case of *bianisotropic* media and it is *biisotropic* if the chiral inclusions are randomly oriented. Several relations have been proposed to characterize the constitutive parameters of chiral media [7, 27, 54]. These constitutive relations are interchangeable [27] and the relationships between the equations are summarized in Appendix A.

The equations that will be used in this thesis are those proposed by Post and by Jaggard, Mickelson and Papas [53],

$$\mathbf{D} = \epsilon \mathbf{E} + i\xi \mathbf{B}, \tag{2.1}$$

$$\mathbf{H} = i\xi \mathbf{E} + (1/\mu)\mathbf{B}, \tag{2.2}$$

with ξ the chiral admittance (ohm^{-1}), ϵ the permittivity, and μ the permeability of the chiral medium. All are frequency dependent in general, and may be complex to account for energy dissipation. The field vectors are printed in boldface. The harmonic time convention is $\exp(-i\omega t)$ and will be used throughout the thesis. For an isotropic chiral media $\mathbf{E}, \mathbf{H}, \mathbf{D}$ and $\mathbf{B}$ are scalar quantities.

Although it seems as if these constitutive relations are sufficient to describe the characteristics of chiral media, Raab and Cloete suggest in a physically rigorous model [55] that they are incomplete and should include more terms. Their argument is based on a multipole description in which, for non-magnetic chiral media, the constitutive relations for use in Maxwell's equations are expressed to the order of an electric quadrupole and a magnetic dipole. It is also shown that for randomly oriented helices the sum of all the electric-quadrupole moments is zero, resulting in a set of constitutive relations that are similar to the Post and Jaggard form.

2.5 General Wave Propagation

The source-free chiral Helmholtz equation can be obtained from the constitutive relations (2.1) and (2.2) and the source-free Maxwell equations [1, 56, 57],

$$\nabla \times \nabla \times \mathbf{E} - 2\omega\mu\xi \nabla \times \mathbf{E} - \omega^2 \mu\epsilon \mathbf{E} = 0. \tag{2.3}$$

The solution of this equation shows that there are two eigenmodes of propagation in a chiral medium, a right-circularly and a left-circularly polarized (RCP and LCP)[5] wave with the following wavenumbers [1],

$$k_r = +\omega\mu\xi + \sqrt{k^2 + (\omega\mu\xi)^2}, \tag{2.4}$$

$$k_l = -\omega\mu\xi + \sqrt{k^2 + (\omega\mu\xi)^2}, \tag{2.5}$$

where $k = \omega\sqrt{\mu\epsilon}$. This double-mode propagation is called circular birefringence. From these equations it is clear that in a chiral medium, where $\xi \neq 0$, the RCP wave will have a lower phase velocity ω/k_r than the LCP wave if $\mathrm{Re}(\xi) > 0$ (and *vice versa* if $\mathrm{Re}(\xi) < 0$), resulting in the rotation of a linearly polarized wave as it travels through the chiral medium (i.e. optical activity); see Fig 2.1. If there are losses involved the two eigenmodes will experience unequal attenuation causing the transmitted wave to be elliptically polarized (see Fig G.1). This is referred to as circular dichroism.

Another important parameter of a chiral medium is the intrinsic impedance which is given by [56],

$$\eta_c = \frac{1}{\sqrt{\epsilon/\mu + (\xi)^2}}. \tag{2.6}$$

These are the only properties of wave propagation that are needed to be able to determine the scattering parameters from a chiral slab. Once the scattering parameters are known the constitutive parameters of a chiral slab can be determined by inversion, as will be explained in Chapter 3.

2.6 Scattering Parameters of a Chiral Slab

The reflection and transmission coefficients of a linearly polarized plane wave (general incidence) from a chiral slab has been solved analytically by Bassiri *et al.* [2].

It is assumed that a chiral slab, of thickness d, is placed in a right handed (unit vectors $\hat{\mathbf{x}} \times \hat{\mathbf{y}} = \hat{\mathbf{z}}$) Cartesian coordinate system with its two faces coincident with the planes $z = 0$ and $z = d$. Space $z < 0$ and $z > d$ is filled with a homogeneous, lossless non-chiral medium with constitutive parameters ϵ_1 and μ_1, intrinsic wave impedance $\eta_1 = \sqrt{\mu_1/\epsilon_1}$, and wave number $k_1 = \omega\sqrt{\mu_1\epsilon_1}$. The slab's face $z = 0$ is illuminated by a normally incident plane[6] (or TEM) wave, $\mathbf{E}_i$, propagating in the $+z$-direction with its electric field vector polarized in the x-direction; thus $\mathbf{E}_i = \hat{\mathbf{x}} E_{ix} \exp(i k_1 z)$ as in Figure 2.1.

The scattering parameters for normal incidence were derived from [2, equations (67–72)] to be the following:

$$S_{11} \equiv \frac{E_{rx}(z=0)}{E_{ix}(z=0)} = \frac{\Gamma(1 - P_r P_l)}{1 - \Gamma^2 P_r P_l}, \tag{2.7}$$

$$S_{21x} \equiv \frac{E_{tx}(z=+d)}{E_{ix}(z=0)} = \frac{\frac{1}{2}(1-\Gamma^2)(P_r + P_l)}{1 - \Gamma^2 P_r P_l}, \tag{2.8}$$

[5]Throughout the thesis the subscripts l and r are associated with the left and right circularly polarized eigenwaves.

[6]Not necessarily uniform in amplitude.

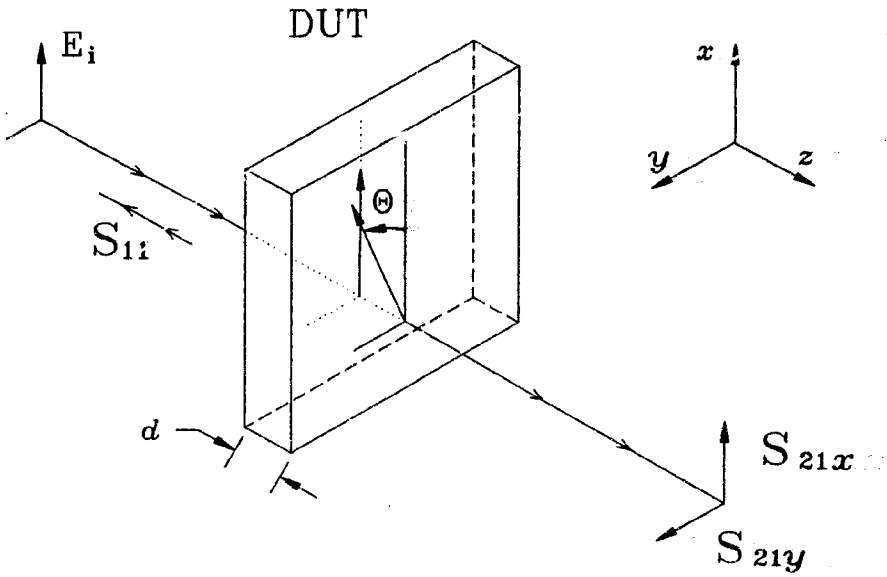

Figure 2.1: Orientation of the incident, the reflected and the transmitted waves from a chiral slab. The rotation angle Θ is defined to be positive if rotation is from the +x-axis to the +y-axis.

$$S_{21y} \equiv \frac{E_{ty}(z=+d)}{E_{ix}(z=0)} = \frac{i\frac{1}{2}(1-\Gamma^2)(P_r - P_l)}{1-\Gamma^2 P_r P_l} \tag{2.9}$$

The subscripts i, r, and t identify the incident, reflected and transmitted waves; the subscripts x and y define the Cartesian components of the associated electric field vectors.

The symbols in (2.7) to (2.9) are chosen for consistency with those of Weir [58]. Thus

$$\Gamma = \frac{\eta_c - \eta_1}{\eta_c + \eta_1} \tag{2.10}$$

is the reflection coefficient for a chiral slab of semi-infinite thickness [37].

The propagation factors for the right-circularly and left-circularly polarized eigenwaves in the chiral medium are,

$$P_r = \exp(ik_r d), \tag{2.11}$$
$$P_l = \exp(ik_l d). \tag{2.12}$$

The three complex scattering parameters are measurable by means of a free-space system. As will be shown in Chapter 3 they contain sufficient information from which the three unknown complex constitutive parameters, μ, ϵ and ξ, of the chiral slab may be obtained by mathematical inversion.

Chapter 3

Constitutive Parameters of a Lossy Chiral Slab by Inversion of Plane-Wave Scattering Coefficients

> To tell us that every species of thing is endowed with an occult specific quality by which it acts and produces manifest effects, is to tell us nothing; but to derive two or three general principles of motion from phenomena, and afterwards to tell us how the properties and actions of all corporeal things follow from those manifest principles, would be a very great step.
>
> — Isaac Newton (1642-1727), *Optics*

3.1 Inversion of the Scattering Parameters

The reflection and transmission coefficients of an isotropic homogeneous chiral slab are derived in an analytical form in terms of the constitutive parameters of the slab in Section 2.6.

With the scattering parameters known, they can be inverted to get the three constitutive parameters μ, ϵ and ξ in terms of the three scattering parameters S_{11}, S_{21x} and S_{21y}, in an analytical form [59]. The inversion method is an extension of the methods developed by Nicolson and Ross [60] and Weir [58], to determine the permittivity and permeability of non-chiral media.

The inversion of the equations, to obtain a set which give the unknown chiral wave parameters in terms of the known variables, can be achieved in the following three steps. The first step is to determine the propagation factors P_r, P_l and the reflection coefficient Γ in terms of the scattering parameters. In the second step the wave numbers k_r, k_l and the intrinsic impedance η_c are determined from P_r, P_l and Γ. In the last step the constitutive parameters μ, ϵ and ξ are determined from k_r, k_l and η_c.

Step One: From (2.7) follows

$$P_r P_l = \frac{S_{11} - \Gamma}{\Gamma(S_{11}\Gamma - 1)}, \tag{3.1}$$

while from (2.8) and (2.9) follows

$$S_{21x} - iS_{21y} = \frac{(1-\Gamma^2)P_r}{1-\Gamma^2 P_l P_r}, \tag{3.2}$$

$$S_{21x} + iS_{21y} = \frac{(1-\Gamma^2)P_l}{1-\Gamma^2 P_l P_r}. \tag{3.3}$$

Equation (3.1) can be used to eliminate the factor $P_r P_l$ in the right hand sides of (3.2) and (3.3), to yield the propagation factors as

$$P_r = \frac{S_{21x} - iS_{21y}}{1 - \Gamma S_{11}}, \tag{3.4}$$

$$P_l = \frac{S_{21x} + iS_{21y}}{1 - \Gamma S_{11}}. \tag{3.5}$$

Equating (3.1) and the product of (3.4) with (3.5) yields the quadratic equation

$$\Gamma^2 - 2\chi\Gamma + 1 = 0. \tag{3.6}$$

The coefficient term,

$$\chi = ((1 + S_{11}^2) - (S_{21x}^2 + S_{21y}^2))/(2S_{11}), \tag{3.7}$$

is known in terms of the scattering parameters. Thus the solution for Γ is

$$\Gamma = \chi \pm (\chi^2 - 1)^{1/2}, \tag{3.8}$$

with the sign chosen such that $|\Gamma| \leq 1$, because the chiral medium is assumed to be passive.

Combining the solution for Γ with (3.4) and (3.5) yields the propagation factors in terms of known variables S_{11}, S_{21x} and S_{21y}.

Step Two: With P_r, P_l and Γ known the intrinsic impedance, η_c, and wave numbers, k_r and k_l, can be obtained from Equations (2.10)–(2.12):

$$\eta_c = \eta_1 \frac{(1+\Gamma)}{(1-\Gamma)}, \tag{3.9}$$

$$k_r = \frac{1}{id}\ln(P_r) = \frac{1}{id}\ln\left(\frac{S_{21x} - iS_{21y}}{1 - \Gamma S_{11}}\right), \tag{3.10}$$

$$k_l = \frac{1}{id}\ln(P_l) = \frac{1}{id}\ln\left(\frac{S_{21x} + iS_{21y}}{1 - \Gamma S_{11}}\right). \tag{3.11}$$

The solutions for the wave numbers, (3.10) and (3.11), are ambiguous because the logarithm of a complex argument has a multiple valued imaginary part. Since use of the principal value for the natural logarithm will yield drastic errors if the slab

thickness exceeds one wavelength, which is not known *a priori*, due care must be taken [58, 61, 62]. The ambiguity in the logarithm is solved in Section B.1.

Step Three: In the third and last step the desired constitutive parameters can be found in terms of the now *known* intrinsic impedance η_c and the wave numbers k_r, k_l. This is done by inversion of Equations (2.4), (2.5) and (2.6) as shown in Section B.2. The result is,

$$\mu = \frac{\eta_c}{2\omega}(k_r + k_l), \tag{3.12}$$

$$\epsilon = \frac{2}{\omega\eta_c}\frac{k_r k_l}{(k_r + k_l)}, \tag{3.13}$$

$$\xi = \frac{1}{\eta_c}\frac{(k_r - k_l)}{(k_r + k_l)}. \tag{3.14}$$

These constitutive parameters, which are in the Post-Jaggard form, can be converted to any desired form, Appendix A.

These inversion equations can also be used for the achiral case where $\xi = 0$ can be substituted in the equations above. The result is that $k_r = k_l$ and $P_r = P_l$, which implies there is no cross-polarized transmission coefficient, $S_{21y} = 0$. There is therefore no optical activity.

3.2 Other Methods Used

Similar inversion methods to get the constitutive relations of a chiral medium have been developed by other researchers. In all these methods the constitutive parameters are determined by inverting the scattering parameters from a chiral slab.

The inversion method developed by Ro uses the Drude-Born-Fedorov constitutive parameters [48]. The research group from the Helsinki University of Technology have developed inversion equations for a chiral slab using the Sihvola-Lindell constitutive relations [63, 64, 65].

Bassiri *et al.* [2] show that there is a direct relationship between the rotation angle, θ, (see Fig.2.1) and the real part of the chirality parameter,

$$\theta = -\omega\mu\xi d. \tag{3.15}$$

In [63, 64, 65] a similar relationship is used directly to obtain the real part of the Sihvola-Lindell chirality parameter, κ,

$$\kappa_{re} = -\frac{\theta}{k_0 d} - \frac{n\pi}{k_0 d} \quad n = 0, 1, 2... \tag{3.16}$$

or[1]

$$\kappa_{re} = -\frac{(\pi - 2\theta)}{2k_0 d} - \frac{n\pi}{k_0 d} \quad n = 0, 1, 2... \tag{3.17}$$

They also show that the imaginary part of the chirality parameter, κ, is related to the axial ratio (AR) of the emerging wave,

$$\kappa_{im} = \frac{\text{arccoth}(|\text{AR}|)}{k_0 d}. \tag{3.18}$$

Measured constitutive parameters of artificial chiral media have been reported using this method [63].

Another method to measure the constitutive parameters of a chiral medium was developed by Ougier *et al.* [66]. It differs from the three inversion methods [48, 63, 59] in that three transmission and reflection measurements are made in three different configurations, namely normal incidence illumination of a slab, a magnetic shield (slab backed by a perfect conductor), an electric shield (where an achiral spacer with thickness $d = \lambda/4$ is placed between the chiral sample and the perfect conductor). The scattering parameters for oblique incidence on the chiral slab is used to eliminate the phase ambiguity in the wave number determination. The constitutive parameters are determined from these measurements using a numerical convergence method.

Guerin *et al.* [50] also use a reflection-transmission method to determine the constitutive parameters of artificial chiral media. Luebbers *et al.* [46] have also developed a method to determine the chirality parameter, β, from the rotation angle and the ellipticity of the transmission coefficient.

It is believed that all these methods complement each other and only further investigation and a comparison of their respective sensitivities to errors in the measured parameters will determine which is better.

Tretyakov *et al.* [67] have recently proposed a theoretical free-space method to determine all four of the material parameters μ, ϵ, κ and χ of a general biisotropic medium.

Inversion equations of the transmission and reflection coefficients are not the only methods used to determine the constitutive parameters of artificial chiral media. A method using the Brewster angle has been proposed for measuring microwave material parameters of biisotropic and chiral media [68]. However, no reports or publications of measured constitutive parameters using this method have been made. A waveguide and resonator perturbation technique for measuring chirality has been developed by Tretyakov *et al.* [69], and used by Semenenko *et al.* [70] to measure the permeability of a single conductive helix.

The methods that use inversion of the reflection and transmission coefficients to determine the constitutive parameters are all sensitive (and therefore inaccurate) to

[1]Note however that in [63, 65] (using $e^{j\omega t}$ convention) the the second condition is given as,

$$\kappa_{re} = \frac{(\pi - \theta)}{2k_0 d} + \frac{n\pi}{k_0 d} \quad n = 0, 1, 2...$$

i.e., a factor 2 discrepancy in θ.

measurement errors if the materials have low loss and are multiples of half a wavelength thick [71, 72, 73, 74, 75]. The sensitivity of the inversion equations that will be used in this thesis to determine the constitutive parameters of chiral media will be discussed in Chapter 8.

The inaccuracy caused by the half-wave effect in low loss dielectric and magnetic media has led to other less sensitive numerical methods [73, 74, 75]. The method developed by Baker-Jarvis [73, 74] can also determine the permittivity and permeability for samples where the sample length and position are not known precisely. These methods are very effective in reducing errors but are complicated and it would be difficult to use similar methods to solve the constitutive parameters of a chiral sample.

3.3 Conclusions

A systematic algorithm has been developed for inverting normal incidence free space scattering parameter data to yield the complex constitutive parameters of a chiral slab.

The algorithm has been tested in a simulation where values for the constitutive parameters are assumed and the scattering parameters for such a chiral slab calculated. These "measured" values for S_{11}, S_{21x} and S_{21y} are then inverted to get the "measured" values of μ, ϵ and ξ.

This inversion method will be used in Chapter 9 to determine the constitutive parameters of some artificial chiral media. A sensitivity analysis of these inversion equations is done in Chapter 8 and used to determine the expected errors in the measurements of the constitutive parameters of the chiral media.

Chapter 4

The Free-Space Measurement System

> Science is an investigation by the mind which begins with the ultimate origin of a subject beyond which nothing in nature can be found to form part of the subject. Take, for example, the continuous quantity in the science of geometry: if we begin with the surface of a body we find that it is derived from lines, the boundaries of the surface. But we do not let the matter rest there, for we know that the line in its turn is terminated by points, and that the point is that ultimate unit that which there is nothing smaller. Therefore the point is the first beginning of geometry, and neither in nature nor in the human mind can there be anything which can originate the point....No human investigation can be called true science without passing through mathematical tests; and if you say that the sciences which begin and end in the mind contain truth, this cannot be conceded and must be denied for many reasons. First and foremost because in such mental discourses experience does not come in, without which nothing reveals itself with certainty.
>
> — Leonardo da Vinci (1452–1519)

4.1 Introduction

Many related methods have been used to determine the constitutive parameters of dielectric and magnetic media [76, 77]. These methods can be divided into two basic classes. In one, the sample is inserted into a volume where the irradiating fields are physically confined by conducting walls. In the other, the irradiating fields are unbounded, but focused in a beam propagating in free-space.

The confined field techniques can be subdivided into reflection-transmission measurements using coaxial or wave-guide systems, and resonant cavity perturbation measurements.

The free-space methods can also be subdivided into reflection-transmission measurements, and open resonator configurations of the Fabry-Perot type [78].

Free-space methods have several advantages over confined systems (like waveguide) [77, 78, 79]. Some of the advantages are the following:

1. Specifications on the dimensions of samples need not be as tight as those for confined systems where errors can become substantial, due to air gaps for example, if the specifications are not met.

2. In free-space systems the only dimensional specifications are that the samples be large enough to minimize diffraction and that the sample have a homogeneous thickness over the measured region. This advantage also makes quicker measurements possible.

3. In confined systems higher order modes can decrease accuracy if they are not properly accounted for.

4. The free-space measurements are contactless and non-destructive, making measurement of samples at high and low temperatures possible.

5. Small composite medium samples, like artificial chiral samples, can be "inhomogeneous" in confined systems whereas in free-space system the larger measurement region (focal spot) can result in a more "homogeneous" medium.

6. In free-space systems the incidence angle can be changed.

7. The polarization angle can also be changed. This makes them ideally suited for the measurement of bianisotropic and especially biisotropic or chiral media.

Some of the main disadvantages of a free-space system are the following:

1. The fields are not exactly known in the focal region. A knowledge of these fields is necessary to quantify to what extent they approximate the ideal conditions assumed for the calibration and for the inversion process.

2. Samples need to be large enough to minimize diffraction.

3. Although the diffraction from the sample is minimized by a focussed beam system it cannot be removed completely.

4. No calibration standards are commercially available and have to be developed.

5. The dispersion in the focal region of such focussed beam systems need to be accounted for in the calibration and measurements.

The method used to find constitutive parameters from the scattering parameters assumes a plane wave which is normally incident upon a slab that is infinite in the x- and y-direction with uniform thickness in the z-direction, which is also the direction of propagation. This theoretical condition requires that there should be no diffraction from the edges of the material which is being measured. The extent to which this condition is met in a free-space measurement system depends upon the radiation characteristics of the antennas, the alignment of the sample and the antennas, and the physical properties like the dimensions of the sample itself.

The focused plane waves can be generated either by a dielectric lens antenna [79] or by focusing reflectors [63, 66, 77, 78]. Although focusing reflectors operate over a wider frequency band than dielectric lens antennas, the feed is usually in the way of the outgoing wave and this partial screening can be a disadvantage when making accurate measurements in the focal region.

It is shown in Section 3.1 that, because a chiral medium has three complex constitutive parameters, it is necessary to have three independent measurements to determine the constitutive parameters of such a medium. Since the chirality parameter is directly responsible for the rotation of the polarization plane of a linearly polarized wave that travels through a chiral medium [2, 65], the obvious choice for an additional independent measurement is the rotation characteristic.

The rotability of circular waveguide [21] and free-space methods [19] make them particularly suitable for rotation measurements. However, it is interesting to note that a perturbation technique in a cylindrical resonator has been developed by Tretyakov *et al.* [69] to measure the constitutive parameters of artificial chiral media, and was used by Semenenko *et al.* [70] to determine the permeability of a single conductive helix.

The free-space method has been used successfully to measure the constitutive parameters of dielectric [77, 79, 80] and magnetic media [61, 77]. Free-space systems have also been used to study the rotation characteristics [19] as well as absorption or reflection characteristics of artificial chiral media [10, 20, 48]. Recently, free-space systems have been used by several researchers to measure the constitutive parameters of artificial chiral media [48, 50, 63, 66, 81, 82].

4.2 The Measurement System

The configuration of the equipment is illustrated in Figure 4.1 and Figure 4.2.

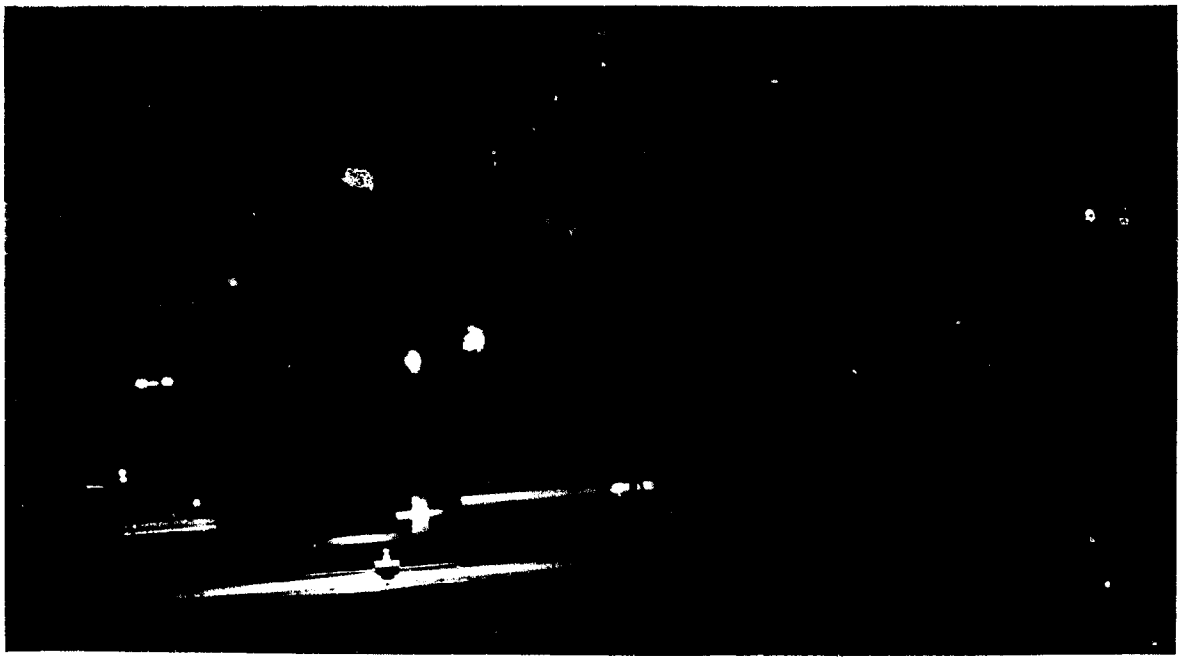

Figure 4.1: Configuration of equipment.

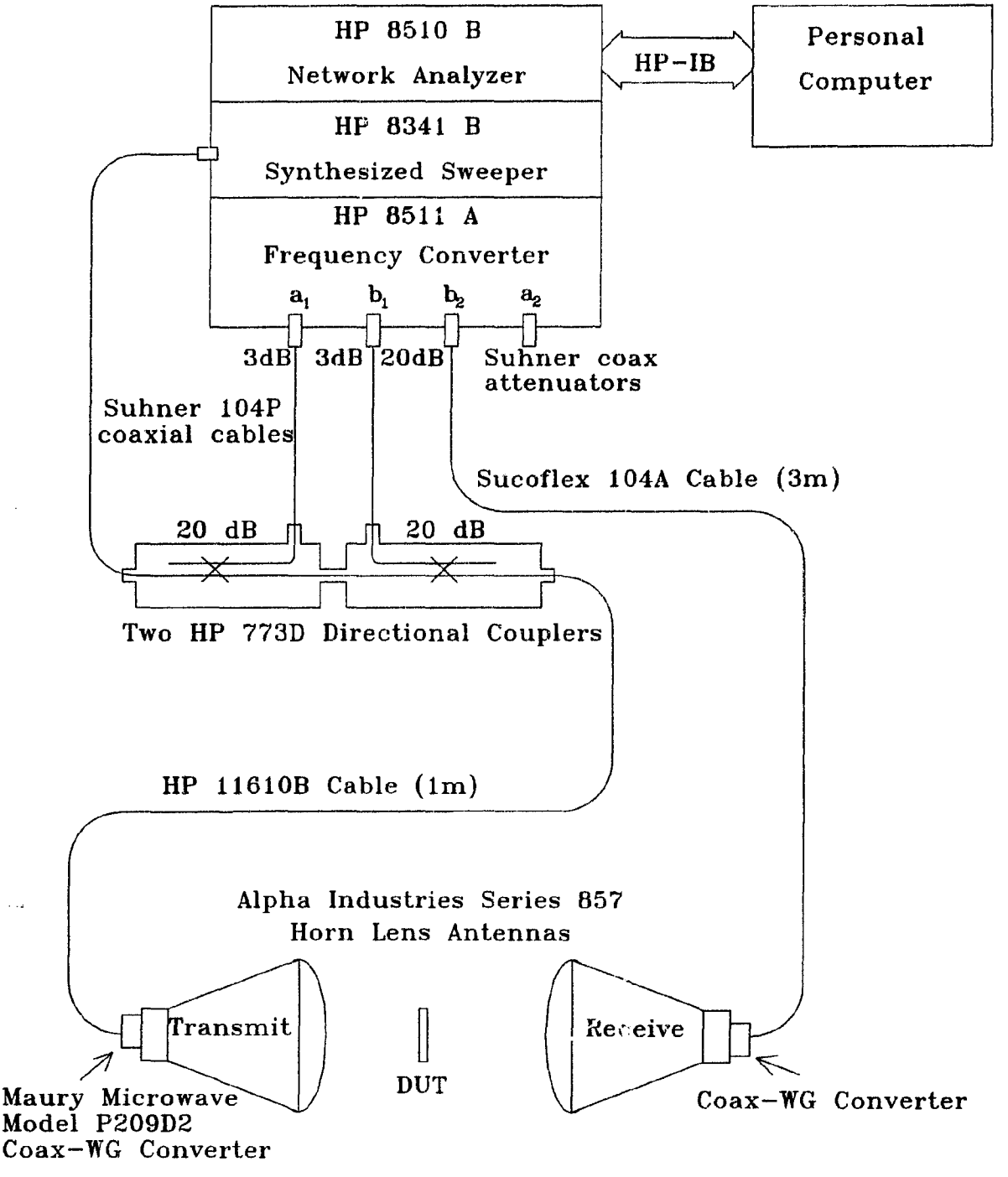

Figure 4.2: Configuration of equipment.

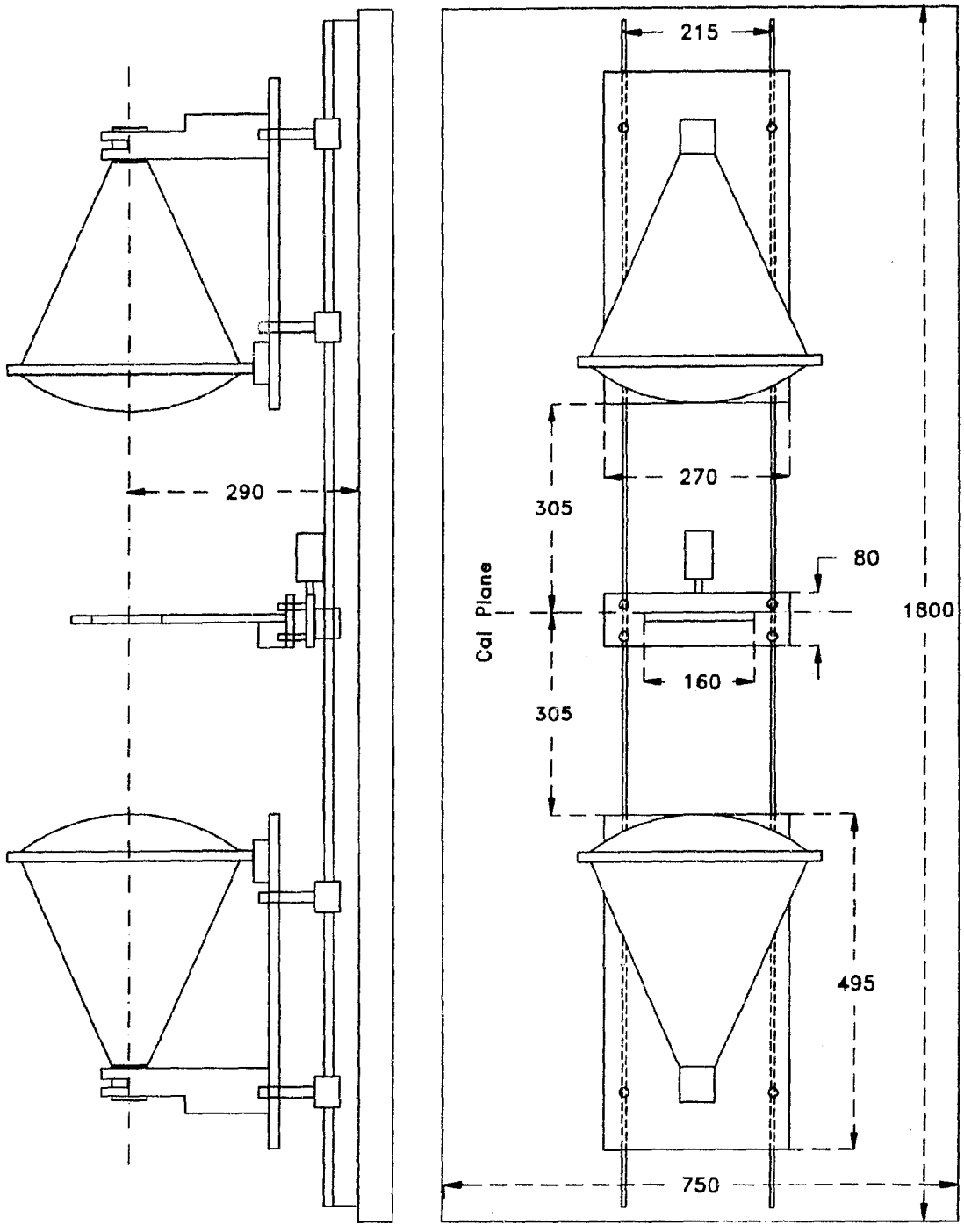

Figure 4.3: Measurement bench. All dimensions are in mm.

The basic operation of the system can be explained from Figure 4.2. The Hewlett Packard network analyzer is controlled by a personal computer via the HP Interface Bus. The microwave signal, generated by the synthesized sweeper, is divided in the two directional couplers. This is done to have a reference signal a_1 and a reflected signal b_1. The main signal goes through the directional couplers via a coaxial cable to the transmitting antenna. The transmitting antenna focuses the energy where the DUT (Device Under Test) will be placed. The reflected signal from the DUT is received by the Transmit antenna and measured at the b_1 port of the frequency converter. The transmitted signal that goes through the DUT is collected by the Receiver antenna and via coaxial cable it is measured at the b_2 port of the frequency converter. The signals that are received in the frequency converter are processed by the HP 8510 network analyzer. The receiving antenna can be rotated through 360 degrees to make cross polarization measurements possible.

The dimensions of the measurement bench are shown in Figure 4.3. The antennas are mounted on top of metal platforms that are fitted with rollers onto rails that extend over the whole length of the table. The antennas can therefore be moved closer or further from each other along the rails. The rails are fitted to a laminated wood surface that is 45 mm thick. The antennas can also be shifted sideways on the metal-platforms. At each corner the metal-platforms are attached to adjustable bolts and nuts which are connected to the rollers on the rails. This configuration enables the antennas to be moved in any desired direction, making it possible to align them with great accuracy. The sample holder is also fitted to a stable platform that can be moved along the rails. The position of the sample holder can be determined accurately by a micrometer fitted to the measurement bench. The micrometer is accurate to 0.01 mm.

The dimensions of the antennas used are shown in Figure 4.4.

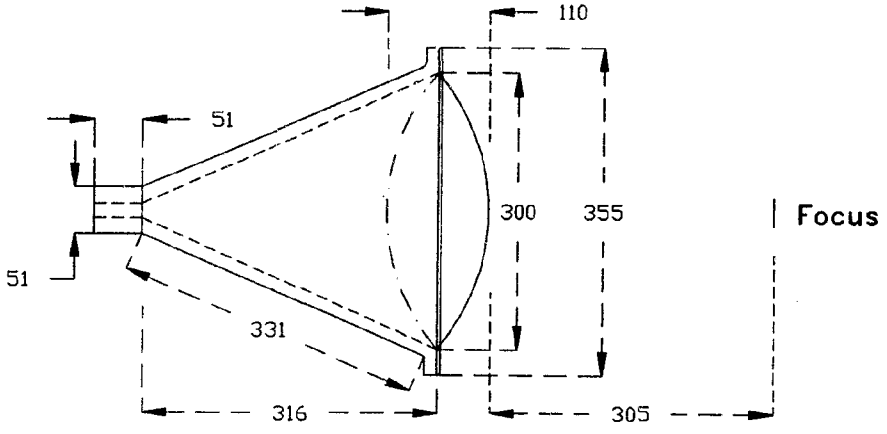

Figure 4.4: Alpha Industries Series 857 Horn Lens Antenna (Ku-band). All dimensions are in mm

In the next chapter the radiation characteristics of the antennas will be determined. This is done to make sure that the assumptions made in Section 2.6 regarding the incident wave (i.e. uniform plane wave and semi-infinite slab (no diffraction)) are met.

The free-space setup described in this thesis is similar to the one in use at the Pennsylvania State University [61, 79]. More detail on the components used in the measurement system can be found in Appendix C.

Chapter 5

Study of the Fields in the Focal Region

> In nature there is no effect without a cause;
> understand the cause and you will have no need of the experiment
>
> — Leonardo da Vinci (1452–1519)

5.1 Introduction

As stated previously, the theory developed to measure the constitutive parameters of a slab (chiral or achiral) assumes that a *plane wave* is incident upon a *transversely infinite slab*. The extent to which these assumptions are met in the free-space measurement system will be determined in this chapter.

The following aspects of the radiation pattern are important for their application in the measurement system:

1. Focus: The position of the focus must be known since the calibration standards and the sample must be placed at this point. The antennas are placed facing each other so that their respective focal planes are coincident.

2. Amplitude distribution in the focal plane[1]: The amount of diffraction from the sample edges or the sample holder can be determined from the amplitude distribution in the focal plane.

3. Phase distribution in the focal plane: During calibration with the conducting plate (*i.e. short*) as well as during measurement, a plane wave (i.e. flat phase front) is assumed.

4. Amplitude and phase distribution in planes before and behind the focal plane (focal depth): During calibration an offset short is placed up to half a wavelength from the focal plane, and it is therefore important that the reflection amplitude

[1]The focal plane is defined as a plane normal to the direction of propagation and passing through the focus.

from the plate (and the sample, after calibration) be the same over a small distance around the focal plane.

5. Phase distribution along the direction of propagation: The beam radiated by the focused lens antenna is approximately Gaussian. Since the wavelength in the focal region of a Gaussian beam is longer than that of a plane wave in free space this should be accounted for in the calibration of the free-space setup.

There are two methods to obtain the radiation characteristics of the horn lens antennas. The first is to get the radiation pattern from a theoretical analysis. The advantage of this method is that if the analysis is accurate, the radiation pattern can be computed at any position of interest. However, an accurate theoretical analysis of the radiation pattern is very difficult and is based on certain assumptions regarding the field distribution in the aperture of the antenna.

The second method is to measure the radiation pattern in an anechoic chamber. The result obtained is very accurate because the actual field is probed and no assumptions are made. The disadvantage of this method is that the radiation pattern is known only at the measured positions and frequencies.

In the sections that follow, both methods will be used and their respective results compared.

5.2 Measured Radiation Pattern of Antenna

5.2.1 Method of Measurement

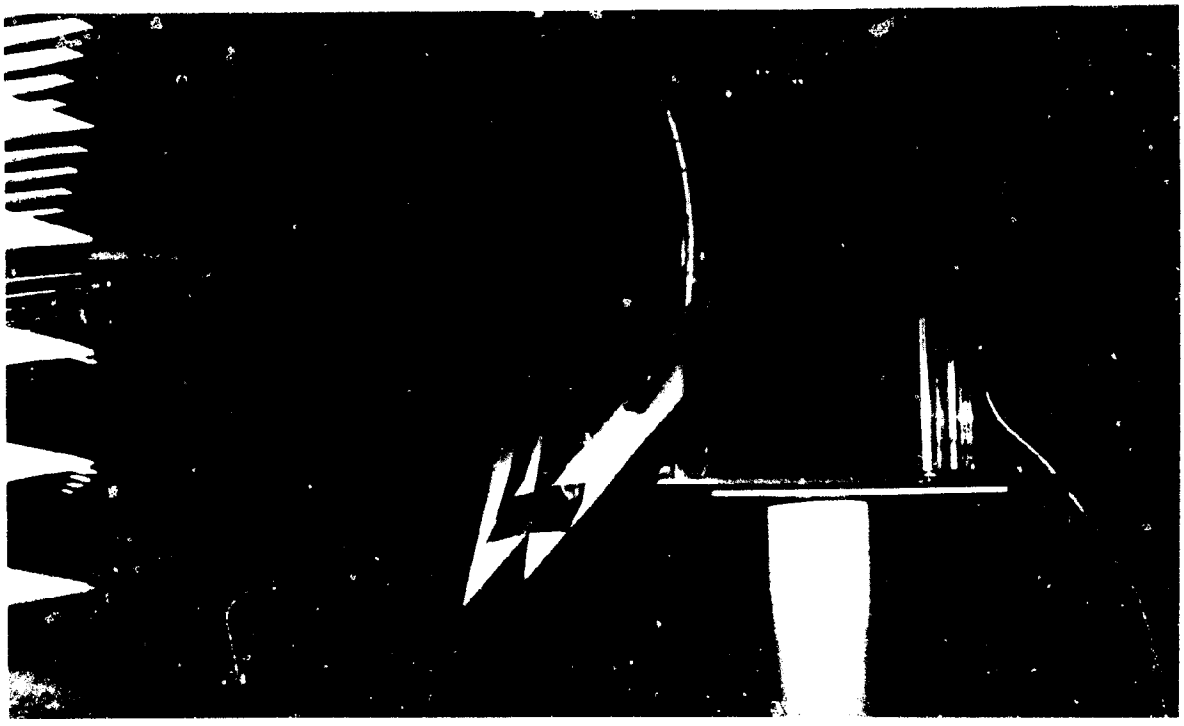

Figure 5.1: Position of the probe and antenna to measure the radiation pattern of the antenna.

The measurements were done in the anechoic chamber at the University of Stellenbosch[2]. A comparison between the radiation patterns of the two antennas showed that they are identical for all practical purposes and the results of only one will therefore be shown in the thesis.

The antenna was placed on a stable pedestal inside the anechoic chamber as shown in Figure 5.1. The antenna was then carefully aligned to the planar scanner in both the x- and the y-directions. The radiation pattern was then measured using open ended Ku-band (12.4-18.0 GHz) and X-band (8.2-12.4 GHz) waveguide as probes for the high and the low frequency measurements respectively.

5.2.2 Probe Correction

The electric field in the aperture of the open ended waveguide has a sinusoidal distribution in the H-plane and a uniform distribution in the E-plane. The measured field (i.e. the S_{21} value) is therefore a convolution of the E-field distribution in the probe aperture and the radiated E-field of the antenna at that position. The actual field at the center of the waveguide opening can be found by deconvolution [83, Sections 4.3.1 and 4.3.2]. Probe correction was done using a code [84], that uses both the co-polarized and cross-polarized measured data to give the probe-corrected radiation pattern. The difference between the probe-corrected and the un-corrected measurements was not significant and it was concluded that the measurements, without probe-correction, are sufficient to study the radiation patterns of the antennas for the purpose of this thesis.

5.2.3 The Electric Field Along the Focal Axis

The coordinates used are shown in Figure 5.2. The axis of the antenna is defined to

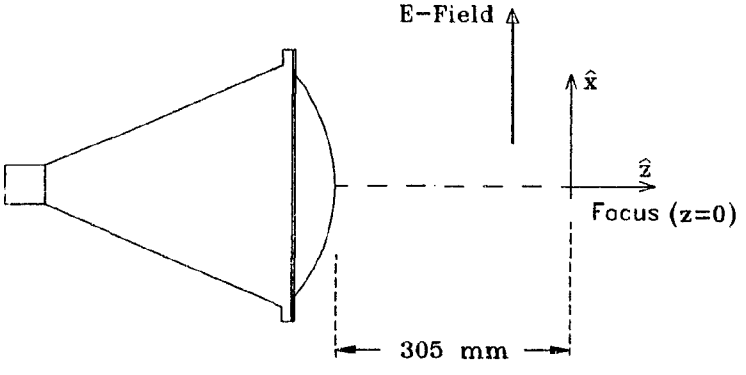

Figure 5.2: Coordinate system for the measured radiation pattern. The focus (z=0) is 305 mm from the front surface of the lens. The x- and z-axes lie in the E-plane and the z- and y-axes lie in the H-plane.

[2]The inside dimensions of the anechoic chamber are 9.1 m× 5.5 m× 3.7 m and the walls are fully covered with microwave absorbing material. The near-field probe is positioned on a planar scanner and its position can be accurately controlled by computer.

be the z-axis. Measurements showed that the focus is approximately 305 mm from the front surface of the lens of the antenna and the focal plane will be defined to be the transverse plane at z=0.

The radiation pattern along the direction of propagation is shown in Figure 5.3 and Figure 5.4. Measurements are shown for the specified center frequency of the antennas, 13.5 GHz. The focus is defined as the position where the beam waist is the smallest and where the phase of the wave traveling through the focal plane is flat in both the E- and the H-plane.

From Figure 5.3 and Figure 5.4 it was found that the focus is approximately 305 mm in front of the lens of the antenna. The "exact" location of the focal plane was determined by making planar cuts around this point. The measured amplitude and phase in the E- and the H-planes in this region are shown in Figure 5.5 and Figure 5.6. From Figure 5.5 and Figure 5.6 it can also be seen that neither the amplitude nor the phase changes significantly along the axis from 10 mm in front to 10 mm behind the focal plane. It can therefore be concluded that the transverse properties of the field illuminating the calibration plate, or the sample, at any position from 10 mm in front to 10 mm behind the focal plane can be assumed to be essentially invariant. It is therefore tempting to conclude that the magnitude of the reflection coefficient from the plate, or the sample, will be independent of its position in this region around the focal plane. However in Section 6.6 it will be shown that the measured reflection coefficient is in fact not independent of the position of the calibration plate. This is the result of multiple reflections between the calibration plate and the antenna and not the "actual" reflection coefficient of the plate since the incident field is approximately constant in this region around the focal plane.

5.2.4 The Electric Field in the Focal Plane

The radiation pattern of the co-polarized component of the field in the focal plane can be seen in Figure 5.7, and that of the cross-polarized component in Figure 5.8. From the contour graph in Figure 5.7 it can be seen that the change in the phase, from the focal axis (middle) to where the amplitude is -10 dB, is approximately 17 degrees in the H-plane and in the E-plane the change in phase is approximately 4 degrees. This change in phase can also be seen from Figure 5.6. Since most of the radiated energy is inside the -10 dB spot of the antenna and the phase change is less than 20 degrees in this region it can be concluded that the error contribution because of this variation in phase will be very small. This can be motivated by the Rayleigh far-field criterion where a phase deviation from planar of $\pi/8$ radians is assumed to be acceptable [83].

Measurements in front and behind the focal plane have shown that the phase front curvature in the two planes becomes more significant as the distance from the focal point increases.

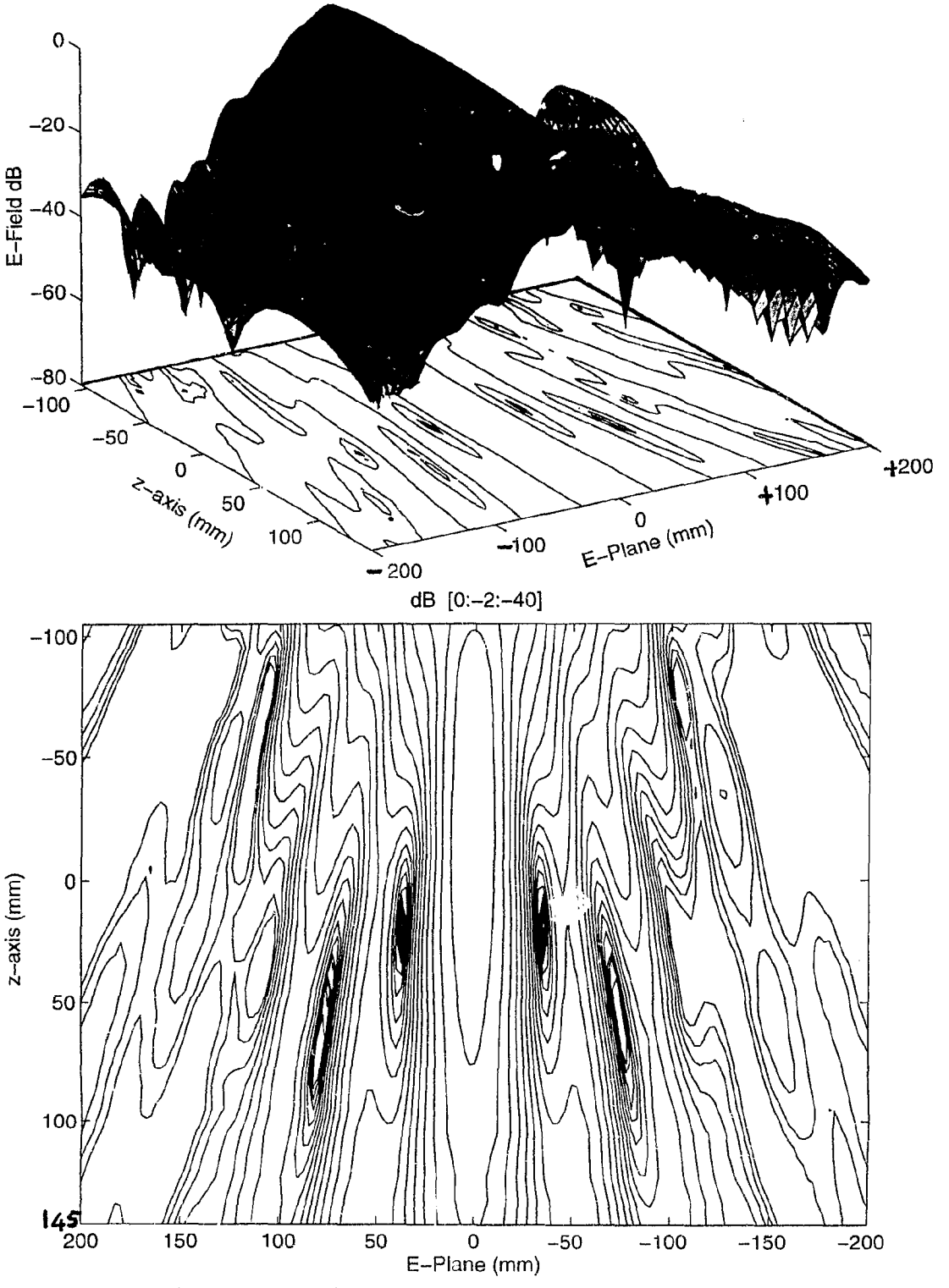

Figure 5.3: Amplitude in dB of the radiation pattern in the E-plane along the z-axis: from z=-105 mm to z=+145 mm. Frequency 13.5 GHz. Spatial dimensions all in mm. 2 dB difference between contours with the -2 dB contour in the middle.

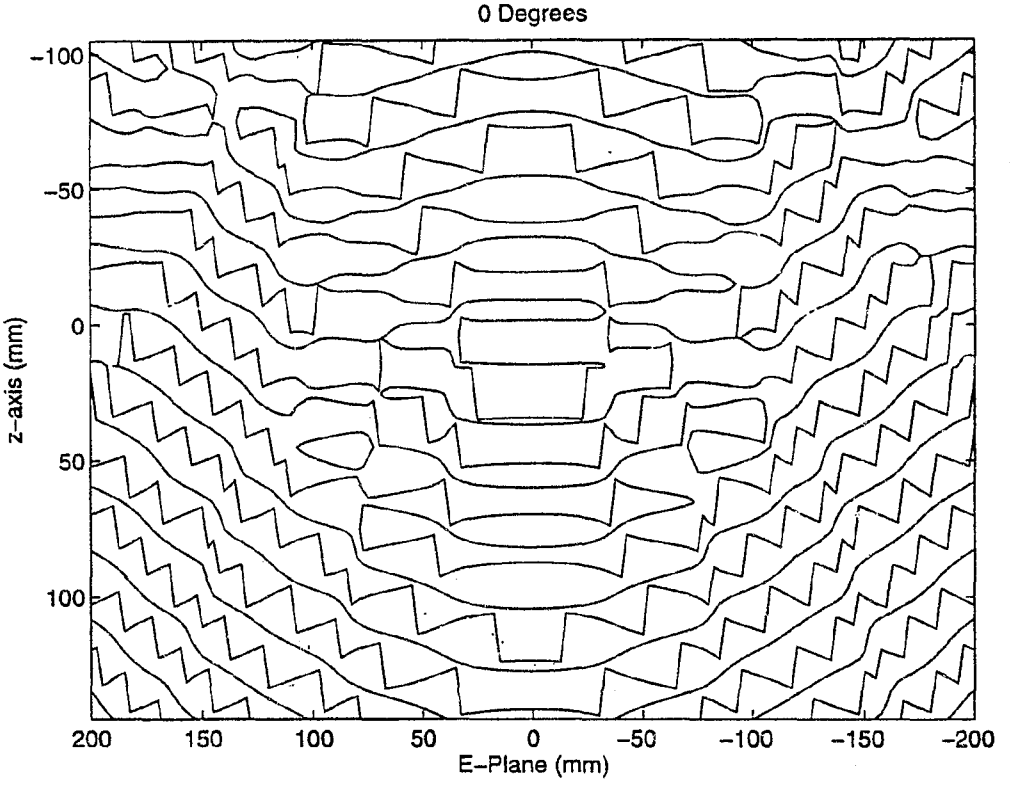

Figure 5.4: 0 Degrees contour graph of the phase (at 13.5 GHz) of the radiation pattern along the z-direction: from z=-105 mm to z=+145 mm. All spatial dimensions are in mm.

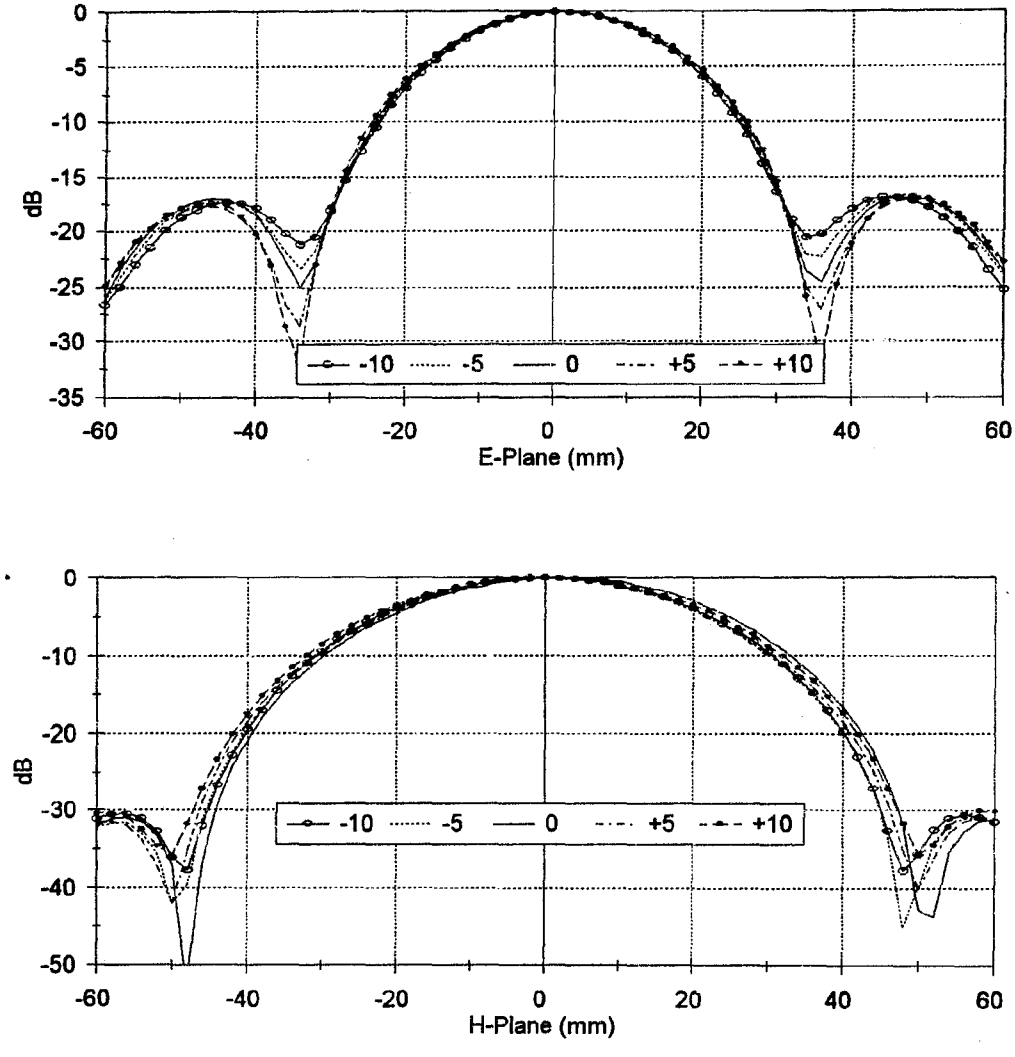

Figure 5.5: Amplitude radiation patterns in the E- and H-planes at 5 mm intervals from 10 mm in front to 10 mm behind the focal plane. Frequency 13.5 GHz.

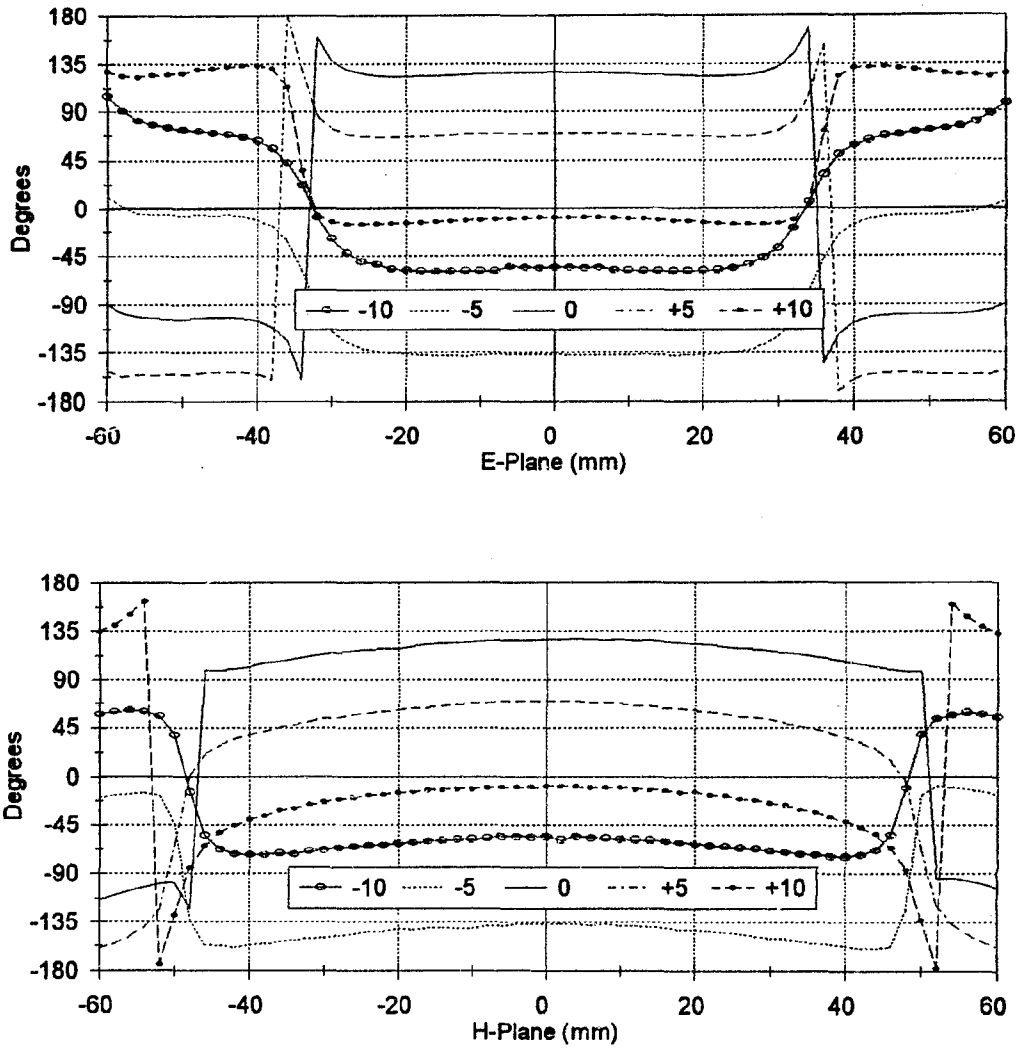

Figure 5.6: Phase radiation patterns in the E- and H-planes at 5 mm intervals from 10 mm in front to 10 mm behind the focal plane. Frequency 13.5 GHz.

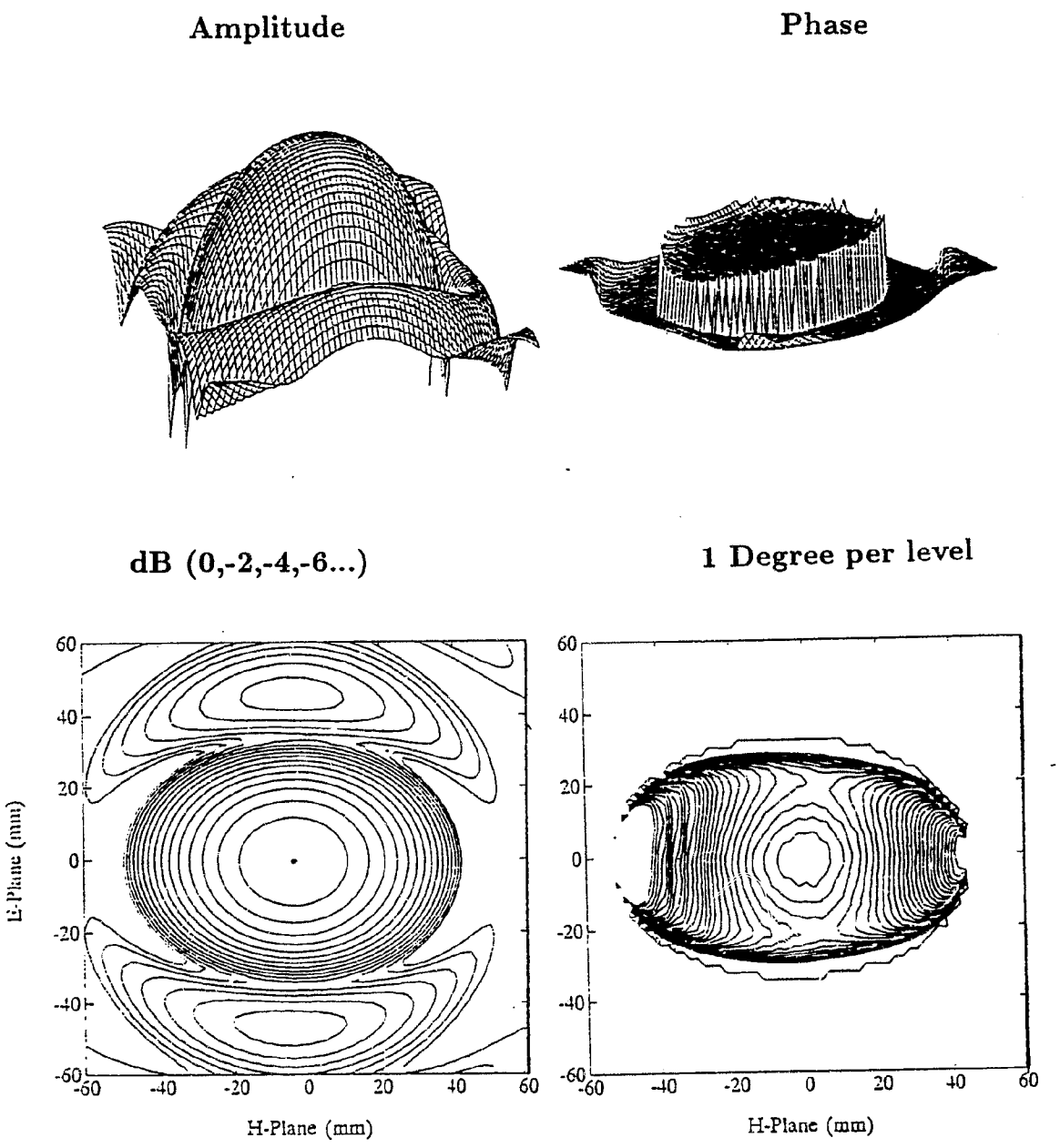

Figure 5.7: Radiation pattern of co-polarized component in the focal plane at 13.5 GHz; showing 3D plots and contour plots of the amplitude (dB) and the phase (Degrees).

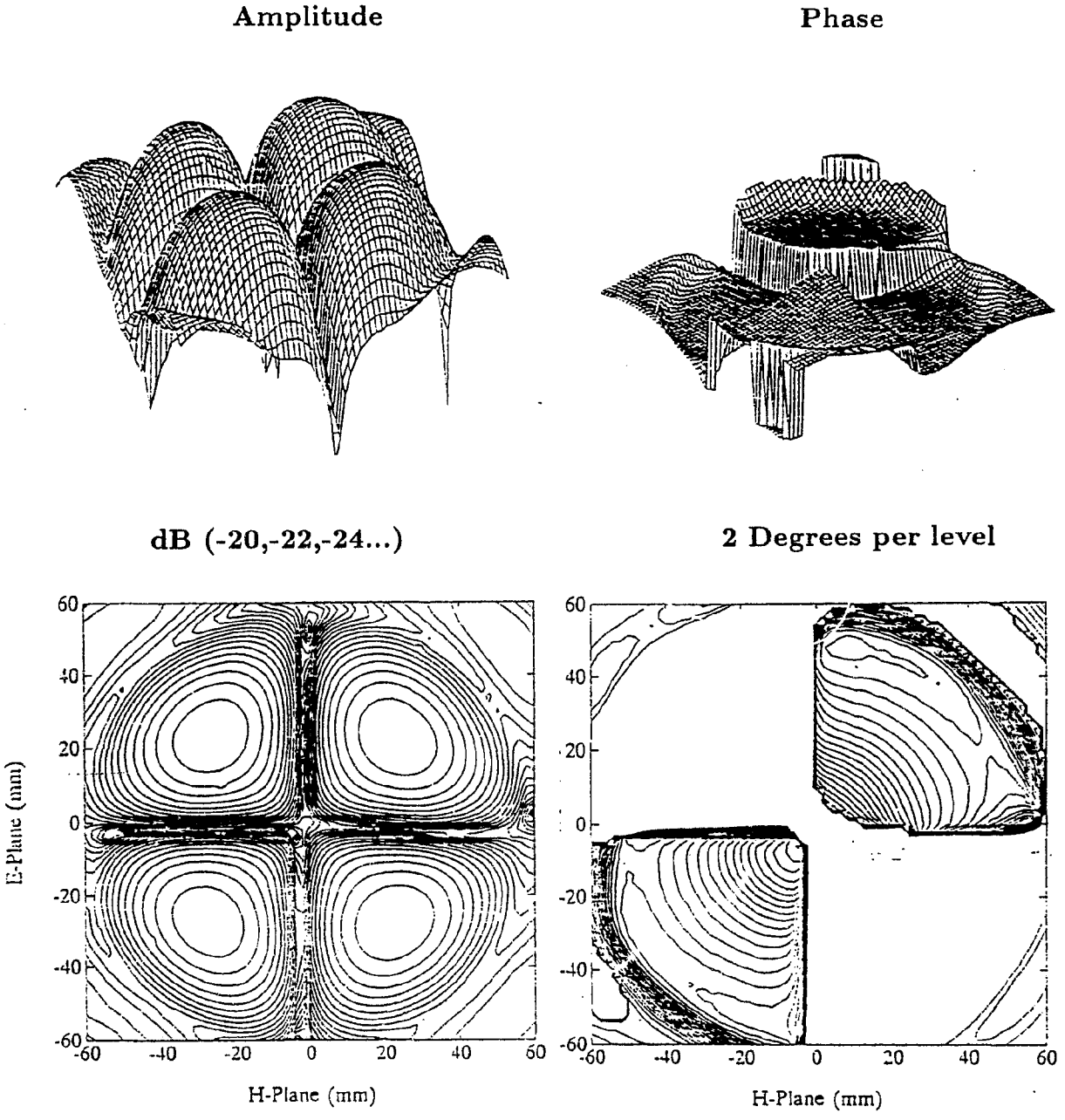

Figure 5.8: Radiation pattern of cross-polarized component in the focal plane at 13.5 GHz; showing 3D plots and contour plots of the amplitude (dB) and the phase (Degrees).

5.2.5 Cross Polarization of the Radiated Field in the Focal Plane

Since polarization measurements are required to characterize artificial chiral media it is necessary that the field incident upon the chiral slab and the field of the antenna that measures the transmitted wave, S_{21}, are linearly polarized. A measure of the linearity of the field radiated by the antenna was obtained by taking cuts, along the E- and H-planes, through the maximum of the four lobes of Figure 5.8. These cross-polarized components were then normalized to the maximum of the co-polarized field of Figure 5.7. The results are shown in Figure 5.9.

The maximum value of the cross-polarization component is 20 dB lower than the maximum of the co-polarized component. However it is important to notice that this is off boresight (i.e. off the z-axis). On boresight the cross-polarized component is more than 50 dB below the maximum of the co-polarized component. The polarization linearity of the antennas was confirmed by measurements of the cross-polarized component of the transmission coefficient of achiral (dielectric) samples. The measurements of Polyurethane (Figure F.1) and Quartz-Silicone (Figure F.4) show that the cross-polarized component of the transmission coefficient, S_{21y}, is less than -50 dB. Since the transmission coefficient should be linearly polarized (and with no rotation), i.e. $S_{21y} = 0$, these measurements give a good indication of the capability of the antennas to make accurate polarization measurements.

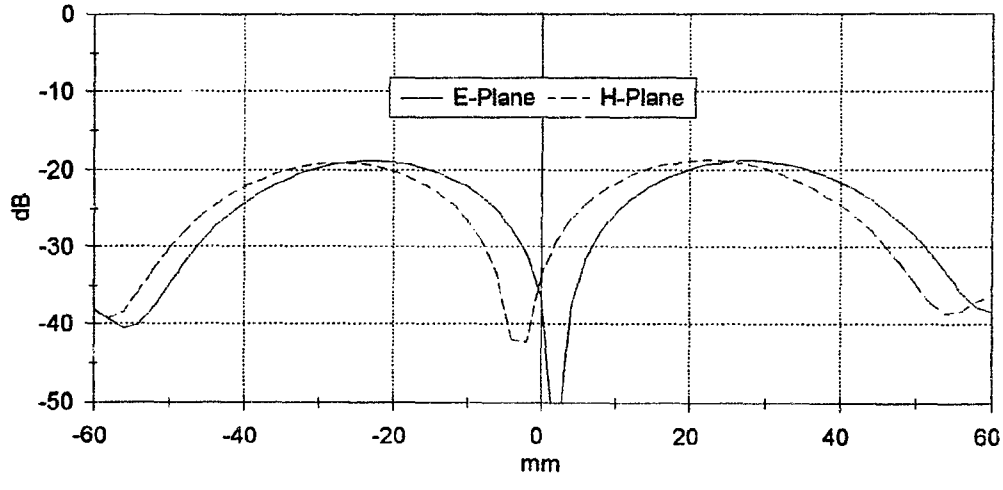

Figure 5.9: Amplitude plots (in the focal plane at 13.5 GHz) of the cross-polarized component normalized to the maximum of the co-polar component.

5.2.6 Frequency Dependence of the Radiation Pattern in the Focal Plane

The fields in the focal region were also measured at 11, 13.5 and 16 GHz. The fields in the E- and H-planes are shown in Figure 5.10 and Figure 5.11 respectively.

As expected Figures 5.10 and 5.11 also show that there is a notable decrease in the spot sizes as the frequency increases. Table 5.1 gives quantitative details in this regard.

Contour graphs of the fields in the focal plane at 11 GHz and 16 GHz are shown in Figure 5.12 and Figure 5.13.

The ratio between the co- and the cross-polarized components of the field in the focal plane at 11 and 16 GHz was found to be approximately the same as that at 13.5 GHz. From the phase data of Figures 5.10 and 5.11 it can be concluded that the wave front adequately approximates a plane wave in the focal region at the higher and the lower frequencies.

	11 GHz		13.5 GHz		* 13.5 GHz		16 GHz	
	H-Plane	E-Plane	H	E	H	E	H	E
-3 dB	45	35	36	30	33	25	31	25
-8.68 dB (1/e)	73	56	58	47	52	39	49	40
-10 dB	78	59	62	50	55	42	53	42

Table 5.1: Measured spot size in mm. (* Measured by supplier, Appendix C.)

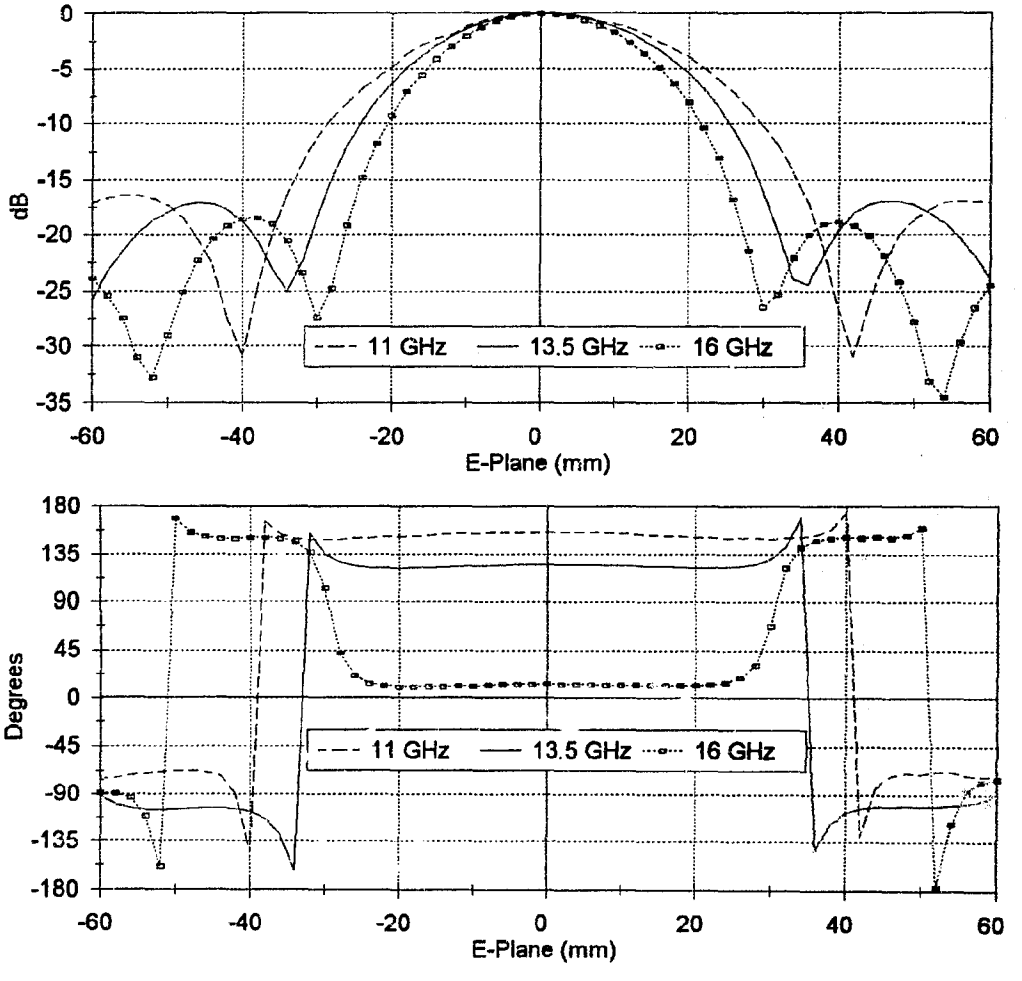

Figure 5.10: Amplitude and phase plots in the E-plane of the co-polarized component in the focal plane at 11, 13.5 and 16 GHz.

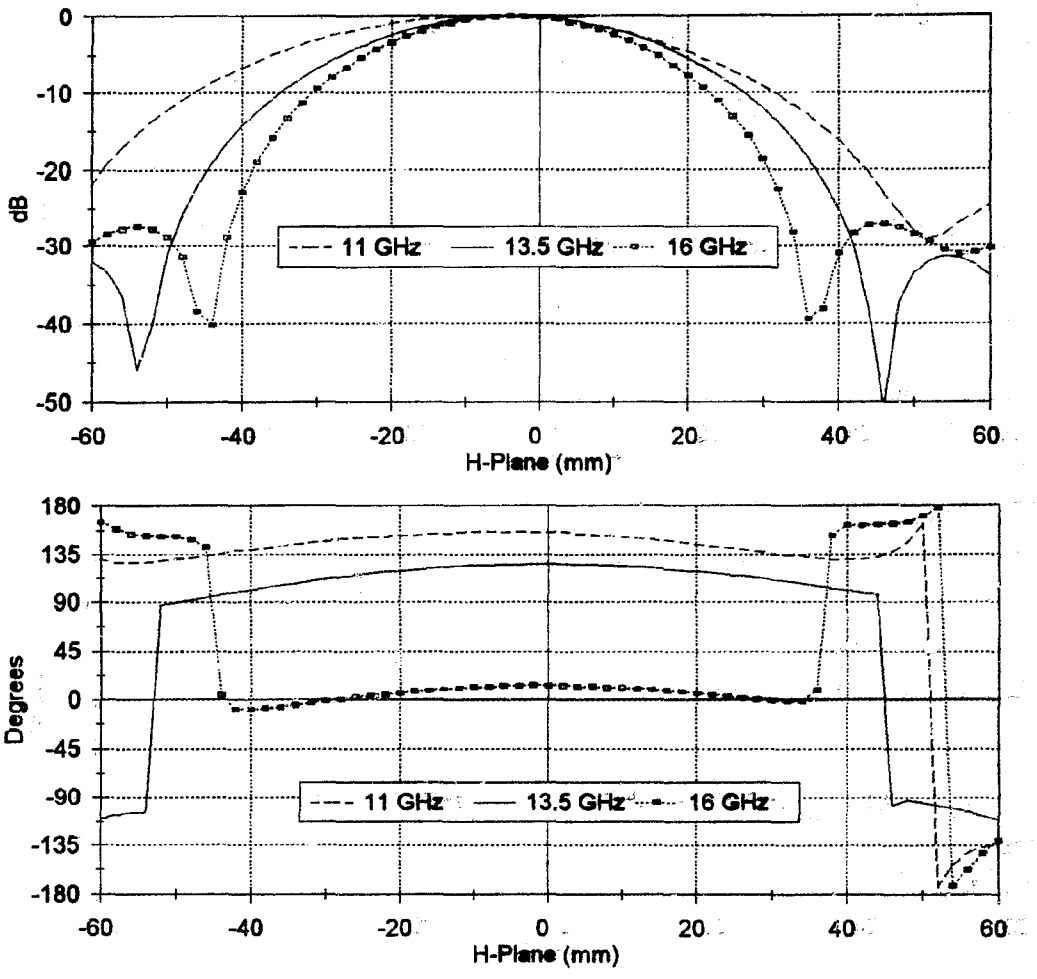

Figure 5.11: Amplitude and phase plots in the H-plane of the co-polarized component in the focal plane at 11, 13.5 and 16 GHz.

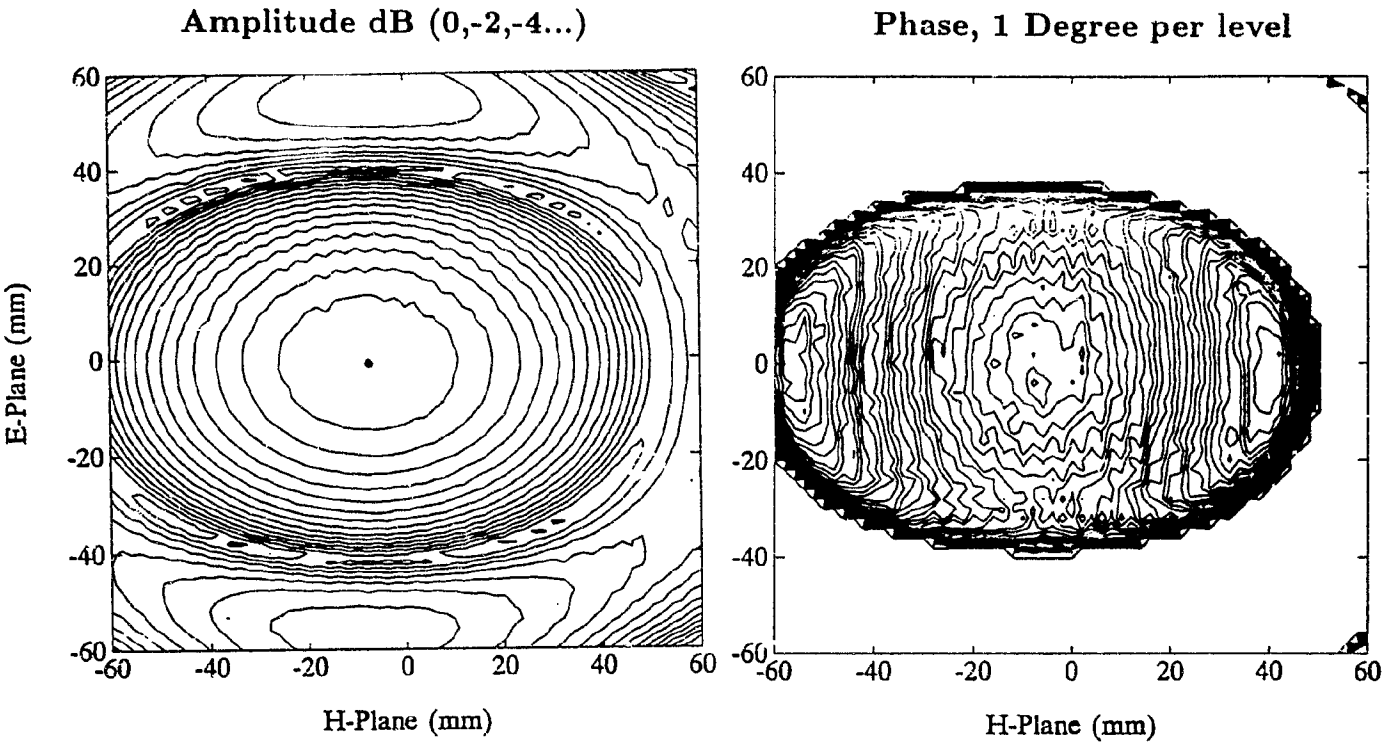

Figure 5.12: Amplitude and phase contour plots of the co-polarized component in the focal plane at 11 GHz.

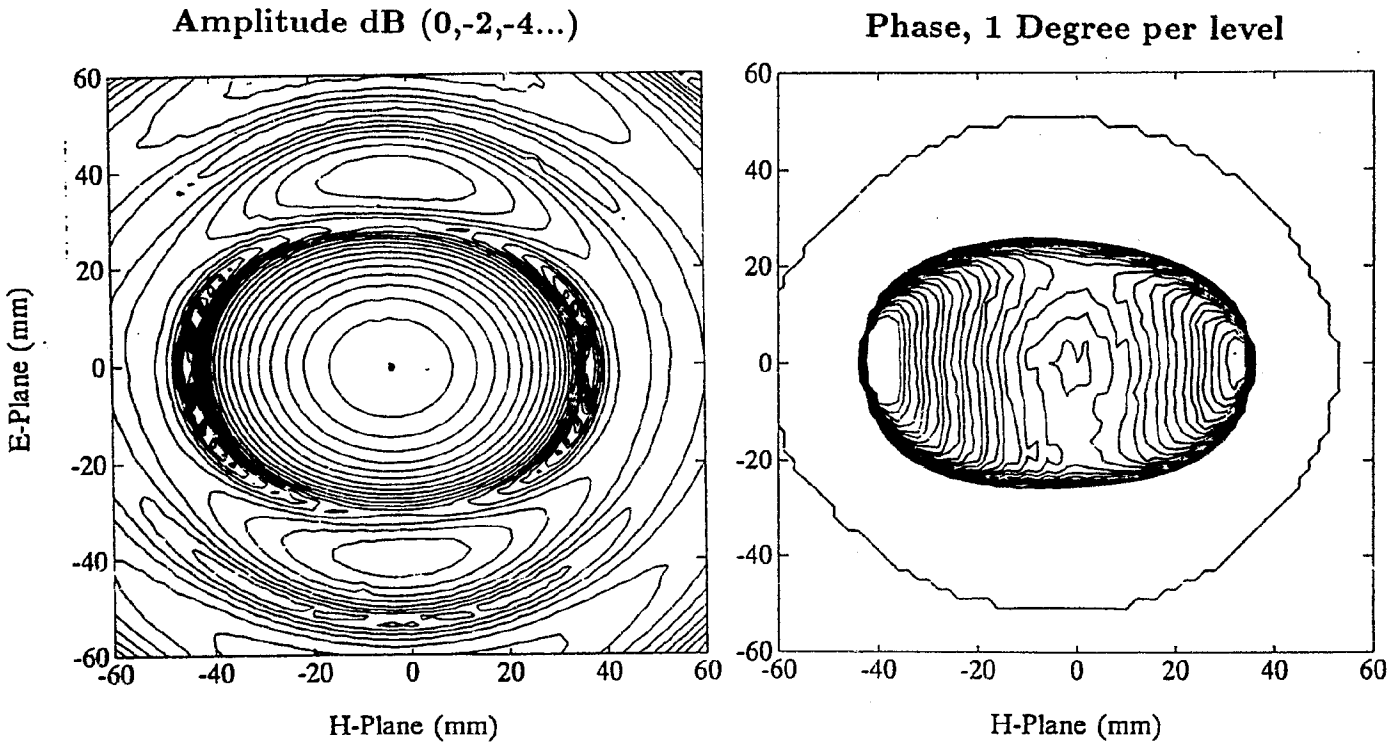

Figure 5.13: Amplitude and phase contour plots of the co-polarized component in the focal plane at 16 GHz.

5.2.7 Focused Beam Depth

The focused beam depth can be defined as the distance along the focal axis at which the beamwidth rises by 50 per cent at a level of say -10 dB [78, Section 3.2.1] The theoretically predicted field depth can be found in Table 5.4. The amplitud ur plot of Figure 5.3 shows that the -10 dB beamwidth does not increase by 50 pe cent in the measured region (z=−105 mm to z=+145 mm with z=0 at 305 mm in front of lens) which should include the predicted focal beam depth of approximately 200 mm.

Although the beam depth gives an indication of the region over which the field amplitude is relatively constant it does not imply that the phase front will also be relatively plane in this large region.

However, from the amplitude and phase data shown in Figures 5.5 and 5.6 it can be concluded that the field properties are satisfacto y in the region of length 20 mm centred on the focal plane where measurements and calibration will be done.

5.2.8 Dispersion in the Focal Region

A wave that travels along the inside of a waveguide gets dispersed (i.e. the wavelength of the bounded wave will be longer than that of a plane wave in free-space). Dispersion is also present in systems that radiate Gaussian or quasi-Gaussian beams as is the case with lens antennas [78, 85, 86, 87, 88]. The dispersion can be explained as the result of a superposition of plane waves that form the focused beam. The wavelength in the focal region must be known since it plays a vital role in the calibration of the free-space setup (see Chapter 6). The wavelength was measured using the following two methods.

In the first the wavelength was measured by probing the field along the focal axis as described in Section 5.2.1. The difference in the measured phase between these positions was then used to calculate the elongated wavelength on the focal axis. The phase was measured at intervals of 3 mm from z=-5 mm to z=+7 mm at 13.5 GHz. The measured wavelength (at 13.5 GHz) in the focal region on the focal axis was found to be $\lambda \approx 23.1$ mm whereas the wavelength for a plane wave in free space is $\lambda_o = 22.2$ mm. This is an elongation of the wavelength of about 4.0%. The accuracy with which the probe could be moved along the focal axis was limited and it was decided to measure the wavelength using another method.

The second method was to measure the phase of the reflection coefficient of a sliding plate along the focal axis. The measurements were done with the antenna and the plate in the normal configuration of the free-space measurement setup (Fig 5.14).

Measurements were done at intervals of 1 mm, from 8 mm in front to 8 mm behind the focal plane. The wavelength was calculated by fitting a least squares line through the phase as a function of axial distance. The gradient of this line was then used to determine the wavelength, for every measured frequency, as follows. The change in the phase of the reflection coefficient because of a change in the position of the calibration plate (short) is,

$$\Delta\phi = \beta\, 2\Delta z, \tag{5.1}$$

Figure 5.14: Configuration used to measure the wavelength in the focal region from the reflection coefficient of a sliding calibration plate

and with

$$\beta = 2\pi/\lambda, \tag{5.2}$$

the wavelength in the focal region can be determined from the following equation,

$$\lambda = 4\pi/\frac{\partial\phi}{\partial z}, \tag{5.3}$$

where $\frac{\partial\phi}{\partial z}$ is the gradient of the phase along the z-axis in the region of the focus.

The phase of the reflection coefficient was measured after two different calibration methods were used to calibrate the reflection coefficient. In the first a 7 mm calibration[3] (7C) was done at the end of the coaxial cable where the transmitting antenna is connected. The results after 7 mm calibration (7C and 7C-Gated) are shown in Figure 5.15 (b) and (c). The severe ripple in Figure 5.15 (b) is caused by multiple reflections between the shifting calibration plate and the antenna not being removed in the 7 mm calibration. For the results of Fig 5.15 (c) a time domain gate (centered around the plate with a span of 1.5 ns) was used to remove the multiple reflections between the plate and the antenna. The results obtained from the uncalibrated[4] data were approximately the same as those for the ungated (7C) data (Fig 5.15 (b)).

In the second method a free-space calibration[5] (FS) was done at the focus of the antenna and the results obtained from this method are shown in Figure 5.15 (d) and (e).

[3] Hewlett Packard calibration procedure for 7 mm coaxial connectors.

[4] Uncalibrated data is also referred to as raw data.

[5] The free-space calibration method is described in detail in Chapter 6.

The free-space calibration (FS) will remove most of the multiple reflections between

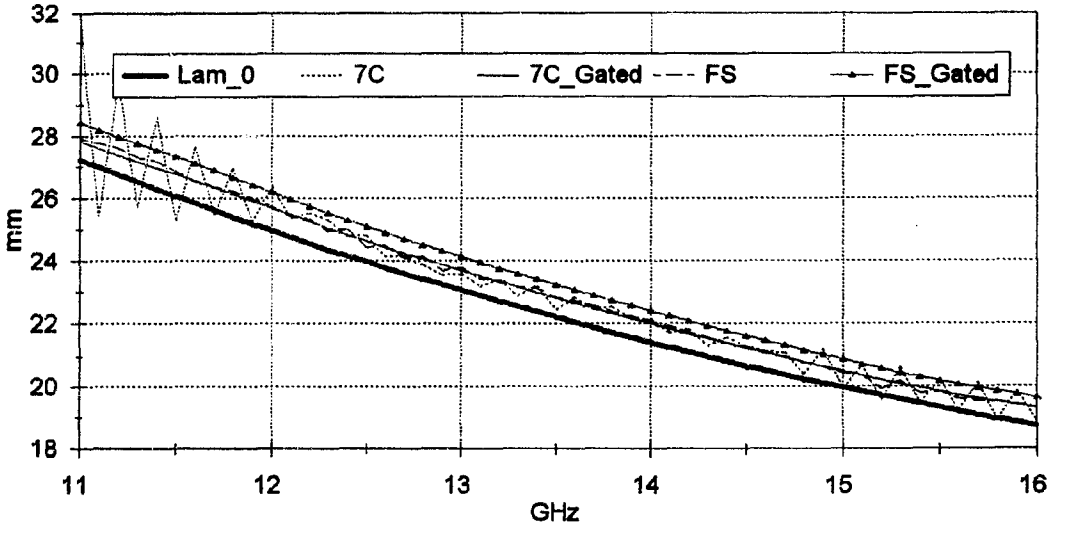

Figure 5.15: Wavelength measured with a sliding calibration plate.
Two methods used: 7mm calibration (7C) and Free-space calibration (FS).
(a) Lam-O: free space wavelength λ_0 with no dispersion,
(b) 7C: 7mm cal,
(c) 7C-Gated: 7mm cal with time domain gating,
(d) FS: free-space cal,
(e) FS-Gated: free-space cal with time domain gating.

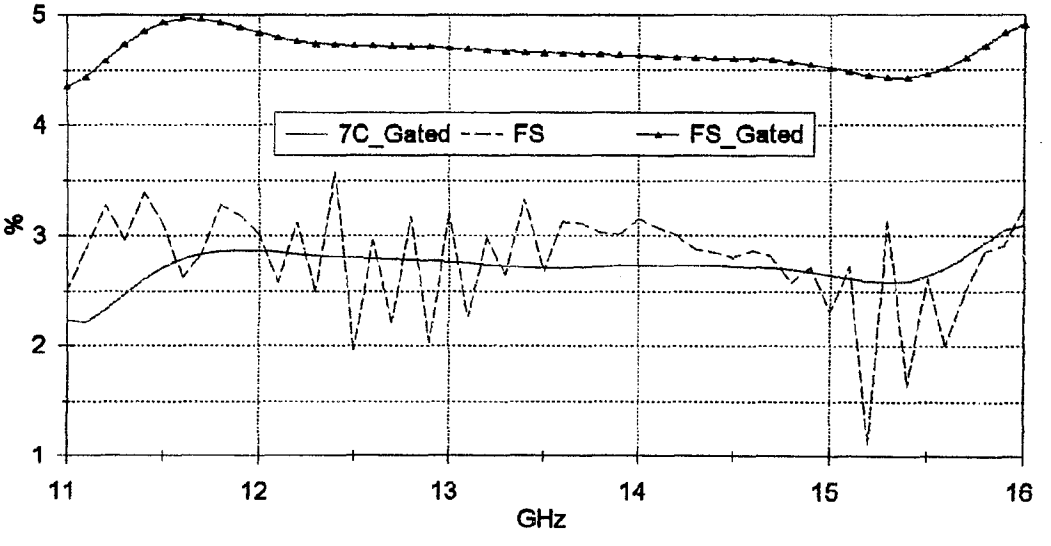

Figure 5.16: Elongation of wavelength as measured with a sliding calibration plate.

the plate and the antenna. This is because in the FS calibration the multiple reflections occur between the calibration plane and the measurement instrument but in the 7 mm calibration method the multiple reflections are beyond the calibration plane and are not present during calibration and can therefore not be removed by calibration. Note, however, that even with free-space calibration multiple reflections still cause significant residual effects. This will be discussed in Chapter 6 and 7.

The effects of unwanted multiple reflections can be removed after calibration by placing a time domain gate around the calibration plate. The result is a much smoother wavelength measurement, as shown in Figure 5.15 (c) and (e).

Figure 5.16 shows the wavelength elongation as a percentage of the free space wavelength λ_0. The measured wavelength after free-space calibration before gating (Fig 5.15 (d)) is very similar to that after 7 mm calibration with time domain gating (Fig 5.15 (c)). The small ripple is a result of the multiple reflections not being removed completely by the free-space calibration procedure. However, if a time domain gate is used after free-space calibration, the resulting wavelength is smoother but about 1.5% longer than the ungated (FS) measurement. This phenomenon can not be explained without further investigation. The choice concerning the "correct" wavelength for use in the calibration procedure is discussed in the conclusion of this chapter, Section 5.4.

The unexpected behavior at the high and the low frequencies of the gated measurements is believed to be due to mathematical "windowing" introduced by the Hewlett Packard time domain algorithms, the details of which are not published. Consequently it was decided to use extrapolation from the middle of the band to determine the values at the low and high frequencies.

5.3 Theoretical Analysis of a Lens Focused Conical Horn Antenna

If the radiation pattern of the antennas could be predicted accurately by a theoretical model, pattern measurements would be unnecessary and the radiation pattern could be determined at any desired position. A good theoretical model would also make it possible to design similar horn lens antennas.

There are several methods to determine the radiation characteristics of antennas in general. It is not the purpose of this thesis to do a thorough theoretical analysis of the radiation characteristics of focused lens antennas. Only a basic theoretical analysis based on the book by Musil and Žáček [78] and Gaussian beam theory [86] will be presented as a basis for testing the experimental work.

The electric field strength, $E(P)$, of a focused antenna having an arbitrary aperture field distribution is approximated by [78, eqn (3.20)]

$$E(P) = \frac{ik}{4\pi}\int_S F(\xi,\eta)\frac{e^{-ikr_1}}{r_1}[\mathbf{z}\cdot\mathbf{s}+\mathbf{z}\cdot\mathbf{r_1}]dS. \tag{5.4}$$

with P an arbitrary point in the far-zone or Fraunhofer region, as shown in Figure 5.17.

The complex aperture field distribution of the antenna is assumed to be rotationally symmetric and of the form [78, eqn (3.21)],

$$F(\xi,\eta) = [1-l^2]^n \exp\left(ik\frac{l^2a^2}{2f}\right), \tag{5.5}$$

where l is the ratio of the distance of an arbitrary point P_o on the aperture from its center to the radius a of the circular aperture, n is the degree of aperture illumination,

and f is the focal distance of the focused antenna. The phase distribution is chosen so that a wave emerging from the aperture is spherical and is directed at the focus F.

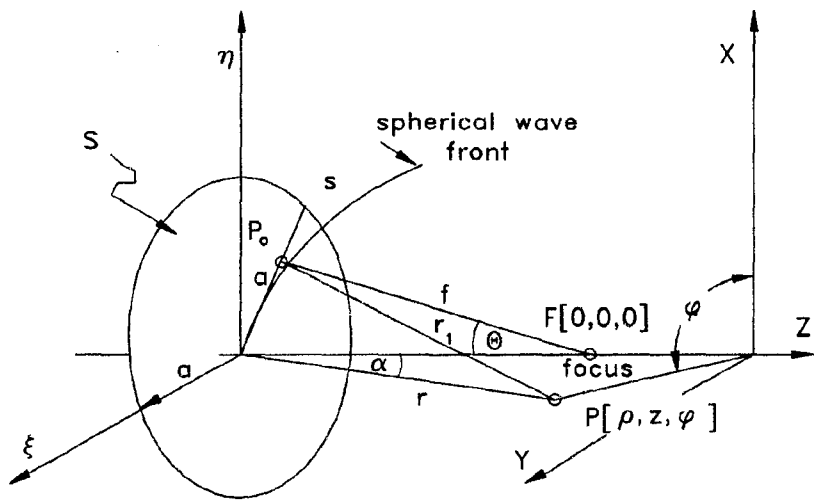

Figure 5.17: Coordinate system for theoretical analysis of the radiation pattern of the focused beam formed by an antenna with a circular aperture. ($\rho' = \rho/a$ and $z' = z/a$.) [78, Fig. 3.8]

5.3.1 The Electric Field in the Focal Plane

A focused beam has a minimum diameter in the focal plane (i.e. at the focus F), and microwave energy is concentrated in the close vicinity of the focus, Figure 5.18. With

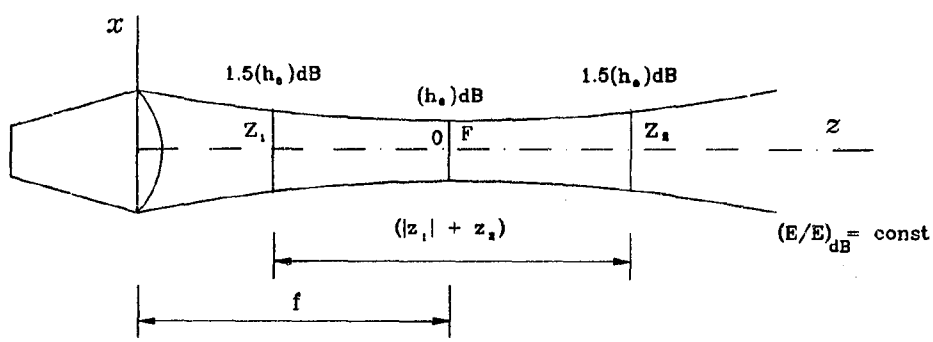

Figure 5.18: Field distribution of a focused lens antenna.

some approximations made, the value of the electric field (normalized to the value of the field strength at the focus) in the focal plane is [78, eqn (3.31)].

$$E_N(\varrho', 0) = i2^{n+1}(n+1)\Gamma(n+1)\frac{J_{n+1}(x)}{x^{n+1}}, \tag{5.6}$$

with $x = \frac{k'\varrho'}{r'}$, $k' = ka$, and $r' = [(f' + z')^2 + \varrho'^2]^{1/2}$. This equation is used to determine the width of a focused beam in the focal plane. The analysis predicts that the beamwidth is reduced by reducing the wavelength, λ_o, reducing the focal distance, f, and increasing the radius of the circular aperture. It is consistent with the physical properties of aperture antennas.

The dimensions of the antennas used in the free-space system[6] (at 13.5 GHz) are,

$$\begin{aligned} a/\lambda_o &= 6.75, \\ f/\lambda_o &= 13.73. \end{aligned}$$

and the ratio between the focal distance, f, and the aperture radius, a is,

$$f/a = 2.033.$$

Using these values and the method described in [78] the calculated spot width in the focal plane is shown in Table 5.2. The electric field in the focal plane can be

	11 GHz		16 GHz		13.5 GHz	
	n=0	n=1	n=0	n=1	n=0	n=1
-3 dB	28.2	35.3	19.4	24.3	23.0	28.7
-8.68 dB (1/e)	45.6	57.1	31.4	39.3	37.1	46.5
-10 dB	48.4	60.0	33.3	41.3	39.4	48.9

Table 5.2: Spot width as obtained from (5.6) [78, eqn.(3.31) and Table 3.1]. (All measurements are in mm.)

determined by solving Equation (5.6) for different values of ϱ'. A comparison between the theoretically predicted and the actual measured radiation patterns is shown in Figure 5.19. Although none of the graphs are identical there is some agreement between the measured radiation pattern in the E-plane and the predicted pattern for $n = 1$ degree aperture illumination. This is also evident from a comparison of Table 5.1 and Table 5.2.

The measured and the predicted (Musil *et al.*) values of the 1/e beamwidth will now be compared to that of Gaussian beam theory [85, 86]. The Gaussian beam theory is based on the paraxial wave approximation, which assumes that the propagating free space wave is fairly parallel to the axis of propagation. The beam radius at which the amplitude decreases to $1/e$ (or -8.686 dB) of its value on the focal axis is [86, eqn (5.8)],

$$w = w_0\sqrt{1 + (\frac{\lambda_0 z}{\pi w_0^2})^2}. \tag{5.7}$$

The minimum beam radius at the focus is w_0, and $\lambda_0 = c/f$ is the wavelength in free space.

[6] Details are given in Appendix C.

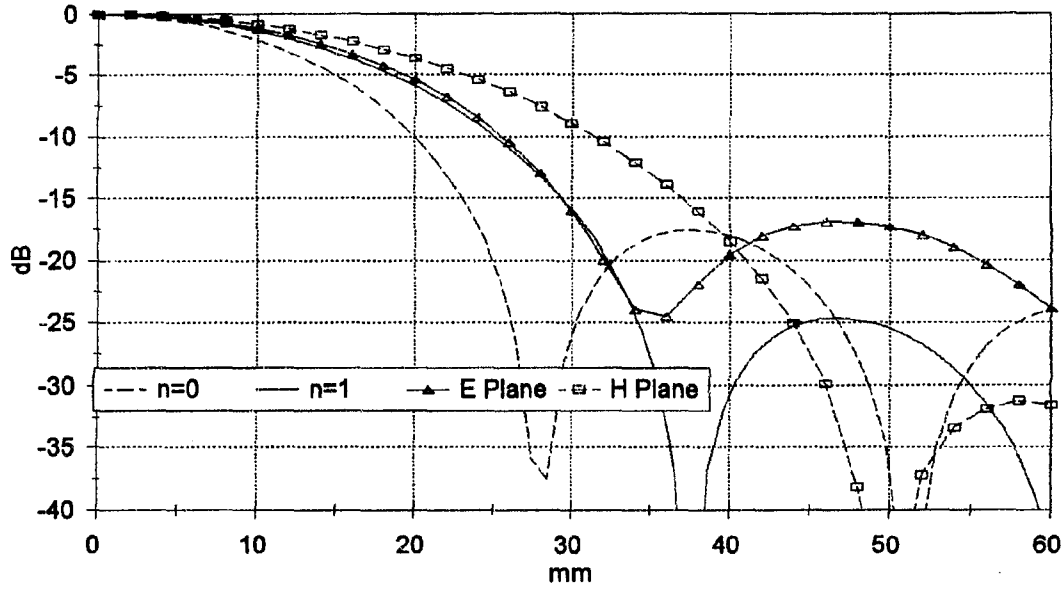

Figure 5.19: Radiation pattern in the focal plane at 13.5 GHz. Theoretical (Eqn 5.6): Degree of aperture illumination n=0 and n=1, Measured: H-Plane and E-Plane.

The wave number at the focus of a Gaussian beam is given by [86, eqn (5.14)],

$$k = k_0 - \frac{2}{k_0 w_0^2}, \tag{5.8}$$

or,

$$\lambda/\lambda_0 = 1/(1 - \frac{2/w_0^2}{k_0^2}), \tag{5.9}$$

with, k_0, the free space wave number. This important equation allows the wavelength in the focal region to be computed if the beam radius w_0 is known. For example if $w_0 = \lambda_0$ then $\lambda/\lambda_0 = 1.053$ which corresponds to 5.3% elongation. From (5.8) the minimum beam radius w_0 can be calculated from the following equation,

$$w_0 = \sqrt{\frac{2}{k_0(k_0 - k)}}, \tag{5.10}$$

where $k_0 = 2\pi/\lambda_0$ and $k = 2\pi/\lambda$, with λ the wavelength at the focus.

To make a connection between the measured results and the Gaussian beam theory the measured wavelengths of Figure 5.15 are used as λ in the equation (5.10). The results are shown in Figure 5.20. The effect of time domain gating is again evident at the lower and higher frequencies of the gated data.

The spot size where the field strength is $1/e$ of the maximum value on the focal axis is shown in Table 5.3. In this table a comparison is made between the $1/e$ spot size values as obtained by three different techniques:

1. Theoretical prediction by Equation (5.6) (i.e. the theory of Musil *et al.* [78, eqn (3.31)]).

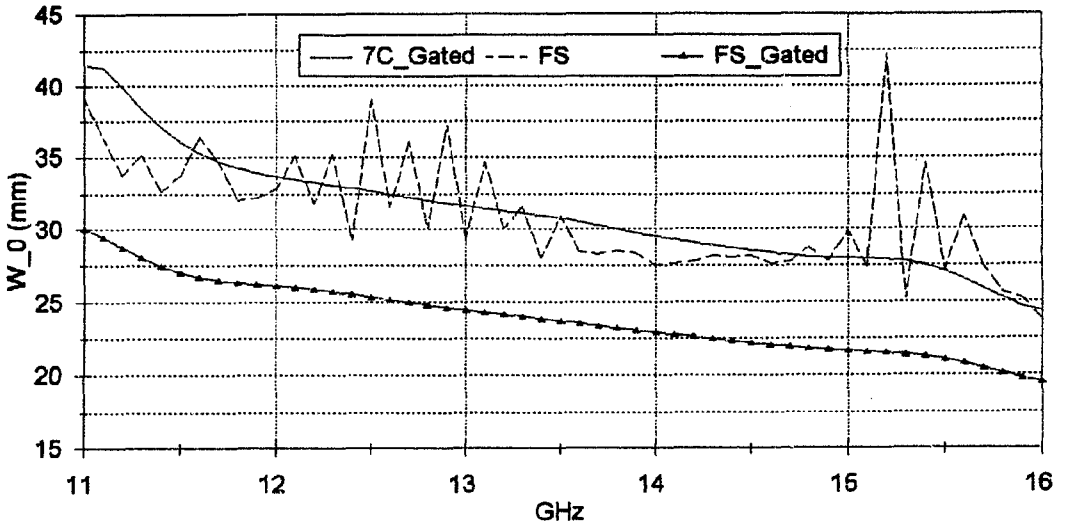

Figure 5.20: The minimum beam waist, w_0, predicted using Gaussian beam theory and λ measured with a sliding calibration plate. (See Table 5.3 for a comparison of directly measured $1/e$, or w_0, spot size.)

2. Combination of wavelength measurements (Section 5.2.8) and then use of Equation (5.10) (from the Gaussian beam theory).

3. Radiation pattern measurements as described in Section 5.2 (Figures 5.7, 5.12 and 5.13).

This table shows that there is very good agreement between the theoretical prediction by Musil ($n = 1$, Eqn (5.6)), the Gaussian beam theory (Eqn (5.10) using the wavelength as obtained by a sliding calibration plate (FS-Gated) Fig 5.15), and by probing the field in an anechoic chamber as described in Section 5.2. The spot size in the E-plane corresponds better with the theoretical predictions. Note that there is also an interesting similarity between the (7C-Gated) result and the measured pattern in the H-Plane. These results are discussed in Section 5.4.

Freq	Theoretical		Theory and Measured		Measured	
	Eqn.5.6, Musil [78]		w_0, Fig 5.20, Gaussian Beam			
	n=0	n=1	7C-Gated	FS-Gated	H-Plane	E-Plane
11 GHz	47	57	72	55	73	56
13.5 GHz	37	47	62	47	58	47
16 GHz	31	39	51	40	49	40

Table 5.3: Comparison of the spot sizes where the field strength is $1/e$ of the maximum on the focal axis.

5.3.2 The Electric Field in Transverse Planes

In this section an attempt is made to determine the field at all positions in front and behind the focal plane. The normalized values of the electric field in planes of constant z' may be expressed in the following form [78, eqn (3.38)],

$$E_N(\varrho', z') = \frac{E(\varrho', z')}{|E(0, z')|} = \frac{ie^{-i(k'r'+w/2)}[C^n W_o(w,x) + iE^n W_1(w,x)]}{\left|C\left(\frac{2}{i}\right)^{n-1}\frac{\partial^n}{\partial w^n}\left\{\frac{i}{w}[1-e^{iw/2}]\right\}\right|} \tag{5.11}$$

with $C = (1+\cos\alpha)/r'$, $E = (1+2\cos\alpha)\varrho'/r'^3$, $w = k'(f'-r')/(f'r')$. The special functions ${}^nW_{\nu-1}(w,x)$ are defined in [78].

For the free-space measurement system it is important to know the depth of the focused beam. This parameter can be defined as a distance, $L = |z_1| + z_2$, along the focal axis at which the beamwidth rises by x percent. (See Fig 5.18). The beam depth, L, is determined from the field distribution in the planes of constant z', using Equation (5.11). The normalized field depth z_2/λ_o is defined as the distance between the focus $F[0,0,0]$ and a plane $z = \text{const} > 0$, at which the beam width (at the -10 dB level) increases by 50 percent. This parameter was determined using Fig 3.11 and Fig 3.12 of the book by Musil and Žáček [78]. If the field distribution is assumed to be symmetric with respect to the focal plane $z' = 0$, the focused beam depth is,

$$L = 2z_2.$$

For the antennas used in the free-space system the results are shown in Table 5.4.

Aperture illumination	
$n = 0$	$n = 1$
$z_2/\lambda_o = 5$	$z_2/\lambda_o = 4.12$
$L = 222.2$ mm	$L = 183.11$ mm

Table 5.4: Field depth corresponding to an increase of beam width by 50 percent at a level of -10dB.

In Figure 5.3 it was found that the distance between the focal axis and the -10 dB contour, does not increase by 50 percent in the measured region and it can be concluded that the measured beam depth, L, exceeds the theoretical prediction of approximately 200 mm. (See also the conclusions made in Section 5.2.7.)

5.3.3 Phase Distribution in Transverse Planes

The theory developed to calculate the constitutive parameters from the measured scattering parameters requires that the incident wave be a uniform plane wave. This condition requires that the phase distribution in the focal plane, $z = 0$, be constant. The phase distribution in the focal plane, according to the theory developed in [78, eqn.(3.41)], can be approximated by,

$$\varphi(\varrho', z') = \arctan\left[-\frac{2}{3}\frac{f'}{\varrho'}\frac{J_{n+1}(x)}{J_{n+2}(x)}\right]. \tag{5.12}$$

The theoretical results show that the phase in the focal plane is constant inside the -5 dB spot (see also Fig 5.7) and that there is a change in phase of 180 degrees approximately in the region where there is a null in the field strength.

A comparison between the theoretical and the measured pattern shows that there is reasonable agreement between the theoretical (with n=1 degree aperture illumination) and the measured fields (along the E-plane). This was also the case for the amplitude distribution (Fig 5.19).

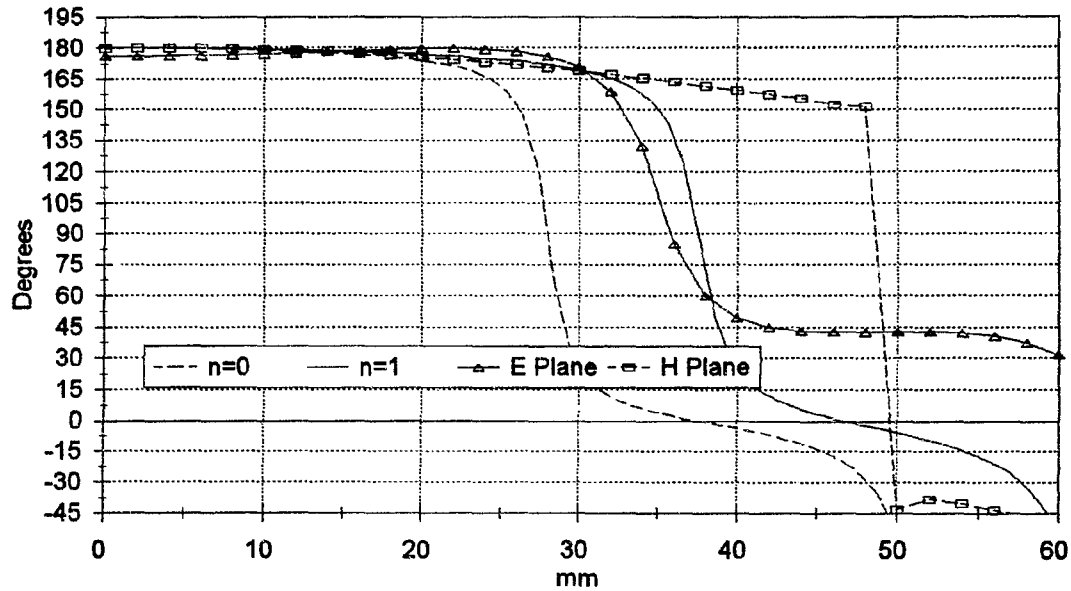

Figure 5.21: Theoretical and measured phase distribution in the focal plane at 13.5 GHz.

The phase distribution in planes of constant z can be found in [78, eqns (3.40), (3.42) and (3.43)]. For uniform illumination $n = 0$, the phase distribution can be expressed in the form [78, eqn (3.44)],

$$\varphi(\varrho', z') = -(k'r' + \frac{1}{2}w) + \arctan\left[-\frac{U_1(w,x)}{U_2(w,x)}\right], \tag{5.13}$$

where $r' \simeq f' + z'$ and $w \simeq -(k'z'/f'r')$. A solution of this equation shows that the phase front becomes less flat the further the plane is from the focal plane. This was also found with the measurements, Figure 5.6. Solution of this equation also shows how the waves travelling towards the focal plane converge and diverge as they travel towards and away from the focus.

5.3.4 Phase Distribution along the Focal Axis

It has been said that because of the nature of focused beams, dispersion can be expected in the focal region of these antennas. In Section 5.2.8 this dispersion (or elongation of

the wavelength) was measured (Fig 5.15) and in this section the measured results will be compared with the theoretical prediction of the elongation.

Musil and Žáček [78, Section 3.2.1.4] showed theoretically that the wavelength in a focused beam, λ, is greater than the wavelength in free space, λ_0. They found that the wavelength in the focused beam can be approximated by the following equation [78, eqn (3.38)],

$$\lambda = \frac{\lambda_o}{1 - \frac{1}{2(n+2)}\frac{a^2}{rf}}, \tag{5.14}$$

where n is the aperture illumination and $r = f + z$.

For the antennas used, the values calculated from this equation were found to be 6.9% for $n = 0$, and 4.5% for $n = 1$ aperture illumination, both at z=0 (i.e. in the focal plane). The value of 4.5% for $n = 1$ agrees well with the measured value of approximately 4.6% for the free-space (FS) calibration and time domain gated value of Figure 5.16.

5.3.5 Comparison of Measured Dispersion of the Free-Space Beam and a Metallic Waveguide

The relevance of this section will become evident in Section 6.5 where the calibration standards are specified. As was said earlier, dispersion is a phenomena that is associated with non-TEM bounded waves. The elongation in the focal region will now be compared to the elongation inside a metallic waveguide. The wavelength in a waveguide is [88],

$$\frac{\lambda_{WG}}{\lambda_0} = \frac{1}{\sqrt{1 - \frac{f_c^2}{f^2}}}, \tag{5.15}$$

where f_c is the cutoff frequency. If the operating frequency is far above the cutoff frequency such that $(f_c/f)^2 << 1$, the dispersion equation (5.15) can be approximated by,

$$\frac{\lambda_{WGaprx}}{\lambda_0} = \frac{1}{(1 - \frac{f_c^2/2}{f^2})}. \tag{5.16}$$

Equation (5.16) and Equations (5.9) and (5.14) are mathematically identical in form. The Gaussian wave model can thus be approximated by the weakly dispersive "waveguide" model by choosing the cutoff frequency of the "waveguide" as,

$$f_c = \frac{c}{\pi w_0}. \tag{5.17}$$

The values for the minimum beam waist, w_0, can be obtained from Figure 5.20. The case for w_0 as obtained after 7mm calibration (7C-Gated) will be illustrated. The cutoff frequency, f_c, with w_0 from Figure 5.20 (7C-Gated) is shown in Figure 5.22.

It is clear from this figure that the "cutoff frequency" is a function of the operating frequency, which is in contrast to the dispersion in a metallic waveguide where the cutoff frequency is only a function of the dimensions of the waveguide.

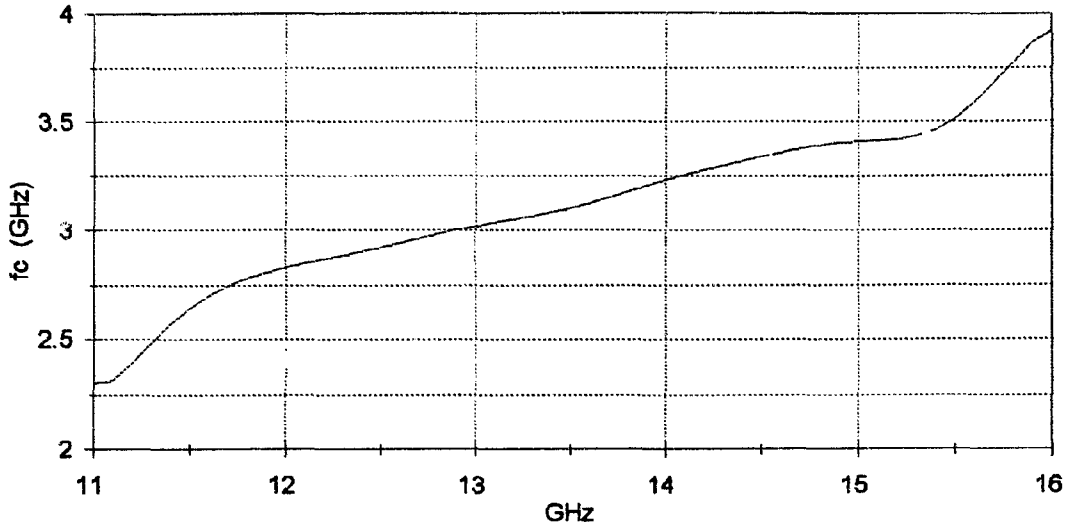

Figure 5.22: Cutoff frequency of the dispersed field in the focal region if the dispersion is modeled as dispersion in a waveguide.

Using these values for the "cutoff frequency" f_c, in Equations (5.15) and (5.16) the results obtained are shown in Figure 5.23 where they are compared to the "actual" measured wavelength (7C-Gated) of Figures 5.15 and 5.16. The results of two different cases are of particular interest. They are where the cutoff frequency, f_c, is assumed to be frequency dependent and secondly where the cutoff frequency is assumed to be frequency independent i.e. constant with a value $f_c = f_c(13.5) \approx 3.125$ GHz. In both of these cases the waveguide model Equation (5.15) and the approximation to the waveguide model Equation (5.16) are shown in Figure 5.23. It is clear that Equation (5.16) approximates Equation (5.15) well.

However the predicted elongation, for both Equation (5.15) and Equation (5.16) for constant $f_c \approx 3.125$, does not compare well with the actual measured elongation (Fig 5.23 (a)) since it predicts much more elongation at low frequencies and less at the higher frequencies.

The importance of this fact will become evident in Section 6.5 where the effect of dispersion on the definition of the offset calibration standards and the calibration model is discussed. It is also important to note that although this analysis was done for w_0 as obtained after 7 mm calibration and time domain gating (7C-Gated) it can also be done for free-space calibration and time domain gating (FS-Gated). Although the results will be slightly different the same conclusion regarding frequency dependent and constant cutoff frequency, f_c, can be made.

5.4 Conclusion

The radiation patterns of the antennas were measured in the focal region and compared to two theoretical models. Some of the results obtained from the theoretical models agreed very well with the measured radiation pattern of the antennas. From

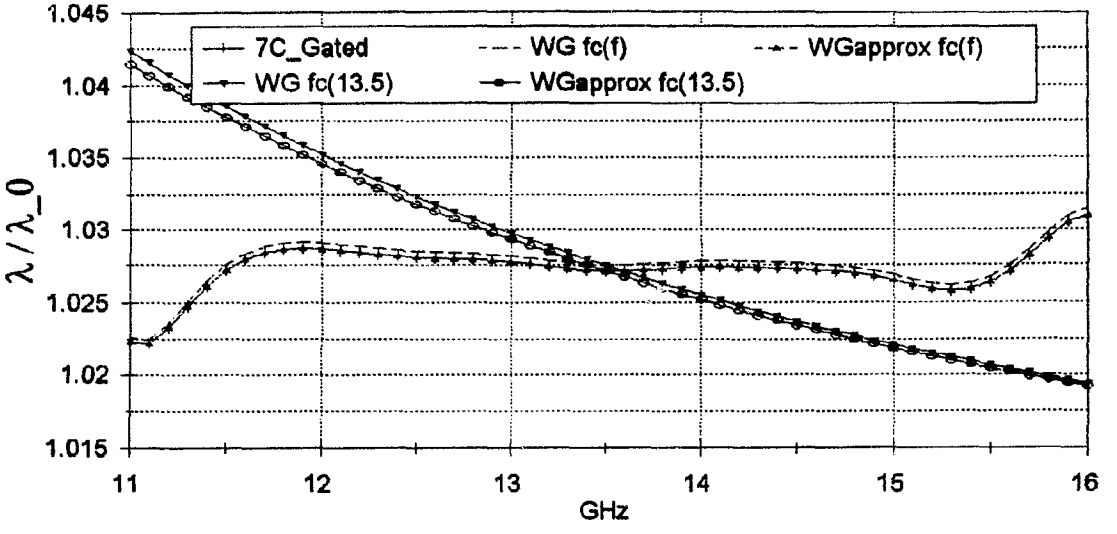

Figure 5.23: Wavelength normalized to λ_0:
(a) 7C-Gated: 7mm Cal with time domain gating,
(b) WG fc(f): Waveguide, eqn. (5.15) with f_c as in Fig 5.22,
(c) WGapprox fc(f): Waveguide approximation, eqn. (5.16) with f_c as in Fig 5.22,
(d) WG fc(13.5): Waveguide, eqn. (5.15) with f_c constant as at 13.5 GHz in Fig 5.22,
(e) WGapprox fc(13.5): Waveguide approximation, eqn. (5.16) with f_c constant as at 13.5 GHz in Fig 5.22.

Figure 5.19 and Figure 5.21 it is seen that there is reasonable agreement between the measured radiation pattern in the E-plane and the theoretical radiation pattern with degree $n = 1$, aperture illumination. The agreement between the theoretical and the measured results are especially good for $\rho/\lambda \leq 1$. Agreement between the measured and theoretical values is also evident from a comparison of Table 5.1 and Table 5.2.

Although the measured radiation patterns (from Section 5.2 and as provided by the supplier of the antennas, Appendix C) are not shown on the same figure, a comparison between the spot size (at 13.5 GHz) in both the E- and the H-planes is made in Table 5.1. The supplied spot sizes are on average approximately 7 mm smaller in diameter than the measured results. This difference could be ascribed to either different measurement techniques or errors in the measurements.

The difference between the measured (actual) and the theoretically predicted radiation patterns (especially in the H-plane) shows that the theoretical analysis is not accurate enough to predict the overall radiation patterns of lens focused conical horn antennas. This difference can be ascribed to the actual aperture field distribution not being the same as assumed in Equation (5.5).

The difference between the radiation patterns can be reduced by using an equation that models the actual aperture field distribution more accurately but to then solve Equation (5.4) for such an aperture field distribution will be more complex and beyond the scope of this thesis.

Initially it was believed that the wavelength in the focal region is approximately $\lambda \approx 1.0275\lambda_0$ (as was measured by the 7 mm calibration and gated (7C-Gated) and the free-space calibration (FS) methods Figure 5.16). All the calculations in Chapter 6

and Appendix D were done with $\lambda \approx 1.0275\lambda_0$. However it is now believed that the elongation is in the region of 4.5 % (i.e. $\lambda \approx 1.045\lambda_0$). This value was obtained by three different methods. The first of these methods, measurement by a probe in an anechoic chamber (Section 5.2.8), resulted in an approximately 4% elongation. In the second method the wavelength was measured from the reflection coefficient of a sliding calibration plate. The values obtained after 7 mm calibration and time domain gating (7C-Gated) and free-space calibration and time domain gating (FS-Gated) were different (Fig 5.16). The question was then posed: "which is the correct value for the elongation, that as obtained after 7mm calibration (7C-Gated) or that after free-space calibration (FS-Gated) ?"

An answer to this question will now be proposed. The comparison in Table 5.3 shows that the measured 1/e spot size (in the E-plane) corresponds very well with the value as predicted by Equation (5.6) for n=1, (see also Figure 5.19). This value for the 1/e spot size also corresponds very well as shown in Figure 5.20, with the value as determined through Gaussian beam theory using the value of λ as obtained after free-space calibration and time domain gating (FS-Gated) in Equation 5.10. The 1/e spot size after 7 mm calibration (7C-Gated) does not agree with the other values and it is therefore believed that the wavelength as measured after free-space calibration and time domain gating (FS-Gated) is closer to the actual wavelength in the focal region. The elongation as predicted by Equation (5.14) for n=1, is also close to this value. It is therefore concluded that the wavelength in the focal region can be approximated by the following equation,

$$\lambda \approx 1.045\ \lambda_0$$

This also agrees with the previously mentioned value obtainable directly from near-field measurements (Section 5.2.8). A very accurate measure of the wavelength could possibly be obtained by moving a small coaxial E-field probe along the axis, but this was not done.

Although there are still some remaining uncertainties regarding the radiation patterns of the horn lens antennas used in the free-space system their most important characteristics have been determined and they are:

1. Focal point.
   The focal position was found to be 305 mm from the front surface of the lens antenna along its bore-sight axis. This is the position where the phase was flattest in the E- and H-planes. Because the -3 dB spot width is given as 4.7 degrees and 25.02 mm in the specifications of the antenna (Appendix C), simple trigonometry yields that the focus is at 304.78 mm from the front of the lens.

2. Spot size.
   It was found that the radiated beam has a narrow waist around the focal point. This will minimize, but not eliminate completely, the diffraction from the edges of a sample placed at the focal point. The -3 dB spot size is approximately 1.35 λ_0 in the E-plane and approximately 1.62 λ_0 in the H-plane. The $1/e$ spot size is approximately 2.1 λ_0 and 2.6 λ_0 in the two planes respectively.

3. Phase distribution.
   The phase distribution in the focal plane was measured and found to be reason-

ably flat inside the -3 dB spot, simulating that of a plane wave. It has been shown that the wave front is very uniform over a field depth of approximately 15 mm around the focus. The fact that the phase is not as flat outside the -3 dB spot, or in front of and behind the focal plane, might act as a source of error both during and after calibration. The quantitative effect of these two imperfections (diffraction and non flat phase) is very difficult to determine theoretically but is expected to be small.

4. Polarization.
   In Section 5.2.5 it was shown and argued that the antennas have good linear polarization on the bore axis (i.e. z-axis), making the antennas suitable for the envisaged polarization measurements.

5. Dispersion.
   The wavelength in the focal region was measured to be $\lambda \approx 1.045\lambda_0$, and this elongation can be accounted for in the calibration procedure.

6. Bandwidth.
   Although the radiation patterns of the antennas were measured only from 11 to 16 GHz they are used up to 17 GHz.

In general it can be concluded that the radiation characteristics of the antennas are as desired. They provide an essentially linearly polarized plane wave over a small area at the focus, and are suitable for accurate free-space measurements.

Chapter 6

Calibration of the Free-Space System

> But before you base a law on this case test it two or three times and see whether the tests produce the same effects.
>
> — Leonardo da Vinci (1452–1519)

6.1 Introduction

In any measurement there are errors that can be attributed to error sources, classified as follows:

1. Systematic.
   Systematic errors are those that are stable and repeatable, and can be reduced significantly by a good calibration procedure.

2. Random.
   These errors can not be removed because of their random nature. They can be reduced substantially by averaging measurements.

3. Drift.
   Drift (or environmental) errors are those associated with temperature, humidity, pressure or other time dependent factors. These factors can be controlled to some extent but their effect, although very small, can not be completely eliminated.

The effect of systematic errors can be calibrated out by using a calibration error model in which the systematic errors are represented by error terms, determined by measuring "known[1]" calibration standards during a calibration procedure.

A full two-port error model contains twelve error terms [89, 90]. The error terms can be determined by either a "Full 2-Port" or a "TRL (Thru-Reflect-Line) 2-Port[2]" calibration routine. The TRL calibration method, developed by Engen *et al.* [91],

[1]The properties of the calibration standards are not always exactly known.

[2]Terms used by Hewlett Packard to describe two calibration methods to determine all 12 the error terms [89, 90].

is simple to implement and is particularly attractive for non-coaxial measurements because the calibration standards can be realized easily and accurately.

Since the twelve term error model is a full two-port model it requires that the system be able to transmit and receive at both the ports (i.e. S_{11}, S_{12}, S_{21} and S_{22} measurements can be done.). In the system used for this research it is not possible to transmit and receive with both the antennas without disconnecting any cables (See Fig. 4.2). This is because the HP 8511A Frequency Converter which is used, as part of an HP 8510C network analyzer system, does not have a built in computer controllable switch, unlike the HP 8515A S-Parameter Test Set. It is therefore not possible to use either of the existing calibration methods available on the HP 8510C network analyzer to determine all the error terms of the full two-port model. This research is therefore restricted to a calibration model that contains less terms (Fig. 6.1). A calibration model that contains less error coefficients will not be as accurate in reducing the errors as a full two-port (twelve term) error model would. This is because more error terms will lead to a better representation of all the systematic errors, a better calibration and therefore more accurate measurements.

Nevertheless by using the methods to be described high quality measurements are possible. In addition, by not "blindly" using commercial calibration software, in particular the TRL procedure of Hewlett Packard, deep insight is gained into the phenomena which affect the precision of the free-space system.

6.2 Error Model

The error model that will be used for the free-space calibration is shown in Figure 6.1. The symbols in this model are defined as follows:

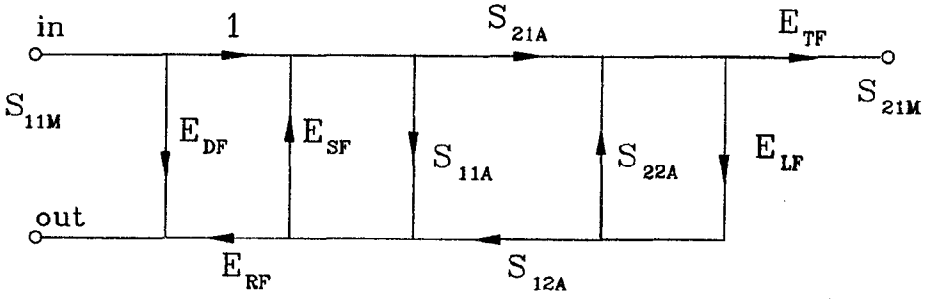

Figure 6.1: Calibration error model.

- S_{11A}, S_{21A}, S_{12A} and S_{22A}: the actual scattering parameters.
- S_{11M} and S_{21M}: the measured scattering parameters.
- E_{DF} (Directivity): the directivity error coefficient due to the signal which is detected at the coupled port but which has not been reflected by the DUT (Device Under Test).
- E_{RF} (Reflection Tracking): the reflection tracking error coefficient will effectively scale the signal reflected from the DUT.

- E_{SF} (Source Match): this term gives an indication of the impedance mismatch between the DUT and the system (looking back into the S_{11}-port of the system). If the DUT and system are not matched, signals will bounce back and forth between the DUT and the system.
- E_{TF} (Transmission Frequency Response): similar to the reflection tracking error coefficient, but for the transmission coefficient.
- E_{LF} (Load Match): equivalent to E_{SF} but on the other side i.e. impedance mismatch looking into the S_{22}-port. For the time being it is assumed that there is a perfect match (i.e. $E_{LF} = 0$). The validity of this assumption will be discussed in more detail in Section 6.3.3.

6.3 Reflection Coefficient

The measured reflection coefficient can be determined from Figure 6.1 using signal flow graph analysis [92], with the assumption $E_{LF} = 0$ mentioned above, as

$$S_{11M} = E_{DF} + \frac{S_{11A}E_{RF}}{1 - E_{SF}S_{11A}}. \tag{6.1}$$

If the error coefficients are known, the actual reflection coefficient can be calculated with the following equation,

$$S_{11A} = \frac{S_{11M} - E_{DF}}{E_{SF}(S_{11M} - E_{DF}) + E_{RF}} \tag{6.2}$$

The error terms are determined by measuring "known" *calibration standards.* Since there are three complex error coefficients in the reflection measurement, Equation (6.2), three independent complex calibration measurement are needed to characterize them. Several calibration standards can be used to obtain the error coefficients of the error model. The most widely used calibration standards for calibration of the reflection coefficient are:

Standard Type	Ideal reflection coefficient
Load	$S_{11A} = 0$
Open	$S_{11A} = 1$
Short or Offset Short	$S_{11A} = -1e^{i2kz}$ with z the distance between the calibration plane and the offset short, and k the wave number.

Table 6.1: Calibration standards generally used for calibration of the reflection coefficient.

These standards can be used in different combinations (see Table 6.2) to determine the error coefficients. The results obtained from different calibration methods are not the same and the error in the measurements, after the calibration, are dependent on the choice of the calibration standards.

6.3.1 Minimum Sensitivity Calibration

Bianco *et al.* [93] derived a method to evaluate the errors in calibration procedures for reflection coefficient measurements. A statistical method is used to determine a quality factor, Q, for a certain calibration procedure. The higher the quality factor the lower the influence, in the mean, of the standard inaccuracies on the measured components. They have shown that the quality factor obtained when three shorts are used is higher than if a load and two shorts are used.

A similar approach was used by Ladvánszky *et al.* [94] to reduce the measurement error by minimum sensitivity calibration. The calibration standards can thus be chosen to minimize the sensitivity, P, of the reflection coefficient. The parameter, P, is the sum of the absolute values of the three sensitivities of the three chosen calibration standards,

$$P = |S_1| + |S_2| + |S_3|, \tag{6.3}$$

where the sensitivities are defined as

$$S_1 = \frac{\partial x}{\partial x_1}, \quad S_2 = \frac{\partial x}{\partial x_2} \text{ and } S_3 = \frac{\partial x}{\partial x_3}, \tag{6.4}$$

with x the reflection coefficient and x_i $(i = 1, 2, 3)$ the reflection coefficient of the calibration standards (calibrating elements). The minimum of the sum of P is 1 [94].

Contour graphs of the function $P - 1$, for two different sets of calibration standards, (L2S and 3S)[3] are shown in Figure 6.2. The figures show that the sensitivity of a reflection measurement will be minimum (i.e. $P - 1 = 0$) if the measured reflection coefficient has the same value as the standard used (i.e. if $x = x_i$). Ladvánszky *et al.* also give a geometrical and a numerical method to choose the calibration standards, x_1, x_2 and x_3, that will minimize P for a certain known (or expected) value of the reflection coefficient.

From these figures it is also clear that measurements of reflection coefficient that have approximately the same values as those of the calibration standards are more accurate than those that are not near any of the calibration standards. The results in Figure 6.2 indicate that the uncertainty in the measurement of the reflection coefficient after calibration using three shorts (3S) should be less, in general, than if a load and two shorts (L2S) are used as calibration standards.

L2S Load and Two Shorts		3S Three Shorts		3C Three Shorts Centred	
Std	Ideal	Std	Ideal	Std	Ideal
Load	$S_{11A} = 0$	Short	$S_{11A} = -1e^{i0}$	Short	$S_{11A} = -1e^{i2\beta(-\lambda/6)}$
Short	$S_{11A} = -1e^{i0}$	Short	$S_{11A} = -1e^{i2\beta(\lambda/6)}$	Short	$S_{11A} = -1e^{i0}$
Short	$S_{11A} = -1e^{i2\beta(\lambda/4)}$	Short	$S_{11A} = -1e^{i2\beta(2\lambda/6)}$	Short	$S_{11A} = -1e^{i2\beta(\lambda/6)}$

Table 6.2: Three possible combinations of the calibration standards.

[3]The abbreviations L2S for load, short, offset short and 3S for short and two offset shorts and 3C for three shorts centered around the calibration plane, will be used for the three calibration methods of Table 6.2.

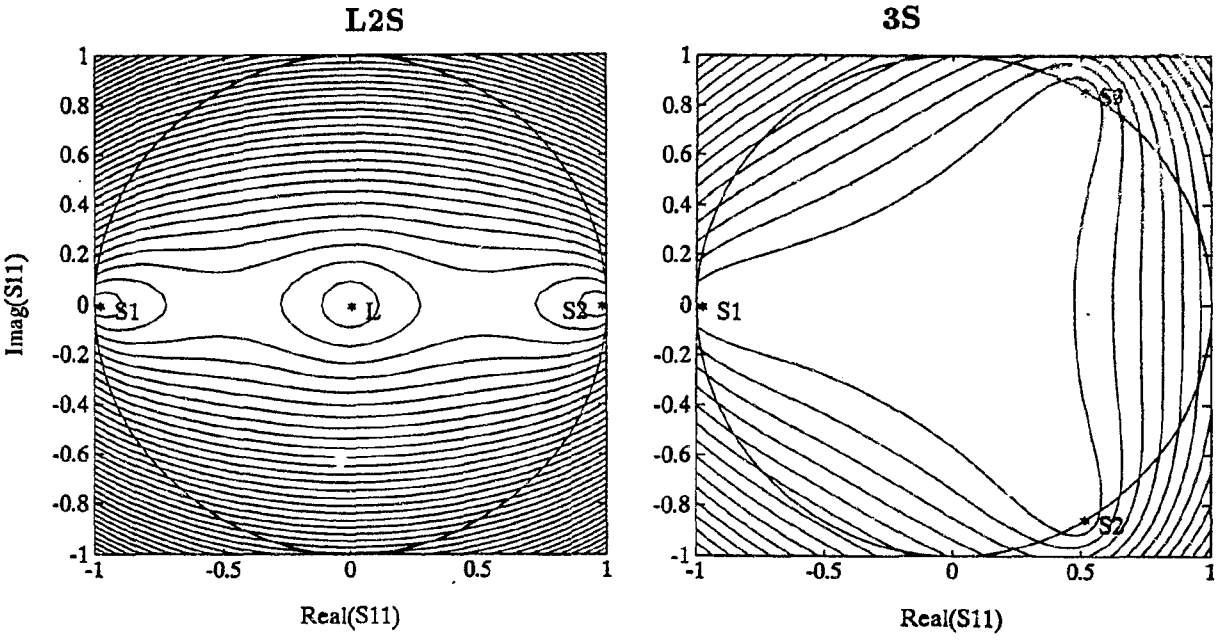

Figure 6.2: Sensitivity $P - 1$, as a function of the measured reflection coefficient S_{11}. The contours increase from 0 (at calibration standards) in steps of 0.1. The circle indicates the boundary of $|S_{11}|$ or $|x| \leq 1$.

6.3.2 Free-Space Calibration

The calibration standards available for free-space calibration are summarized in Table 6.3. Only three standards are necessary for calibration allowing several possible combinations. The three combinations that will be used in the thesis are summarized in Table 6.2.

Standard Type	Ideal reflection coefficient	Physical standard
Load	$S_{11A} = 0$	Pyramidal absorbing material behind focal plane, Fig D.1. Eccosorb VHP-8-NRL, (-50 dB at 15 GHz)
Short	$S_{11A} = -1e^{i2\beta z}$	Flat aluminium plate 26cm by 26cm, Fig D.1. z is the physical offset distance and $\beta = 2\pi/\lambda$.
Open	$S_{11A} = 1$	The *Open* standard will not be considered because a reflection of $S_{11A} = 1$ can not be measured at the calibration plane. An offset short with $S_{11A} = 1$ is not considered to be an *Open* calibration standard.
Impedance Plate	S_{11A} known precisely	The use of an impedance plate or a similar standard is not recommended [95].

Table 6.3: Calibration standards for reflection coefficient measurements.

The equations used to calculate the calibration coefficients from the measurements of the calibration standards are shown in Appendix D.

The calibration coefficients obtained by the two methods (L2S and 3S) are compared in Figures 6.3 and 6.4. It is clear from these figures that the calibration coefficients obtained from the two methods are very similar. The calibration coefficients from the

3C calibration method are not shown since they are very similar to those obtained from the 3S method.

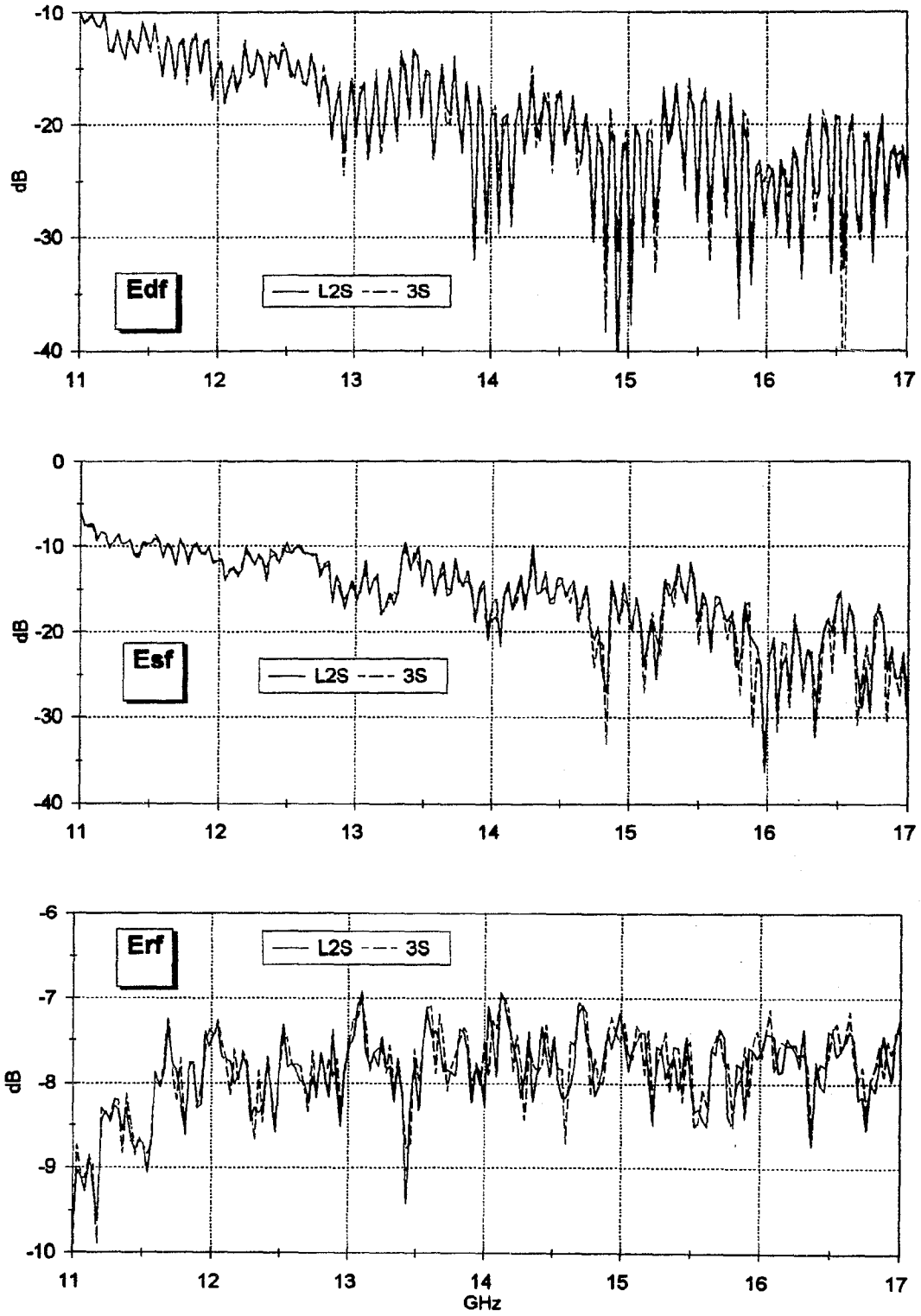

Figure 6.3: Amplitudes of E_{DF}, E_{SF}, E_{RF} from the two calibration methods (L2S and 3S).

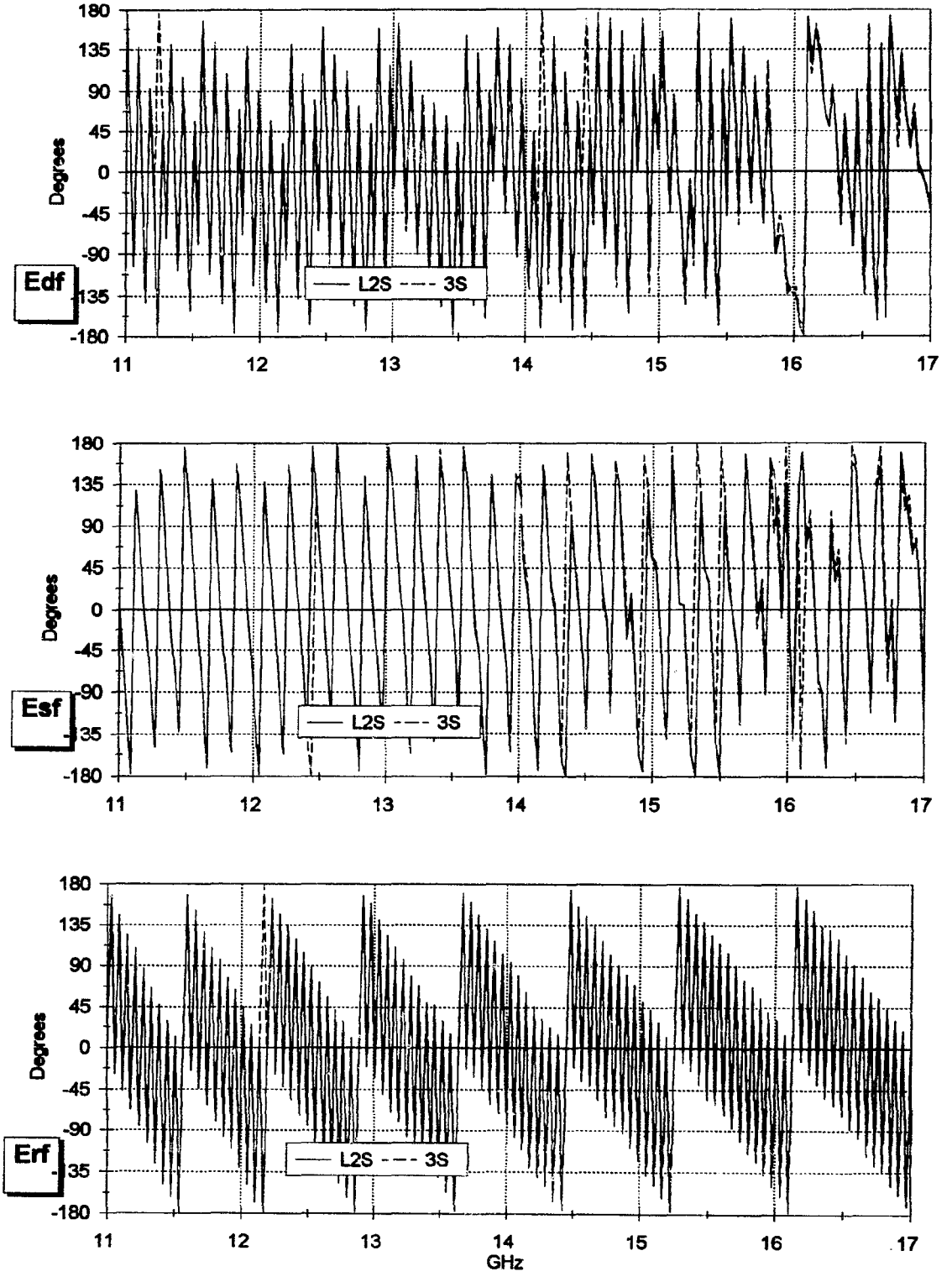

Figure 6.4: Phase of E_{DF}, E_{SF}, E_{RF} from the two calibration methods (L2S and 3S).

The ideal value for the directivity error coefficient is $E_{DF} = 0$. This implies that the only reflected signal is that from the DUT. A value of -20 dB is considered to be good. The poor performance of the system in this regard is a result of the poor match of the antenna. (See Figure C.5 for the reflection coefficient of the antenna and coax to waveguide converter combination.) Ideally the source should be perfectly matched i.e. $E_{SF} = 0$. The poor match of the system can again be attributed to the poor match of the antenna. (A time domain analysis of the reflection coefficient of the antenna (Figure 6.13) showed that the "neck" or transition from the rectangular waveguide to the conical horn is responsible for the high reflection of the antenna.) The reflection tracking error coefficient for an ideal system should be $E_{RF} = 1$ or 0 dB. This is also true for the transmission frequency response error coefficient E_{TF}.

Although the calibration coefficients for the L2S and 3S calibration methods are very similar, the results obtained when they are used to calculate the actual reflection coefficient, S_{11A}, are not the same. This was predicted in Section 6.3.1. For example the measured reflection coefficient when there is no sample in the focal plane is shown in Figure 6.5.

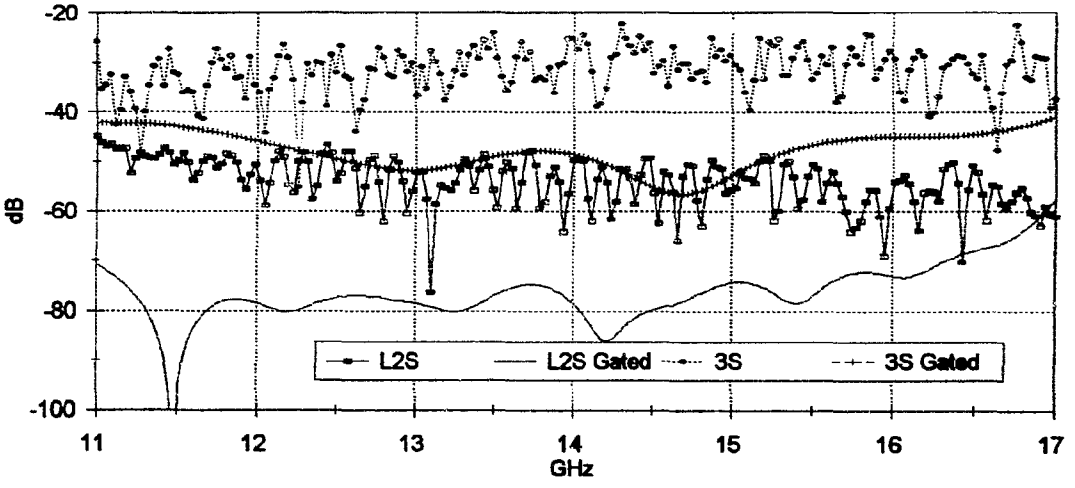

Figure 6.5: Reflection coefficient from no sample, using two different calibration methods (L2S and 3S).

The measurements show that, as predicted in Figure 6.2, the measured reflection coefficient after L2S calibration is closer to the ideal $S_{11A} = 0$ than after 3S (or 3C) calibration. This measurement also gives an indication of the dynamic range of the system and it can therefore be concluded that the L2S calibration method gives a better dynamic range than the 3S method (70 dB vs. 45 dB). These figures also show how the reflection coefficient is reduced by the time domain gate. (The use of a time domain gate to enhance the accuracy of the measurement is discussed in Section 6.6.1.)

The difference between the results obtained using the two calibration methods is not always as large as shown in Figure 6.5 and can be much smaller depending on the value of S_{11}. To illustrate this the measured reflection coefficient from a Perspex sample with a thickness of 3.37 mm, using L2S and 3S calibration, is compared in Figure 6.6. The difference between the two calibration methods is much less in this case.

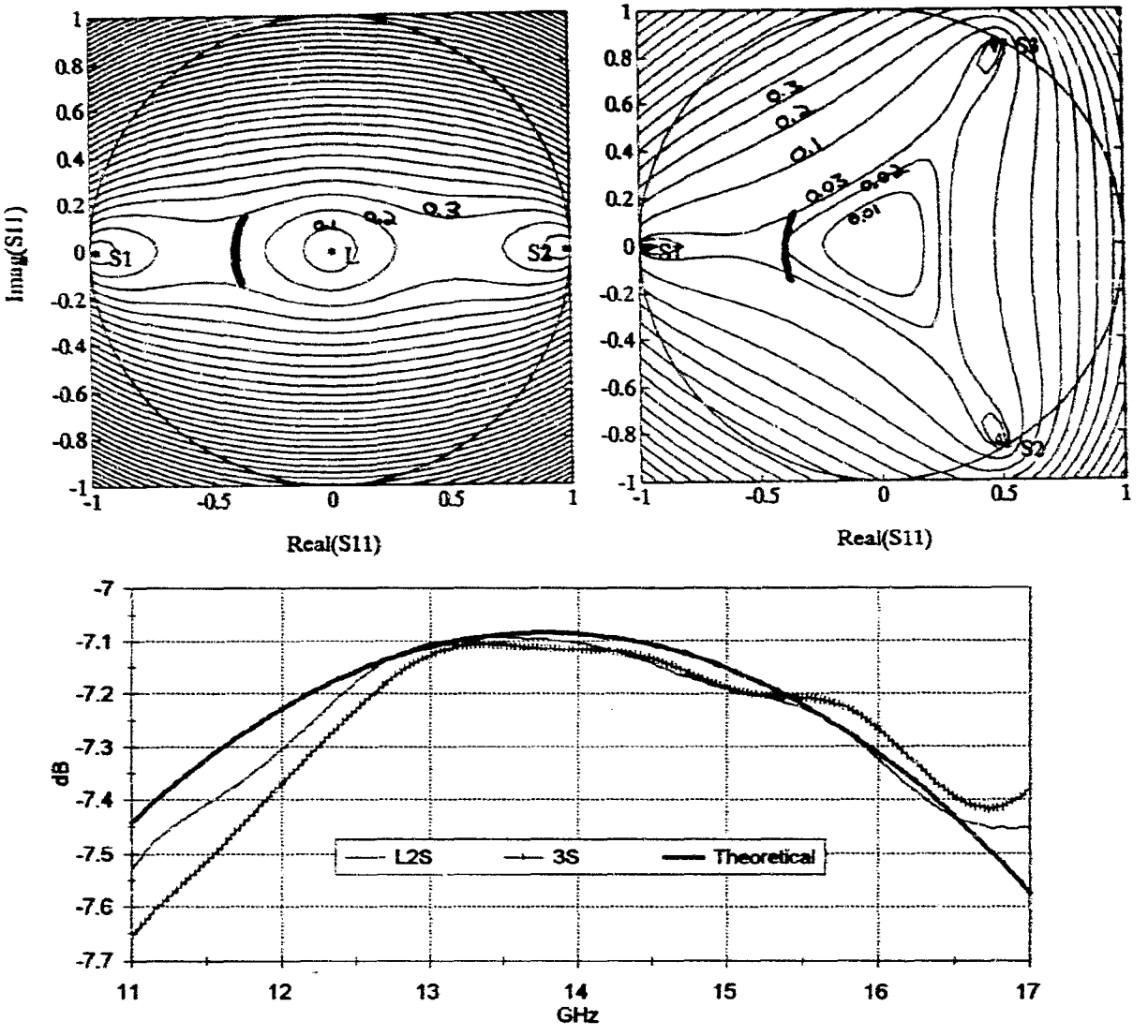

Figure 6.6: Comparison of the measured reflection coefficient of Perspex (3.37mm thick) using the two different calibration methods (L2S and 3S).
Theoretical calculation with $\epsilon_r = 2.59 + i\ 0.017353$ [96, 27°C and 10 GHz]. The solid thick line in the sensitivity plots is the theoretical reflection coefficient.

6.3.3 Load Match

The load match, E_{LF}, is expected to have approximately the same amplitude as the source match E_{SF} (Fig. 6.3) because of the symmetry of the system. Since it is difficult to determine the E_{LF} term with the available system[4] its value will be assumed to be $E_{LF} = 0$, i.e. a perfect match.

The assumption of a perfect load match implies that there will be no multiple reflections between the DUT and the receiving antenna. This is achieved in practice by

[4]It is possible to determine E_{LF} by making S_{11M} measurements in the following configurations (a) Thru: two antennas facing each other (Ideal: $S_{11A} = 0$ and $S_{21A} = 1$) and (b) Line: antennas facing each other but separated by $z = \lambda/4$ (Ideal: $S_{11A} = 0$ and $S_{21A} = 1e^{ikz}$). With the other terms E_{DF}, E_{SF} and E_{RF} known the value of E_{LF} can then be determined. This method of calibration is not available on the HP 8510C.

having the receiving antenna covered with a block of absorbing material both during calibration and measurements after calibration of the reflection coefficient (See Figure D.1). With a good absorbing material the reflections from the receiving antenna (load mismatch) will be removed and the assumption of a perfect match (i.e. $E_{LF} = 0$) is justified and good[5].

6.4 Transmission Coefficient

For the error model shown in Figure 6.1 the measured transmission coefficient is

$$S_{21M} = \frac{S_{21A}E_{TF}}{1 - E_{SF}S_{11A} - E_{LF}S_{22A} - E_{SF}E_{LF}S_{12A}S_{21A}}. \tag{6.5}$$

After calibration, when all the error terms are known, the actual transmission coefficient can be determined from the following equation,

$$S_{21A} = \frac{S_{21M}(1 - E_{SF}S_{11A} - E_{LF}S_{22A})}{E_{TF} + E_{LF}E_{SF}S_{12A}S_{21M}}. \tag{6.6}$$

It is clear from these equations that it is necessary to measure all four S-parameters if this error model is used. However all four S-parameters cannot be measured without disconnecting cables with the system used for this work, as mentioned earlier.

To overcome this difficulty it is assumed that the load match is $E_{LF} = 0$ which gives an approximate measured transmission coefficient as

$$S_{21M} = \frac{S_{21A}E_{TF}}{1 - E_{SF}S_{11A}}, \tag{6.7}$$

and the actual transmission coefficient is then approximated by

$$S_{21A} = \frac{S_{21M}(1 - E_{SF}S_{11A})}{E_{TF}}. \tag{6.8}$$

In this equation E_{SF} is known from the reflection coefficient calibration, and S_{11A} from the subsequent error corrected reflection coefficient measurement of the DUT. The determination of E_{TF} is described below.

In the measurement of the reflection coefficient, S_{11A}, the assumption, $E_{LF} = 0$ was justified by placing absorbing material in front of the receiving antenna. However when the transmission coefficient is measured $E_{LF} \neq 0$ (although $E_{LF} = 0$ is assumed in the error model). This means that the error model used does not account for the reflections caused by the load mismatch in S_{21} measurements. These multiple reflections are removed by a time domain gate as described in Section 6.6.

6.4.1 Transmission Frequency Response

The calibration standard used to calibrate the transmission coefficient is summarized in Table 6.4.

[5]With free-space calibration using the TRL method [48, 61, 79, 80] the receiving antenna is not covered with absorbing material in order to determine the load match. Reflection coefficient measurements are then also made without covering the receiving antenna with absorbing material.

Standard Type	Ideal coefficients	Physical standard
Thru	$S_{11A} = 0$ and $S_{21A} = 1$	Focal planes of 2 antennas coincident, Fig 4.1 i.e. with the antennas facing each other.

Table 6.4: Calibration standard for calibration of the transmission coefficient.

The transmission coefficient is calibrated by having the two lens-antennas facing each other with their respective focal planes coinciding. By substituting $S_{11A} = 0$ and $S_{21A} = 1$ (for the calibration standard) into Equation (6.7) the transmission frequency response term, E_{TF}, can be calculated directly from the measured transmission coefficient, S_{21M}, as

$$E_{TF} = S_{21M}. \tag{6.9}$$

The measured transmission frequency response term for the free-space setup is shown in Figure 6.7.

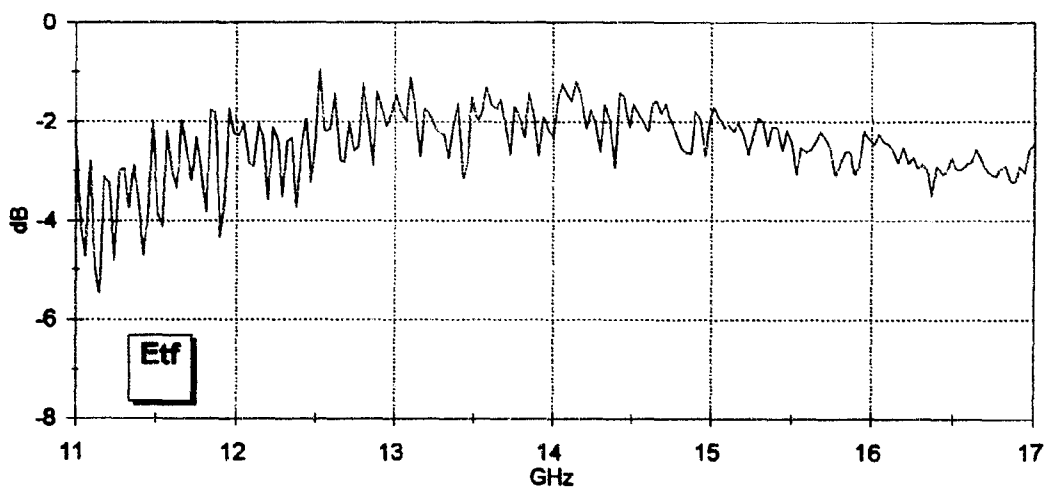

Figure 6.7: Amplitude of the transmission frequency response E_{TF}.

6.5 Dispersion and Calibration

In Sections 5.2.8 and 5.3.4 it was shown theoretically and by measurement that the wavelength in the focal region of the focused lens antenna is greater than the free space wavelength, λ_0, due to dispersion; thus

$$\lambda = \Lambda \, \lambda_0, \tag{6.10}$$

with Λ the elongation factor. In this section it will be shown how this elongation is accounted for in the free-space calibration.

The phase characteristics of the offset standards, i.e. the offset shorts[6], are specified by the time it takes for the wave to travel from the calibration plane to the offset

[6]For the TRL calibration this would be the Line standard.

standard,

$$t_d = l/\nu, \tag{6.11}$$

where l is the distance between the calibration plane and the offset standard and ν the propagation velocity of the wave. (For the HP 8510C Network Analyzer this time is entered as the *Offset Delay* when the calibration standard is defined [89].)

Because of the dispersion in the focal region of the antenna, the phase propagation velocity is higher than in free-space i.e,

$$\nu = \Lambda\, c. \tag{6.12}$$

The specified time delays of the various offset calibration standards are summarized in Table D.1.

In Section 5.3.5 the measured dispersion in the focal region of the antennas was compared to the dispersion found in a waveguide. This was done because the HP 8510C network analyzer allows the user to choose between either WG (Wave Guide) or COAX (non-dispersive) models during the specification of calibration standards for the calibration procedure [89].

For the COAX model it is assumed that the phase velocity is constant (frequency independent) and thus displays no dispersion. The WG model, which is built into the HP 8510, assumes the dispersion equation (5.15) which holds for metallic waveguides

$$\lambda_{WG}/\lambda_0 = 1/\sqrt{1 - \frac{f_c^2}{f^2}}, \tag{6.13}$$

in which f_c is a frequency independent constant.

The analysis in Section 5.3.5 and especially Figure 5.23 showed that using a constant value for the "cutoff" frequency of the quasi-Gaussian beam results in dispersion that is more frequency dependant (i.e. more dispersion at the lower frequencies and less dispersion at the higher frequencies) than the actual measured dispersion. If the cutoff frequency, f_c, is allowed to be frequency dependant (as in Fig 5.22) the dispersion of this "waveguide" model is approximately the same as the actual measured dispersion in the focal region (Fig 5.23).

It was therefore concluded that although a "waveguide" model where the cutoff frequency, f_c, is frequency dependent, could be used for calibration, and since this option is not available on the HP 8510 network analyzer, the COAX model with $\nu = \Lambda\, c$ should be used. This results in a very good model for the free-space beam in the focal region. Note that it is physically equivalent to a medium with refractive index, $n = 1/\Lambda$, of *less* than unity.

6.6 Multiple Reflections

If the reflection coefficient from the calibration plate is measured at different positions along the focal axis after the free-space calibration, it is found that the reflection coefficient is 0 dB at the positions where the short calibrations were done (i.e. at $z = 0$

and 5.7 mm for L2S, at $z = 0$, 3.8 and 7.6 mm for 3S, and at $z = -3.8$, 0 and 3.8 mm for 3C). However, S_{11} is not 0 dB, as it ideally should be, at other positions around the calibration plane. The ripple in the reflection coefficient of the sliding calibration plate for L2S calibration is shown in Figure 6.8 (at 11.25 GHz) and in Figure 6.9 (at 13.5 GHz). The measured ripple after 3C calibration is shown in Figure 6.10 and 6.11. The ripple in the measured reflection coefficient is also present in the raw data (i.e. the uncalibrated data, S_{11M}) as shown in Figure 6.12.

It will now be shown that this ripple in S_{11} is caused by multiple reflections between the calibration plate and the lens antenna.

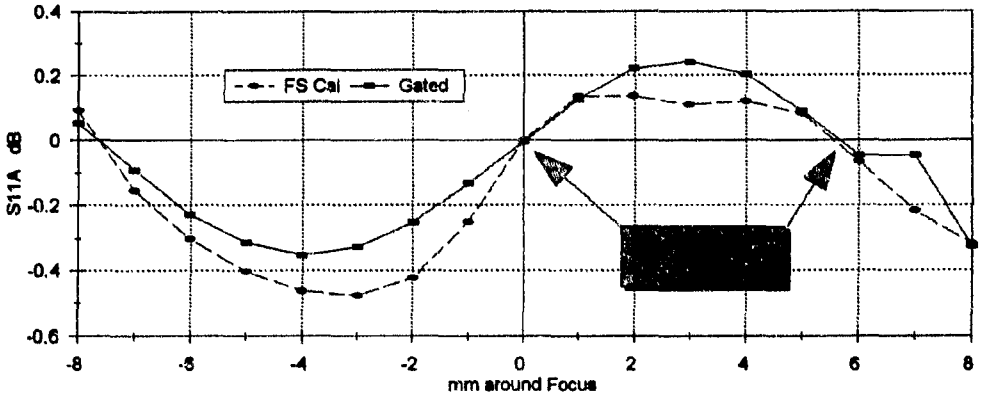

Figure 6.8: Reflection from sliding calibration plate (at 11.25 GHz) after L2S free-space calibration.

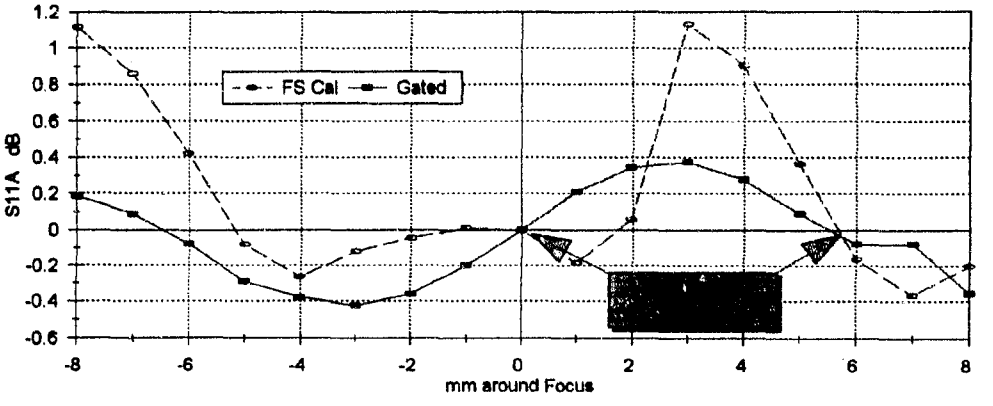

Figure 6.9: Reflection from sliding calibration plate (at 13.5 GHz) after L2S free-space calibration.

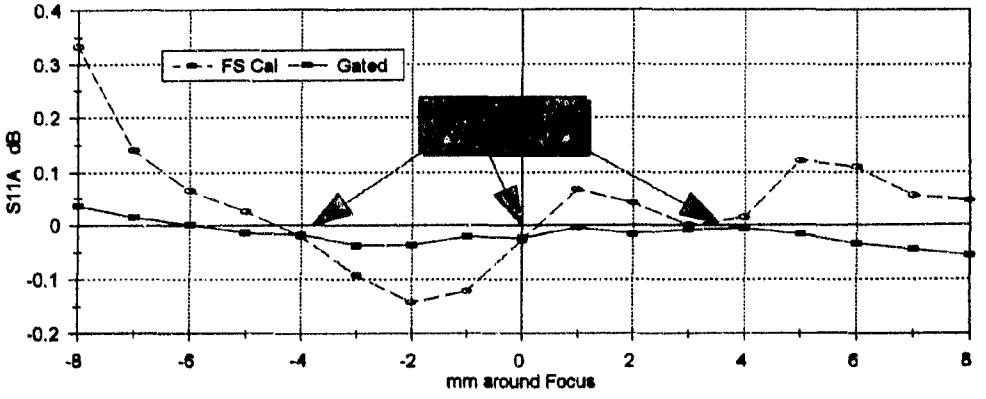

Figure 6.10: Reflection from sliding calibration plate (at 11.25 GHz) after 3C free-space calibration.

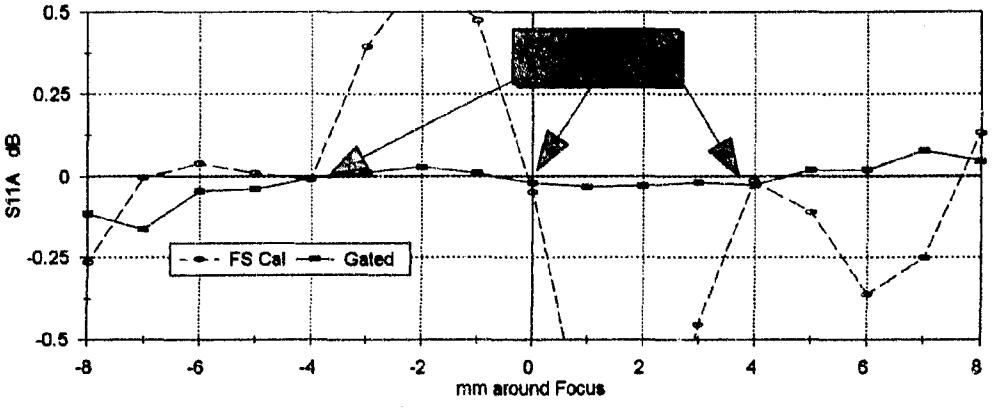

Figure 6.11: Reflection from sliding calibration plate (at 13.5 GHz) after 3C free-space calibration.

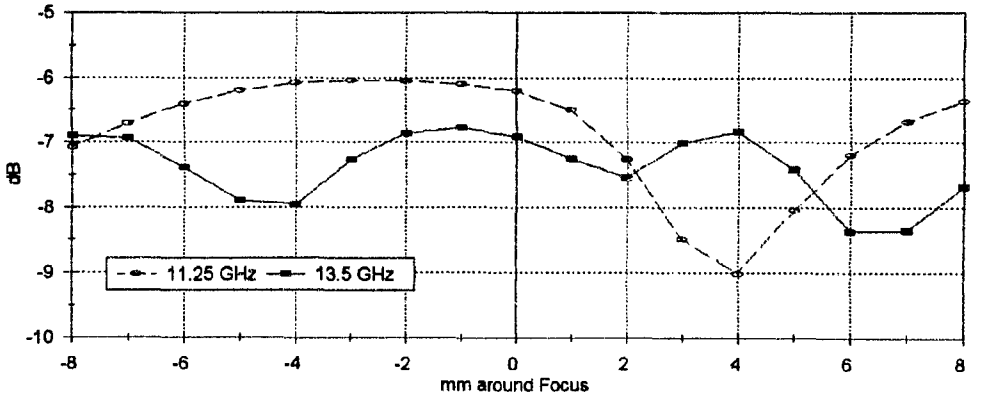

Figure 6.12: Uncalibrated reflection coefficient, S_{11M}, from sliding calibration plate (at 11.25 GHz and 13.5 GHz).

It is very convenient to isolate the multiple reflections by using a time domain representation of the reflection coefficient. The reflection coefficient of the antenna after a 7 mm calibration[7], Figure 6.13, shows that there are several positions in the antenna that contribute to its total reflection coefficient. The time domain representation of the

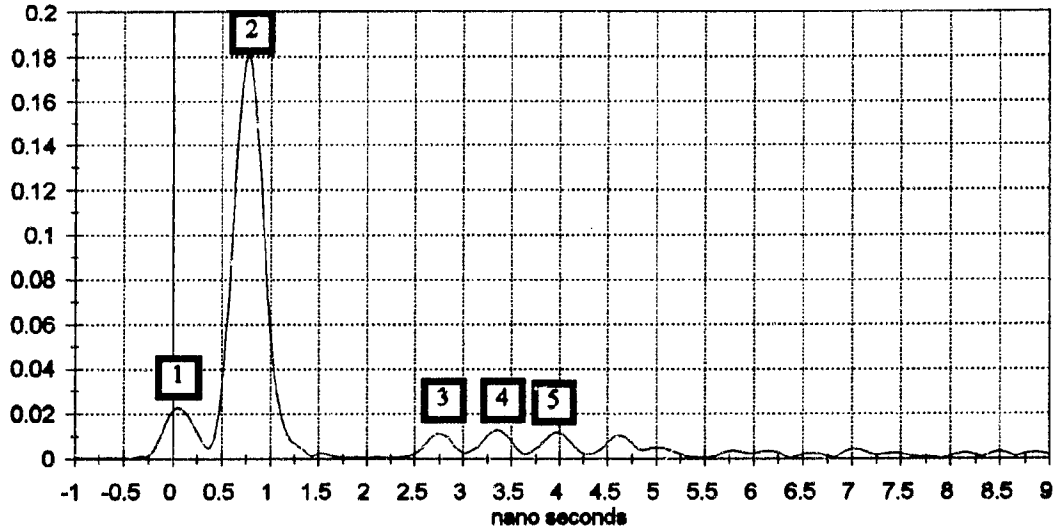

Marker	Reflection	Physical Position
1	0.023	Coax to waveguide converter
2	0.181	Neck: waveguide to cylindrical cone base transition
3	0.014	Front of the lens (inside the antenna)
4	0.013	Center of the lens or the front edge of the conical horn
5	0.017	Lens to free space transition

Figure 6.13: Time domain reflection from the lens antenna on a linear amplitude scale. Data obtained from a 11-17 GHz frequency domain measurement.

reflection coefficient from the antenna and the calibration plate, in the configuration of Figure D.1, is shown in Figure 6.14. This figure shows that an impulse that is launched into the system will first be reflected by the base of the antenna (Marker 1 of Fig 6.14) but a substantial part of it will proceed through the cone and the lens of the antenna, through the free space and then bounce back from the calibration plate and return via the same path to the base of the antenna. At this discontinuity most of the pulse will go through the neck and be detected at the 7 mm calibration plane as a pulse after 6 ns (Marker 2 of Fig 6.14) but some of it will be reflected and the same process is repeated so that a second reflection from the plate (Marker 3), a third (Marker 4) and a fourth reflection (Marker 5) is measured until its amplitude is so small that it is insignificant. The pulses that return from the system are "absorbed" by the network analyzer since they do not encounter further uncalibrated discontinuities.

The reflection received after 6 nanoseconds is not only the reflection from the plate but may also contain second reflections from the lens itself (markers 3, 4 and 5 Fig 6.13).

[7]The 7 mm calibration is done at the end of the coaxial cable that is connected to the feed of the antenna.

Since the reflection from the lens is small in comparison to the reflection from the plate it is difficult to distinguish between them.

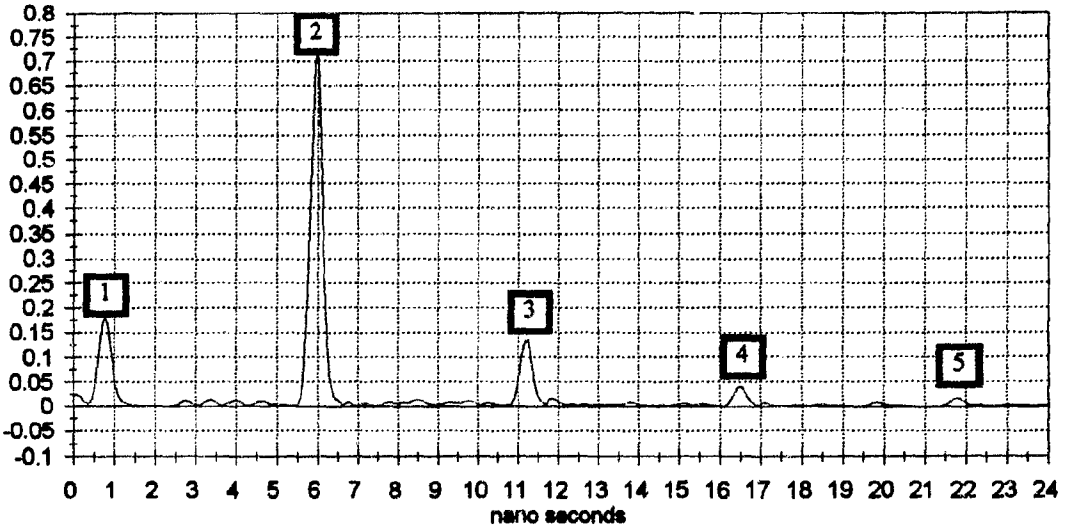

Marker	Reflection	Physical Position
1	0.181	Neck: waveguide to cylindrical cone base transition
2	0.720	First reflection from calibration plate
3	0.135	Second reflection from calibration plate
4	0.040	Third reflection from calibration plate
5	0.017	Fourth reflection from calibration plate

Figure 6.14: Time domain reflection from the lens antenna and the calibration plate at the focus.

The ripple in the raw data of the reflection coefficient, S_{11M}, (Fig 6.12) was simulated using bounce diagram analysis [97, Section 14.4]. With such an analysis the discontinuities can be isolated and their respective contributions to the reflection coefficient be determined. The distance between them will determine whether the waves add in a constructive or a destructive way. Only three discontinuities, or points of reflection, were used in the analysis. These are located at the transition from waveguide to the conical horn of the antenna (Marker 2, Fig 6.13), at the lens (Markers 3, 4 and 5 combined, Fig 6.13) and at the calibration plate (Marker 2, Fig 6.14).

The results obtained with this model agreed very well with the measured results although there were certain minor features in the measured ripple that could not be explained with such a simple model. This analysis revealed that the ripple effect in the reflection coefficient of the sliding calibration plate is caused by multiple reflections between the calibration plate and the lens antenna. The analysis also showed that the discontinuities used in the bounce diagram analysis make the largest contribution to the multiple reflections.

The problem of multiple reflections in free-space measurements has also been mentioned by other researchers [80, 95, 98, 99].

6.6.1 Time Domain Gating

Multiple reflections between the DUT and a poorly matched source are taken into account by the source match error coefficient E_{SF}. Smith *et al.* [95] showed that the function of this term can effectively be replaced by use of a time domain gate in the reflection coefficient. The use of a source match term in the calibration model does not remove the multiple reflections completely since some higher order modes remain [95].

These remaining effects of multiple reflections can be reduced further by use of a time domain gate, which is placed around the focal plane so that the reflection from the device under test is unaffected but reflections from other sources are "filtered out". The effect of time domain gating can be seen in Figure 6.5, Figures 6.8, 6.9 (for L2S) and Figures 6.10, 6.11 (for 3C).

The measured reflection and transmission coefficients of a Perspex sample, with and without time domain gating, is shown in Figure 6.15. It is clear from this figure (as expected from Section 6.4) that the time domain gate is especially important in the transmission coefficient measurement. Although the time domain gate enhances the

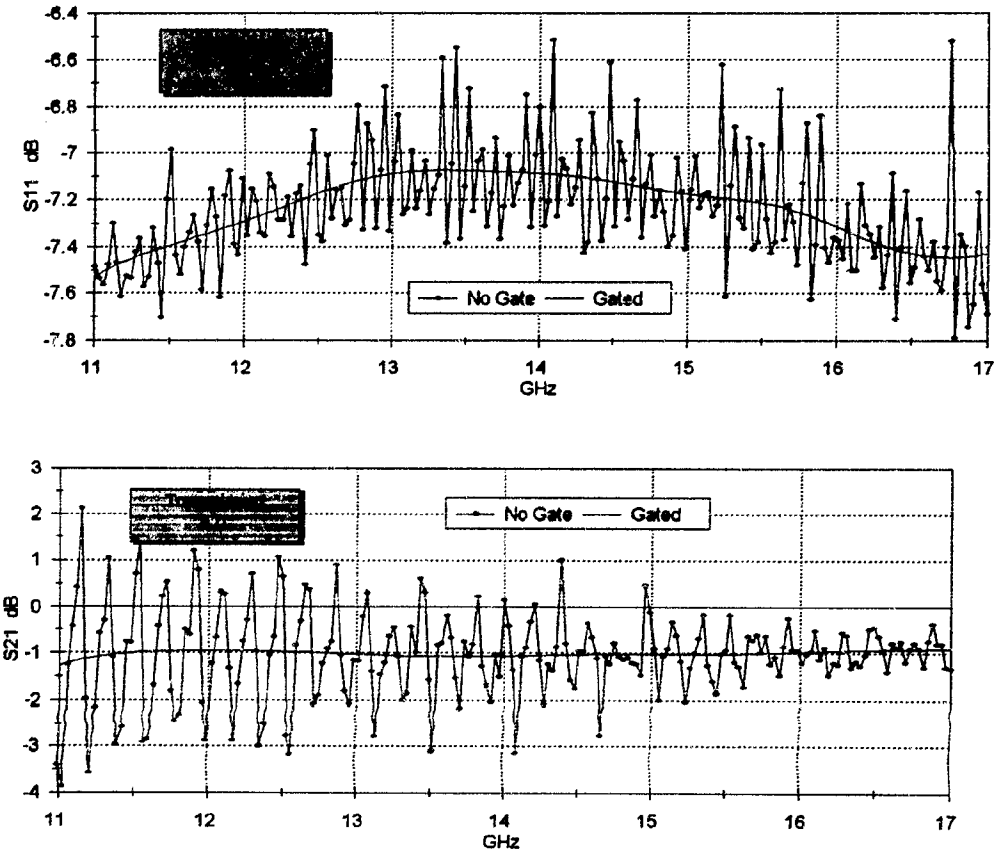

Figure 6.15: The effect of a time domain gate (centered around the calibration plane with a span of 1.5 ns) on the reflection coefficient and the transmission coefficient of a 3.37 mm thick Perspex sample.

accuracy of the measurement it is important to realize that errors can be introduced by its use. The magnitude of these errors is a function of the gate shape, center position

and span[8]. Also, a time domain gate should not remove wanted reflections. It is important to remember that unwanted multiple reflections that appear inside the time domain gate will not be removed. Quantification of the errors associated with the time domain gating will not be attempted.

The theoretically predicted transmission coefficient of a Perspex sample is compared to the measured value in Figure 6.16 to quantify the accuracy of the measurement. The large error between the measured and the predicted value in the region of 11 to 11.5 GHz is believed to have been caused by the transformation of bandlimited frequency domain measurements, using a windowing function and Fourier transforms,to the time domain. These operations are performed in the Hewlett Packard network analyzer using unpublished algorithms. Their quantitative effects at band edges are not known and it is concluded that care must be taken with the interpretation of measurements at low and high frequencies.

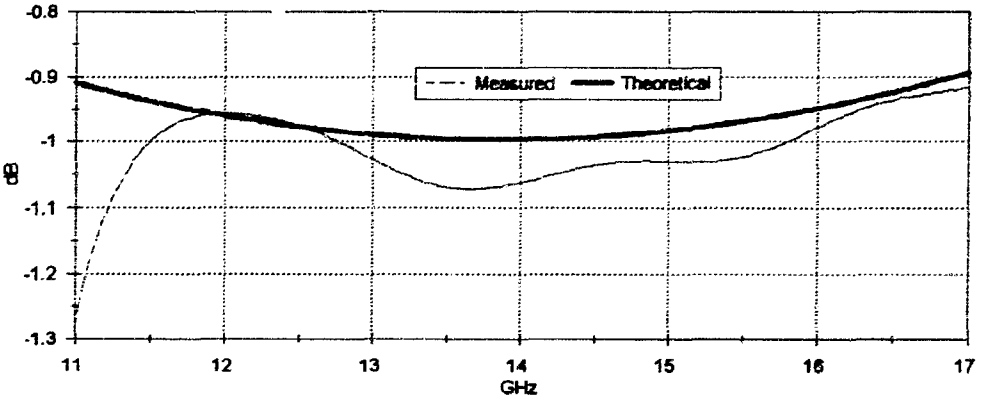

Figure 6.16: Comparison of the measured and theoretical transmission coefficient of a 3.37 mm thick Perspex sample (with $\epsilon_r = 2.59 + i\ 0.017353$ [96, 27°C and 10 GHz]).

6.7 Free-Space Calibration by Other Researchers

Free-space calibration has also been done by other researchers using similar error-models as that shown in Figure 6.1 [95, 98, 99].

Umari *et al.* [99] used three shorts (metal plates) as calibration standards. The first short was placed at the calibration plane and the other two at a distance of $\lambda_{zm}/8$ and $\lambda_{zm}/4$ from the reference plane respectively, where λ_{zm} is the wavelength in free space in the direction normal to the metal plate at mid band.

To determine the error coefficients, Gagnon [98] used a matched load, a short and an offset short as calibration standards. The matched load was a two-foot ($\approx$ 60 cm)

[8]Although there are several choices available to the HP 8510 user [100], a detailed study to optimize the time domain gating for minimum errors was not done. It was found that the *Normal* windowing function and the *Normal* gate shape (centered around the calibration plane and with a span of 1.5 nanoseconds) gave satisfactory results and these were used in all the measurements.

square, two-inch ($\approx$ 5 cm) thick, wedged absorbing material. Gagnon concludes that the small reflections from the microwave absorber, which is placed some distance beyond the focal plane, are poorly coupled to the Gaussian mode of the lens antenna, resulting in a nearly ideal termination.

A good article on calibration of the reflection coefficient of a free-space system was written by Smith *et al.* [95]. In this article the contribution of each of the error terms is discussed in detail. Some of the interesting effects that are discussed are higher order residuals in the source match, E_{SF}, and the possible errors associated with the shadow region behind the calibration plate, or the sample that is being measured, and the subsequent effect of the quality of absorbing material that is being used. They show that the errors associated with the shadow region can be reduced by using either a good quality absorbing material or only shorts (metal plates) as calibration standards. They also investigated the phase stability of the calibration methods, and concluded that a calibration method using a load, $S_{11A} = 0$, as one of the standards is much less sensitive to phase errors than using three shorts as calibration standards.

A calibration method, using the TRL method, for two-port free-space measurement system has been developed by the research group at the Pennsylvania State University [48, 61, 79, 80] and a similar method is used by other researchers [77]. The TRL calibration method is used with the following three calibration steps:

1. Thru: the focal planes of the two antennas are coincident.
2. Reflect: a metal plate is placed in the focal plane.
3. Line: similar to the Thru but here the antennas are separated (and therefore also the focal planes of each antenna) by a quarter wavelength in free-space at mid band [48, 80].

It is expected that a TRL calibration [48, 61, 79, 80] would yield more accurate measurements than the error-model shown in Figure 6.1. The superiority of the TRL calibration is expected since it contains more error terms and the required conditions on the calibration standards are less strict than in a one-port calibration. A quantitative comparison between the two calibration methods can unfortunately not be done.

6.8 Conclusion

A method has been developed to calibrate the reflection and transmission coefficients of the free-space measurement system available for this research. The error model used contains only four error coefficients, E_{DF}, E_{SF}, E_{RF} and E_{TF}. The inability of the system to measure and include the load match error term, E_{LF}, was overcome by using a high quality absorbing material (effectively assuming $E_{LF} = 0$) behind the calibration plate and the sample during calibration and measurement of the reflection coefficient. The remaining unwanted reflections were removed by use of a time domain gate. The effect of a poor load match (i.e. multiple reflections) on the transmission coefficient was reduced by using a time domain gate.

The dispersion in the focal region of the antennas was incorporated in the specification of the offset calibration standards.

The method of minimum sensitivity calibration was investigated and illustrated by experiment. Two calibration methods were compared, one using a load, a short, and an offset short (L2S), and the other one short and two offset shorts (3S and 3C). It was found that although L2S and 3S gave different values for very low reflection coefficient $S_{11} \approx 0$ measurements, this was not the case for typical values of S_{11}, such as for Perspex, where the measured results were approximately the same. The method of minimum sensitivity calibration should be investigated further by experiments if a more decisive conclusion is required.

It was found that there is a ripple in the reflection coefficient of a calibration plate that is moved along the focal axis. This ripple was found to be the result of multiple reflections that add in either a constructive or a destructive way. It was also found, as expected, that the ripple is 0 dB where the short calibration measurements were done. The results also showed that the ripple in amplitude was less after the 3S calibration method than after the L2S calibration method was used.

The effect of multiple reflections was investigated and time domain gating implemented, but possibly not using optimal parameters.

A difference between the measured and the predicted reflection and transmission coefficients of Perspex was measured. These errors showed that the measurements and the calibration (model, standards and measurements) are not perfect and contain errors which will be investigated further in the next chapter.

Chapter 7

Post Calibration Errors in the Scattering Parameters

> This experiment should be made many times so that no accident may occur to hinder or falsify this proof, for the experiment may be false whether it deceived the investigator or not.
>
> — Leonardo da Vinci (1452–1519)

7.1 Introduction

The total uncertainty of a calibrated measurement is the sum of the errors because of an imperfect calibration, the random and the drift errors.

To be able to predict the errors in the measured constitutive parameters it is necessary to determine the expected errors in the measurements of the scattering parameters. In the next chapter it will be shown how the expected errors in the constitutive parameters can be calculated if the expected errors in the measured scattering parameters are known.

In this chapter many of the individual error sources that contribute to the errors in the scattering parameters will be discussed, but not quantified, since it is not an easy task to fulfill.

However, typical values for the total expected errors in the measurements will be determined by measuring a material with known properties. The results are presented in Section 7.4 and will be used in the accuracy analysis in the next chapter.

7.2 Imperfect Calibration

In Chapter 6 it was shown how the systematic errors can be reduced by calibration, and in Section 6.3.1 it was shown that a given set of calibration standards can be chosen to give a calibration procedure that will minimize the uncertainty of the post calibration errors.

The calibration is not perfect, mainly because the error model is not complete and the calibration standards are not perfect. When the calibration standards are measured during calibration, it is assumed that the standards are perfect, i.e. for the short, $S_{11A} = -1e^{i\theta}$, and for the load, $S_{11A} = 0$. Since the actual reflection coefficient, S_{11A}, is not exactly known there will be an error included in the measured coefficients of the error model. In other words, if the calibration standards were known exactly then the calibration coefficients could have been calculated exactly.

Bianco *et al.* [93] argued that the actual imperfect calibration standard can be considered to be the sum of a perfect (desired or assumed) term and an error term. For the Kth standard component, let

$$\sigma_K = \Gamma_K + \epsilon_K. \tag{7.1}$$

Here Γ_K is the desired (or perfect) term and ϵ_K the error term composed of two distinct terms, $\epsilon_K = \Delta_K + n_K$, where Δ_K is the systematic error due to intrinsic inaccuracy (uncertainty in the geometric dimensions, losses in conductors, etc.), and n_K the "noise term" which accounts for all erratic disturbances such as thermal noise, non-repeatability of connectors, drifts in microwave signals, roundoff and quantization errors in the computer section of the instrument etc. Thus Γ_K is the value assumed during the calculation of the error coefficients whereas σ_K is the value that was actually measured. For example for the measurement of the *Short* calibration standard the reflection coefficient from the calibration plate is assumed to be $\Gamma_K = -1$, and for a perfect standard $\Delta_K = 0$, and for a perfect measurement $n_K = 0$. However in practice $\Gamma_K \neq -1$ and the error terms, ϵ_K, and especially, Δ_K, are unknown or very difficult to determine exactly.

The systematic error, Δ_K, can be caused by the following factors in the free-space measurement setup. The uncertainty in the reflected signal can be caused by:

1. Diffraction from the plate edges.
2. Plate not being a perfect conductor.
3. Plate not normal to the focal axis of the antenna.
4. Plate not at the correct position along the focal axis,
5. Non-ideal radiation pattern of the lens antenna.
6. Multiple reflections and the subsequent degeneration of the ideal TEM waves.

The reflection from the calibration plate is not exactly constant over the calibration region of the slidin$_{\cup}$ short. This inconsistency is caused by the fact that the radiation pattern is not exactly the same at the different calibration positions.

The reflection from the *Load* calibration standard (pyramidal absorbing material) is assumed to be $\Gamma_K = 0$. However, although this is a very good termination for the transmitted waves [98], there will be small reflections from the absorbing material and from surrounding structures on the measurement bench, to the effect that $\sigma_K \neq 0$.

The error, Δ_K, of the calibration standard due to intrinsic inaccuracy can be determined by using other independent calibration standards to calibrate and then to measure the unknown standard, σ_K, to get the error Δ_K. An accurate theoretical prediction of the error, Δ_K, would be difficult to make and will not be attempted in this thesis. However if these errors were known, by measurement or calculation, the expected errors in measurements after calibration could be calculated as was done by Bianco *et al.* [93].

Finally, the inexact modeling of dispersion in the focal region is also expected to contribute to errors in the calibration procedure.

7.3 Error Sources After Calibration

Even if the calibration was perfect (i.e. perfect error model, perfect calibration standards and perfect calibration measurements) there would still be random and drift errors after calibration. The following sub-systems can be classified as measurement error sources after calibration: network analyzer, cables, directional coupler, antennas, sample holder, sample and time domain gating.

7.3.1 Network Analyzer

The accuracy with which a network analyzer can measure is ultimately limited by its hardware. This includes the quality (i.e. accuracy and stability) of all the signal processing devices and detectors. The dynamic accuracy of the HP 8510B/8511A is given in Appendix C. The system performance of a Hewlett Packard system using a S-parameter test sets is also included in the Appendix for comparison.

From these specifications it can be seen that the expected errors in the measurements are dependent on the frequency but more importantly also on the signal levels that are being measured

7.3.2 Cables

Errors in both the phase and the magnitude can be caused by cables. The phase errors are expected to be more important than the errors in magnitude of the cables. This is because the losses in the cables can be calibrated out but the phase stability of the cables can not be enhanced by calibration. Movement or bending of the cables will cause a much greater change in the phase than in the magnitude of the measured signal. It is for this reason that the cables are kept very stable both during and after calibration. However, the cable that is connected to the receiving antenna will inevitably be moved when the antenna is rotated to measure the cross-polarized transmission coefficient, S_{21y}.

Although high quality phase stable cables are used in the setup (Appendix C) a substantial change in the phase of the transmission coefficient, S_{21}, was measured if the receiving antenna was rotated, Figure 7.1. These measurements were done as follows.

After an S_{21} calibration the receiving antenna was rotated through +45, +60 and +80 degrees and the change in phase measured. Since the phase of S_{21} should be 0 degrees with no sample in the transmission path, the measurements are a direct measure of the error in the phase of the transmission coefficient.

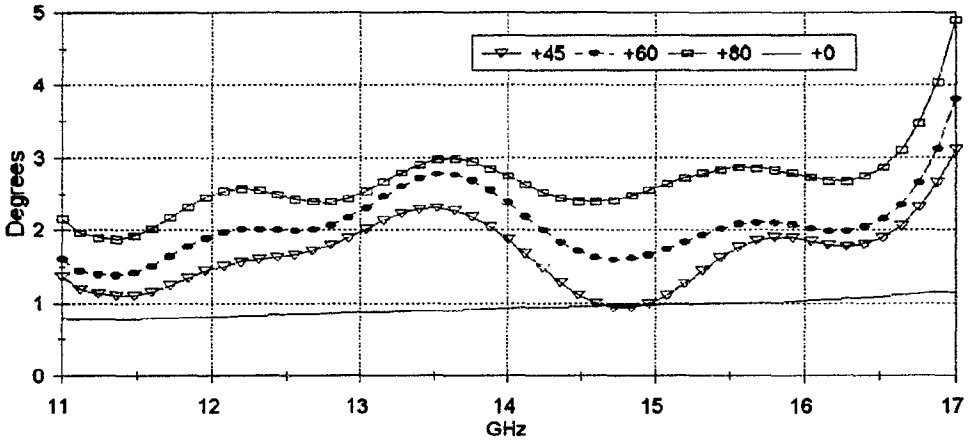

Figure 7.1: Change in the phase of the transmission coefficient, S_{21}, as the receiving antenna is rotated. The value for +0 degrees is the measured phase after the receiving antenna was rotated through +90 degrees and then back to 0 degrees. The cable length in the transmission path is 3 m.

There is an increase in the amount of phase change as the rotation angle is increased. The phase shift is more severe at frequencies above 16.5 GHz. From these measurements it can be concluded that the expected phase uncertainty because of cable movement in the cross-polarized component of the transmission coefficient measurement, S_{21y}, is approximately 3 degrees. The phase uncertainty in the co-polarized component, S_{21x}, is much smaller before the receiver has been rotated. However if the receiving antenna is returned to the 0 degree position (S_{21x}) after it had been rotated though +90 degrees (clockwise looking in the z-direction) the phase shift is approximately 1 degree. It is therefore good practice to recalibrate the transmission coefficient after each S_{21y} measurement.

It was also found that if the receiving antenna was rotated through 90 degrees in the opposite direction (i.e. 90 degrees anti-clockwise looking in the z-direction) the phase change was approximately double that of the values shown in Figure 7.1. This happened because the transmission cable was bent more severely. Measurement of S_{21y} should therefore be made by rotating the receiving antenna in such a way as to minimize the physical stress (or bending) of the cable.

7.3.3 Antennas

The radiation patterns of the antennas were discussed in detail in Chapter 5. During the calibration and measurement after calibration, plane-wave reflection with no diffraction is assumed. An analysis of the radiation patterns of the antennas showed that the phase distribution in the focal plane is not perfectly flat (i.e. not exactly a plane wave, see

Fig. 5.6) and also that there will be some, although very little, diffraction from the sample edges.

Even if the radiation patterns were known exactly it is very difficult to quantify the contribution of diffraction from the sample edges to the total measurement error.

The uncertainties regarding the dispersion in the focal region of the antenna will also contribute to an imperfect calibration.

Due to the nature of the radiation patterns of the antennas, and the measurements done, it is very important that the antennas are properly aligned and very stable. It is also important that the focal spot remains at the same position during rotation of the receiving antenna. The measurement bench was designed to fulfill these requirements.

7.3.4 Sample Holder

The sample holder is made of Perspex with dimensions as shown in Figure 7.2.

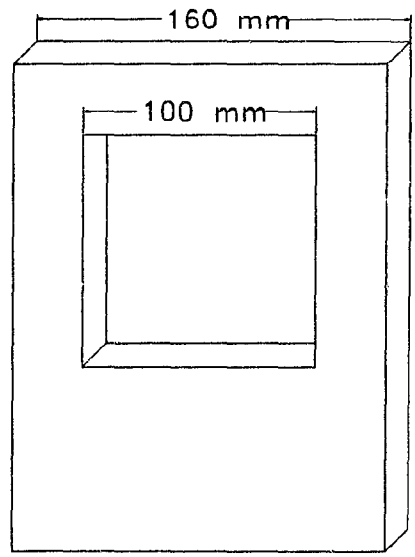

Figure 7.2: Perspex sample holder. The center hole is 100mm by 100mm. The sample holder is 12mm thick.

Besides good alignment of the two antennas the sample, held by the sample holder, should be normal to the propagation path of the wave.

If the sample is not placed exactly at the calibration plane, the phase of the reflection coefficient will be incorrect by $\Delta\angle S_{11} = 2k\Delta z$ radians, where k is the actual wave number in the focal region and Δz the positioning error. A small error in the position of the sample should not affect the phase of the transmission coefficient. The amplitude of the reflection and the transmission coefficient should also not be affected by a small error in position, since the amplitude of radiation pattern does not change very much along the direction of propagation in the focal region (see Fig 5.5).

To ensure that the sample holder does not influence the transmitted field behind the

sample holder (and thus the transmission coefficient) the transmitted field was probed behind the sample holder and compared with the field without the sample holder.

The measurements were done as explained in Section 5.2.1. The sample holder was placed in the focal plane and the field was then probed 55 mm behind the sample holder on the receiving antenna's side as shown in Figure 7.3. The distance between the probe and the sample holder is to ensure that the measurements were not done in the reactive region of the scattered field. Three measurements were done: the fields without a sample holder; with the sample holder; and with the sample holder covered by a thin copper plate (i.e. the hole was "framed" by the copper plate).

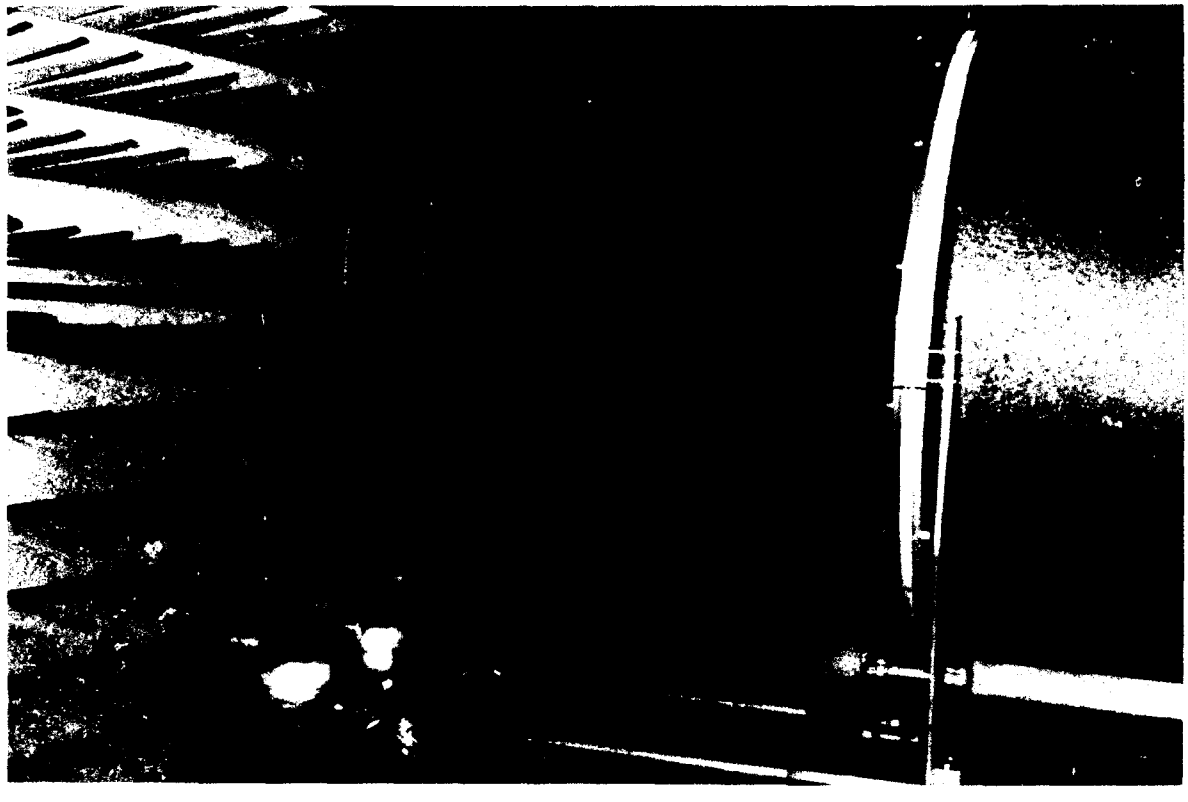

Figure 7.3: Photo of setup used to measure the diffraction from the sample holder.

The measured fields in the E- and H-planes are shown in Figures 7.4 and 7.5. These measurements show that although there is a difference between the unobstructed field and the field with the sample holder at the focal plane, the difference is only significant at a distance of approximately 60 mm from the focal axis where the field is approximately 20 dB below the maximum value on the focal axis. It can therefore be concluded that the sample holder will have a very small influence on the measurements. However these measurements can not be used to quantify the effect of diffraction on the accuracy of the measured reflection and transmission coefficients.

It is also noted that the sample holder is placed in the focal plane when the transmission coefficient is calibrated. This is done so that its effect on the transmission coefficient is calibrated out.

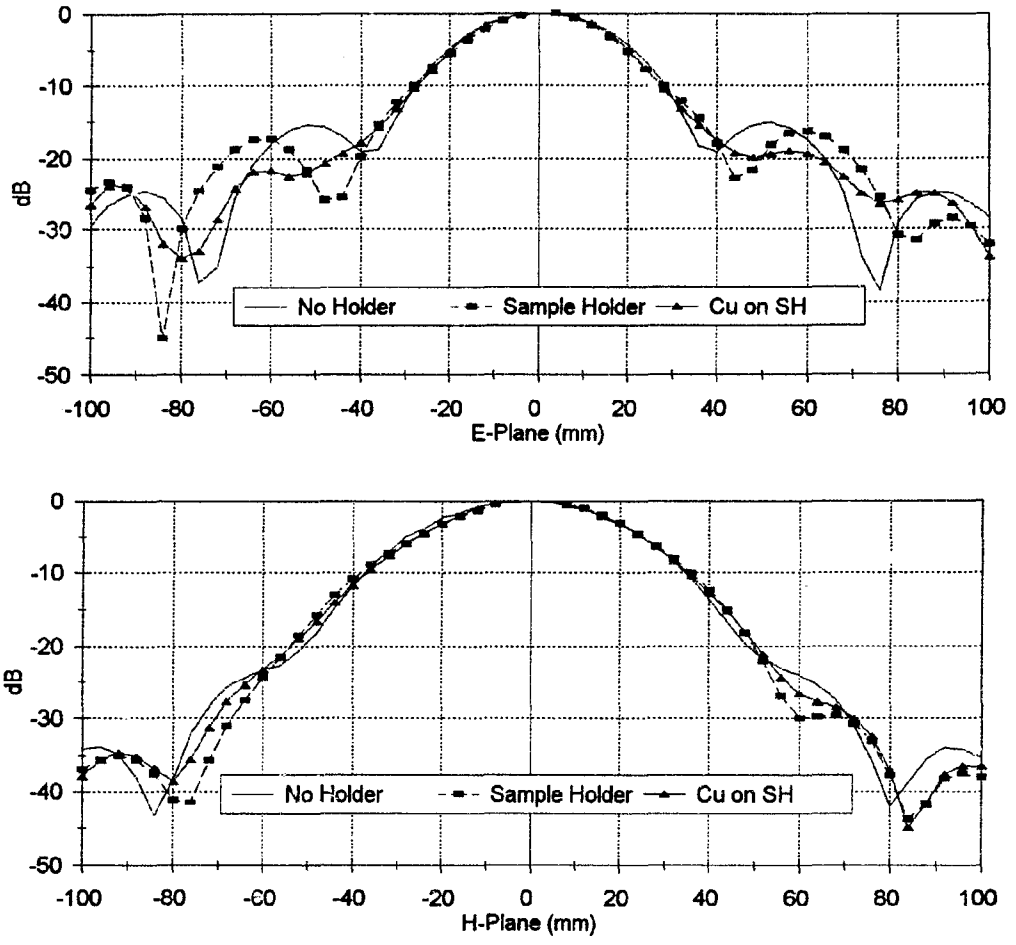

Figure 7.4: Amplitude of the field behind the sample holder in the E- and H-planes. The following are shown: (a) No holder, (b) Perspex sample holder, (c) Sample holder with front covered by a copper plate.

7.3.5 Sample

The inversion equations assume that a *plane wave* is *normally* incident upon a *flat*, *semi-infinite* slab with *uniform* thickness and *homogeneous* intrinsic properties. The condition that the incident wave be plane and that the sample be semi-infinite (i.e. no diffraction) was discussed in Chapter 5 and Section 7.3.4. Using a sample that is sufficiently large will minimize diffraction from the edges of the sample because of the focused beam.

Some of the samples measured are expected to be inhomogeneous. This is especially true for chiral samples, where the embedded helix concentration can be higher in certain regions. This problem can be reduced by making several measurements at different positions and then taking the average value. However it is important to note that if the inhomogeneity is along the transmission axis it will not help to shift the sample around and that turning the sample around may still not be sufficient. These possible inhomogeneities should be considered with all measurements.

The sample should have a uniform thickness since the thickness is a variable in

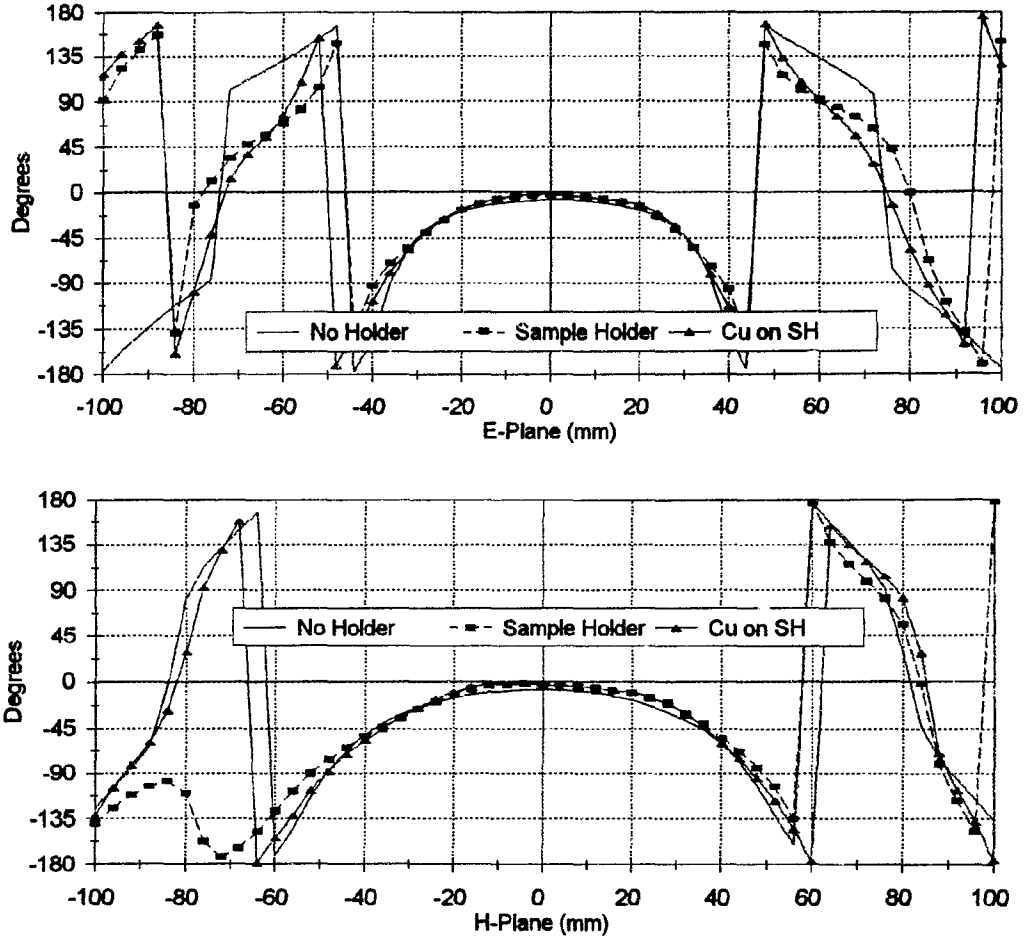

Figure 7.5: Phase of the field behind the sample holder in the E- and H-planes. The following are shown: (a) No holder, (b) Perspex sample holder, (c) Sample holder with front covered by a copper plate.

the inversion equations, and the reflection and transmission coefficients from the ideal sample with uniform thickness differs from a sample with non-parallel surfaces.

If the sample is not flat, the front of the sample may either be before or behind the calibration plane resulting in an error of the phase of the reflection coefficient. It is also well known that the reflection coefficient from a rough surface is different to that of an ideal smooth surface.

Baker-Jarvis *et al.* [73, 74] have used iterative (regression) methods to determine permittivity and permeability where both the sample thickness and the sample positions are treated as unknowns. They have also made a sensitivity analysis of the method to determine the accuracy with which the permittivity of a dielectric sample can be measured. An extension of these methods for chiral material measurements should be possible.

Even for a perfect sample there will be an uncertainty in the thickness of the sample since the measured thickness will differ from the actual thickness. The micrometer used to measure the sample thickness has a resolution of 0.01 mm.

7.3.6 Multiple Reflections Between the Sample and the Antenna

The effect of multiple reflections between the transmitting antenna and the calibration plate is discussed in Section 6.6. The amplitude of the multiple reflections between a sample and the antenna are expected to be much less than between the calibration plate and the antenna since the reflection coefficient from the samples are in general much smaller than the reflection coefficient of the calibration plate.

In Figures 6.8 to 6.11 it was shown that the measured reflection coefficient from a calibration plate is not 0 dB (as it ideally should be) if the plate is not placed in the calibration plane. A similar inaccuracy can be expected if the sample that is being measured is not placed at the calibration plane (i.e. at z=0).

The use of a time domain gate to remove unwanted multiple reflections is discussed in Section 6.6.1. It was pointed out that although a time domain gate will increase the measurement accuracy measurement errors are introduced at the band edges by the time domain transformation of the network analyzer.

7.3.7 Cross-Polarized Component Upon Reflection

Although the polarization of the reflection coefficient from an isotropic chiral medium is theoretically supposed to be the same as that of the incident wave (Section 2.6) this need not be the case in practice since the actual composite media are not perfect. A knowledge of the cross-polarized component of the reflection coefficient might be very important especially in measurements of the absorption coefficient of such composite media (Chapter 10). If the cross-polarized component is substantial and neglected in calculations the results will be incorrect and will lead to optimistic claims for absorption.

The free-space system used for this research cannot measure the cross-polarized component of the reflection coefficient without a third antenna and a linear polarization selective mirror.

7.4 Total Expected Measurement Errors

It is clearly very difficult to theoretically determine the quantitative contribution of each of the post-calibration errors to the overall uncertainty in the measured scattering parameters S_{11}, S_{21x} and S_{21y}.

However, the accuracy with which reflection and transmission coefficients can be made by the free-space setup can be determined by measuring those of a material with known constitutive parameters and then comparing the measured values to the theoretically predicted values.

The constitutive parameters of the samples will be assumed using published data, in particular that of Von Hippel [96]. Then the difference between the theoretical and the measured values of the S-parameters can be taken as the total error in the measurement of the free-space system.

Perspex (Plexiglas) was chosen as such a "standard" because of its availability and its desirable physical properties (i.e. very flat with smooth surfaces). The permittivity of Perspex was measured by Von Hippel to be $\epsilon_r = 2.59 + i\ 0.017353$ at 10 GHz and 27°C [96]. The theoretically predicted reflection and transmission coefficients of Perspex samples for this value of ϵ_r and various thicknesses are shown in Figure 7.6.

The reflection and transmission coefficients were measured after free-space calibration L2S (load and two shorts) and 3S (three shorts) calibration were done. The difference between the measured and the theoretical values are shown in Figures 7.7 to 7.10.

It is interesting to note that the errors in the measured reflection coefficient after L2S and 3S calibration, Figure 7.7, do not only have approximately the same maximum values but they also have very similar characteristics for the different samples.

Unfortunately the transmission coefficients do not cover such a wide dynamic range as the reflection coefficients for these samples, and the measurements are therefore not as suitable to illustrate the errors in S_{21} as they are for the errors in S_{11}. The measurements of the transmission coefficient after L2S calibration show large errors in the 15 to 17 GHz frequency range. It has been found that this is an isolated case. The large error in this single case is the result of a poor transmission calibration. The errors in the transmission coefficient are expected to be as shown in Figure 7.9 (b) and Figure 7.10 (b) for 3S calibration.

Apart from the isolated case of poor transmission calibration (L2S) these measurements show that there is not a big difference between the measurement accuracy after L2S (load, short and offset short) and 3S (short and two offset shorts) calibration respectively. From these figures it can also be concluded that, in general, the inaccuracies in the measurements of S_{11} and S_{21} are essentially independent of both the frequency and the actual reflection or transmission coefficient.

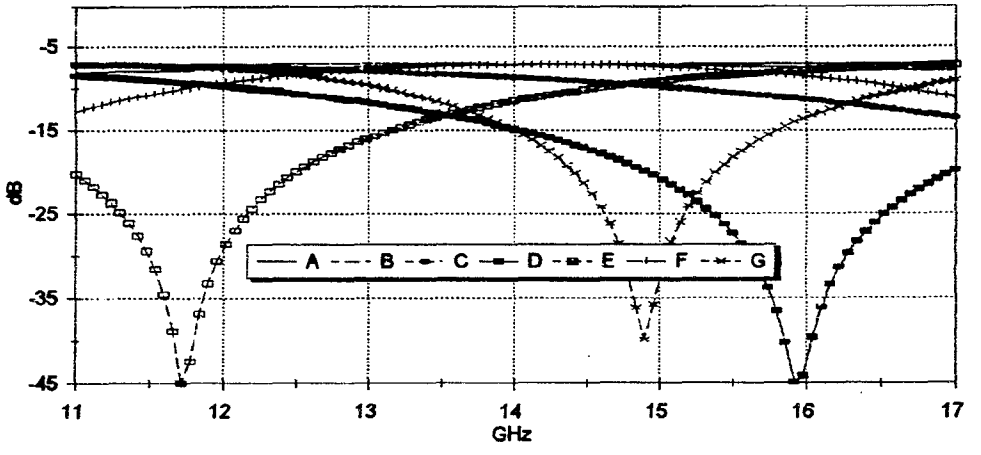

(a)

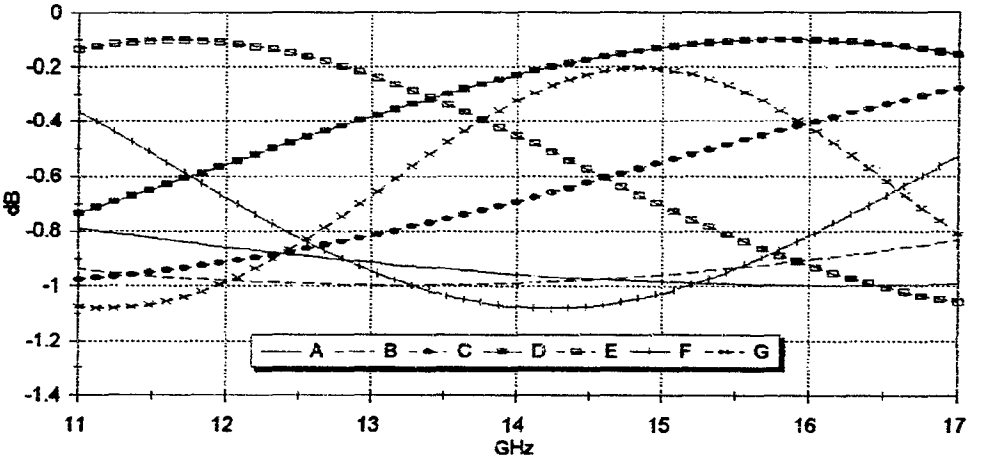

(b)

Figure 7.6: (a) Theoretical reflection and (b) transmission coefficients of Perspex samples with the following thickness:
A (2.88mm), B (3.54mm), C (4.68mm), D (5.83mm),
E (7.92mm), F (9.82mm), G (12.48mm).

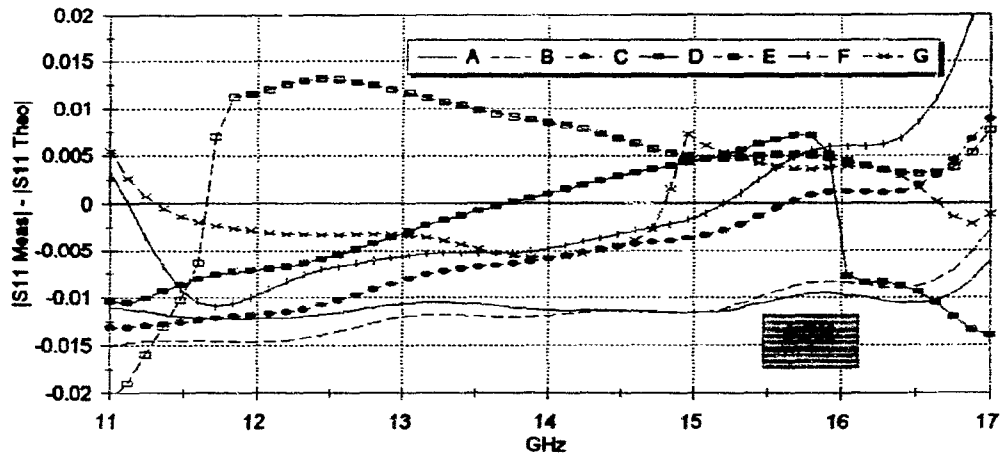

(a)

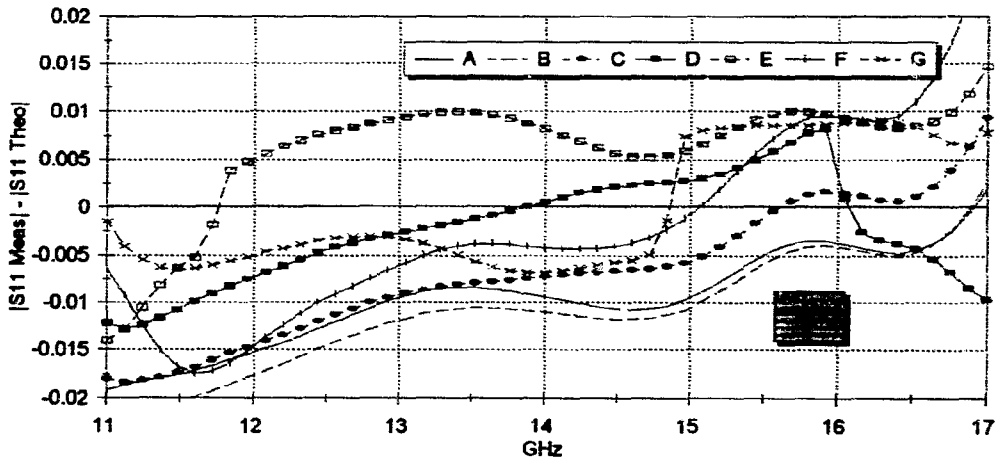

(b)

Figure 7.7: Errors in the amplitude, $\Delta|S_{11}|$, of the measured reflection coefficient of Perspex after (a) L2S and (b) 3S calibration. Note: the data show the difference in absolute values and are not in dB.
A (2.88mm), B (3.54mm), C (4.68mm), D (5.83mm),
E (7.92mm), F (9.82mm), G (12.48mm).

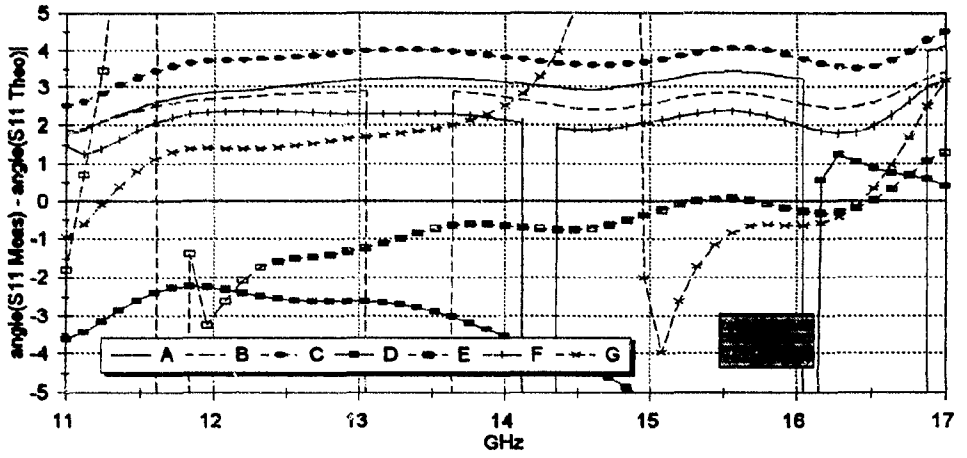

(a)

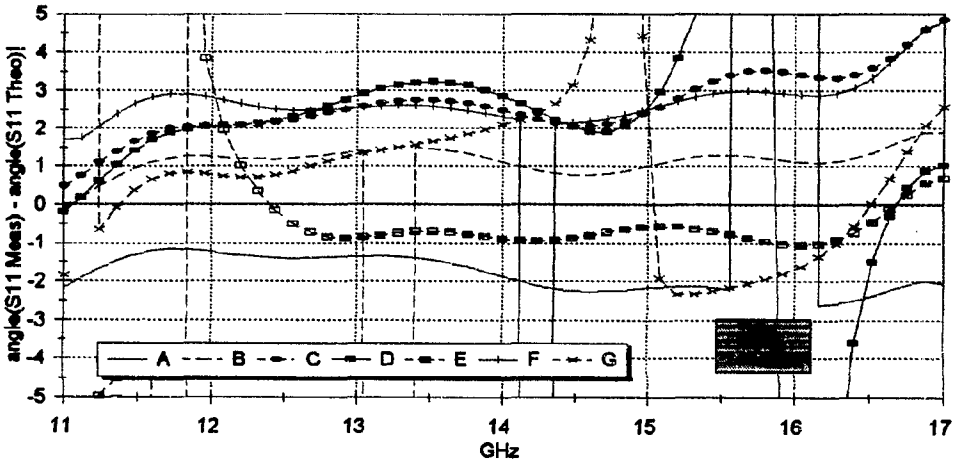

(b)

Figure 7.8: Errors in degrees of the phase, $\Delta\angle S_{11}$, of the measured reflection coefficient of Perspex after (a) L2S and (b) 3S calibration. Note: the data show the difference in absolute values and are not in dB.
A (2.88mm), B (3.54mm), C (4.68mm), D (5.83mm),
E (7.92mm), F (9.82mm), G (12.48mm).

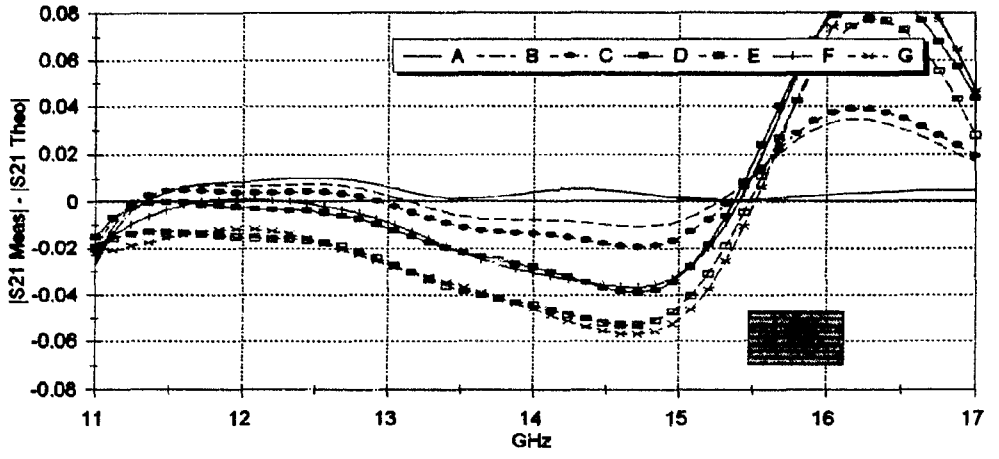

(a)

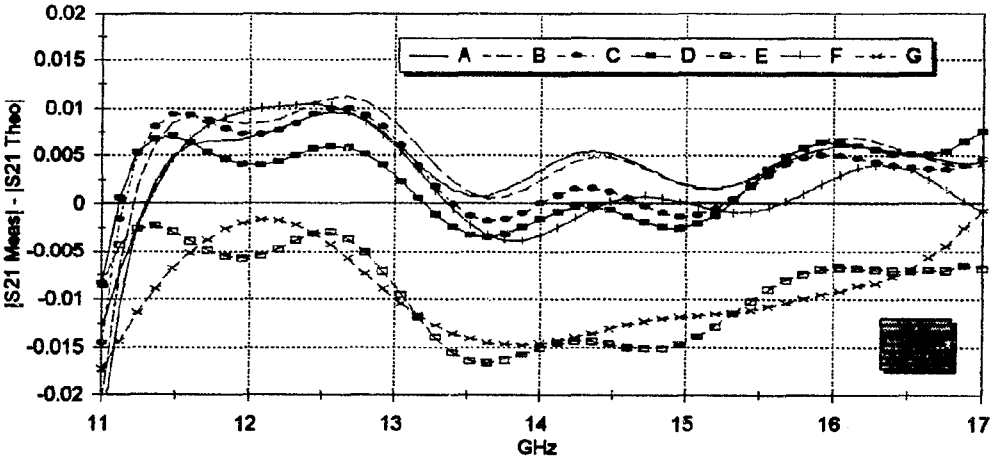

(b)

Figure 7.9: Errors in the amplitude, $\Delta|S_{21}|$, of the measured transmission coefficient of Perspex after (a) L2S and (b) 3S calibration.
A (2.88mm), B (3.54mm), C (4.68mm), D (5.83mm),
E (7.92mm), F (9.82mm), G (12.48mm).

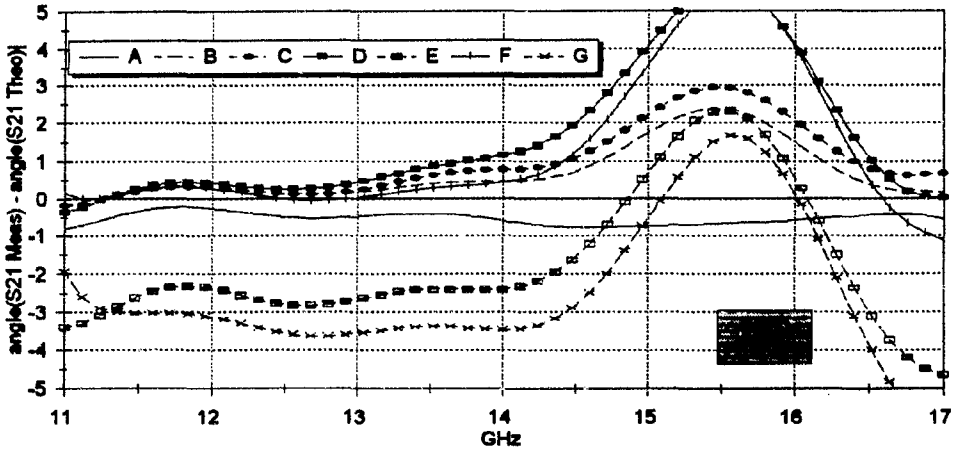

(a)

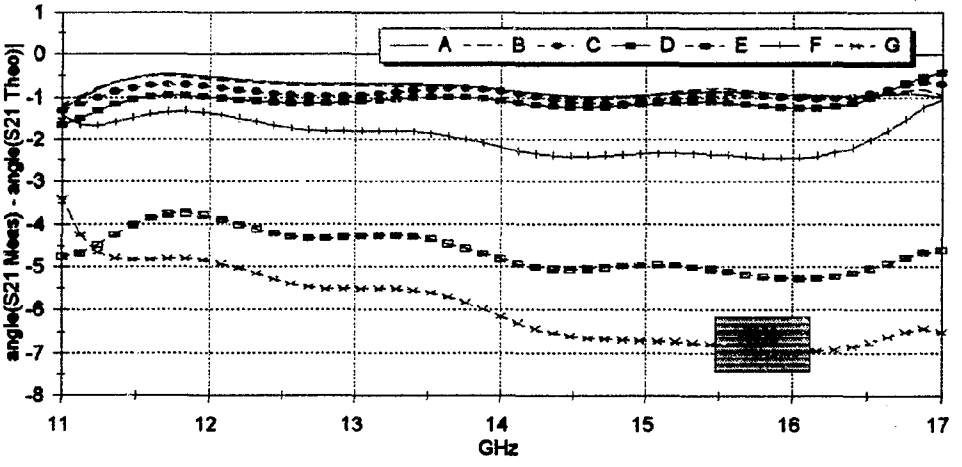

(b)

Figure 7.10: Errors in degrees of the phase, $\Delta\angle S_{21}$, of the measured transmission coefficient of Perspex after (a) L2S and (b) 3S calibration.
A (2.88mm), B (3.54mm), C (4.68mm), D (5.83mm),
E (7.92mm), F (9.82mm), G (12.48mm).

The expected measurement errors deduced from these experiments are summarized in Table 7.1. The errors in cross-polarized component of the transmission coefficient, S_{21y}, can not be determined from these measurements and other methods should be found to do so. The error in the phase of S_{21y} because of the movement of the coaxial cable is shown in Figure 7.1. If this error is assumed to be statistically independent from the error as measured in this section the expected error in phase can be calculated to be approximately $5 = \sqrt{4^2 + 3^2}$ degrees. If $S_{21y} \approx 0$ (say for achiral media) the expected error in the amplitude can be determined by measuring that of an achiral media and the measured value $|S_{21y}|$ should therefore be $\Delta|S_{21y}|$. This was done in Chapter 9 and a typical value obtained is $|S_{21y}| \approx 0.003$ (Fig F.1 and Fig F.4.) This is substantially lower than the measured error in the co-polarized component $\Delta|S_{21x}| \approx 0.01$ (Fig 7.9). It can therefore be concluded that $0.003 \leq \Delta|S_{21y}| \leq 0.01$.

Measured Parameter	Uncertainty in Amplitude	Uncertainty in Phase
Reflection coefficient	$\Delta\|S_{11}\| \approx 0.1$ dB	$\Delta\angle S_{11} \approx 4$ Degrees
Transmission coefficient (Co-polarized)	$\Delta\|S_{21x}\| \approx 0.1$ dB	$\Delta\angle S_{21x} \approx 4$ Degrees
Transmission coefficient (Cross-polarized)	$\Delta\|S_{21y}\| \approx 0.1$ dB	$\Delta\angle S_{21y} \approx 5$ Degrees

Table 7.1: Expected errors in the amplitude and phase of the transmission and reflection coefficients of the free-space system. These values are assumed to be frequency independent and also not dependent on the actual power level of the measurement.

Further investigation into the accuracy of the measurements should show that the errors *are* in fact dependent on the frequency and the actual reflection or transmission coefficient, as in the case of some other calibration systems [101] (see Appendix C).

Finally, note that the practice of measuring the reflection coefficient from the calibration plate after calibration, to "determine" the measurement errors, is incorrect since an independent standard must be used. The reflection coefficient from the calibration plate, was assumed to be $S_{11A} = -1$ in the calibration procedure (Section 6.3 and Appendix D) and a measurement of a similar device under test (or in this case an exact re-measurement) *should* therefore give a calibrated value of $S_{11} = -1$. This measurement therefore does not give an indication of how accurate the measurement is, but only a measure of the *repeatability* of the measurement.

Chapter 8

Uncertainty Analysis of the Constitutive Parameters Obtained by Inverting the Scattering Parameters

> Experience never errs; it is only your judgement that errs in promising itself results as are not caused by your experiments. Because, given a beginning, what follows from it must be its true consequence unless there is an impediment. And should there be an impediment, the result which ought to follow from the aforesaid beginning will partake of this impediment in a greater or less degree in proportion as this impediment is more or less powerful than the aforesaid beginning. Experience does not err, it is only your judgement that errs in expecting from her what is not in her power. Wrongly do men complain of Experience and with bitter reproaches accuse her of leading them astray. Let Experience alone, and rather turn your complaints against your own ignorance, which causes you to be carried away by your vain and foolish desires as to expect from Experience things which are not within her power; saying that she is fallacious. Wrongly do men complain of innocent Experience, accusing her often of deceit and lying demonstrations.
>
> — Leonardo da Vinci (1452–1519)

8.1 Introduction

In the previous chapter it was argued that the scattering coefficients produced by any practical measurement system are subject to errors from a variety of sources. Thus the quantities of interest, in particular the constitutive parameters obtained by the inversion procedures, will also contain errors. Consequently, when presenting the experimentally determined constitutive parameters, a quantitative measure of the uncertainty should be assigned to each of them. It goes without saying that without an associated uncertainty the data produced by any measurement lacks scientific credibility.

Most of the methods used to experimentally determine the constitutive parameters of artificial chiral media employ time-harmonic swept frequency waveforms to measure the amplitude and phase of the transmission and reflection coefficients of a chiral slab [48, 50, 63, 65, 66, 59, 81, 82]. The inversion methods used to obtain the constitutive parameters from the measured scattering parameters are closely related, and are generalizations of the procedure described by Nicolson and Ross [60], and Weir [58] for homogeneous materials with unknown permittivity and permeability.

It is known that the Nicolson-Ross and Weir equations suffer from increased uncertainty around frequencies where the sample thickness is a multiple of half a wavelength in the sample ($d = n\frac{\lambda}{2}$ with $n = 0, 1, 2...$), [71, 72, 73, 74, 75, 102]. Here it is shown that this is also the case for the inversion method presented in Chapter 3 of this thesis[1]. This serious disadvantage must be weighed against the advantages arising from the mathematical simplicity of the formulation and the fact that numerical iteration is not required.

Recently Baker-Jarvis *et al.* developed powerful and robust non-linear least-squares procedures for permittivity [73], and permittivity and permeability [74] measurements. These procedures are well-conditioned at all frequencies and it should be possible to generalize them for chiral materials, but this has not been attempted.

In the sections that follow, a sensitivity analysis will be done on the inversion equations that are used in this thesis to determine the constitutive parameters of a chiral slab [59]. This sensitivity analysis will then be used to determine the expected errors in the measured constitutive parameters, and an example of the method is given.

A major advantage of the method described is that the sensitivities, or partial derivatives, and uncertainties are closed form analytical expressions. This is clearly more convenient than the numerical perturbation methods which are often used [48, 71, 72].

Much more important however is the fact that the sensitivity analysis allows the sources of measurement uncertainty to be isolated and identified. This in turn makes it possible to improve the calibration and measurement procedures in a systematic way, by concentrating on the major error mechanisms.

8.2 Chiral Inversion Equations

The inversion equations derived in Chapter 3 are summarized here for convenience. The reflection coefficient, S_{11}, and the transmission coefficients of the co-polarized component, S_{21x}, and the cross-polarized component, S_{21y}, are

$$S_{11} \equiv \frac{E_{rx}(z=0)}{E_{ix}(z=0)} = \frac{\Gamma(1-P_rP_l)}{1-\Gamma^2P_rP_l}, \tag{8.1}$$

$$S_{21x} \equiv \frac{E_{tx}(z=d)}{E_{ix}(z=0)} = \frac{\frac{1}{2}(1-\Gamma^2)(P_r+P_l)}{1-\Gamma^2P_rP_l}, \tag{8.2}$$

[1] And presumably the related ones referenced in the previous paragraph.

$$S_{21y} \equiv \frac{E_{ty}(z=d)}{E_{ix}(z=0)} = \frac{i\frac{1}{2}(1-\Gamma^2)(P_r - P_l)}{1-\Gamma^2 P_r P_l}. \tag{8.3}$$

The reflection coefficient for a chiral slab of semi-infinite thickness is

$$\Gamma = \frac{\eta_c - \eta_1}{\eta_c + \eta_1}, \tag{8.4}$$

while

$$P_r = \exp(ik_r d) \tag{8.5}$$

and

$$P_l = \exp(ik_l d) \tag{8.6}$$

are the propagation factors for the right-circularly and left-circularly polarized eigenwaves in the chiral medium. These equations for the scattering coefficients of a linearly polarized plane wave that is normally incident upon a chiral slab are inverted to obtain the constitutive parameters as follows,

$$\epsilon = \frac{2}{\omega\eta_c}\frac{k_r k_l}{(k_r + k_l)}, \tag{8.7}$$

$$\mu = \frac{\eta_c}{2\omega}(k_r + k_l), \tag{8.8}$$

$$\xi = \frac{1}{\eta_c}\frac{(k_r - k_l)}{(k_r + k_l)}, \tag{8.9}$$

where the two wave numbers are calculated from,

$$k_r = \frac{1}{id}\ln(P_r) = \frac{1}{id}\ln\left(\frac{S_{21x} - iS_{21y}}{1-\Gamma S_{11}}\right), \tag{8.10}$$

$$k_l = \frac{1}{id}\ln(P_l) = \frac{1}{id}\ln\left(\frac{S_{21x} + iS_{21y}}{1-\Gamma S_{11}}\right). \tag{8.11}$$

The intrinsic wave impedance of the chiral medium is given as,

$$\eta_c = \eta_1\frac{(1+\Gamma)}{(1-\Gamma)}, \tag{8.12}$$

with η_1 the intrinsic impedance of the non-chiral medium surrounding the slab. The reflection coefficient from a semi-infinite chiral medium can be obtained from

$$\Gamma = \chi \pm \sqrt{\chi^2 - 1}, \tag{8.13}$$

where the sign is chosen so that $|\Gamma| \leq 1$, because the chiral medium is passive. The coefficient term

$$\chi = ((1 + S_{11}^2) - (S_{21x}^2 + S_{21y}^2))/(2S_{11}) \tag{8.14}$$

is known in terms of the scattering parameters.

8.3 Uncertainty Analysis

In the analysis it is assumed that there are seven measurement errors. These are the errors made in measuring the magnitudes of the scattering parameters, $\Delta|S_{11}|$, $\Delta|S_{21x}|$, $\Delta|S_{21y}|$, the errors made in measuring the phase of the S-parameters, $\Delta\angle S_{11}$, $\Delta\angle S_{21x}$, $\Delta\angle S_{21y}$, and the error made in measuring the slab thickness, Δd.

As a result of these errors the measured S-parameters differ from the true S-parameters in the following way,

$$S_{11m} = S_{11} + \Delta S_{11} = \{|S_{11}| + \Delta|S_{11}|\}e^{i(\angle S_{11}+\Delta\angle S_{11})}, \tag{8.15}$$

$$S_{21xm} = S_{21x} + \Delta S_{21x} = \{|S_{21x}| + \Delta|S_{21x}|\}e^{i(\angle S_{21x}+\Delta\angle S_{21x})}, \tag{8.16}$$

$$S_{21ym} = S_{21y} + \Delta S_{21y} = \{|S_{21y}| + \Delta|S_{21y}|\}e^{i(\angle S_{21y}+\Delta\angle S_{21y})}, \tag{8.17}$$

$$d_m = d + \Delta d. \tag{8.18}$$

The uncertainty analysis makes use of two measures, *sensitivity* and *uncertainty*.

In general the *sensitivity* of ν to a small change in Ψ is defined as [103, p.52]

$$\mathcal{S}_{\Psi}^{\nu} \equiv \lim_{\Delta\Psi\to 0} \frac{\left|\frac{\Delta\nu}{\nu}\right|}{\left|\frac{\Delta\Psi}{\Psi}\right|}. \tag{8.19}$$

However the following specific definitions will be used in the thesis. Let $\nu = \nu' + i\nu''$ represent any of the measured complex constitutive parameters (μ, ϵ or ξ), and $S = |S|e^{i\angle S}$ any one of the measured complex S-parameters (S_{11}, S_{21x} or S_{21y}).

The sensitivity of the real part of a constitutive parameter to the magnitude of any of the measured scattering parameters is defined as

$$\begin{aligned} \mathcal{S}_{|S|}^{\nu'} &\equiv \lim_{\Delta|S|\to 0} \frac{\frac{\Delta\nu'}{|\nu|}}{\frac{\Delta|S|}{|S|}} \\ &= \frac{\partial\nu'}{\partial|S|}\frac{|S|}{|\nu|}. \end{aligned} \tag{8.20}$$

The sensitivity of the real part of a constitutive parameter to the thickness d is

$$\begin{aligned} \mathcal{S}_{d}^{\nu'} &\equiv \lim_{\Delta d\to 0} \frac{\frac{\Delta\nu'}{|\nu|}}{\frac{\Delta d}{d}} \\ &= \frac{\partial\nu'}{\partial d}\frac{d}{|\nu|}. \end{aligned} \tag{8.21}$$

The sensitivity of the real part of a constitutive parameter to the phase of any of the measured S-parameter is defined as

$$\begin{aligned} \mathcal{S}_{\angle S}^{\nu'} &\equiv \lim_{\Delta\angle S\to 0} \frac{\frac{\Delta\nu'}{|\nu|}}{\frac{\Delta\angle S}{2\pi}} \\ &= \frac{\partial\nu'}{\partial\angle S}\frac{2\pi}{|\nu|}. \end{aligned} \tag{8.22}$$

The ratio $\frac{\Delta \angle S}{2\pi}$ is used since $\frac{\Delta \angle S}{\angle S}$ will have singularities where $\angle S = 0$ and the percentage change in angle should not depend on the actual angle.

The same definitions are used for the imaginary part of the constitutive parameters with only a substitution of ν' with ν'' in the above equations. Since ϵ'', μ'', ξ' and ξ'' can all attain very small values normalization by $|\nu|$ and not $|\nu'|$ or $|\nu''|$, is used in Equations (8.20-8.22) to avoid ill-conditioning of the sensitivity parameters.

In the limit $\Delta\epsilon$, the change in ϵ due to a small change in one of the scattering parameters, say ΔS_{11}, can be found from the following first order approximation,

$$\Delta\epsilon = \frac{\partial \epsilon}{\partial S_{11}} \Delta S_{11}. \tag{8.23}$$

If the errors in the scattering parameters ΔS_{11}, ΔS_{21x}, ΔS_{21y} and the thickness Δd are "small" and known the total error in ϵ, μ and ξ can be estimated from,

$$\Delta\mu = \frac{\partial \mu}{\partial S_{11}} \Delta S_{11} + \frac{\partial \mu}{\partial S_{21x}} \Delta S_{21x} + \frac{\partial \mu}{\partial S_{21y}} \Delta S_{21y} + \frac{\partial \mu}{\partial d} \Delta d, \tag{8.24}$$

$$\Delta\epsilon = \frac{\partial \epsilon}{\partial S_{11}} \Delta S_{11} + \frac{\partial \epsilon}{\partial S_{21x}} \Delta S_{21x} + \frac{\partial \epsilon}{\partial S_{21y}} \Delta S_{21y} + \frac{\partial \epsilon}{\partial d} \Delta d, \tag{8.25}$$

$$\Delta\xi = \frac{\partial \xi}{\partial S_{11}} \Delta S_{11} + \frac{\partial \xi}{\partial S_{21x}} \Delta S_{21x} + \frac{\partial \xi}{\partial S_{21y}} \Delta S_{21y} + \frac{\partial \xi}{\partial d} \Delta d. \tag{8.26}$$

The worst case error can be determined by taking the sum of the absolute values of each contributing term.

The complex scattering parameters make more physical sense if they are written in polar form $S = |S|e^{i\angle S}$. Then the error $\Delta\epsilon$ in Equation (8.23) can also be given as a combination of the error in the amplitude and the error in the phase of the measured scattering parameters,

$$\Delta\epsilon = \frac{\partial \epsilon}{\partial |S_{11}|} \Delta |S_{11}| + \frac{\partial \epsilon}{\partial \angle S_{11}} \Delta \angle S_{11}. \tag{8.27}$$

For example the total error in the real part of the chirality parameter, ξ, is

$$\begin{aligned} \Delta\xi' = {} & \frac{\partial \xi'}{\partial |S_{11}|} \Delta |S_{11}| + \frac{\partial \xi'}{\partial |S_{21x}|} \Delta |S_{21x}| + \frac{\partial \xi'}{\partial |S_{21y}|} \Delta |S_{21y}| + \frac{\partial \xi'}{\partial d} \Delta d \\ & + \frac{\partial \xi'}{\partial \angle S_{11}} \Delta \angle S_{11} + \frac{\partial \xi'}{\partial \angle S_{21x}} \Delta \angle S_{21x} + \frac{\partial \xi'}{\partial \angle S_{21y}} \Delta \angle S_{21y} \end{aligned} \tag{8.28}$$

The partial differentials, $\frac{\partial \nu'}{\partial |S|}$ and $\frac{\partial \nu'}{\partial \angle S}$, can be obtained from $\frac{\partial \nu}{\partial S}$ using the following two equations which are derived in Appendix E,

$$\frac{\partial \nu'}{\partial |S|} = \mathrm{Re}\left(\frac{\partial \nu}{\partial S} e^{i\angle S}\right), \tag{8.29}$$

$$\frac{\partial \nu'}{\partial \angle S} = \mathrm{Re}\left(\frac{\partial \nu}{\partial S} iS\right). \tag{8.30}$$

Similar equations are used for the imaginary value ν''.

Since the exact measurement errors are not known, statistical methods should be used to determine the expected errors in the constitutive parameters.

Assuming that the measurements are statistically independent the standard deviation of the measured constitutive parameters can be found from the root mean square of the contributing errors [104]. For example $\sigma_{\xi'}$ can be obtained from

$$\begin{aligned}\sigma_{\xi'} = [&(\frac{\partial\xi'}{\partial|S_{11}|}\sigma_{|S_{11}|})^2 + (\frac{\partial\xi'}{\partial|S_{21x}|}\sigma_{|S_{21x}|})^2 + (\frac{\partial\xi'}{\partial|S_{21y}|}\sigma_{|S_{21y}|})^2 + (\frac{\partial\xi'}{\partial d}\sigma_d)^2 \\ &+(\frac{\partial\xi'}{\partial\angle S_{11}}\sigma_{\angle S_{11}})^2 + (\frac{\partial\xi'}{\partial\angle S_{21x}}\sigma_{\angle S_{21x}})^2 + (\frac{\partial\xi'}{\partial\angle S_{21y}}\sigma_{\angle S_{21y}})^2]^{1/2} \end{aligned} \tag{8.31}$$

where $\sigma_{|S|}$ and $\sigma_{\angle S}$ are the standard deviations of the measured S-parameters. It will be assumed that the errors ($\Delta|S|$, $\Delta\angle S$) tabulated in the previous Chapter are representative of these standard deviations. If the assumption of independence is not made the relation that should be used to determine the total expected error becomes much more complicated and will not be attempted in this thesis[2].

8.4 Partial Derivatives

The partial derivatives of all the constitutive relations to the scattering parameters, in all the necessary combinations, are given by the following equations.

The notation $(A)_B$ is used for the partial derivative term $\frac{\partial A}{\partial B}$ where A and B are any of the symbols used in Equations (8.1 to 8.14).

Permittivity: The partial derivative of ϵ to S_{11} is,

$$\begin{aligned}\frac{\partial\epsilon}{\partial S_{11}} = &-\frac{2k_lk_r(\eta_c)_\Gamma(\Gamma)_\chi(\chi)_{S_{11}}}{\omega\eta_c^2[k_l+k_r]} \\ &+\frac{2k_r(k_l)_{P_l}[(P_l)_\Gamma(\Gamma)_\chi(\chi)_{S_{11}}+(P_l)_{S_{11}}]}{\omega\eta_c[k_l+k_r]} \\ &+\frac{2k_l(k_r)_{P_r}[(P_r)_\Gamma(\Gamma)_\chi(\chi)_{S_{11}}+(P_r)_{S_{11}}]}{\omega\eta_c[k_l+k_r]} \\ &-\frac{2k_lk_r\{(k_l)_{P_l}[(P_l)_\Gamma(\Gamma)_\chi(\chi)_{S_{11}}+(P_l)_{S_{11}}]+(k_r)_{P_r}[(P_r)_\Gamma(\Gamma)_\chi(\chi)_{S_{11}}+(P_r)_{S_{11}}]\}}{\omega\eta_c[k_l+k_r]^2}.\end{aligned} \tag{8.32}$$

The partial derivatives for $\frac{\partial\epsilon}{\partial S_{21x}}$ and $\frac{\partial\epsilon}{\partial S_{21y}}$ are exactly the same as the above with S_{11} replaced by S_{21x} and S_{21y} respectively.

The partial derivative of ϵ to the thickness d is

$$\frac{\partial\epsilon}{\partial d} = \frac{2k_r(k_l)_d}{\omega\eta_c[k_l+k_r]} + \frac{2k_l(k_r)_d}{\omega\eta_c[k_l+k_r]} - \frac{2k_lk_r[(k_l)_d+(k_r)_d]}{\omega\eta_c[k_l+k_r]^2}. \tag{8.33}$$

[2]Note for example that, strictly speaking, there should be a correlation between the measurements of S_{21x} and S_{21y}.

Permeability: The partial derivative of μ to S_{11} is

$$\frac{\partial \mu}{\partial S_{11}} = \frac{[k_l + k_r](\eta_c)_\Gamma(\Gamma)_\chi(\chi)_{S_{11}}}{2\omega} + \frac{\eta_c\{(k_l)_{P_l}[(P_l)_\Gamma(\Gamma)_\chi(\chi)_{S_{11}} + (P_l)_{S_{11}}] + (k_r)_{P_r}[(P_r)_\Gamma(\Gamma)_\chi(\chi)_{S_{11}} + (P_r)_{S_{11}}]\}}{2\omega}, \tag{8.34}$$

and again are the partial derivatives $\frac{\partial \mu}{\partial S_{21x}}$ and $\frac{\partial \mu}{\partial S_{21y}}$ the same as in the equation above with S_{11} substituted by S_{21x} and S_{21y} respectively.

The partial derivative of μ to the thickness d is simply

$$\frac{\partial \mu}{\partial d} = \frac{\eta_c[(k_l)_d + (k_r)_d]}{2\omega}. \tag{8.35}$$

Chirality: The partial derivative of ξ to the reflection coefficient, S_{11}, is

$$\frac{\partial \xi}{\partial S_{11}} = -\frac{[k_r - k_l](\eta_c)_\Gamma(\Gamma)_\chi(\chi)_{S_{11}}}{\eta_c^2[k_l + k_r]} + \frac{(k_r)_{P_r}[(P_r)_\Gamma(\Gamma)_\chi(\chi)_{S_{11}} + (P_r)_{S_{11}}] - (k_l)_{P_l}[(P_l)_\Gamma(\Gamma)_\chi(\chi)_{S_{11}} + (P_l)_{S_{11}}]}{\eta_c[k_l + k_r]} - \frac{[k_r - k_l]\{(k_r)_{P_r}[(P_r)_\Gamma(\Gamma)_\chi(\chi)_{S_{11}} + (P_r)_{S_{11}}] + (k_l)_{P_l}[(P_l)_\Gamma(\Gamma)_\chi(\chi)_{S_{11}} + (P_l)_{S_{11}}]\}}{\eta_c[k_l + k_r]^2}. \tag{8.36}$$

Again the partial derivatives for $\frac{\partial \xi}{\partial S_{21x}}$ and $\frac{\partial \xi}{\partial S_{21y}}$ are exactly the same as the above with S_{11} replaced by S_{21x} and S_{21y} respectively.

The partial derivative of ξ to the thickness d is

$$\frac{\partial \xi}{\partial d} = \frac{(k_r)_d - (k_l)_d}{\eta_c[k_l + k_r]} - \frac{[k_r - k_l][(k_r)_d + (k_l)_d]}{\eta_c[k_l + k_r]^2}. \tag{8.37}$$

In these equations the partial derivative terms $(A)_B$ as defined in the beginning of this section are

$$(\eta_c)_\Gamma = \frac{2\eta_1}{(1-\Gamma)^2}, \tag{8.38}$$

$$(\Gamma)_\chi = 1 \pm \frac{\chi}{\sqrt{\chi^2 - 1}}, \tag{8.39}$$

$$(\chi)_{S_{11}} = 1 - \frac{(1 + S_{11}^2 - (S_{21x}^2 + S_{21y}^2))}{2S_{11}^2}, \tag{8.40}$$

$$(\chi)_{S_{21x}} = \frac{-S_{21x}}{S_{11}}, \tag{8.41}$$

$$(\chi)_{S_{21y}} = \frac{-S_{21y}}{S_{11}}, \tag{8.42}$$

$$(k_r)_{P_r} = \frac{1}{idP_r}, \tag{8.43}$$

$$(k_l)_{P_l} = \frac{1}{idP_l}, \tag{8.44}$$

$$(k_r)_d = -\left(\frac{k_r}{d}\right), \tag{8.45}$$

$$(k_l)_d = -\left(\frac{k_l}{d}\right), \tag{8.46}$$

$$(P_r)_\Gamma = \frac{S_{11}(S_{21x} - iS_{21y})}{(1 - S_{11}\Gamma)^2}, \tag{8.47}$$

$$(P_l)_\Gamma = \frac{S_{11}(S_{21x} + iS_{21y})}{(1 - S_{11}\Gamma)^2}, \tag{8.48}$$

$$(P_r)_{S_{11}} = \frac{\Gamma(S_{21x} - iS_{21y})}{(1 - S_{11}\Gamma)^2}, \tag{8.49}$$

$$(P_l)_{S_{11}} = \frac{\Gamma(S_{21x} + iS_{21y})}{(1 - S_{11}\Gamma)^2}, \tag{8.50}$$

$$(P_r)_{S_{21x}} = \frac{1}{1 - S_{11}\Gamma}, \tag{8.51}$$

$$(P_l)_{S_{21x}} = \frac{1}{1 - S_{11}\Gamma}, \tag{8.52}$$

$$(P_r)_{S_{21y}} = \frac{-i}{1 - S_{11}\Gamma}, \tag{8.53}$$

$$(P_l)_{S_{21y}} = \frac{i}{1 - S_{11}\Gamma}. \tag{8.54}$$

The partial derivatives in Equation (8.31) and similar equations for the other constitutive parameters are now known in terms of the analytical expressions (8.32–8.54). The expected errors (standard deviations) in the measured constitutive parameters can therefore be calculated if the expected errors (standard deviations) in the measured scattering parameters are known.

The method of determining the error in the constitutive parameters from the partial derivatives, if the error in the scattering parameters is known (as in Equations (8.24–8.26)), was tested by comparing them with the results obtained from a perturbation method. This was done as follows: in the perturbation method simulated $\Delta|S|$, $\Delta\angle S$ and Δd were added to the *error free* S-parameters and sample thickness, Equations (8.15–8.17). The resulting S-parameters were then inverted using the equations of Chapter 3 to give the constitutive parameters with errors. The errors in the constitutive parameters obtained by this perturbation method were then compared to the errors obtained using the partial derivatives Equations (8.32–8.37), and Equations (8.24–8.26). The results obtained from the two different methods were the same, provided that the errors ΔS and Δd were not very large as required by the analytical formulation. The condition for "small" measurement errors is satisfied by the calibration procedure.

8.5 Numerical Example

A sensitivity analysis will now be done on the measurement of a typical artificial chiral slab (220RH-S)[3].

The measured scattering parameters of this sample are shown in Figure 8.1. Inversion of these S-parameters yield the constitutive parameters shown in Figure 8.2 and Figure 8.3. The standard deviation of the respective measured constitutive parameters are also shown and the method used to obtain these values will now be discussed.

It will be assumed that the errors in the measured S-parameters as determined in Chapter 7 and summarised in Table 7.1, are representative of the standard deviation in the measurements (eg. $\sigma_{|S|} = \Delta|S|$). The standard deviation in the measured sample thickness, σ_d, will be assumed to be 0.1 mm. The contribution of each of these errors to the standard deviation of the constitutive parameters will now be determined.

The measured scattering parameters are used to determine the partial derivatives as described in the previous section. The sensitivity of the real and imaginary parts of the constitutive parameters (μ, ϵ and ξ) to the *magnitude* values of the S-parameters (S_{11}, S_{21x} and S_{21y}) and the sample thickness, d,

$$\mathcal{S}^{\nu'}_{|S|} = \frac{\partial \nu'}{\partial |S|}\frac{|S|}{|\nu|},$$
$$\mathcal{S}^{\nu'}_{d} = \frac{\partial \nu'}{\partial d}\frac{d}{|\nu|},$$

are shown in Figures 8.4 and 8.5 respectively. Likewise the sensitivity of the constitutive parameters to the *phase* of the S-parameters,

$$\mathcal{S}^{\nu'}_{\angle S} = \frac{\partial \nu'}{\partial \angle S}\frac{2\pi}{|\nu|},$$

are shown in Figures 8.6 and 8.7. A sensitivity of 1 means that a one percent change in the measured scattering parameter will result in a one percent change in the constitutive parameter. For this particular example the figures reveal that both the real and the imaginary parts of the constitutive parameters are particularly sensitive to S_{21x} at the lower frequencies where $d \approx \lambda/2$. It is also evident that the constitutive parameters are approximately 7 times more sensitive to the phase than to the absolute value of S_{21x}.

Since the measurement errors are known (Table 7.1) the expected errors in the constitutive parameters can be determined as in Equation 8.31,

$$\sigma_{\xi'} = [(\frac{\partial \xi'}{\partial |S_{11}|}\sigma_{|S_{11}|})^2 + (\frac{\partial \xi'}{\partial |S_{21x}|}\sigma_{|S_{21x}|})^2 + (\frac{\partial \xi'}{\partial |S_{21y}|}\sigma_{|S_{21y}|})^2 + (\frac{\partial \xi'}{\partial d}\sigma_d)^2$$
$$+(\frac{\partial \xi'}{\partial \angle S_{11}}\sigma_{\angle S_{11}})^2 + (\frac{\partial \xi'}{\partial \angle S_{21x}}\sigma_{\angle S_{21x}})^2 + (\frac{\partial \xi'}{\partial \angle S_{21y}}\sigma_{\angle S_{21y}})^2]^{1/2}.$$

The standard deviation of the measured constitutive parameters are shown in Figure 8.2 and Figure 8.3. The contribution of each of the measurement errors ($\Delta|S_{11}|$,

[3]Further details of the sample (220RH-S) can be found in Chapter 9.

$\Delta|S_{21x}|$, $\Delta|S_{21y}|$, Δd and $\Delta\angle S_{11}$, $\Delta\angle S_{21x}$, $\Delta\angle S_{21y}$) to the total standard deviation in the constitutive parameter can be calculated from each corresponding term in Equation 8.31 and is shown in Figures 8.8 to 8.13. For example the error in ξ' because of an error $\Delta|S_{11}|$ is,

$$\left|\frac{\partial\xi'}{\partial|S_{11}|}\,\sigma_{|S_{11}|}\right|.$$

As expected from the sensitivity analysis, the major contributors to the errors in μ and ϵ are $\Delta|S_{21x}|$ and $\Delta\angle S_{21x}$. However it is important to note that although the sensitivity of μ' and ϵ' to $|S_{11}|$ is only approximately ± 1 (see Fig 8.4) for all frequencies, the fractional error $\frac{\Delta|S_{11}|}{|S_{11}|}$ is high at the lower frequencies since $\Delta|S_{11}|$ is approximately constant but $|S_{11}|$ changes with frequency and has minimum of -20 dB at 11.5 GHz (Fig 8.1). From the definition of the sensitivity parameter, Equation (8.20), it should be clear that $\Delta|S_{11}|$ will therefore also make a major contribution to the errors $\Delta\mu$ and $\Delta\epsilon$ as can be seen in Figures 8.8 to 8.11.

This example illustrates the errors in the constitutive parameters as obtained from inversion methods when the sample is half a wavelength thick[4]. The importance of an accurate measurement of the cross-polarized transmission coefficient, $|S_{21y}|$, (and thus the rotation angle) for an accurate measure of the real part of the chirality parameter ξ' is evident from Figure 8.12 where the main error contribution at the high frequencies is from $\Delta|S_{21y}|$. (Note that $\Delta\angle S_{21x}$ makes the larger contribution where $d \approx \lambda/2$.) The large contribution of $\Delta|S_{21y}|$ (except for $d \approx \lambda/2$) is expected since ξ' is directly responsible for the rotation of the transmitted field, ($\theta = -\omega\mu\xi d$, [2, eqn.72] and [35, eqn.7]).

8.6 Conclusion

A method to determine the expected errors in the measured constitutive parameters of a chiral slab has been developed. A sensitivity analysis has been done on the inversion equations used to determine the constitutive parameters from the measured scattering parameters. The partial differential equations used in this analysis are in a convenient analytical form. With this method the contribution of each measurement error to the overall error can be determined. The accuracy with which the constitutive parameters of a chiral slab can be measured could be improved by this knowledge.

The expected errors in the measured constitutive parameters could also be determined by a perturbation technique where the errors in the measured scattering parameters are added to the measured values and the resulting constitutive parameters calculated by inversion. However with this method it is difficult to determine the contributions of the respective measurement errors ($\Delta|S|$, $\Delta\angle S$ and Δd).

This sensitivity analysis shows that the constitutive parameters are very sensitive to errors in the measured scattering parameters in the frequency region where the sample thickness is half a wavelength thick or multiples thereof. This would be especially true

[4]The average wavelength of the LCP and the RCP waves is $\lambda_{av} = \frac{1}{2}(\lambda_r + \lambda_l)$. The wavelength inside the sample in terms of the thickness d is shown in Figure F.23.

for low loss media where the reflection coefficient, S_{11}, goes through a deep minimum where $d = n(\lambda/2)$. The analysis can also be used to show that the best accuracy is obtained if $d = (2n + 1)(\lambda_{Avg}/4)$, where $\lambda_{Avg} = \frac{1}{2}(\lambda_r + \lambda_l)$ for a chiral medium.

It is important to note that the method can also be used for the measurement of dielectric and magnetic media using the method of inversion of the scattering parameters S_{11} and S_{21}. For such achiral ($\xi = 0$) media, $k_r = k_l$ and therefore $P_r = P_l$ and $S_{21y} = 0$. These conditions can be introduced in all of the equations in this chapter to determine the partial derivatives of the inversion equations for achiral media.

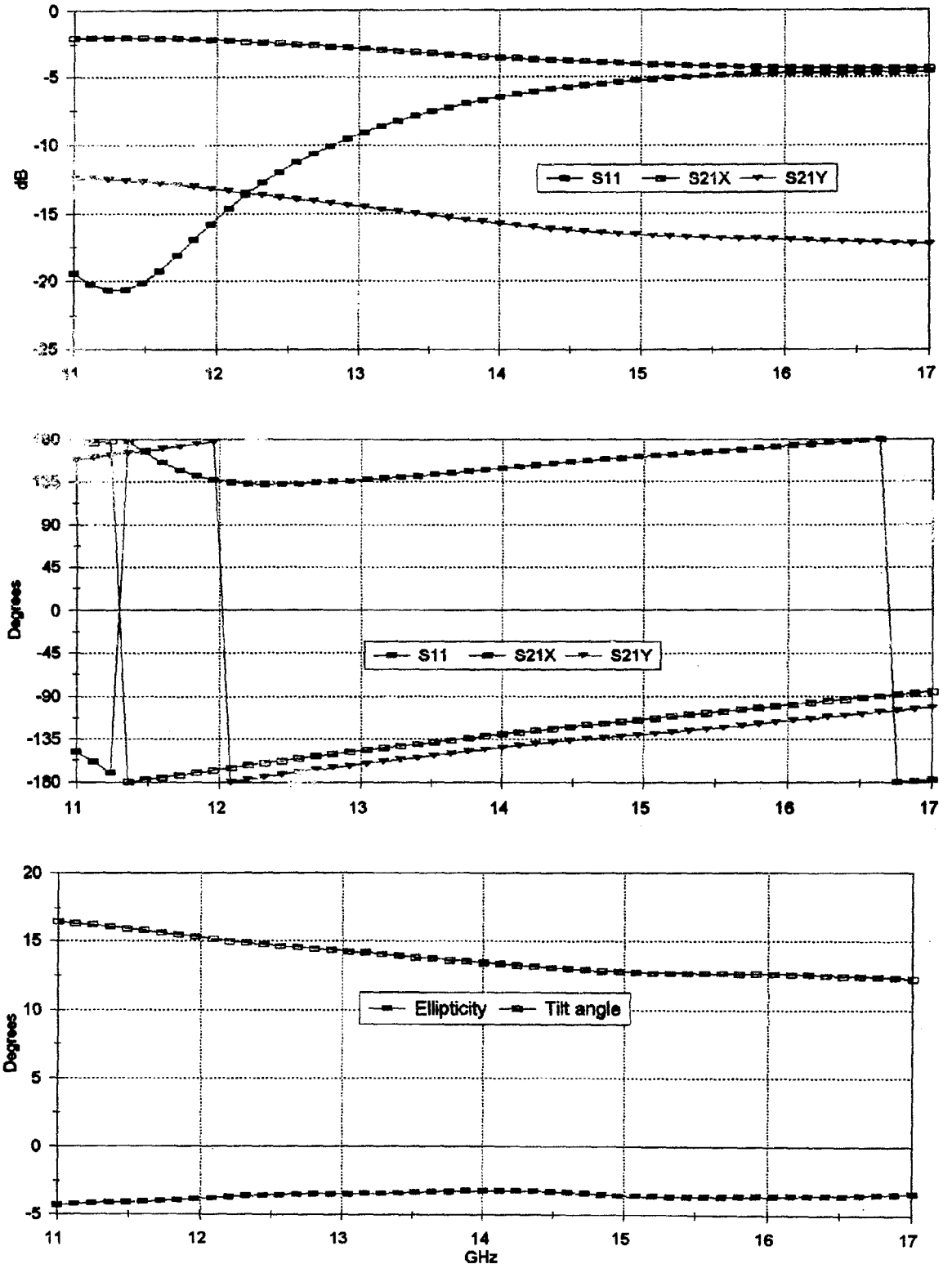

Figure 8.1: Measured scattering parameters and polarization of the 220RH-S sample.

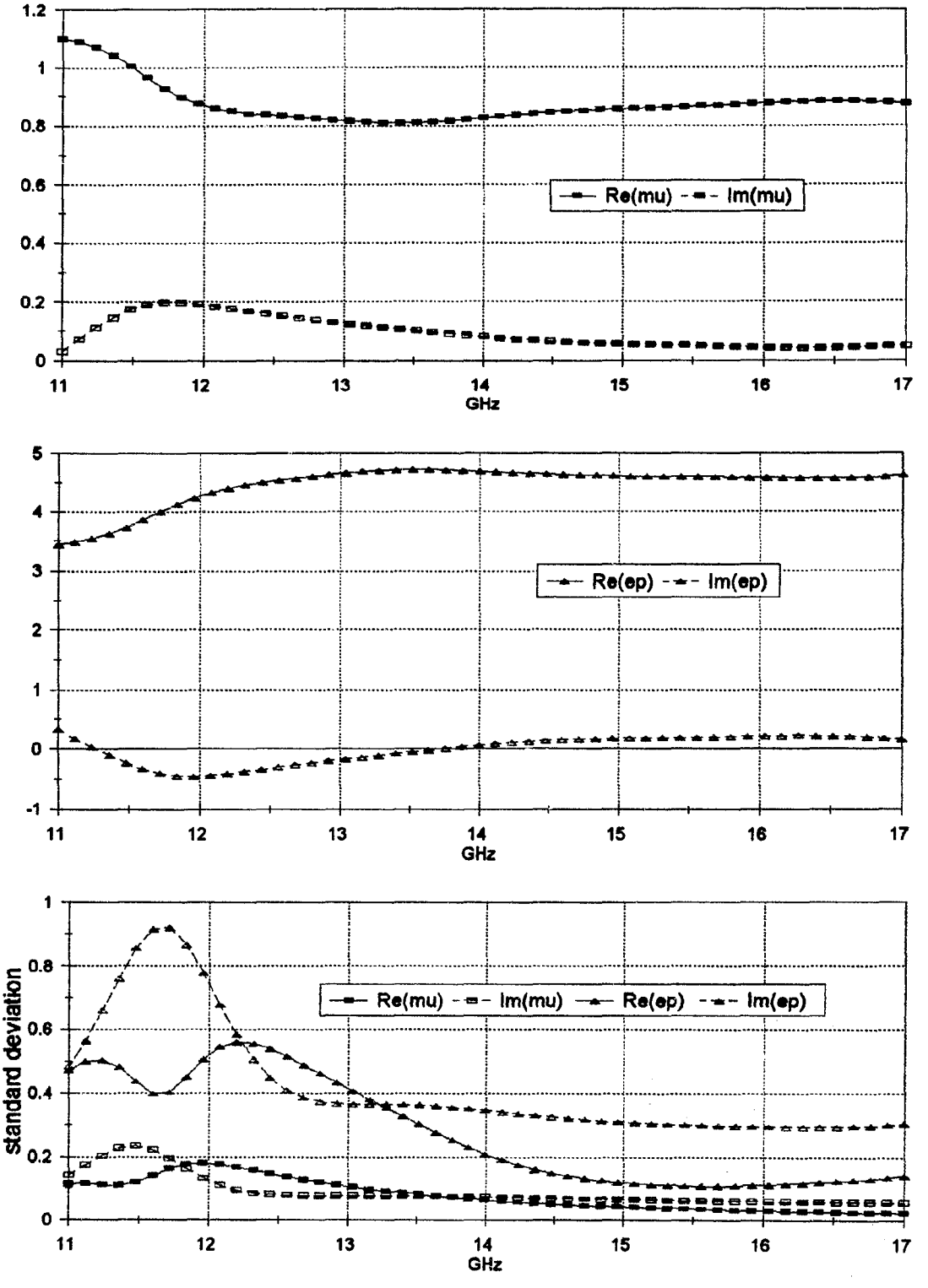

Figure 8.2: Measured constitutive parameters (μ, ϵ) and their respective standard deviations.

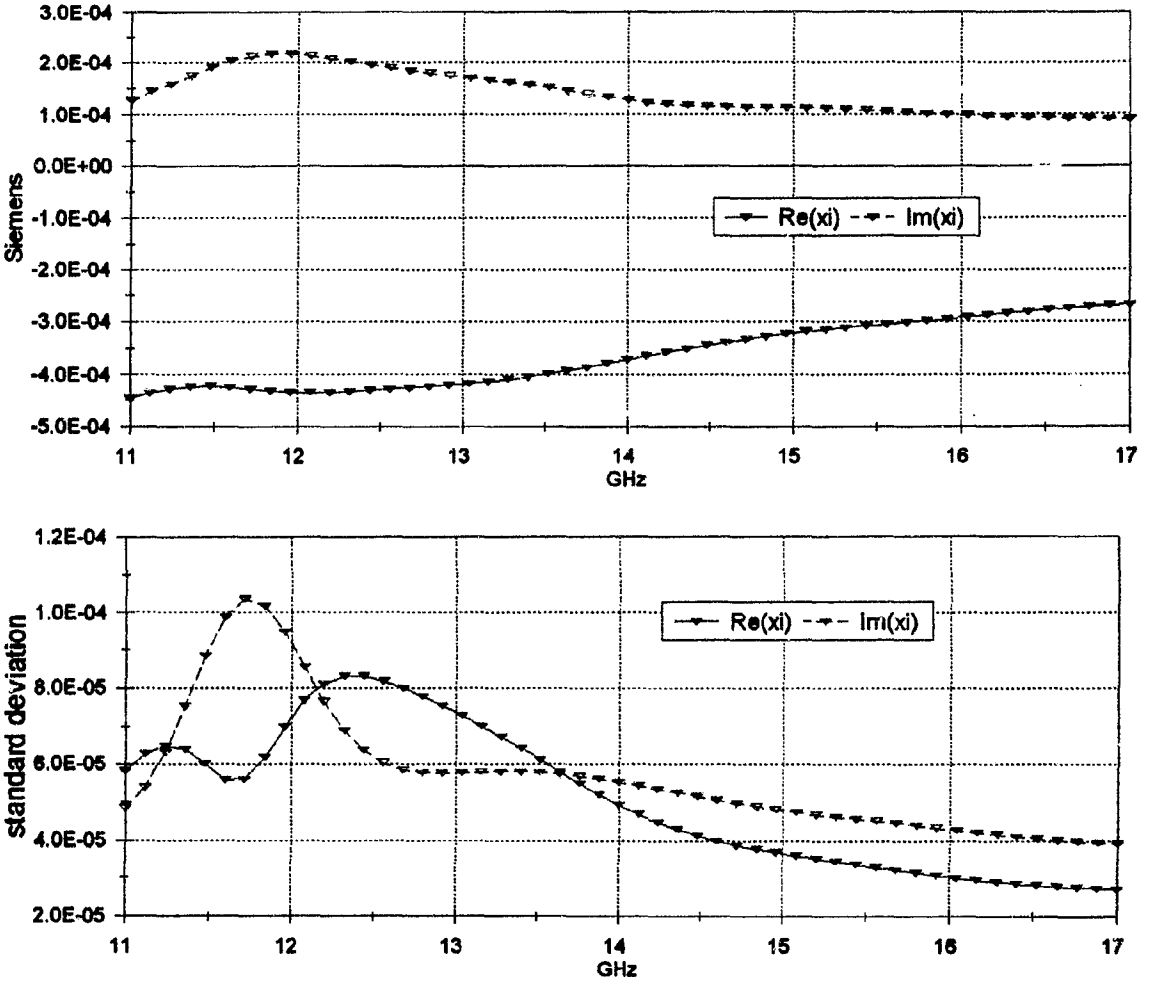

Figure 8.3: Measured chirality parameter ξ and its standard deviation.

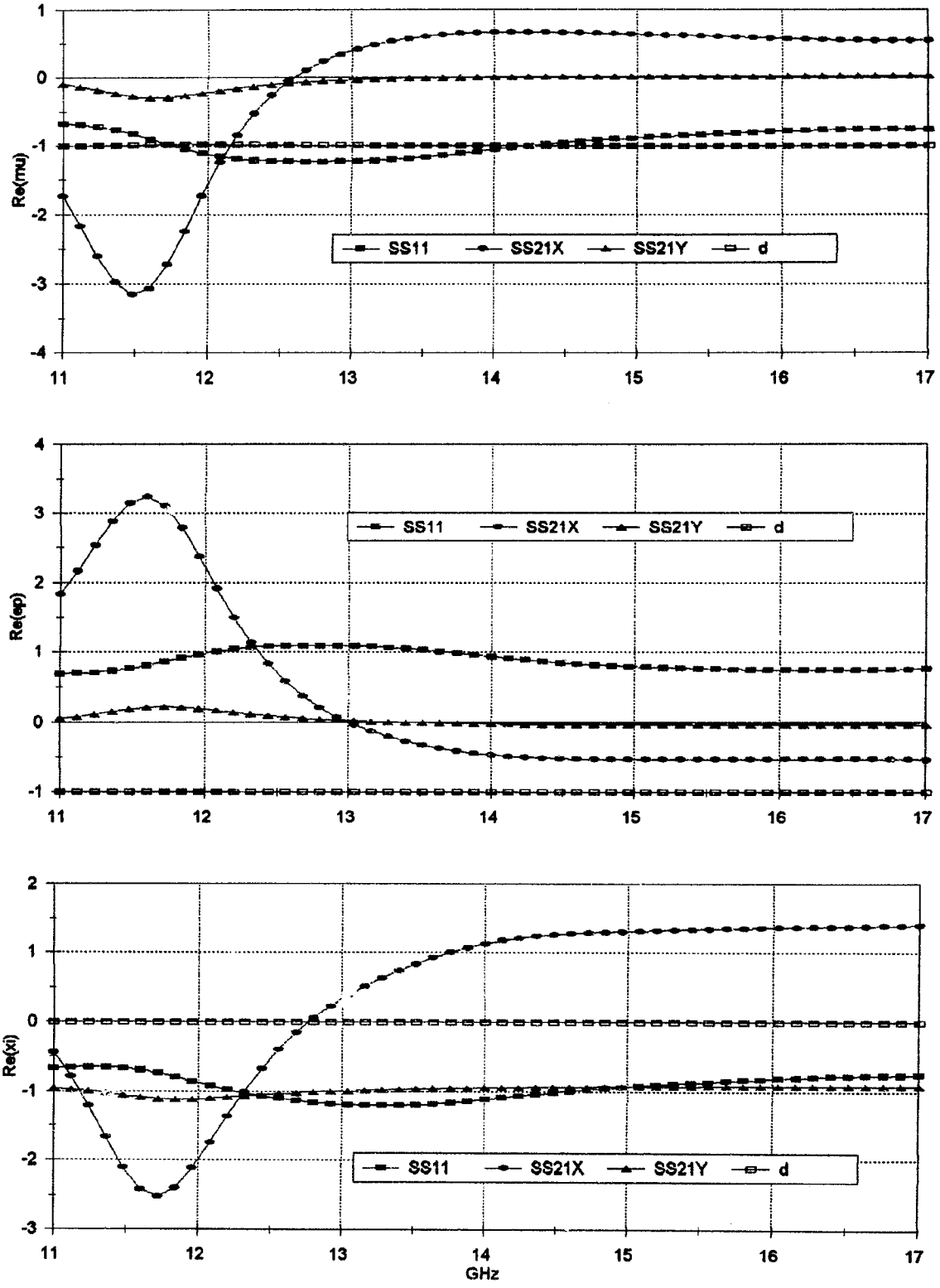

Figure 8.4: The sensitivities of the **real** parts of μ, ϵ and ξ to the **absolute** values of the measured parameters S_{11}, S_{21x}, S_{21y} and the sample thickness d.

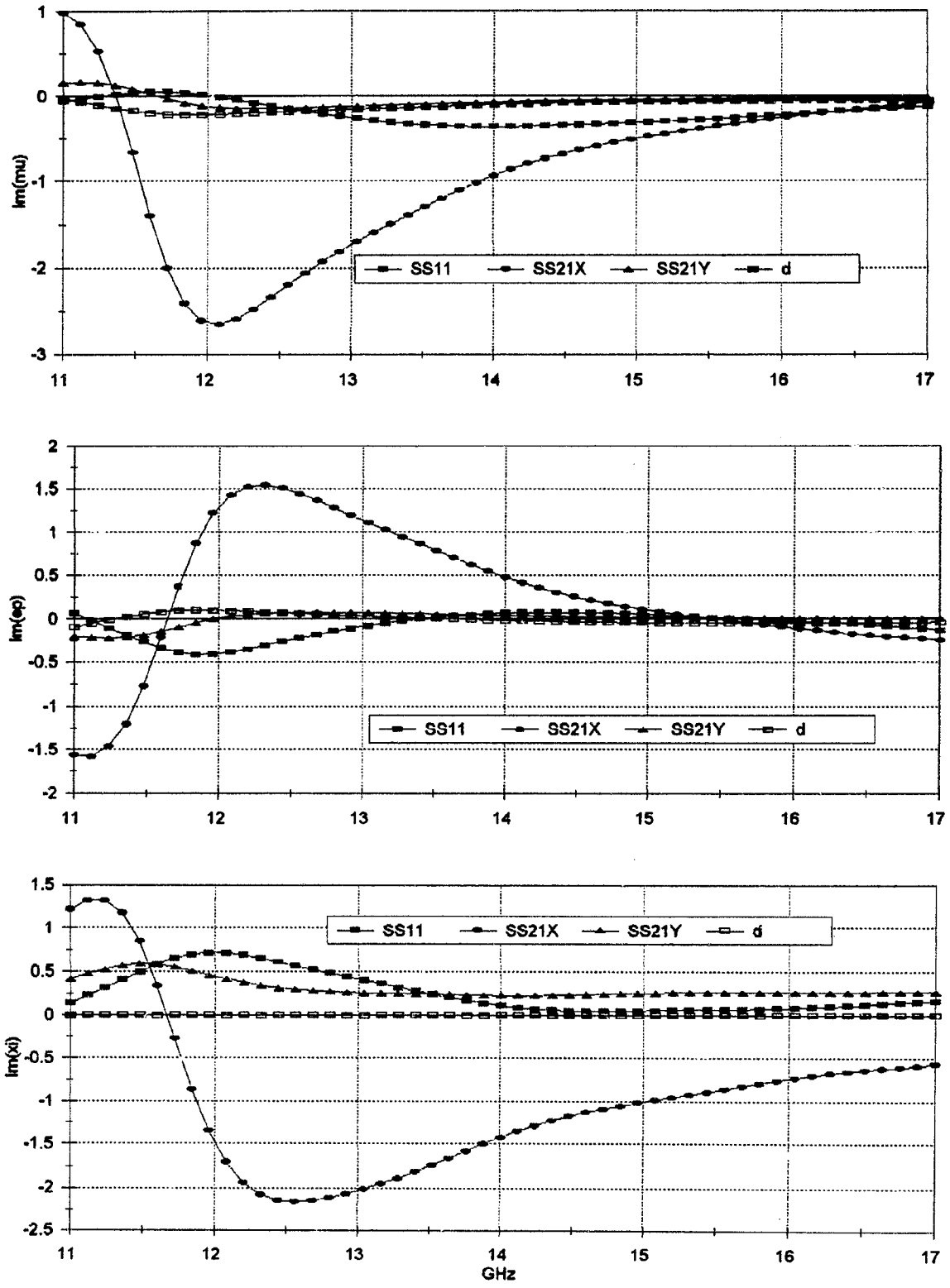

Figure 8.5: The sensitivities of the **imaginary** parts of μ, ϵ and ξ to the **absolute** values of the measured parameters S_{11}, S_{21x}, S_{21y} and the sample thickness d.

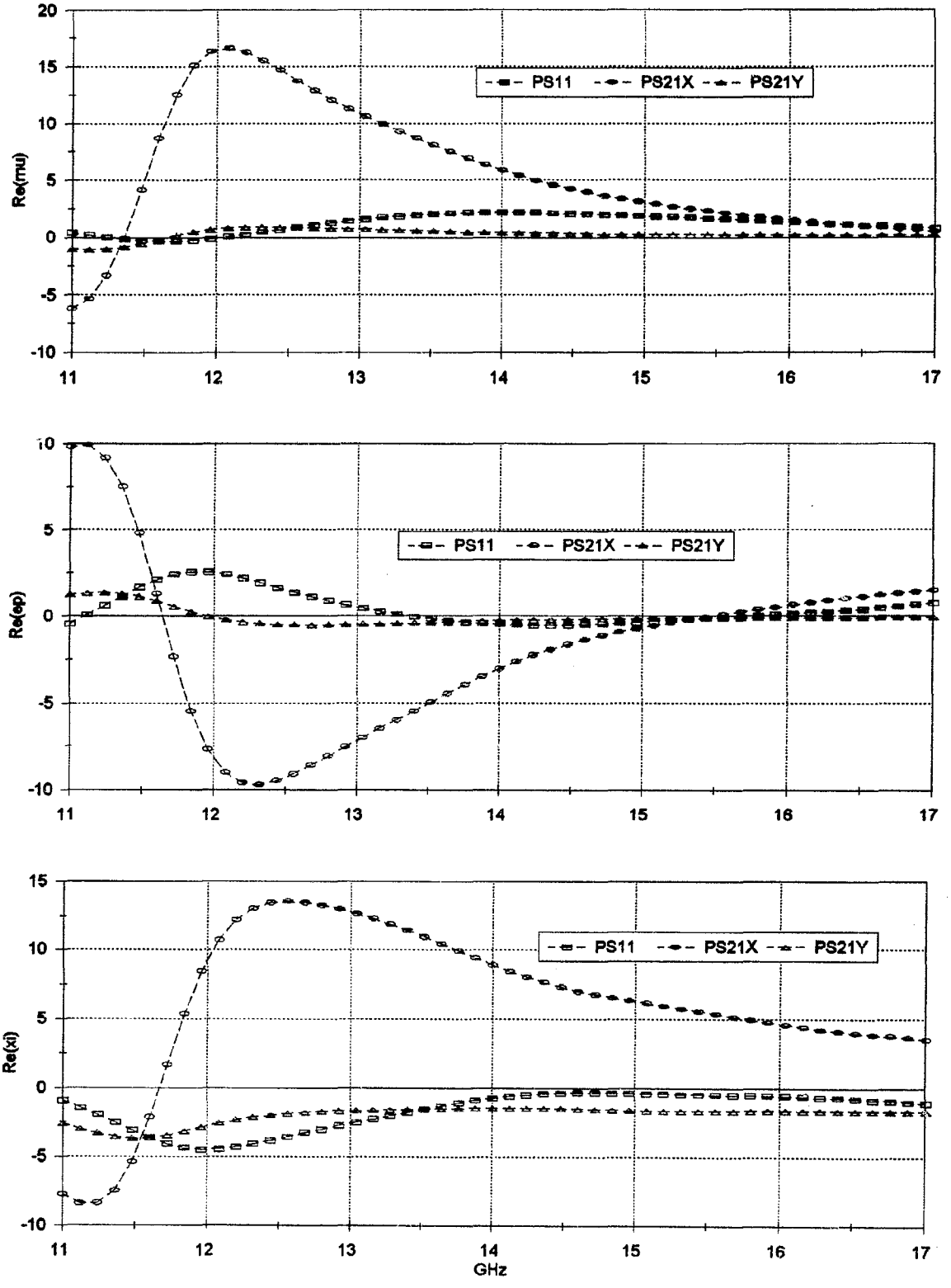

Figure 8.6: The sensitivities of the **real** parts of μ, ϵ and ξ to the **phase** of the measured parameters S_{11}, S_{21x} and S_{21y}.

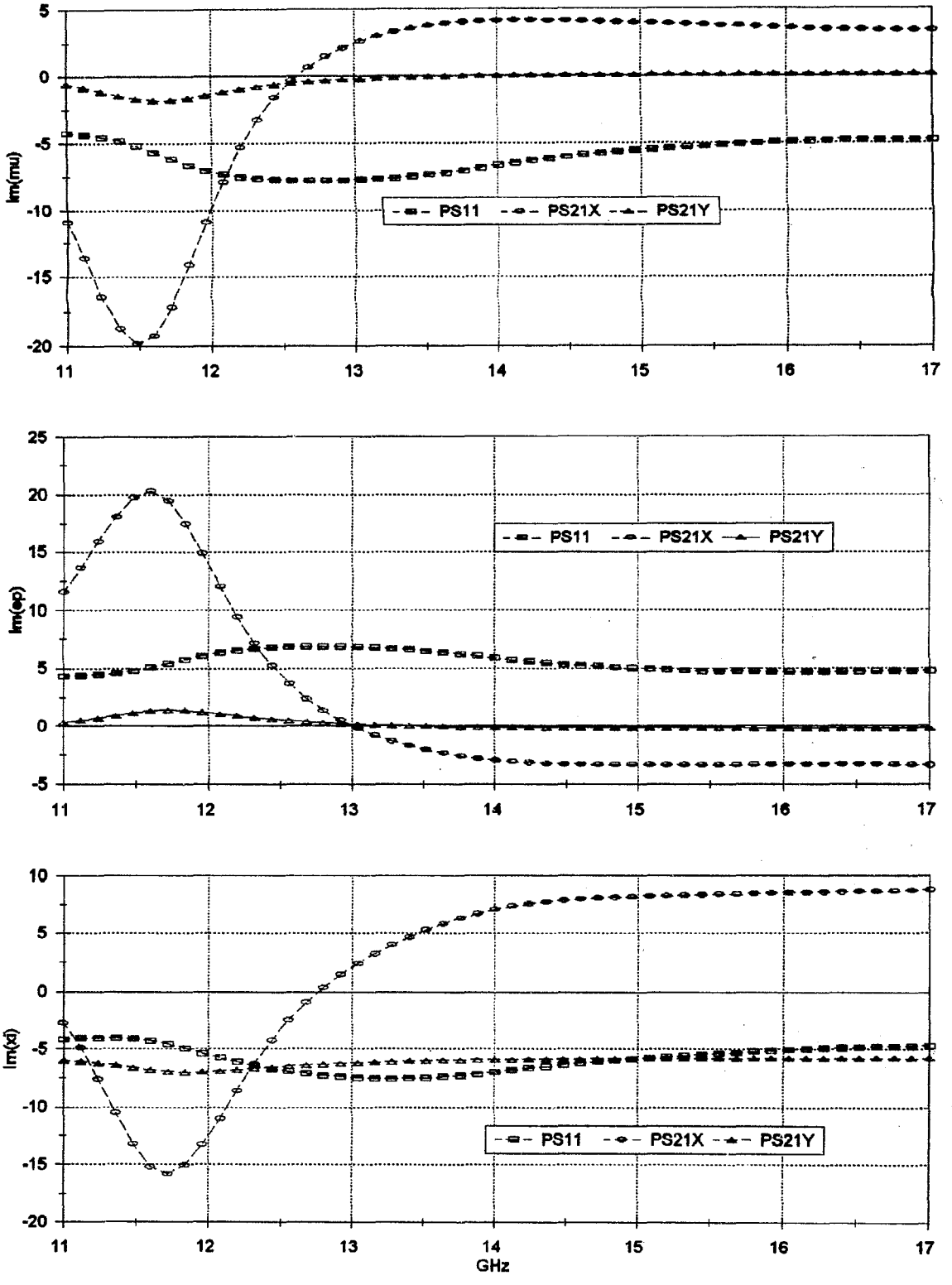

Figure 8.7: The sensitivities of the **imaginary** parts of μ, ϵ and ξ to the **phase** of the measured parameters S_{11}, S_{21x} and S_{21y}.

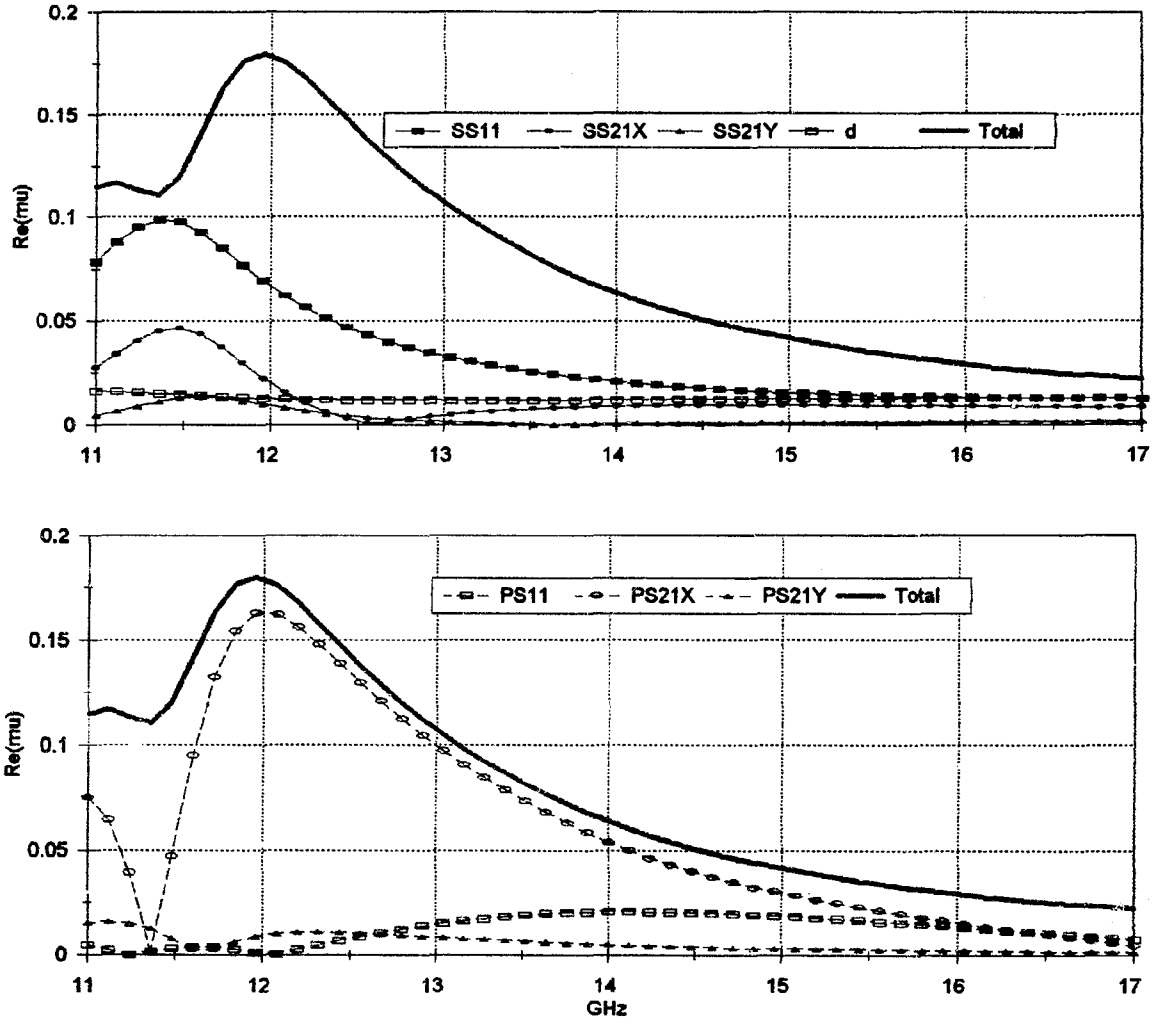

Figure 8.8: Contribution of each of the measurement errors $\Delta|S_{11}|, \Delta|S_{21x}|, \Delta|S_{21y}|, \Delta d$ (top figure) and $\Delta\angle S_{11}, \Delta\angle S_{21x}, \Delta\angle S_{21y}$ (bottom figure) to the total error in the **real** part of μ.

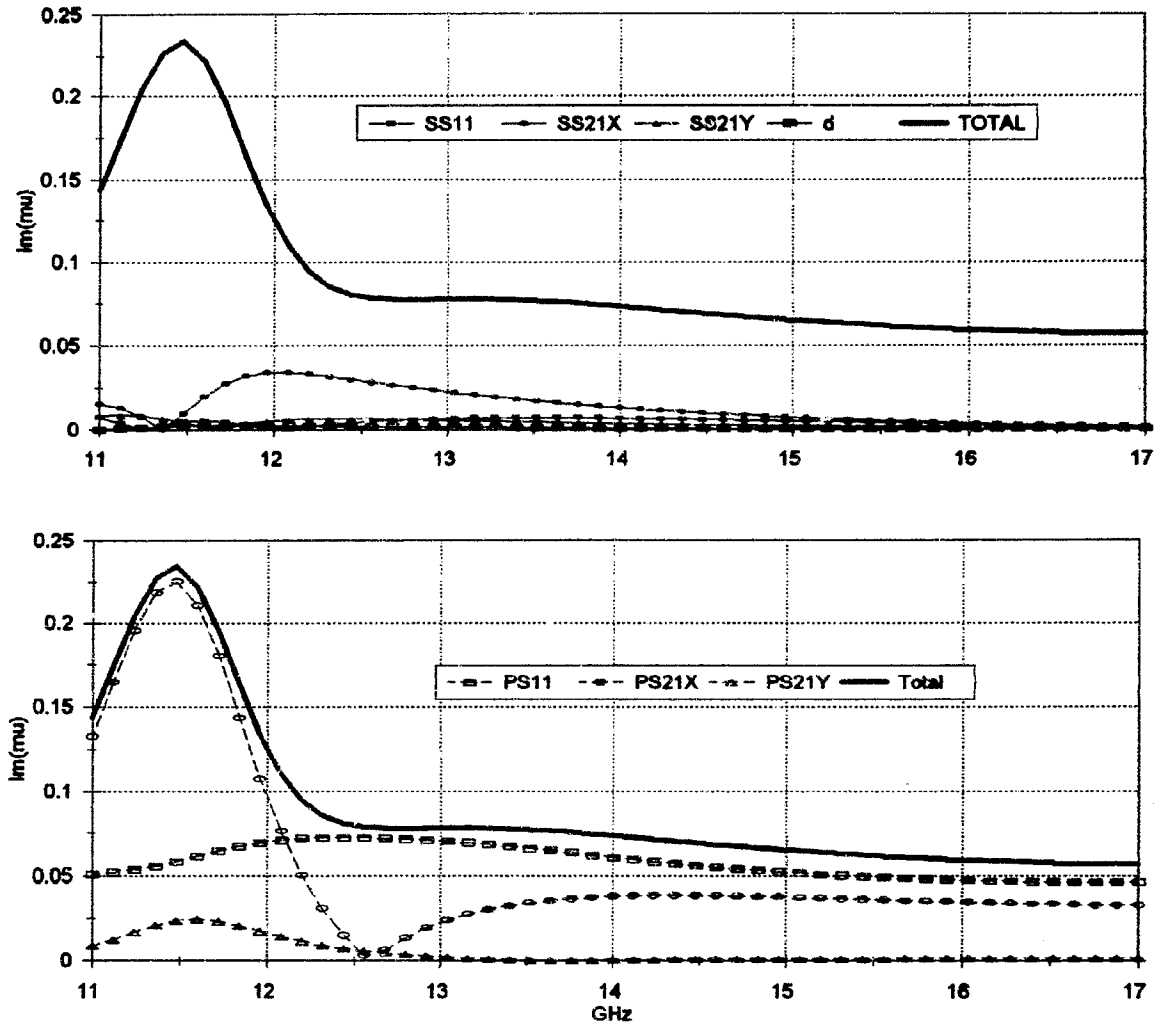

Figure 8.9: Contribution of each of the measurement errors to the total error in the **imaginary** part of μ.

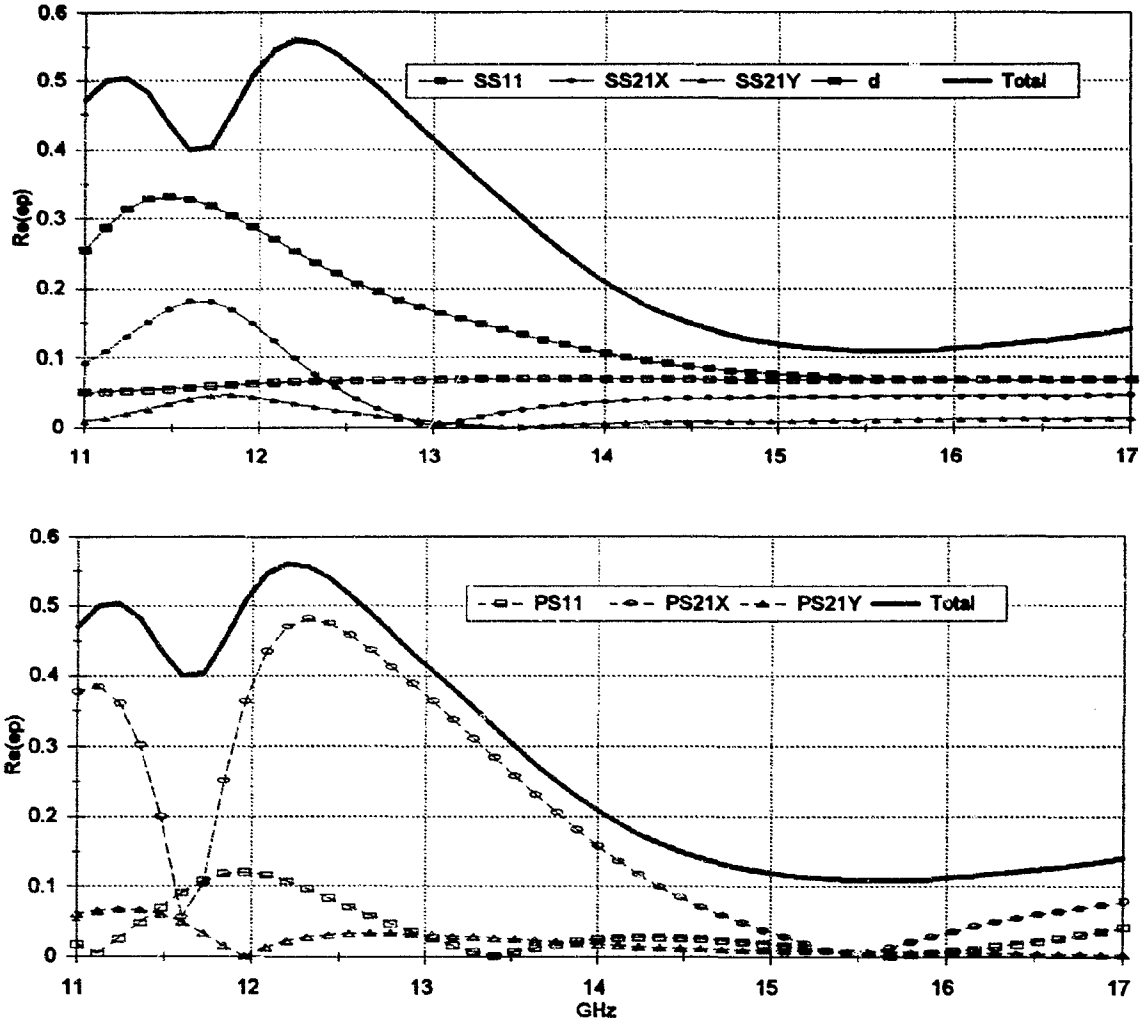

Figure 8.10: Contribution of each of the measurement errors to the total error in the **real** part of ϵ.

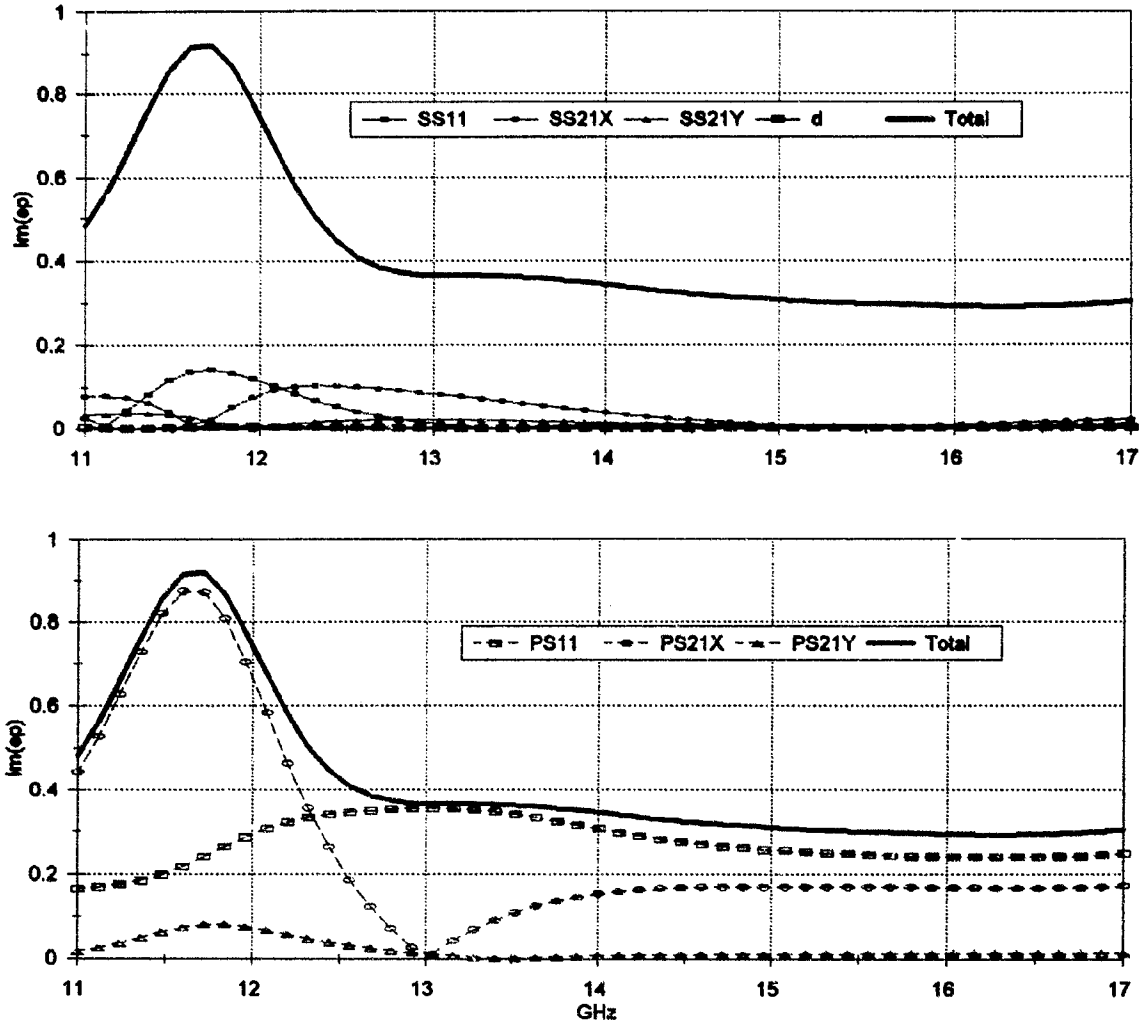

Figure 8.11: Contribution of each of the measurement errors to the total error in the **imaginary** part of ϵ.

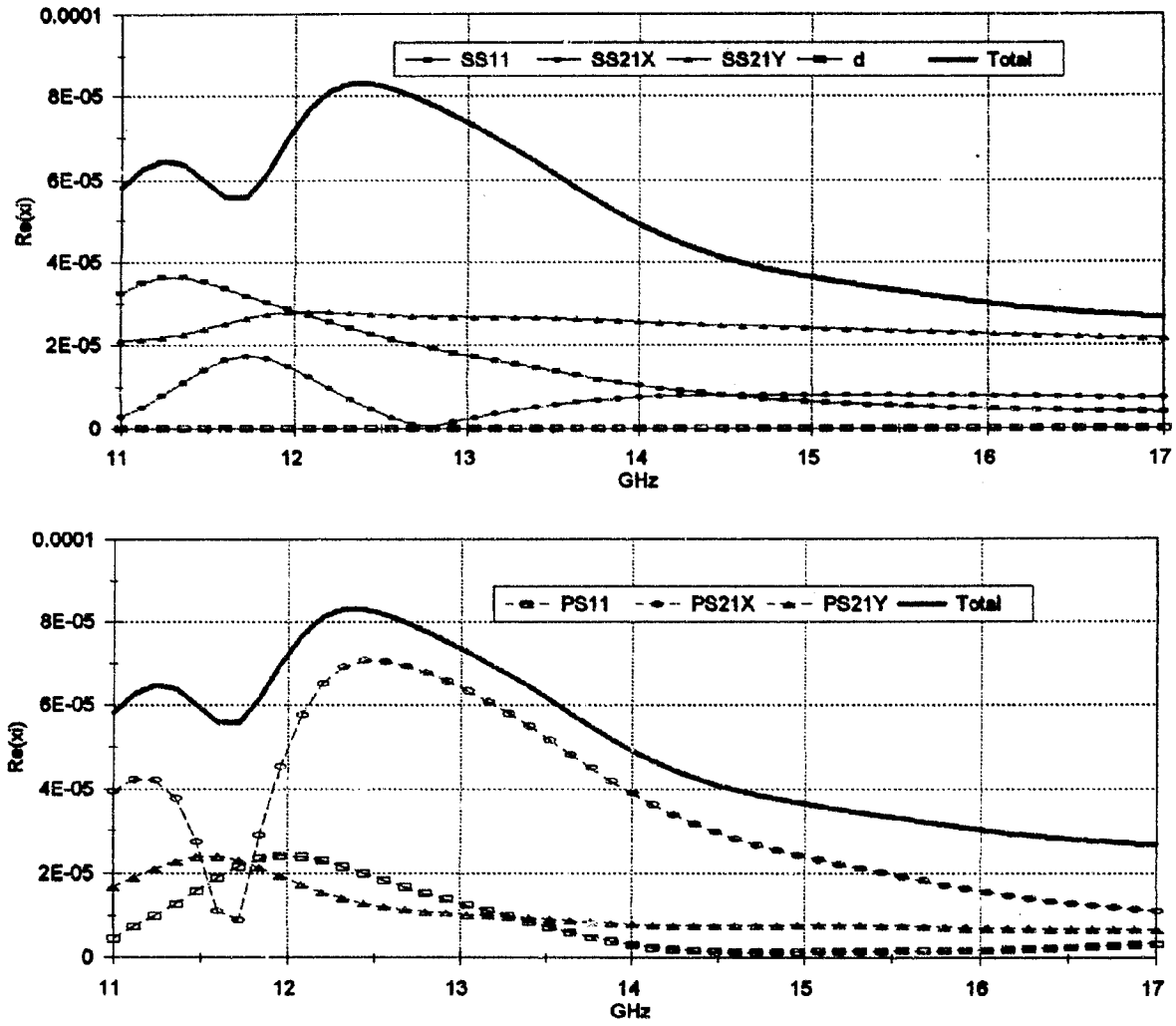

Figure 8.12: Contribution of each of the measurement errors to the total error in the **real** part of ξ.

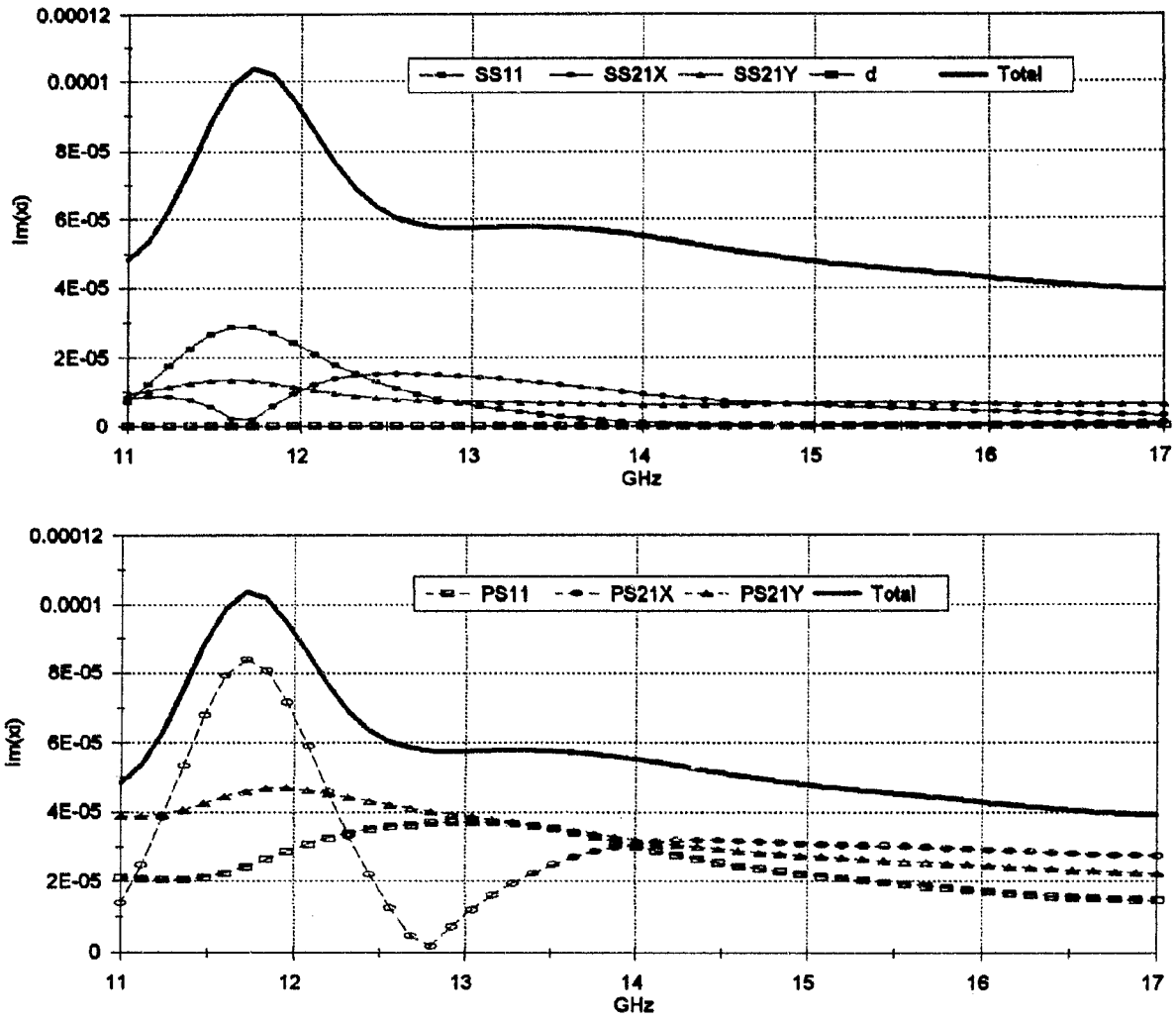

Figure 8.13: Contribution of each of the measurement errors to the total error in the **imaginary** part of ξ.

Chapter 9

Experimental Results

> First I shall test by experiment before I proceed farther, because my intentions is to consult experience first and then with reasoning show why such experience is bound to operate in such a way. And this is the true rule by which those who analyse the effects of nature must proceed: and although nature begins with the cause and ends with the experience, we must follow the opposite course, namely, begin with the experience, and by means of it investigate the cause.
>
> — Leonardo da Vinci (1452–1519)

9.1 Introduction

A historical overview of the experiments done on artificial chiral media was given in Section 2.3. Recent experimental work on artificial chiral media in the microwave region is summarized in Table 9.1. Apart from the measurements of Hollinger [21] that were done in a circular waveguide, all the other measurements were done with free-space systems where the samples were placed in the focal region of either a lens antenna or a parabolic reflector. The experiments evolved from the measurement of the rotation characteristics, to scattering parameters, to the measurement of the constitutive parameters of artificial chiral media. Various methods have been developed to determine the constitutive parameters from the scattering parameters of a chiral medium (see Section 3.2). Although various researchers have measured the constitutive parameters of chiral media, the accuracy with which these constitutive parameters were measured (apart from Ro [48]) has not been given.

To check the inversion method used to determine the constitutive parameters of a chiral medium from scattering parameter measurements (Chapter 3) and the subsequent accuracy with which the parameters can be determined (Chapter 8) a variety of artificial chiral media were manufactured and measured in the free-space measurement system described earlier. It was decided to use helices as the chiral inclusions since they are also popular with other researchers [10, 19, 20, 21, 46, 48, 50, 63, 66] and several theoretical models have been developed to describe the characteristics of this type of chiral inclusion [46, 47, 53, 107, 108, 109]. Although there are many other

	Freq (GHz)	Helix Pitch	Helix Diam	Wire Diam	Wire	Host Medium	Measurement
Lindman [14, 15, 16]	1–3		10	1.2	Copper 2.5 turns 9cm total length	Cotton	Rotation
Winkler [18]	1.5–3	7	10	18-gage	Copper 2.5 turns 4.7cm total length	Cotton	Rotation
Tinoco and Freeman [17]	8.2–15	3	5	1.2	Copper 3 turns 4.7cm total length	Oriented in Polystyrene foam	Rotation
Guire [20]	14.5–17.5	0.53	1.32	0.152	Cu-coated stainless steel	Eccogel 1365-90	Reflection measurements from chiral Dallenbach (0.4 0.8 1.6 3.2% vol conc.)
Varadan [105]	12.4–18				Cu-coated stainless steel.	Eccogel 1365-90 epoxy and carbon, conductive polymer.	Reflection in Dallenbach config.(147 helices per cc.)
Ro [48, 10]	9–36	0.53	1.17	0.152		Eccogel 1365-90	Constitutive parameters. Rotation and ellipticity. Power absorption. (0.4 0.8 1.6 3.2% vol conc.)
Hollinger [21]	5.5–8.5	0.67	1.25	0.152	Cu-coated stainless steel	Dow Corning 3110 RTV silicon rubber.	Rotation and ellipticity. (0.4 0.8 1.6 3.2% vol conc.) Circular waveguide.
Timmerman [49]	2–27						Absorption, Any incidence
Grace [51, 52]	18–27	0.78	2.50	0.320	Metal	Eccosorb Eccofoam FPH	Absorption
Umari [19]	12–18	0.38	1.16		Cu	Eccogel	Rotation and ellipticity. (0.4 0.8 1.6 3.2% vol conc.)
Ougier [66]	15	8.0	3.00		Cu 1 Turn		Rotation and constitutive parameters (5%vol conc.)
Hujanen [63]	10–19						Constitutive parameters.
Smith [62]	11–16	0.33	1.20	0.132	Ni-Cr	Polyurethane	Constitutive parameters. (50 helices per cc.)
Guerin [50]	8–40	3.00	3.00		BST	Epoxy-carbon matrix	Constitutive parameters and refection in Dallenbach config (3.4% in Vol)
Semenenko [70]	4.55–4.85 2.8–4.5 3.0–5.2	1.00 1.00 1.00	3.00 3.00 3.00	0.07 0.03 0.30	Cu 2.5 Turn Ni-Cr 3.73 T Carbon 2.75 T		Permeability in cylindrical resonator.
Mariotte [106]	1.7–20						Reflection from a single chiral structure.
Luebbers [46]	2–20	0.5	2.9	0.3	Cu Coated stainless steel	3 Turns Epo-Kwick	Chirality parameter β 12.4 helicess/cc (0.3 Vol%) Free-space.

Table 9.1: Summary of some of the experiments that have been conducted on artificial chiral media at microwave frequencies. Helix dimensions are in mm. Most of the helices used had approximately 3 turns. The sample of Ougier *et al.* had 1 turn. Unless stated otherwise all measurements were done in free space. Blank spaces indicate that the information was not available. It is important to note that some other experiments might have been done but were not adequately published and only reported orally at some conferences.

chiral structures that could be used as inclusions in the composite material, the popularity of helices is possibly due to manufacturing considerations. Even so it was found that manufacturing artificial chiral media using metallic helices is not straightforward, financially costly, and time consuming[1]. These factors have restricted the number of chiral samples that were available for measurement.

The measured scattering parameters are observables (i.e. directly measurable *physical* effects) and are unaffected by the choice of constitutive relations used. In the following it is assumed that the experimental chiral media can be accurately modelled by the constitutive relations incorporated in the inversion equations [27, 53, 59]. This requires the medium to be homogeneous and isotropic, thus the chiral inclusions should be small, evenly spaced and randomly oriented. The manufacturing method used to approximate this state will be described in the next section.

9.2 Manufacturing Method for "Isotropic" Chiral Slabs

The chiral materials were made by Dr. Scott Kuehl of the Institute of Polymer Science at the University of Stellenbosch. The nickel-chrome helices were made by a Johannesburg company called Spring Manufacturers. To prevent the 3 turn nickel-chrome helices from entangling before they are added to the host medium the following procedure was used. Before the long multi-turn helices were cut, they were filled with polyurethane to form a long polyurethane cylinder with a radius that is slightly larger than the enclosed wire helix. These cylinders were then left to cure before they were cut to three turn helices. The nature of these "chiral pellets" were therefore such that the metal helices could not touch each other[2]and could be mixed, without tangling, into a host medium.

The chiral pellets were then carefully added to a dielectric host medium and evenly distributed in such a manner that they were not oriented by the distribution process. The mixture was also made such that as few air bubbles as possible were formed. The unwanted air bubbles were removed by placing the uncured mixture in a vacuum chamber at a pressure of 10 mbar, a process known as de-gassing.

This mixture of the uncured host medium and its chiral inclusions was then carefully poured into an aluminium "jig" with small "bleed" holes at the corners for removal of the excess host medium. The volume of the chiral inclusions and the host medium was carefully calculated to give the required concentration of helices per cubic centimeter and to fill the designated volume exactly. The amount of host medium that seeped through the bleed holes was therefore minimal. If too much of the uncured mixture is in the jig, the flow of the host medium towards and through the bleed holes will cause the helix concentration to be higher in the corners of the sample around the bleed holes. This might also cause the chiral inclusions to be oriented towards the corners

[1]These factors could severely handicap artificial chiral materials for commercial applications, unless they can be proved to exhibit significantly useful properties.

[2]Touching helices will lead to a conducting phenomenon called "percolation" which will severely influence the properties of the chiral samples.

of the sample. The aluminium jig had inner dimensions of 11 cm by 11 cm with an approximate depth of 7 mm.

The same procedure was used to manufacture chiral samples with tungsten helices. However, since the dimensions of these helices were so small and because they could not get tangled, they were not filled with polyurethane before being cut to length.

9.3 Host Media

It was explained earlier that an artificial chiral medium can be made by embedding helices with random orientation in an achiral host medium. The host media used in the experiments were chosen not to achieve maximum absorption but rather to study the effect of the helices on the constitutive parameters of the host media. The host media were also chosen for their physical properties like viscosity before curing and the time needed to cure. This is important since if the host medium's viscosity is too high or the curing time too long the helical inclusions would sag, resulting in a higher helix concentration at the "bottom" of the sample. This effect was minimized by turning (or flipping) the sample regularly during the curing process. An even distribution could also be achieved by curing the sample in layers [48] but then the sample would probably not be isotropic.

Because the required viscosity of the host medium was different for the various helix concentrations three different host media had to be used to maximize homogeneity and randomness. The three host media used in the samples, and their respective permittivities, are summarized in Table 9.2.

Host Medium	Abbreviation	Measured Permittivity
Polyurethane	PU	$\epsilon_r \approx 2.86 + i0.23$
Quartz-Silicone	QS	$\epsilon_r \approx 3.35 + i0.04$
Silicone	S	$\epsilon_r \approx 2.74 + i0.06$

Table 9.2: Dielectric media used as host media in the chiral composites. Measured ϵ_r at 15 GHz.

Blank samples (without any inclusions) were made using these materials and measured as if they were chiral media. By using the chiral inversion equations an estimate of the error made in the measurement of the chirality parameter, ξ, could be made since the chirality should be $\xi = 0$ for these achiral media. The measured results are shown in Appendix F. The measured chirality parameter for the achiral (i.e. $\xi = 0$) polyurethane and the quartz-silicone samples was approximately $\xi = (-2 + j0.5) \times 10^{-6}$ Siemens and $\xi = (-2 + j1) \times 10^{-6}$ Siemens respectively. The error in the measurement of the chirality parameter is thus approximately $\sigma_\xi = (-2 + j1) \times 10^{-6}$ Siemens. The measured rotation of the polarization ellipse for these achiral media will also give an indication to the accuracy with which the rotation angle can be measured since there should be no rotation in these achiral samples. The measured rotation for both the polyurethane and the quartz-silicone is approximately 0.1 degrees and for the silicone

sample it is approximately 0.25 degrees[3].

9.4 Nickel-Chrome Helix

The nickel-chrome[4] wire helix samples are used to study the effect of helix concentration on the constitutive parameters. The experiments are similar to those that were done at the Pennsylvania State University [19, 48] which allows mutual verification of the results. The dimensions of the helices are given in Table 9.3. A helix is defined to be right handed (RH) if it will go into a medium (away from the person) when it is rotated in the direction the fingers are pointing if held in a right hand with the thumb pointing away from the person. A left handed (LH) helix will come out of the medium (towards the person) if rotated in the same direction as above.

Table 9.4 gives a summary of the experiments that were conducted with the nickel-chrome helices[5].

Helix Dimensions

Diameter	1.200	mm
Pitch	0.330	mm
Pitch/Length ratio	0.087	
Wire diameter	0.132	mm
Number of turns	3	
Total wire length	11.35	mm

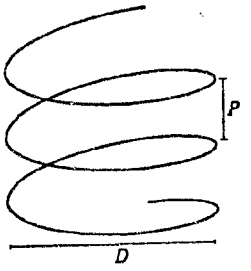

Table 9.3: Dimensions of the Nickel-Chrome helix.

[3]The measurement of the silicone sample (S) was not done with the same accuracy as the other two blank samples.

[4]The wire is Stainless Steel Grade 302 with 8% Nickel and 18% Chrome. Nickel is ferromagnetic with $\mu_r \approx 50$. The helices are therefore expected to be slightly ferromagnetic. The conductivity of the stainless steel wire is 11.1×10^3mho/cm.

[5]A racemic medium contains equal concentrations of left and right handed helices. In this thesis the abbreviation RAC is used for racemic samples.

Nickel-Chrome Helices					
Name	Hand	Concentration Helices/cc	Metal Conc Vol/Vol %	Thickness mm	Host medium
50LH-PU	LH	50	0.77	6.64	Polyurethane
50LH-QS	LH	50	0.77	6.88	Quartz-Silicone
50RAC-QS	LH/RH	25LH/25RH	0.77	6.88	Quartz-Silicone
100RH-QS	RH	100	1.55	6.90	Quartz-Silicone
220RH-S	RH	200	3.42	6.70	Silicone

Table 9.4: Summary of the samples with nickel-chrome helices. All samples are 11×11cm.

The measured parameters for each of the samples can be found in Appendix F. The wavelengths inside the samples are also included to show at which frequencies the samples are half a wavelength thick ($d = \lambda_{Avg}/2$) and where larger inaccuracies are expected as described in Chapter 8.

The difference between the real parts of the wave numbers of the RCP and LCP waves inside the chiral media, $\mathrm{Re}(k_r - k_l)$, are shown in Figure 9.1. This figure shows that $\mathrm{Re}(k_l) > \mathrm{Re}(k_r)$ for the right handed media (100RH-QS and 220RH-QS) and $\mathrm{Re}(k_l) < \mathrm{Re}(k_r)$ for left handed media (50LH-QS and 50LH-PU). The phenomenon of $\mathrm{Re}(k_l) \neq \mathrm{Re}(k_r)$ is referred to as *circular polarization birefringence*, Table 2.1. These measurements show that a RCP wave travels faster than a LCP wave through the right-handed media and *vice versa* for the left-handed media. It is also shown that $\mathrm{Re}(k_l) = \mathrm{Re}(k_r)$ for the racemic and the achiral media (50RAC-QS, PU, QS and S).

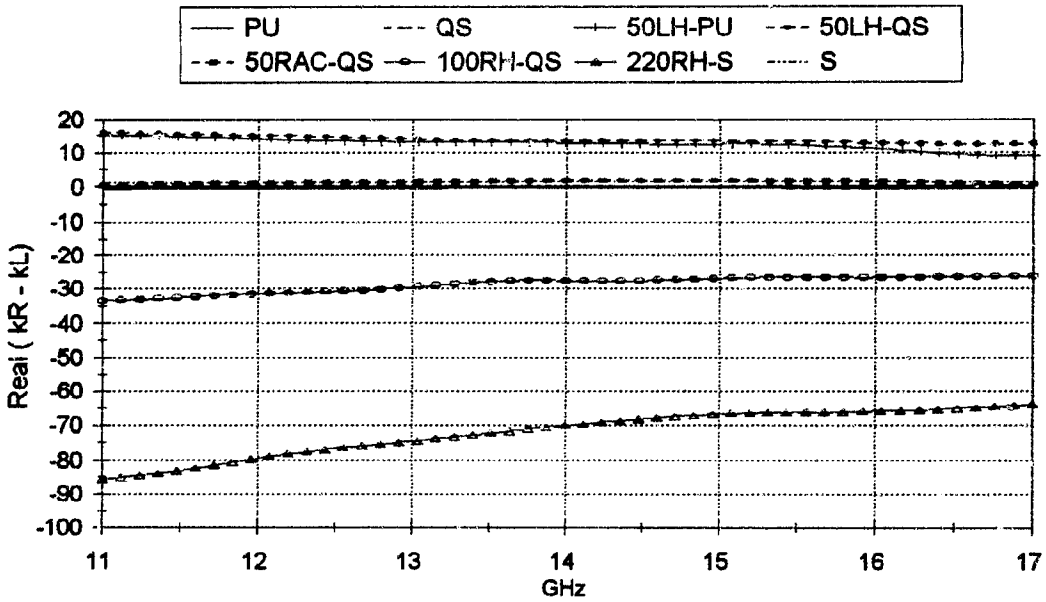

Figure 9.1: Measured difference between the real part of the wave numbers $\mathrm{Re}(k_r - k_l)$ inside the chiral media.

The rotation angle of a linearly polarized field that travels through a chiral medium is given by [2, eqn.72],

$$\theta = \frac{(k_l - k_r)d}{2} = -\omega\mu\xi d. \tag{9.1}$$

It is therefore clear that $\theta > 0$ for the right handed chiral media and $\theta < 0$ for the left handed media. The tilt angle (or rotation) of the polarization ellipse[6] for the different samples is shown in Figure 9.2. The computed rotation angles of Figure 9.2 were confirmed by rotating the receiving antenna to the position where the transmission coefficient $S_{21\theta}$ is minimum, and the actual rotation angle was then calculated from this angle since the maximum component of the elliptically polarized field is normal to the minimum. The rotation was also checked to be reciprocal[7] (i.e. the direction of

[6]The definitions of the polarization ellipse, and the equations used to determine the tilt angle and the ellipticity angle, are given in Appendix G.

[7]The rotation observed due to the Faraday effect is nonreciprocal (i.e. direction of rotation depends on the direction of wave propagation.).

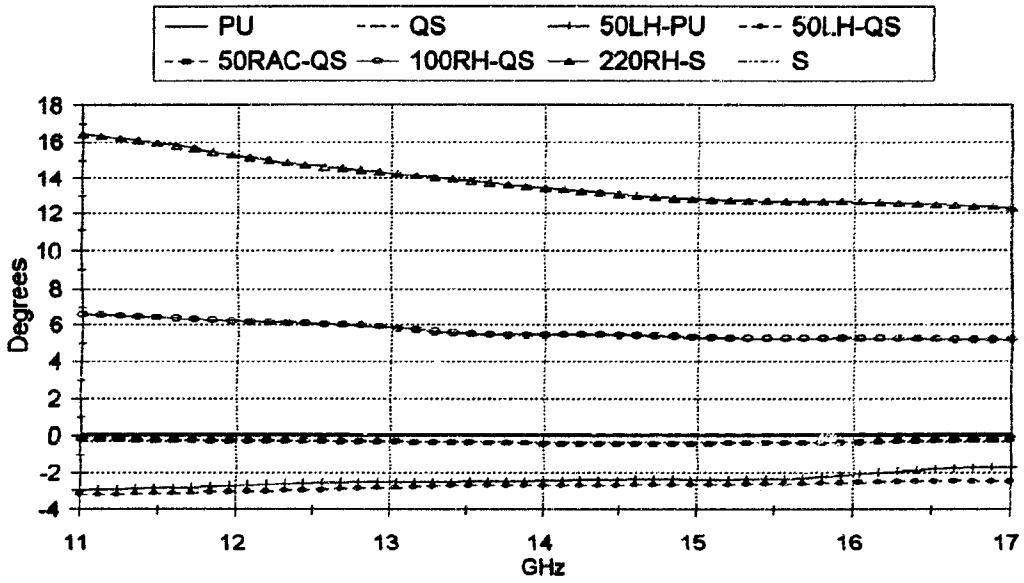

Figure 9.2: Rotation, θ, of the major axis of the polarization ellipse of the transmitted field for the different nickel-chrome wire samples.

rotation does not depend on the direction of wave propagation) by turning the sample around and measuring the rotation. The rotation was found to be in the same direction and therefore confirmed that the samples exhibit *optical activity.*

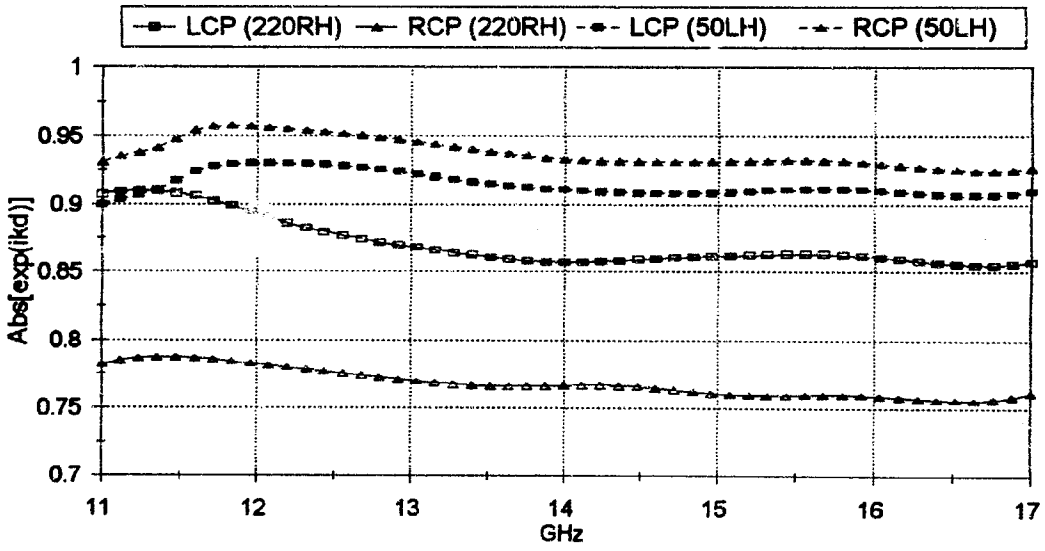

Figure 9.3: Measured attenuation of the RCP and LCP waves, $P_r = e^{-\alpha_r d}$ and $P_l = e^{-\alpha_l d}$, for the samples 220RH-S and 50LH-QS.

The absolute values of the propagation factors, $P_r = e^{ik_r d}$ and $P_l = e^{ik_l d}$, with complex wave numbers, $k_r = \beta_r + i\alpha_r$ and $k_l = \beta_l + i\alpha_l$, are measures of the attenuation of the transmitted RCP and LCP waves. The "magnitudes" of the LCP and the RCP waves at the other side of the chiral slab, $|P_r| = e^{-\alpha_r d}$ and $|P_l| = e^{-\alpha_l d}$, are shown in Figure 9.3. From this figure it can be seen that for the *right handed media* the LCP wave is attenuated *less* than the RCP and for the *left handed media* the LCP wave is

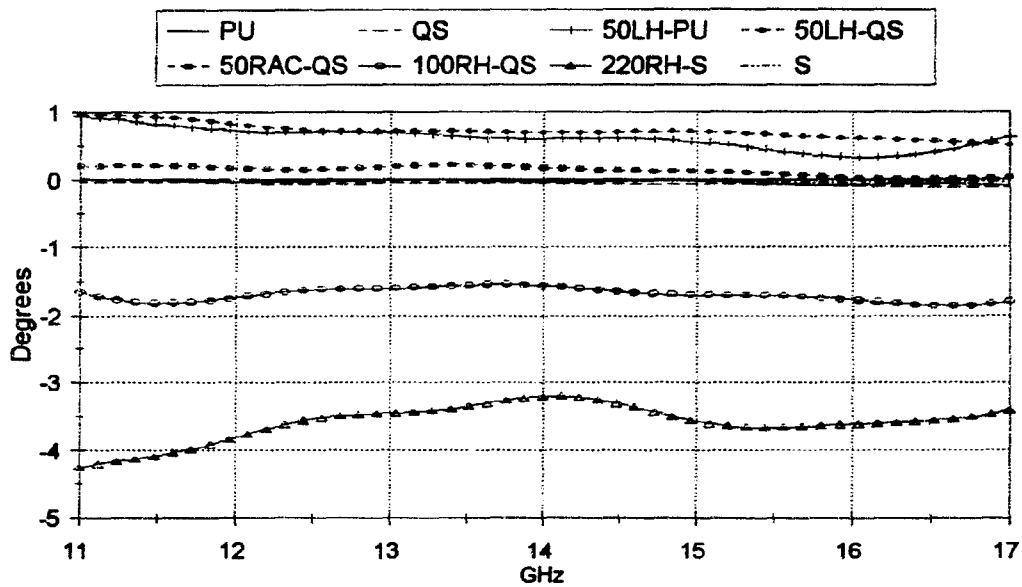

Figure 9.4: Measured ellipticity, of the polarization ellipse of the transmitted field for the different nickel-chrome wire samples. $(LCP)\ -45 \leq \psi \leq 45\ (RCP)$.

attenuated *more* than the RCP. This phenomenon is referred to as *circular dichroism* [1]. On the other side of the chiral slab the two waves, combined, result in an elliptically polarized wave. This means that the wave on the other side of the right handed media is left elliptically polarized (LEP: ellipticity $\psi < 0$) and that on the other side of the left handed media right elliptically polarized (REP: ellipticity $\psi > 0$). The ellipticity of the polarization ellipse for the different chiral media is shown in Figure 9.4. Note that for a chiral sample which is illuminated at its critical frequency (i.e. at helix resonance, where the Cotton effect[8] is observed) the axial ratio of the field on the other side should be $AR = 1$ (i.e. circularly polarized) [21].

The influence of the helix concentration on $\mathrm{Re}(\mu)$, $\mathrm{Re}(\epsilon)$, $\mathrm{Re}(\xi)$ and $\mathrm{Im}(\xi)$ is shown in Figures 9.5 to 9.8. Bearing inaccuracies in mind it seem as if $\mathrm{Re}(\mu) < 1$ only for the high helix concentration samples (100RH-QS) and (220RH-S) (Fig 9.5). The measured $\mathrm{Re}(\mu) < 1$ for the samples with a high helix concentration can be attributed to the accumulative diamagnetic effect of the magnetic dipoles induced in helices [97, Section 9.5].

The increase in $\mathrm{Re}(\epsilon)$ is only significant when the helix concentration becomes very large. This is expected since for high helix concentrations the metal concentration, and hence electric dipole moment density, also becomes large resulting in a higher $\mathrm{Re}(\epsilon)$. From Figure 9.7 it can be seen that $\mathrm{Re}(\xi) < 0$ for a chiral medium containing right handed helices and $\mathrm{Re}(\xi) > 0$ for a chiral medium containing left handed helices. It is also evident that a doubling in the helix concentration results in approximately a doubling of $\mathrm{Re}(\xi)$. This relation between the helix concentration and $\mathrm{Im}(\xi)$ is also seen in Figure 9.8.

[8]The Cotton effect is the phenomenon where the direction of rotation θ change sign (i.e. go through $\theta = 0$) as the frequency is changed[16].

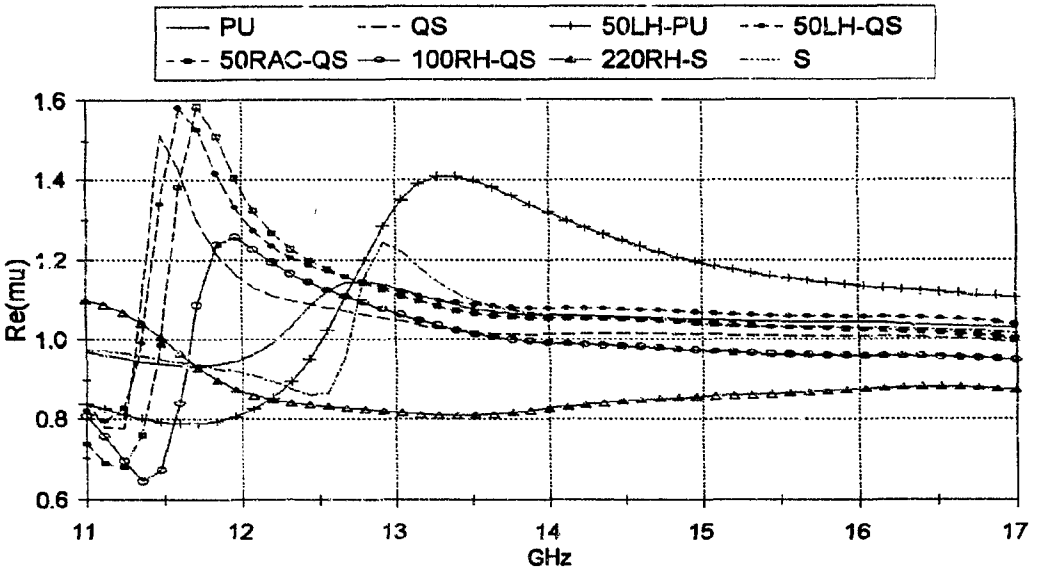

Figure 9.5: Change in the real part of permeability, Re(μ), for different helix concentrations.

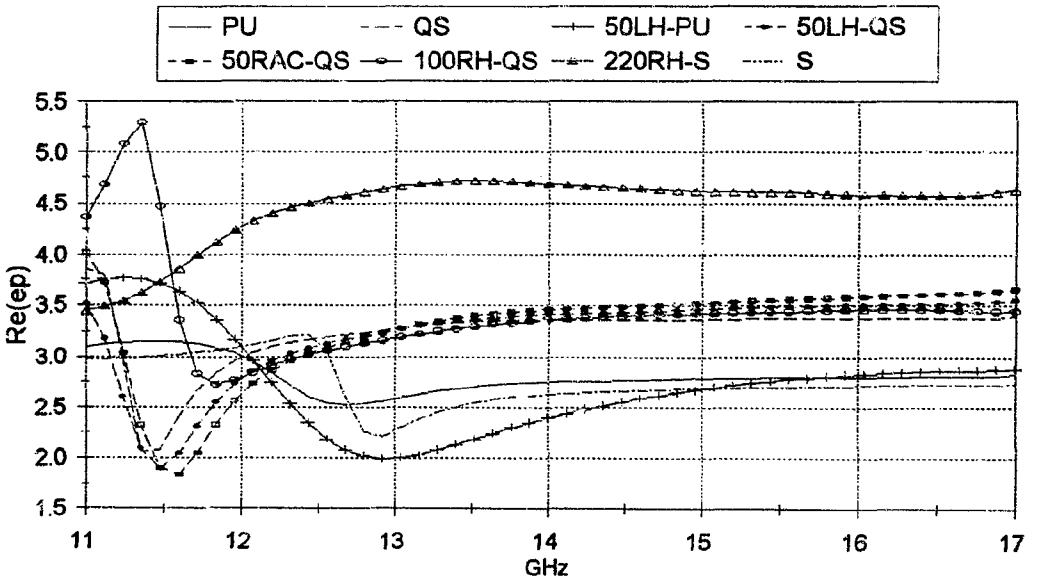

Figure 9.6: Change in the real part of permittivity, Re(ϵ), for different helix concentrations.

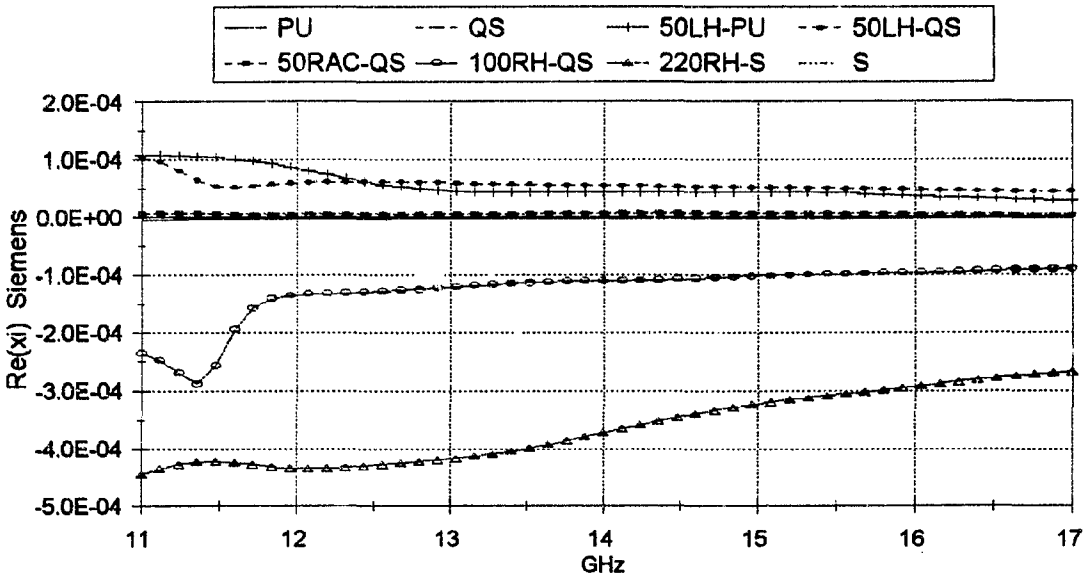

Figure 9.7: Change in the real part of the chirality parameter, Re(ξ), for different helix concentrations.

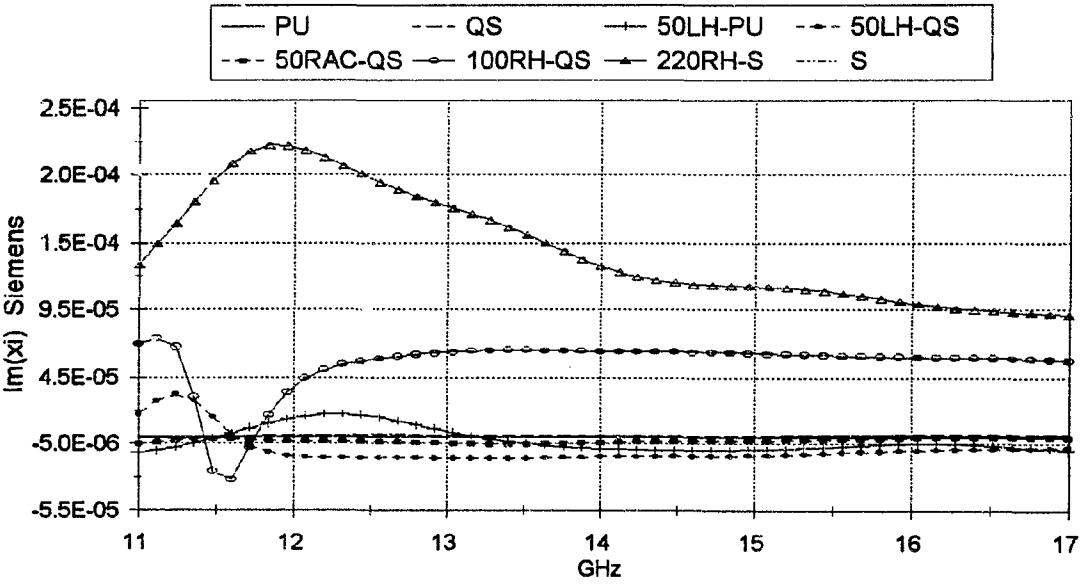

Figure 9.8: Change in the imaginary part of the chirality parameter, Im(ξ), for different helix concentrations.

A comparison between the constitutive parameters of a chiral and a racemic sample of the same helix concentration will now be done. The real and imaginary parts of μ and ϵ for the chiral (50LH-QS), the racemic (50RAC-QS) and the host medium (QS) are shown in Figures 9.9 to 9.12. Although μ and ϵ (both real and imaginary parts) of the chiral and the racemic sample are very similar (at the higher frequencies since the half wave effect at the lower frequencies causes big errors), it is difficult to conclude without any doubt from these sample measurements that both μ and ϵ are equal for a racemic and a chiral sample of equal helix concentration [45, 48]. The uncertainty is caused by the fact that the measured μ and ϵ of the host medium (QS) is not very different from that of (50LH-QS) and (50RAC-QS) although the latter two are "closer". To gain more insight a chiral and a racemic sample with a much higher helix concentration, like 220 helices/cc, should be measured and compared, but such a sample was unfortunately not available.

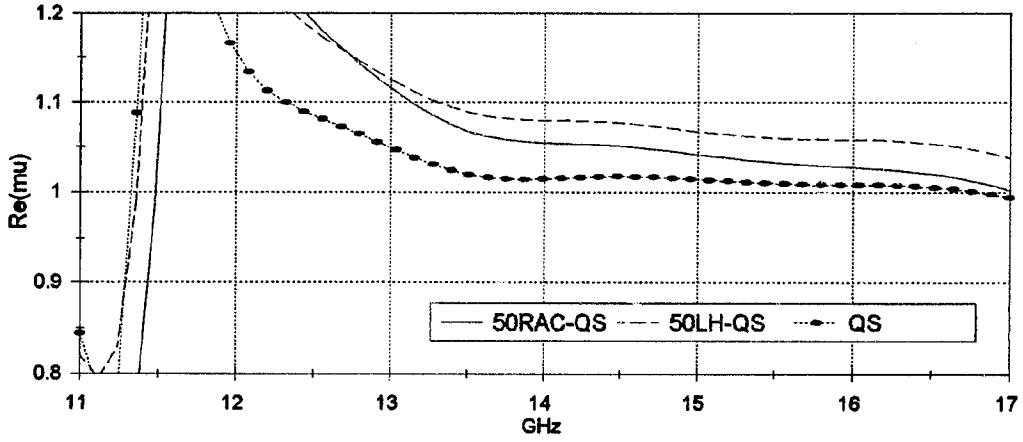

Figure 9.9: Re(μ) of a chiral (50LH-QS), a racemic (50RAC-QS) and the host medium (QS).

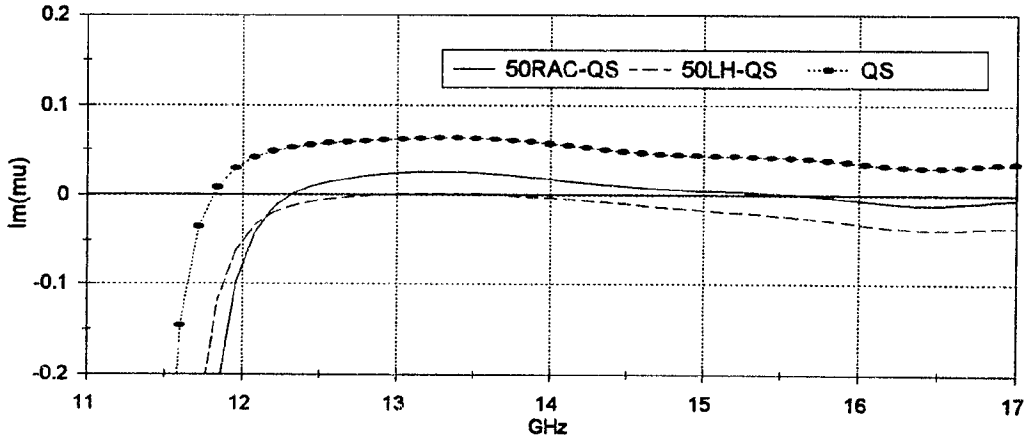

Figure 9.10: Im(μ) of a chiral (50LH-QS), a racemic (50RAC-QS) and the host medium (QS).

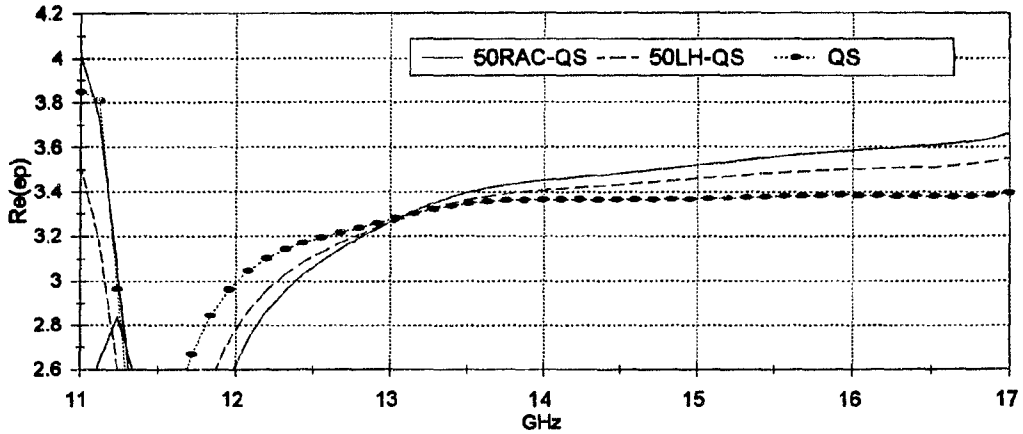

Figure 9.11: Re(ϵ) of a chiral (50LH-QS), a racemic (50RAC-QS) and the host medium (QS).

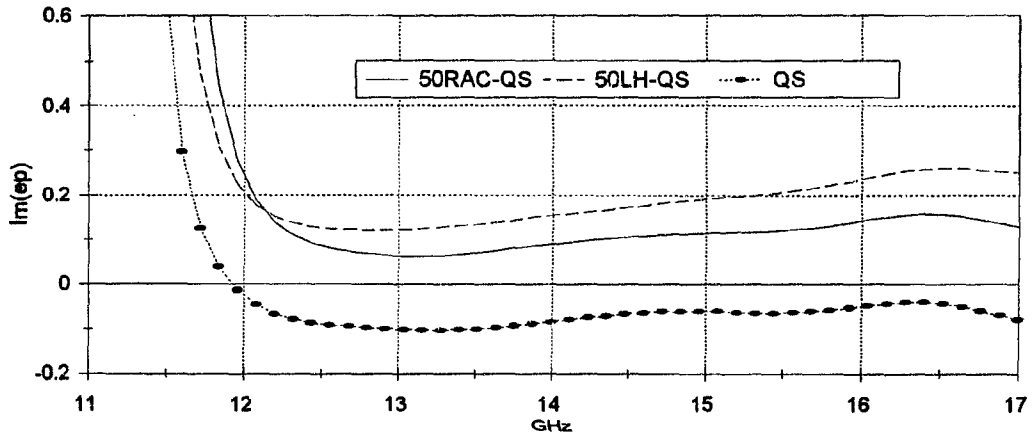

Figure 9.12: *Im (ϵ) of a chiral (50LH-QS), a racemic (50RAC-QS) and the host medium (QS).*

The measured results will now be discussed in the context of the dimensions of the helices. The total length of the nickel-chrome helices is approximately 11.35 mm, and with $\epsilon_r \approx 3$ for the host medium[9] a single helix is expected to have a half wavelength resonance ($l \approx \frac{\lambda}{2}$) at 7.6 GHz and an anti-resonance ($l \approx \lambda$) at 15 GHz[10]. All the measurements were therefore made at frequencies above the first resonance frequency and below the first anti-resonance frequency of the helices.

If the helices were smaller or if the free-space system could measure at lower frequencies (say from 4 GHz) the effect of the first resonance could be studied as was done by Hollinger [21] who observed the Cotton effect in a circular waveguide. The expected chirality parameter as well as the absorption should be maximum in this region as was shown by Bahr *et al.* [47] and Luebbers *et al.* [46]. The maximum in the chirality

[9]The resonance frequency should decrease as the helix concentration is increased since ϵ_r will increase with increasing helix concentration.

[10]Tinoco *et al.* [17, fig.2] measured absorption bands and discontinuities (change in sign) in the rotatory dispersion at resonance ($l \approx \frac{\lambda}{2}(2n+1)$) and at anti-resonance ($l \approx \frac{\lambda}{2}(2n)$) where l is the wire length of the helix. They also explained this phenomena by using a three term Drude equation.

parameter near the helix resonance frequency was also observed by Ro [48] and Guerin *et al.* [50].

In Table 9.5 the measured constitutive parameters of the (220RH-S) sample is compared to those measured by other researchers. Although the measured samples are not exactly the same their chirality parameters are of the same order in magnitude. The chirality parameter of the (220RH-S) sample should have a much higher value near the critical or resonance frequency of the helices.

A gradual decrease in the rotation angle as the frequency is increased can be seen in Figure 9.2. This is typical of rotatory dispersion and is also an indication that the measurements are above the first resonance where the Cotton effect should be observed.

In Table 9.6 the dimensions of the nickel-chrome helix is compared to those used in similar experiments by other researchers. The measured rotation and ellipticity of the polarization ellipse for the different helices are also given. The pitch to length ratio (P/L where L is the length of a single turn helix) of most of these samples are not near the optimum value of $P/L \approx 0.55$ as suggested by Svigelj *et al.* [110] and Varadan *et al.* [107]. Note that Guerin *et al* [50] measured considerably more rotation/cm using a $P/L = 0.3$ which is closer to the optimum than most of the other helices.

	GHz	μ	ϵ	$\xi * 10^6$	κ	$\beta * 10^5$
220RH-S	14	0.83+i 0.08	4.69+i 0.06	-372+i 128	———	———
220/cc		0.83+i 0.08	4.71+i 0.05	———	-0.12+i 0.03	———
3.4% Vol/Vol		0.83+i 0.08	4.69+i 0.06	———	———	-10+i 3.6
	15	0.86+i 0.05	4.62+i 0.17	-322+i 113	———	———
		0.86+i 0.05	4.63+i 0.17	———	-0.11+i 0.03	———
		0.85+i 0.06	4.62+i 0.17	———	———	-8+i 3
Ro [48]	14	0.97–i 0.46	2.77+i 3.29	———	———	7.8–i 6.9
3.2% Vol/Vol	15	0.87–i 0.53	2.60+i 3.75	———	———	7.3–i 5.5
Hujanen [63]	14	0.89+i 0.00	3.95+i 0.32	———	0.19–i 0.02	———
	15	0.88+i 0.00	3.98+i 0.37	———	0.17–i 0.02	———

Table 9.5: Comparison of measured constitutive parameters.

	Freq GHz	Pitch P	Diam D	Total Length	P/L	D/P	Rot deg/cm	Ellipticity deg
Nickel-Chrome 220/cc	15	0.33	1.20	11.4	0.09	3.6	20	3.5
100/cc							8	1.7
50/cc							4	0.8
Ro [48, p. 208] 3.2%	15	0.53	1.17	11.1	0.14	2.2	30	0.18
1.6 %							16	0.05
0.8 %							7	0.0
Umari [19] 3.2%	15	0.38	1.16	11.0	0.10	3.1	29	9.5
1.6 %							17	7.1
0.8 %							8	4.8
Hollinger [21] 3.2%	7.5	0.67	1.25	10.8	0.19	1.7	30	38
1.6 %							26	34
(see also [47]) 0.8 %							18	26
Ougier [66] 5% in Vol	15	8.0	3.00	12.3	0.65	0.4	12	6
(* or if pitch is 0.8 mm)		0.8	3.00	9.5	0.09	3.8		
Guerin [50] 3.4% in Vol	10	3.0	3.00	29.7	0.30	1.0	44	6

Table 9.6: Measured rotation characteristics of artificial chiral media. All helices have three turns except the sample of Ougier *et al.* which has 1 turn. The available data from Hujanen [63] unfortunately do not include details regarding their chiral inclusion geometries and are thus not included in this table. It is also important to note that the concentration of helices per cubic centimeter of the different samples are not necessarily equal. (* It is suspected that there was a printing error in Ougier [66], and that the pitch could be 0.8 mm, because the sample thickness of 6 mm is incompatible with the given pitch of 8 mm.) All helix dimensions are in mm.

9.5 Tungsten Helices

The tungsten helices were obtained from the resistive wire found inside (100 Watt) electric light bulbs. It is important to note that these tungsten helices are helical in two "dimensions" since the "macroscopic" three turn helix is also helical on a "microscopic" level (See the figure in Table 9.7). A chiral object of this nature will be termed "super-chiral". Both the micro helix (the wire) and the macro helix (the 3 turn helix) are left-handed. Tungsten helices were embedded in polyurethane in a rather low density of 200 helices per cubic centimeter. The amount of chirality that was measured from this sample was very small (rotation of only 0.5 degrees) and it was therefore decided to make a sample with a very high helix concentration. Because of the enormous number of helices (26 000) necessary for a high concentration sample it was made by cutting a hole with a diameter of 60 mm in a blank polyurethane sample (11 by 11 cm) and by filling the hole with the tungsten helix and paraffin wax mixture. The helix concentration in this sample was approximately 1100 helices per cubic centimeter. The real part of the permittivity of paraffin wax is $\epsilon_r = 2.3$ and it has $\tan\delta_\epsilon = 3 \times 10^{-4}$ [96].

Dimensions	Macro	Micro	
Diameter	0.58	0.13	mm
Pitch	0.19	0.05	mm
Wire diameter	0.13	0.03	mm
Number of turns	3–4		
Total wire length	6.4[a]	270[b]	mm

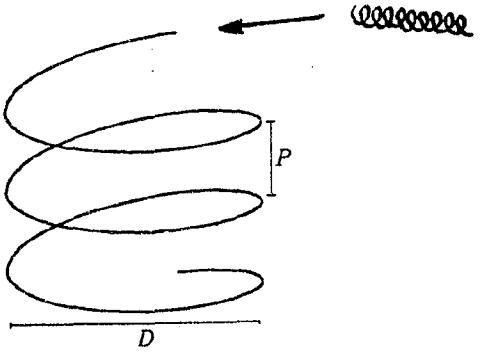

Table 9.7: (a) Contour length of large helix.(b) Contour length of the tungsten wire.

The tungsten wire has conductivity of 182.5×10^3 mho/cm and is non-magnetic (i.e. $\mu_r = 1$). Because the micro helix pitch and diameter is so small relative to the wavelength it is expected that the micro helical wire will act as if it is a solid wire. The resonance frequency of the helix would therefore rather be a function of the macro helix length (6.4 mm) than that of the total micro helix length (270 mm).
The pitch of these helices is very small ($P/L = 0.1$) and a high chirality was not

Tungsten Helices					
Name	Hand	Concentration Helices/cc	Metal Conc Vol/Vol %	Thickness mm	Host medium
Tu-LD	LH	200	3.8	6.60	Polyurethane
Tu-HD	LH	1100	20	8.25	Paraffin Wax

Table 9.8: Summary of the chiral media using Tungsten helices.

expected at the measured frequencies. The tungsten helices should be much more "active" (resonate) at higher frequencies but this could not be investigated by measurement since the free-space system is limited to a maximum of 17 GHz. The amount

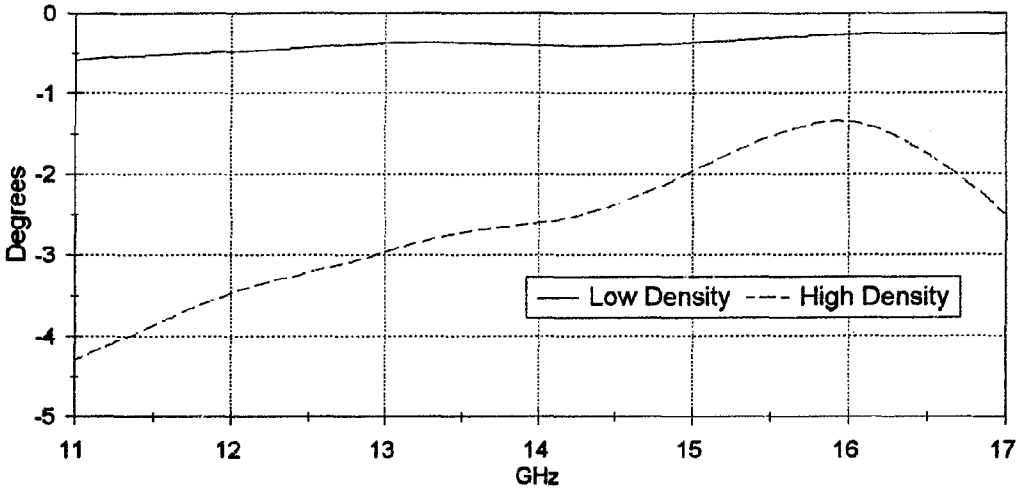

Figure 9.13: Measured rotation of the two chiral samples with tungsten helices (Tu-LD) and (Tu-HD).

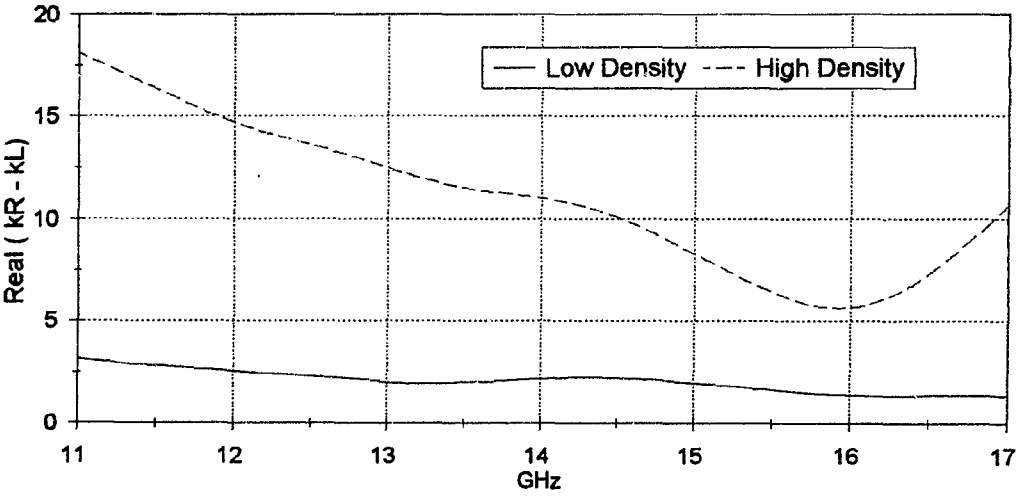

Figure 9.14: Measured difference between the real part of the wave numbers, $\mathrm{Re}(k_R - k_L)$, inside the chiral media.

of rotation increased from 0.5 degrees for the low density sample to a maximum of 4 degrees (at 11 GHz) and a minimum of approximately 1.5 degrees (at 16 GHz) for the high density sample (see Figure 9.13). The increase in the optical activity is also confirmed by the difference between the real part of the wavenumbers of the two circularly polarized waves inside the chiral media, (Fig 9.14) and the real part of the chirality parameter, ξ (Fig 9.15).

Although an increase because of a higher helix concentration was expected, it is interesting to note that the rotation through the high density sample (Tu-HD) is not as frequency independent as through the low density sample (Tu-LD). This could be

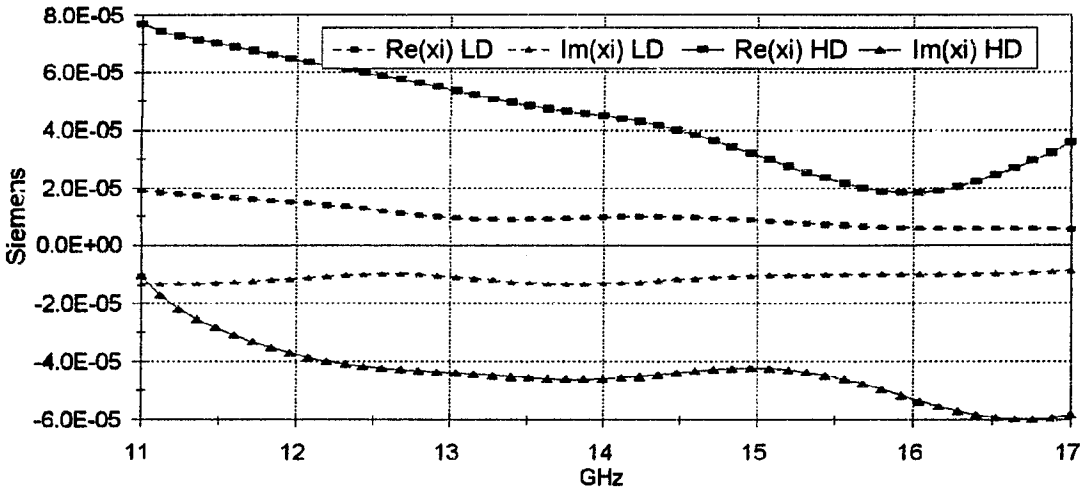

Figure 9.15: Measured chirality parameter for the low density (Tu-LD) and the high density (Tu-HD) tungsten-wire chiral media.

caused by measurement errors or percolation, but no decisive explanation can be offered.

The measurements of the host media (Section 9.3), the nickel-chrome samples (Section 9.4) and the tungsten samples (Section 9.5) show that in all the samples there is a region where there is substantial change in the measured constitutive parameters. This was explained in Chapter 8 to be the result of measurement errors ($\Delta|S|$ and $\Delta\angle S$) and ill conditioning of the inversion equations. The standard deviation in the measured constitutive parameters of all these samples were determined as explained in Section 8.5 with the expected measurements in the S-parameters as shown in Table 7.1 and $\Delta d = 0.1$ mm and are shown with the measured constitutive parameters in Appendix F. It should be clear that where the standard deviation is large, the measured constitutive parameters are inaccurate and should be used with caution.

In all these samples the standard deviation is maximum where the sample is approximately half a wavelength thick. This is especially true for the samples with low loss.

9.6 Conclusion

The following conclusions can be made from the measurements. The samples made with nickel-chrome helices displayed the following characteristics. The chiral samples displayed circular birefringence and dichroism. The rotation was found to be reciprocal, confirming optical activity. The measured amount of rotation was frequency dependent, i.e. rotatory dispersion. The rotation angle for the right handed media (RH) was positive ($\theta > 0$) and negative ($\theta < 0$) for the left handed media (LH). No rotation was measured from the achiral host media and the racemic medium. These media also had very small values for the chirality parameter ξ. The very small rotation and chirality measured for the host media samples are only an indication of the errors involved in these measurements. An approximately linear relation was observed

between the concentration of helices and the amount of rotation and therefore also the real part of the chirality parameter, $\mathrm{Re}(\xi)$. This was also true for the ellipticity, ψ, of the polarization ellipse and $\mathrm{Im}(\xi)$. For the right handed media it was found that $\mathrm{Re}(\xi) < 0$ and $\mathrm{Im}(\xi) > 0$ and for the left handed media $\mathrm{Re}(\xi) > 0$ and $\mathrm{Im}(\xi) < 0$. For the racemic sample the measured chirality was approximately zero, $\xi \approx 0$. The wave that emerged on the other side of a right handed medium was found to be left elliptically polarized ($\psi < 0$, LEP) and that from a left handed medium to be right elliptically polarized ($\psi > 0$, REP). For high helix concentration $\mathrm{Re}(\mu) < 1$ and $\mathrm{Re}(\epsilon)$ increased. From the measurements both μ and ϵ are approximately equal for racemic and chiral samples with the same helix concentrations. However, more measurements on samples with higher helix concentrations are needed to confirm this. It was found that the helices are too large for the critical frequency to be inside the measured frequency band. The frequency where the helices should resonate and cause the Cotton effect is below the frequency range of the free-space system. It is thought that the pitch to length ratio (P/L) of the helices is less than "optimal" and that higher chirality values can be obtained if the P/L ratio is increased. Large inaccuracies in the measured constitutive parameters were found where the samples are half a wavelength thick. These inaccuracies (standard deviation) were determined with an error analysis. Samples that are thicker (approximately 10 mm for most of the samples) should be used if the constitutive parameters are to be measured accurately over the whole frequency band.

The samples with tungsten helices displayed optical activity. An approximately linear relation between the helix concentration and the polarization ellipse was observed at the lower and the high frequencies. However this was not true for the frequencies 15 to 16.5 GHz where less chirality was observed.

Chapter 10

Metal-Backed Chiral Slabs: the Chiral Dallenbach Layer

> When you put together the science of motion of water,
> remember to include in each proposition its application and use,
> in order that these sciences may not be useless.
>
> — Leonardo da Vinci (1452–1519)

10.1 Introduction

Of all the possible applications suggested for artificial microwave chiral media, the possibility of using chiral media as absorbing media has received the most interest [45, 47]. Several applications for patents on artificial chiral media that can be used as microwave frequency absorbers have been filed [37, 42, 51, 52, 111, 112, 113].

The reflection coefficient, for normal incidence, from a chiral slab backed by a perfect conductor, i.e. a chiral Dallenbach layer, is given by the following expression [39, 45, 47, 50, 114, 115, 116]

$$\rho = \frac{-i\eta_c \tan(k_{av}d) - \eta_0}{-i\eta_c \tan(k_{av}d) + \eta_0}, \tag{10.1}$$

with η_c the intrinsic impedance of the chiral medium, η_0 the impedance of the medium in front of the chiral Dallenbach layer and $k_{av} = \frac{1}{2}(k_l + k_r)$ the "average" wave number inside the chiral medium. In this equation η_c and k_{av} are those of any of the three formalisms for the chiral constitutive relations (see Appendix A). For no chirality, $\xi = 0$, this equation reduces to the usual achiral Dallenbach layer equation.

Equation (10.1) can also be presented as

$$\rho = \frac{\rho_0 - \exp(i2k_{av}d)}{1 - \rho_0 \exp(i2k_{av}d)}, \tag{10.2}$$

where ρ_0 is the reflection coefficient between free space and a semi-infinite chiral slab,

$$\rho_0 = \frac{\eta_c - \eta_0}{\eta_c + \eta_0}. \tag{10.3}$$

Two methods of achieving zero reflection are evident from Equation (10.2). For the first method both terms in the numerator should be zero. This means that (a) the intrinsic impedance of the medium should be equal to that of free space so that all of the incident energy enters the medium and none is reflected by the free space/material interface (i.e $\rho_0 = 0$ in Equation 10.3), and (b) the medium should be so lossy that the wave is totally absorbed as it travels towards and from the perfect conductor, i.e. $e^{i2k_{av}d} = 0$.

For the second method it is required that the two terms in the numerator are equal, but not zero. In this case the impedance at the transition from free space to the Dallenbach layer, matches that of free space. This condition is met if the following equation is true,

$$-i\,\eta_c \tan(k_{av}d) = \eta_0. \tag{10.4}$$

The condition that will eliminate reflection of a wave which is normally incident upon a chiral half space was given by Jaggard *et al.* [37]. In this case the reflection is minimized by way of the first method mentioned above. Monzon [38] pointed out that this condition is not practical if the loss in the medium is not enough and a reflection is still present from the perfect conductor. In other words, if the Dallenbach layer does not appear to be infinitely thick for the incident wave.

The reflection from a chiral layer in the Dallenbach configuration (chiral slab against the perfect conductor) and as a Salisbury screen (chiral slab separated by $\lambda_0/4$ from the perfect conductor) was also investigated by Jaggard *et al.* [39] who coined the terms *magnetic chiroshield* and *electric chiroshield* for the two applications. The reflection coefficients from both configurations for normal incidence were given and it was shown that the reflection coefficient is lower, over a wider frequency band, than its achiral counterpart. It should be stressed, however, that the values chosen for the constitutive parameters, and in particular their choice of $\xi = 1/\eta_0$, are not necessarily practically achievable. Similar but more extensive results were also reported by Liu and Jaggard for reflection from planar chiral layers [40] as well as from chiral layers on curved surfaces [41].

The first, to the author's knowledge, published results on the possibility of using (artificial) chiral composites as anti-reflection coatings was by Lakhtakia *et al.* [36]. The chirality parameter, β, [36, fig 4], used in the calculations, is in the range of some measured results by the same research group [48]. The values for permittivity also seem to come from measurements. Some of the conclusions they make are "chirality in the absence of a lossy ϵ is of no use whatsoever in reducing reflected power density ... therefore, chirality serves only as an enhancement factor for absorption, but of itself it is not an absorbing mechanism," and "both ϵ/ϵ_0 and β should be frequency dependent (for absorption)" [36]. Concern has been expressed about the physical validity of the values for the constitutive parameters used in this analysis [38].

The influence of the complex chiral admittance on the absorption capacity and absorption effectiveness of lossy chiral media has also been investigated by Arnaut *et al.* [43]. Their analysis also showed that the reflection coefficient can be reduced under certain conditions, by addition of the chirality parameter.

In [115] the influence of the chiral admittance, ξ, on the reflection coefficient of

a Dallenbach layer was investigated. Because of the many variables (three complex constitutive parameters, and thickness and frequency) it is difficult to optimize the parameters for minimum reflection from a chiral Dallenbach layer. However, it was concluded that the introduction of ξ to an optimal (according to [117]) *achiral* Dallenbach layer will *not* reduce the reflection coefficient if μ and ϵ are kept invariant. On the contrary, it was found that the addition of ξ will *increase* the reflection coefficient of an optimal achiral Dallenbach layer. However if the achiral Dallenbach layer was not optimized a value for ξ could be found such that the reflection coefficient of the chiral Dallenbach layer is *less* than the non-optimum achiral Dallenbach layer.

Despite some encouraging theoretical predictions substantive experimental results are needed to support the claims of enhanced performance of microwave absorbers due to chiral phenomena.

10.2 Absorption Measurements on Artificial Chiral Media

10.2.1 Literature Survey

Measurements of the reflection coefficient from artificial chiral media in the Dallenbach configuration have been done by several researchers. Some of these results will now be mentioned and briefly discussed.

The first experimental measurements on chiral coatings were reported by the Pennsylvania State University [10, 20, 48, 105]. All these measurements were done in free-space. The claim that the host medium should be lossy for the artificial chiral medium to have good absorption characteristics [36] was supported by measurements in [105]. In this article it is shown that the dielectric loss of the host medium can be optimized to produce a chiral medium with optimal absorption characteristics. It is also shown that the reflection from a sample containing metal spheres of the same volume as the chiral objects, displays worse absorption characteristics, confirming the "effect of chirality" [105]. If the metal helix concentration was made too high the reflection coefficient increased. This was believed to be the result of the large impedance mismatch at the air-sample interface caused by the high metal content of the sample. A similar result was obtained for high helix concentration in another sample [20], but in this case it was believed that the higher reflection was the result of percolation causing the conduction currents not to be restricted to individual helices but to flow between touching helices. The measurements reported in this article [20] showed a general decrease in the reflection coefficient over the measured band (14.5 to 17.5 GHz) as the helix concentration was increased to 3.2 % but an increase if the helix concentration was increased further to 6.4 %.

The effect of helix concentration on the reflection coefficient of a chiral Dallenbach layer, and the power absorption coefficient, calculated from the reflection (S_{11}) and the transmission coefficients ($S_{21Co-Pol}$ and $S_{21Cross-Pol}$), of a chiral slab was studied by Ro in his thesis [48]. Some of these results were published in [10]. Once again the absorption is increased as the helix concentration is increased and the absorption

coefficient of a racemic and a chiral sample with equal helix concentration is found to be approximately equal[1]. In this article it was shown that the absorption peak is found in the region where the ratio of the one-turn length of the helix to the average wavelength inside the chiral medium is $L/\lambda_c \approx 0.6037$. They also concluded that the power absorption is maximum in the frequency band where the Cotton effect occurs. This gives support to the notion that the absorption is strongly connected to the resonance of the structure. Ro also did a parametric study where he measured the reflection coefficient from a chiral Dallenbach layer using helices with different dimensions but the same volume concentration [48]. He found that an artificial chiral medium with helices of different dimensions gave better absorption characteristics over a wider frequency range than a medium with uniform helices.

Some successful chiral absorbers have been reported by the research group of Grace N.V. in Belgium [49]. They claim to have shown that the reflection attenuation of traditional absorbing layers was improved significantly if these absorbers were combined with chiral objects. The measurements were done from 2-27 GHz and the angle of incidence was from near-normal to 60° off-normal in a free-space setup. Some of their measured results are also described in patent applications [51, 52].

Recently Guerin *et al.* [50] did measurements and compared the predicted reflection coefficient, using the measured constitutive parameters and Equation (10.1), and the actual measured reflection coefficient with success.

10.2.2 Measurements by the Author

The reflection coefficient of nickel-chrome samples, backed by a metal plate (i.e. in the Dallenbach configuration), was measured and the results can be seen in Figure 10.1. Although some valuable information can be obtained from this figure it is important to note that the respective samples do not have optimum thickness (no resonance) and that the measured reflection coefficients in this configuration could therefore be misleading as to their respective capabilities (with optimum thickness) to reduce the reflection coefficient. Another useful method to study the capability of the respective samples to reduce the reflection coefficient is to compare their power absorption coefficients. Let R be the ratio of the power[2] in the reflected wave to that of the incident wave.

$$R = \frac{P_{reflected}}{P_{incident}} = S_{11}S_{11}^{*}. \tag{10.5}$$

The relative power in the transmitted wave, T, consists of the power in the RCP and the LCP waves which is the same as the power in the co- and cross-polarized coefficient of the transmitted wave,

$$T = \frac{P_{transmitted}}{P_{incident}} = S_{21co}S_{21co}^{*} + S_{21cross}S_{21cross}^{*}. \tag{10.6}$$

[1]The measurements by Guire *et al.* [20, fig 4.] showed a big difference between the chiral and the racemic samples which is in contrast to the measurements by Ro.

[2]Time averaged power, i.e. $\langle P \rangle = \frac{1}{2}\mathrm{Re}(E \times H^{*})$ where Re() means "real part of" and the asterisk denotes the complex conjugate.

The power that is not in either the reflected, R, or the transmitted wave, T, is assumed to be absorbed by the medium[3]. With these assumptions made the power absorption coefficient, A, can be obtained from the following equation,

$$A = 1 - R - T. \tag{10.7}$$

The measured power absorption coefficient for the nickel-chrome samples are shown in Figure 10.2. In this case the absorption coefficients are not as frequency (or sample thickness) dependent as the reflection coefficient from the Dallenbach layer, Figure 10.1. The importance of using both representations (Fig 10.1 and Fig 10.2) can be seen if the (LH50-PU) and (RH220-S) are compared in both figures. From Figure 10.1 it could be concluded that the (RH220-S) sample is a better absorbing material but a comparison in Figure 10.2 shows that the (LH50-PU) sample has similar absorption properties. These measurements should therefore be interpreted with caution and it is recommend that samples with optimum thickness should rather be compared if the optimum absorber is to be found.

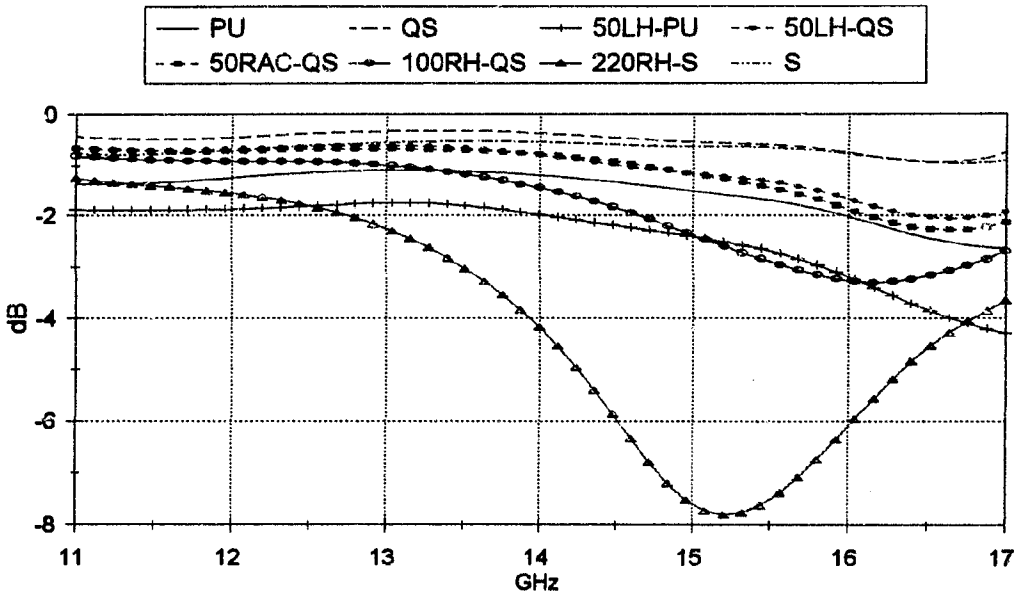

Figure 10.1: Measured reflection coefficient from artificial chiral media (nickel-chrome helices) backed by a perfect conductor. All samples are approximately 7 mm thick.

Since polyurethane is more lossy than quartz-silicone (Table 9.2) its power absorption coefficient will be higher than that of the quartz-silicone as shown in Figure 10.2. Addition of helices to the host media led to an increase in the power absorption coefficient, A, and reduction of the reflection coefficient, ρ. There is a big difference between the reflection coefficient and the absorption coefficient of the samples with the same helix concentration but with different host media (LH50-PU and LH50-QS). This

[3]This assumption is only valid if there is no power in the cross-polarized component of the reflected wave, as expected from a perfect chiral sample (i.e. with random helix orientation), and if all the reflected energy is received by the transmitting antenna. The inclusions in artificial chiral samples can become large compared to the wavelength at high frequencies and the reflection from them can then be in all directions and therefore not measurable by fixed antennas.

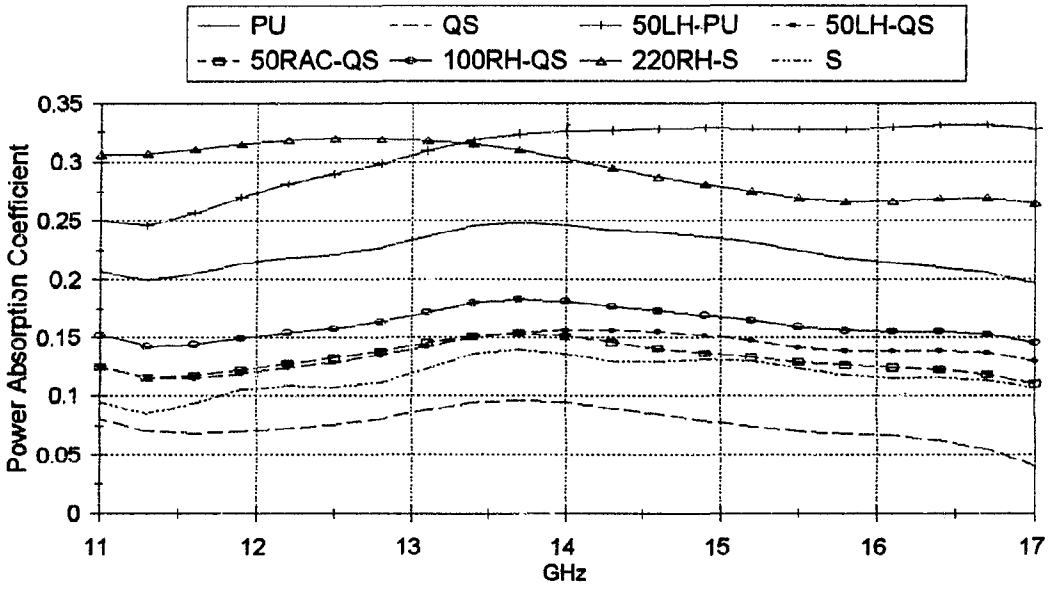

Figure 10.2: Measured power absorption coefficient of the chiral samples (nickel-chrome helix). All samples are approximately 7 mm thick.

phenomenon is not surprising and it suggests that the optimum host medium should be used to reduce the reflection coefficient. This result is similar to what has been measured [105] and predicted [36] by other researchers.

Although the reflection coefficients are high for the chiral (LH50-QS) and the racemic (RAC50-QS) samples it can be concluded that the reflection coefficient of a chiral sample and of a racemic sample of similar helix concentration will give the same absorption characteristics[4]. This was also observed by Ro [10, 48]. These measurements suggest that the enhancement of the absorption characteristics of these materials is rather a result of the effect of the helices on the permeability and the permittivity of the host medium than a "better" performance as a result of the introduction of chirality to the medium. A similar conclusion was made by Bohren *et al.* [45]. Again, as in Section 9.4 where the constitutive parameters of a chiral and a racemic sample were compared, it would be interesting to compare the absorption coefficients of racemic and chiral samples with high helix concentration.

Although the absorption coefficient of the high concentration helices (220/cc) in silicone (i.e. PH220-S) have a considerably higher (almost 3 times) power absorption coefficient than the (LH50-QS) sample it is interesting to note that it is still only approximately the same as that of 50/cc helices in polyurethane. Although nothing can be concluded as to what will happen at lower or higher frequencies these measurements suggest that the host medium is of great importance if chiral media with high power absorption are to be made. The host media should also be lossy in order to dissipate the energy.

[4]This result is not surprising since in Equation 10.2, $k_{av} = \frac{1}{2}(k_l + k_r)$ is the same for a chiral and a racemic sample and the intrinsic impedance, $\eta_c = \frac{\eta}{\sqrt{1+\eta^2\xi^2}}$, is equal if η (i.e. μ and ϵ) is equal for chiral and racemic samples of the same helix concentration and if ξ is sufficiently small so that $\eta^2\xi^2 \ll 1$. Fig 5.17 (for 3.2 %) of [48] also suggests that η is equal for chiral and racemic samples.

In [10] it was shown that the absorption peak of similar chiral media is found to be in the region where the ratio of the one-turn length of the helix to the average wavelength inside the chiral medium is $L/\lambda_c \approx 0.6037$. For the nickel-chrome samples this corresponds to frequencies in the region of 26 GHz and can unfortunately not be measured with the current free-space setup.

10.3 Absorption Mechanism of Chiral Media

Despite all the research that has been done there is still uncertainty as to why artificial chiral media could make better microwave absorbers than achiral media. An overview of comments that have been made regarding this are given in this section.

For homogeneous chiral media in the Dallenbach configuration, Guerin [114] claims that since κ does not appear in η_c or k_{av} of Equation (10.1) in the Lindell-Sihvola formalism, the superiority as microwave absorbers of such chiral (biisotropic) media over more conventional media is not promising. However he states that this is only for normal incidence on reciprocal biisotropic media and need not be the case for oblique incidence on nonreciprocal biisotropic media. It is also important to remember that the equations are for homogeneous media and the situation is different for a composite containing chiral inclusions in an achiral medium (as in actual artificial microwave chiral media) [114]. He goes further and makes the following statements: "In particular, because of the electromagnetic coupling originating from the shape of the inclusions, the macroscopic effective permittivity and the permeability will depend on both the microscopic electric and magnetic polarizabilities, as well as on the microscopic chiral polarizability of the inclusions. Thus, microscopic chirality may play a role at a macroscopic level, and inhomogeneous chiral media may yield interesting combinations of permittivity and permeability. Besides, if properly understood and controlled, other phenomena such as scattering or multiple scattering may be used to enhance global energy absorption. In any case, it turns out increasingly clear that chiral media should present some inhomogeneous character if they are considered as serious candidates for reflection reduction."[114].

Bohren *et al.* [45] believe that there is no reason why artificial chiral media should make better microwave absorbers than more conventional achiral media. They argue that since the average wave number, k_{av}, for a chiral medium is the same as that of a racemic (or achiral) medium, there is no advantage in designing transmission-line-type absorbing layers using chiral materials to increase the electrical thickness of the layers. In a comparison of the refractive indices of a medium that consists of helices and a medium that consists of three connected coaxial loops[5] (achiral) they showed theoretically that the medium of coaxial loops is more lossy over a wider frequency range than the chiral medium. They claim that this supports the hypothesis that chirality is accidental rather than essential to the microwave absorption properties of spring-loaded composite media, at least as regards the effects of chirality on the refractive index and the average wave number [45]. As was measured in Section 9.4

[5]The helix and coaxial loop's outer dimensions were approximately equal and they were both suspended in a host medium of free space.

and as Bohren *et al.* concluded from the measurements of Ro [48] there is virtually no difference between the μ and ϵ of chiral and racemic samples of the same helix concentration. Because of this fact the conjecture that artificial chiral media can outperform conventional achiral absorbing media because they can be tuned so as to give desirable μ and ϵ [37], is not true if similar values can be obtained by conventional achiral media.

Despite this apparent inability of artificial chiral media to be better absorbers than their achiral counterparts, their absorbing capability has been attributed to several mechanisms.

Bahr *et al.* [47] predicted the constitutive parameters of a chiral medium that has been made as described in [21]. Then using the predicted constitutive parameters they show that the reflection coefficient in the Dallenbach configuration from the chiral composite is much lower over a wide band than that from the achiral host medium. They speculate that the power loss is enhanced because the electric fields are concentrated near the helix, causing an increase in the ohmic dissipation in the helix material. The model they developed suggests that most of the dissipation is associated with mutual coupling between the helices. They support this statement by claiming that the mutual resistance in this sample is more than three times larger than each of the resistive components in the helix impedance, therefore making a major contribution to the total loss in the composite medium. It could also be argued that the enhanced dissipation is due to multiple scattering by the randomly oriented helices [47].

Note that during resonance the currents on the helix and the fields in the region surrounding the helix will be maximum. This will lead to maximum ohmic dissipation in the wire of a lossy helix and in the lossy host medium immediately surrounding the helix.

The effect of the resistivity of the wire was studied by Svigelj *et al.* [108] and by Luebbers *et al.* [46]. Luebbers *et al.* [45, 46] developed a theory with which they predict the chirality parameter, β. The theory uses the tumble average scattering of a single helix in a dilute mixture and does not include multiple scattering between the inclusions. The tumble average is used because random helix orientation is assumed. Reasonable results are obtained from this rather simple model. Luebbers *et al.* conclude in [46] "...that the conductivity of the helical wire had a very small effect" and that "the only significant loss mechanism in a chiral composite composed of conducting wire helices is the dissipation (either dielectric or magnetic) of the matrix material."

Svigelj *et al.* [108] investigated the reflection from oriented, lossy, infinite helices backed by a perfect conductor. The helices are in a "host medium" of free space. They show the effect of a varying pitch to length ratio, number of layers and the resistivity of the wires. Although not directly applicable to chiral media (since the helices are infinite), the results show that the energy is dissipated in the resistive wire of the helix and that an optimum pitch to length (P/L) ratio and resistance (of helix wire) per wavelength (R/λ) can be found.

This apparent contradiction can be explained since the helices of Luebbers were embedded in a lossy host medium whereas the helices of Svigelj *et al.* were suspended in air. For the latter case there can be no dissipation in the "host" medium and the resistive helices are the only loss mechanism.

Measurements on single helices in a cylindrical resonator were made by Semenenko *et al.* [70]. They measured the permeability of helices with approximately the same dimensions but made of copper, nickel-chrome and carbon respectively. Their measurements have shown that the resonance values of μ' and μ'' decreases and the resonance frequency band width increases as the resistance of the wire increases. The measurements also show that the resonance effect is stronger in the more conductive helices.

10.4 Conclusion

In general it can be concluded from Figures 10.1 and 10.2 that an increase in the helix concentration leads to an increase in the power absorption coefficient and a reduction of the reflection coefficient. This is similar to the findings of Ro [10, 48]. However, making the helix concentration as high as possible will not result in the lowest reflection since percolation can occur and even if the metal helices do not touch a high metal content will give rise to a large intrinsic impedance of the chiral medium and therefore an increase in the reflection coefficient. It is therefore suggested that lossy dielectric helices be used to make artificial chiral media [105]. The measurements suggest that the absorption is enhanced by using lossy dielectric host media. This has also been suggested by other researchers.

It has also been found that racemic and chiral samples of the same helix concentration have approximately the same absorption characteristics. If this is true in general this result is fundamental in that it supports the theory by Bohren *et al.* [45] that the "good" absorption characteristics of this kind of artificial media should not be attributed to the fact that they are chiral but rather to the shape of the inclusions, be they handed or not.

Skepticism regarding the ability of artificial chiral media to make good absorbers should be tempered with the promising results that have been obtained through measurement by some researchers [47, 50, 51, 52, 105].

Chapter 11

General Conclusions

> There is a hierarchy of facts. Some are without any positive bearing, and teach us nothing but themselves. The scientist who ascertains them learns nothing but facts, and becomes no better able to foresee new facts. Such facts, it seems, occur but once, and are not destined to be repeated.
> There are, on the other hand, facts that give large return, each of which teaches us a new law. And since he is obliged to make a selection, it is to these latter facts that the scientist must devote himself.
>
> — Henri Poincaré (1854-1912)

The purpose of this thesis was to establish a method to measure the characteristics of artificial chiral media at microwave frequencies. This was achieved by deriving a set of inversion equations from which the constitutive parameters of a chiral slab can be determined by inverting the reflection and transmission coefficients of the slab. These scattering parameters are measured by a free-space system. The characteristics of the system and especially those of the focused lens antennas were studied in detail and a suitable free-space calibration method developed. An accuracy analysis was developed to determine the expected errors in the measured constitutive parameters.

It was found that the inversion method is susceptible to large inaccuracies at frequencies where the sample is multiples of half a wavelength thick. This is particularly true for low loss materials. The accuracy analysis, using the partial derivatives of the inversion equations, quantifies the resulting errors. The partial derivative of each of the complex constitutive parameters to the magnitude and phase of each of the scattering parameters are given in an analytical from. This makes it possible to isolate the contributions of each of the measurement errors.

An estimate of the accuracy with which the scattering parameters can be measured was determined by comparing measurements from several Perspex samples with accurate theoretical predictions. These values of the expected errors in the S-parameters were used to determine the standard deviation in the measured constitutive parameters of the artificial chiral media.

An investigation into the radiation patterns of the antennas showed that a linearly polarized plane wave with a finite diameter is formed at the focus. The focused fields minimize diffraction from the sample edges and ensure that the measured scattering

parameters are essentially those of a plane wave illuminating a planar slab, as required by the theory in both the inversion equations for constitutive parameter measurements and the calibration procedure. The linear polarization of the antennas make them suitable for polarization measurements and therefore also for the measurement of chiral media. The similarity between the measured and the theoretical results of the radiation patterns of the antennas illustrate that the theoretical analysis can be used to obtain an estimate of the fields in the focal region of antennas of this type. However, if more accurate results are needed the theoretical model should be extended and the assumptions made regarding the field distribution in the aperture be reviewed. It should be possible to use the same methods to determine the dispersion in the focal region of similar antennas. The incorporation of the dispersion into the calibration standards and the calibration procedure developed in this thesis could be valuable for researchers using similar free-space systems.

The results of Chapter 10 (measurements and a literature survey) show that although the use of artificial chiral media as microwave absorbers looks promising extensive research is still needed to establish artificial chiral media as a viable alternative to achiral absorption media.

The establishment, due to this research, of an independent method to measure the characteristics of chiral media contributes to the sparse amount of measured data and also serves to validate measurements that have been made by other researchers.

Appendix A

Conversion Between Constitutive Relations for Isotropic Chiral Media

The following is a summary of the different constitutive relations which have become known as the Post-Jaggard [1], Drude-Born-Fedorov [7] and Sihvola-Lindell [27] forms.

A more general form of the relations, which also applies to non-isotropic media, have been presented by Raab *et al.*[55]. This formulation, which is based on the theory of multipoles, includes the contribution of the electric quadrupole. (See Section 2.4.)

The harmonic time convention is $exp(-i\omega t)$.

A.1 Constitutive Relations

Post–Jaggard:

$$\begin{bmatrix} \boldsymbol{D} \\ \boldsymbol{H} \end{bmatrix} = \begin{bmatrix} \epsilon_p & i\xi \\ i\xi & 1/\mu_p \end{bmatrix} \begin{bmatrix} \boldsymbol{E} \\ \boldsymbol{B} \end{bmatrix}$$

Drude–Born–Fedorov:

$$\begin{bmatrix} \boldsymbol{D} \\ \boldsymbol{B} \end{bmatrix} = \begin{bmatrix} \epsilon_d \boldsymbol{E} + \beta\epsilon_d \nabla \times \boldsymbol{E} \\ \mu_d \boldsymbol{H} + \beta\mu_d \nabla \times \boldsymbol{H} \end{bmatrix} = \begin{bmatrix} \epsilon_d \boldsymbol{E} + i\beta\epsilon_d\omega \boldsymbol{B} \\ \mu_d \boldsymbol{H} - i\beta\mu_d\omega \boldsymbol{D} \end{bmatrix}$$

$$\begin{bmatrix} \boldsymbol{D} \\ \boldsymbol{H} \end{bmatrix} = \begin{bmatrix} \epsilon_d & i\beta\omega\epsilon_d \\ i\beta\omega\epsilon_d & 1/\mu_d - \beta^2\omega^2\epsilon_d \end{bmatrix} \begin{bmatrix} \boldsymbol{E} \\ \boldsymbol{B} \end{bmatrix}$$

Sihvola–Lindell:

$$\begin{bmatrix} \boldsymbol{D} \\ \boldsymbol{B} \end{bmatrix} = \begin{bmatrix} \epsilon_s & i\kappa\sqrt{\epsilon_o\mu_o} \\ -i\kappa\sqrt{\mu_o\epsilon_o} & \mu_s \end{bmatrix} \begin{bmatrix} \boldsymbol{E} \\ \boldsymbol{H} \end{bmatrix}$$

$$\begin{bmatrix} \boldsymbol{D} \\ \boldsymbol{H} \end{bmatrix} = \begin{bmatrix} \epsilon_s - \epsilon_o\kappa^2\mu_o/\mu_s & i\sqrt{\epsilon_o\mu_o}\kappa/\mu_s \\ i\sqrt{\epsilon_o\mu_o}\kappa/\mu_s & 1/\mu_s \end{bmatrix} \begin{bmatrix} \boldsymbol{E} \\ \boldsymbol{B} \end{bmatrix}$$

A.2 Conversion Equations

Drude–Born–Fedorov and Post–Jaggard:

$$\epsilon_d \rightarrow \epsilon_p \qquad \epsilon_p \rightarrow \epsilon_d$$
$$\mu_d \rightarrow \frac{\epsilon_p\mu_p}{\epsilon_p+\mu_p\xi^2} \qquad \mu_p \rightarrow \frac{\mu_d}{1-\beta^2\epsilon_d\mu_d\omega^2}$$
$$\beta \rightarrow \frac{\xi}{\epsilon_p\omega} \qquad \xi \rightarrow \beta\epsilon_d\omega$$

Drude–Born–Fedorov and Sihvola–Lindell:

$$\epsilon_s \rightarrow \frac{\epsilon_d}{1-\beta^2\epsilon_d\mu_d\omega^2} \qquad \epsilon_d \rightarrow \epsilon_s - \frac{\epsilon_o\kappa^2\mu_o}{\mu_s}$$
$$\mu_s \rightarrow \frac{\mu_d}{1-\beta^2\epsilon_d\mu_d\omega^2} \qquad \mu_d \rightarrow \mu_s - \frac{\epsilon_o\kappa^2\mu_o}{\epsilon_s}$$
$$\kappa \rightarrow \frac{\beta\epsilon_d\mu_d\omega}{\sqrt{\epsilon_o\mu_o}(1-\beta^2\epsilon_d\mu_d\omega^2)} \qquad \beta \rightarrow \frac{\sqrt{\epsilon_o\mu_o}\kappa}{\epsilon_s\mu_s\omega-\epsilon_o\kappa^2\mu_o\omega}$$

Sihvola–Lindell and Post–Jaggard:

$$\epsilon_s \rightarrow \epsilon_p + \mu_p\xi^2 \qquad \epsilon_p \rightarrow \epsilon_s - \frac{\epsilon_o\kappa^2\mu_o}{\mu_s}$$
$$\mu_s \rightarrow \mu_p \qquad \mu_p \rightarrow \mu_s$$
$$\kappa \rightarrow \frac{\mu_p\xi}{\sqrt{\epsilon_o\mu_o}} \qquad \xi \rightarrow \frac{\sqrt{\epsilon_o\mu_o}\kappa}{\mu_s}$$

A.3 Wave Parameters

The wave numbers in the different constitutive relations are:

	Post–Jaggard	Drude–Born–Fedorov	Sihvola–Lindell
$k_l =$	$\omega\sqrt{\mu_e(\epsilon_e+\mu_e\xi^2)}-\omega\mu_e\xi$	$\omega\sqrt{\mu_v\epsilon_v}\,/(1+\omega\sqrt{\mu_v\epsilon_v}\beta)$	$\omega\sqrt{\mu_s\epsilon_s}-\kappa\omega\sqrt{\mu_o\epsilon_o}$
$k_r =$	$\omega\sqrt{\mu_e(\epsilon_e+\mu_e\xi^2)}+\omega\mu_e\xi$	$\omega\sqrt{\mu_v\epsilon_v}\,/(1-\omega\sqrt{\mu_v\epsilon_v}\beta)$	$\omega\sqrt{\mu_s\epsilon_s}+\kappa\omega\sqrt{\mu_o\epsilon_o}$

The intrinsic impedance for the different constitutive relations are:

	Post–Jaggard	Drude–Born–Fedorov	Lindell–Sihvola
$\eta_c =$	$\frac{\eta_p}{\sqrt{1+\eta_p^2\xi^2}}$ with $\eta_p=\sqrt{\frac{\mu_p}{\epsilon_p}}$	$\sqrt{\frac{\mu_d}{\epsilon_d}}$	$\sqrt{\frac{\mu_s}{\epsilon_s}}$

The intrinsic impedance is defined as the the ratio of the electric field to the magnetic field of a travelling wave.

$$\eta_c = \frac{\mathbf{E}}{\mathbf{H}} \tag{A.1}$$

The intrinsic impedance is the same for both the RCP and the LCP waves.

Appendix B

Constitutive Parameters from the Inversion of Scattering Parameters

B.1 Solving the Ambiguity in the Measured Wave Number

As was shown in Section 3.1 the wave numbers k_r and k_l can be found from the measured propagation factors P_r and P_l using the following equations,

$$k_r = \frac{1}{id}\ln(P_r) = \frac{1}{id}\ln\left(\frac{S_{21x} - iS_{21y}}{1 - \Gamma S_{11}}\right), \tag{B.1}$$

$$k_l = \frac{1}{id}\ln(P_l) = \frac{1}{id}\ln\left(\frac{S_{21x} + iS_{21y}}{1 - \Gamma S_{11}}\right). \tag{B.2}$$

However since the logarithm of a complex argument, X, has a multiple valued imaginary part,

$$\ln(X) = \mathrm{Ln}(X) + i2\pi n \qquad n = 0, 1, 2, 3... \tag{B.3}$$

(where $\mathrm{Ln}(X)$ is the principal value of $\ln(X)$) the solution of the wave numbers can be ambiguous.

The ambiguity can be solved by measuring two samples of different thickness or it can be solved for a single slab by using the group velocity in the following way [62]. The solution will be shown only for the RCP wave since exactly the same principle is used for the LCP wave. For a complex value of the propagation factor, P_r (i.e. with a complex wave number k_r),

$$P_r = e^{ik_r d} = e^{\gamma_r d} = |P_r|e^{i\phi_r}, \tag{B.4}$$

$$\gamma_r = \alpha_r + i\beta_r, \tag{B.5}$$

$$|P_r| = e^{\alpha_r d}, \tag{B.6}$$

$$\text{and} \quad \phi_r = \beta_r d. \tag{B.7}$$

Inverting P_r yields

$$\gamma_r = \frac{1}{d}\ln(P_r), \tag{B.8}$$

$$\therefore \quad \gamma_r = \frac{1}{d}\ln(|P_r|e^{i\phi_r}) = \frac{1}{d}\{\mathrm{Ln}(P_r) + i2\pi n_r\}. \tag{B.9}$$

Here $\mathrm{Ln}(P_r)$ maps the complex argument onto its *principal* value so that

$$\mathrm{Ln}(P_r) = \Theta_{Rr} + i\Theta_{Ir}, \tag{B.10}$$

where Θ_{Rr} and Θ_{Ir} are the real and imaginary parts of the *principal* value of $\ln(P_r)$.

The value of the integer n_r is then calculated from the measured values as follows. From Equation (B.9) and (B.10) the complex phase of the propagation factor can be written as

$$\gamma_r d = \alpha_r d + i\beta_r d = \Theta_{Rr} + i\Theta_{Ir} + i2\pi n_r, \tag{B.11}$$

$$\therefore \quad \beta_r d = \Theta_{Ir} + 2\pi n_r, \tag{B.12}$$

$$\text{and} \quad n_r = \frac{\beta_r d - \Theta_{Ir}}{2\pi}. \tag{B.13}$$

But the exact value of β_r is not known from one measurement[1] because $\beta_r d$ (a measure of phase) is modulo 2π. Substitution of the phase velocity, $\nu_{pr} = \omega/\beta_r$, into (B.13), leads to

$$n_r = f\left(\frac{d}{\nu_{pr}}\right) - \frac{\Theta_{Ir}}{2\pi}. \tag{B.14}$$

Since the phase velocity, $\nu_p = \omega/\beta$, is equal to the group velocity, $\nu_g = \partial\omega/\partial\beta$, for waves propagating in unbounded space, the phase delay, $t_p = \frac{d}{\nu_p}$, is equal to the group delay, $t_g = \frac{d}{\nu_g}$, and the integer n_r follows from

$$n_r = \mathrm{Round}(ft_g - \frac{\Theta_{Ir}}{2\pi}), \tag{B.15}$$

$$= \mathrm{Round}(f\frac{d}{(\partial\omega/\partial\beta)} - \frac{\Theta_{Ir}}{2\pi}). \tag{B.16}$$

Thus the arguments of P_r and P_l are differentiated numerically to obtain their respective group velocities $\nu_{gr} = \partial\omega/\partial\beta_r$ and $\nu_{gl} = \partial\omega/\partial\beta_l$. Rounding is necessary since small measurement errors yield non interger values.

Once the integers n_r and n_l are known the wave numbers, k_r and k_l, can be calculated from P_r and P_l using the following equations;

$$k_r = \frac{1}{id}\{ln|P_r| + i(\phi_r + 2\pi n_r)\}, \tag{B.17}$$

$$k_l = \frac{1}{id}\{ln|P_l| + i(\phi_l + 2\pi n_l)\}. \tag{B.18}$$

Other methods can also be used to solve the ambiguity in the logarithm of Equation (B.9) [48, 66].

[1]The value could be determined by measuring a similar sample of different thickness.

B.2 Constitutive Parameters from the RCP and LCP Wave Properties

In this section it is shown how to get the constitutive parameters, μ, ϵ and ξ, in terms of the measured intrinsic impedance, η_c, and wavenumbers, k_r and k_l. The intrinsic impedance of a chiral medium is, (2.6)

$$\eta_c = \frac{\mu}{\sqrt{\mu\epsilon + \mu^2\xi^2}}. \tag{B.19}$$

The wave numbers for the RCP and the LCP waves of a chiral medium are given by Equations (2.4) and (2.5),

$$k_r = \omega\sqrt{\mu\epsilon + \mu^2\xi^2} + \omega\mu\xi, \tag{B.20}$$

$$k_l = \omega\sqrt{\mu\epsilon + \mu^2\xi^2} - \omega\mu\xi. \tag{B.21}$$

(B.20)+(B.21):

$$k_r + k_l = 2\omega\sqrt{\mu\epsilon + \mu^2\xi^2}. \tag{B.22}$$

(B.20)–(B.21):

$$k_r - k_l = 2\omega\mu\xi, \tag{B.23}$$

and from (B.22):

$$\sqrt{\mu\epsilon + \mu^2\xi^2} = \frac{k_r + k_l}{2\omega}. \tag{B.24}$$

(B.24) into (B.19):

$$\eta_c = \frac{2\omega\mu}{k_r + k_l}, \tag{B.25}$$

$$\Rightarrow \quad \mu = \frac{\eta_c}{2\omega}(k_r + k_l). \tag{B.26}$$

(B.23) into (B.25):

$$\eta_c = \frac{k_r - k_l}{\xi(k_r + k_l)},$$

$$\Rightarrow \quad \xi = \frac{1}{\eta_c}\frac{(k_r - k_l)}{(k_r + k_l)}. \tag{B.27}$$

The permittivity, ϵ, is obtained as follows:
(B.22) squared:

$$(k_r + k_l)^2 = 4\omega^2(\mu\epsilon + \mu^2\xi^2), \tag{B.28}$$

and (B.23) in (B.28)

$$(k_r + k_l)^2 - (k_r - k_l)^2 = 4\omega^2\mu\epsilon$$

$$4k_r k_l = 4\omega^2\mu\epsilon$$

$$\Rightarrow \quad \epsilon = \frac{k_r k_l}{\omega\mu},$$

and with μ from (B.26):

$$\epsilon = \frac{2k_r k_l}{\omega\eta(k_r + k_l)}. \tag{B.29}$$

Therefore the constitutive parameters can be determined from the measured intrinsic impedance and the wavenumbers for the LCP and RCP waves using the following equations:

$$\mu = \frac{\eta_c}{2\omega}(k_r + k_l), \tag{B.30}$$

$$\epsilon = \frac{1}{\eta_c}\frac{(k_r - k_l)}{(k_r + k_l)}, \tag{B.31}$$

$$\xi = \frac{2}{\omega\eta_c}\frac{k_r k_l}{(k_r + k_l)}. \tag{B.32}$$

Appendix C

Instrumenta

The following components are used in the free-space measurement system:

1. Network Analyzer:
   (a) HP 8341B synthesized sweeper,
   (b) HP 8511A frequency converter,
   (c) HP 8510C network analyzer.
2. Two HP 773D (2-18 GHz) 20dB directional couplers.
3. Sucoflex 104A (3 m) and HP 11610B (1 m) phase stable cables.
4. Maury Microwave (Model P209D2) coax-to-waveguide converters.
5. Alpha Industries Series 857 (Ku-Band) horn lens antennas.
6. Measurement bench.
7. Personal computer using an Intel 486 processor.

The equipment is configured as illustrated in Figure 4.1 and Figure 4.2 and its basic operation discussed in Section 4.2.

C.1 Network Analyzer

The signal is generated by the HP 8341B synthesized sweeper and is then divided by the directional couplers into a reference signal a_1, a reflection signal b_1, and a transmission signal b_2. The signals a_1, b_1 and b_2 are received by the HP 8511A frequency converter. The S-parameters are calculated in the HP 8510C network analyzer:

$$S_{11} = b_1/a_1$$
$$S_{21} = b_2/a_1.$$

The calibration coefficients are calculated and stored in the HP 8510C. All the signal processing like the calibration and the time domain gating is done in the HP 8510C.

The HP 8510C is controlled via the HP Interface Bus (HP-IB) by a personal computer using Hewlett Packard drivers and a code that was developed in Turbo Pascal. This makes it possible to specify the calibration standards and time domain parameters automatically and to do all measurements without having to select any options from the control panel of the HP 8510C.

The HP 8511A frequency converter does not have an electronic switch between the two ports 1 and 2 as in an HP 8515A S-parameter test set and it is therefore not possible to measure all four S-parameters (S_{11}, S_{21}, S_{12} and S_{22}) without disconnecting the transmission cables. With the HP 8510C network analyzer and HP 8511A frequency converter combination it is therefore not possible to do a full two-port (twelve term error model) or a TRL calibration and an error model containing less error terms must be used (Fig. 6.1).

Typical dynamic accuracy of the HP 8511A frequency converter is shown in Figure C.1. The exact performance of the system in this configuration and with free space calibration is not known but is expected to have similar characteristics to when an S-Parameter test set is used, Figures C.2 and C.3.

HP 8510B/8511A 45 MHz-26.5 GHz

Description

Combining the HP 8511A Frequency Converter with the HP 8510B Network Analyzer results in a four channel receiver/signal processor that operates over the frequency range of 45 MHz to 26.5 GHz. This system offers flexibility in the configuration of a user supplied signal separation network to meet the needs of custom measurements. The HP 8511A contains four separate RF to IF converters all of which can operate over the entire dynamic range of the system. Either the a1 or a2 input must be defined as the reference channel to maintain phase lock and to track the RF source.

The following specifications describe the system performance for the HP 8510B network analyzer with the HP 8511A Frequency Converter.

Dynamic range (on all inputs)[1]

	Frequency range		
	.045-8 GHz	8-20 GHz	20-26.5 GHz
Dynamic range (Averaging factor = 1024)	105 dB (−10 to −115 dBm)	105 dB (−10 to −115 dBm)	98 dB (−15 to −113 dBm)

Dynamic accuracy

The following plots show the worst case magnitude and phase uncertainty due to IF residuals and detector inaccuracies.[2]

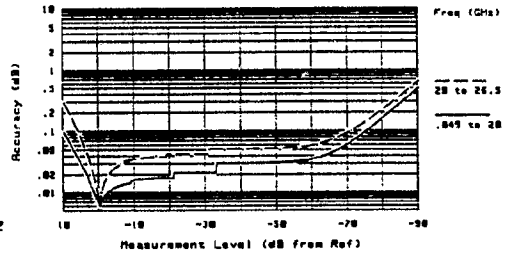

Magnitude

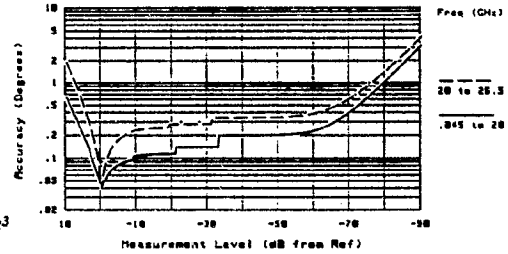

Phase[3]

Input port characteristics

The following specifications show the uncorrected system characteristics at the four measurement ports. Environmental temperature is 23 ± 3°C.

	Frequency range		
	.045-8 GHz	8-20 GHz	20-26.5 GHz
Impedance match (all 4 ports)	17 dB	15 dB	9 dB
Frequency response tracking (ratio measurement of any two ports, excludes slope)	± .5 dB	± .5 dB	± .5 dB
Crosstalk[4]	115 dB	115 dB	113 dB

HP 8511A general information

Input Ports:
Connector type (all inputs): 3.5 mm (F)
Impedance: 50Ω Nominal

Ordering Information: The following option is available for the HP 8511A.
Option 001: Add IF switching.
Description: Allows two test sets to be connected to the HP 8510 at the same time. The test set in use is selected from the HP 8510B front panel. The 20 MHz IF signal is daisychained from the test sets to the HP 8510. IF switching is performed automatically without reconnections.

[1]Limited by compression level and system noise floor.
[2]Excludes uncertainty due to noise, frequency response, directivity, port matches, crosstalk, and connector repeatability.
[3]Phase detector accuracy is better than 0.02 degrees, useful for measurements where only phase changes.
[4]Does not include noise.

Figure C.1: System performance of HP 8510B/8511A [101].

System performance[1]
HP 8510T
45 MHz-26.5 GHz

The following specifications describe the system performance for the HP 8510B network analyzer with the HP 8510T configuration. The system hardware includes the following:

Test Set: HP 8515A S-parameter Test Set
RF source: HP 8340B Synthesized Sweeper
Calibration Kits: HP 85050B 7 mm Calibration Kit (18 GHz)
HP 85052B 3.5 mm Calibration Kit

Dynamic range (for transmission measurements)[2]

	Frequency range		
	.045-8 GHz	8-20 GHz	20-26.5 GHz
Dynamic range (Averaging factor=1024)	105 dB (+2 to −103 dBm)	105 dB (+2 to −103 dBm)	99 dB (−1 to −100 dBm)

For devices with 7 mm connectors

Measurement uncertainty

The following graphs show total worst case uncertainty for the HP 8510T system after accuracy enhancement using full two-port error correction with the HP 85050B 7 mm Calibration Kit. This includes the residual systematic errors, as well as the system dynamic accuracy, 7 mm connector repeatability, noise, and detector errors[3]. Specific points on the graphs are verified by measuring the devices in the HP 85051B Verification Kit.

Reflection measurements[4]

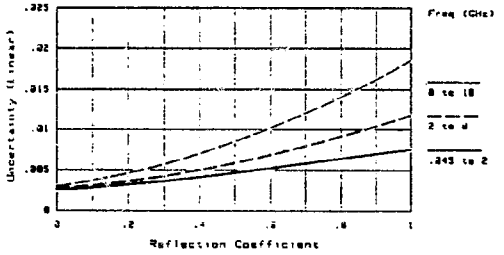

Magnitude

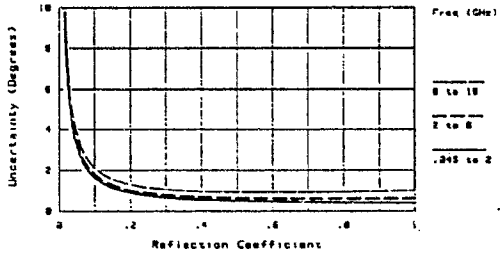

Phase[6]

Transmission measurements[5]

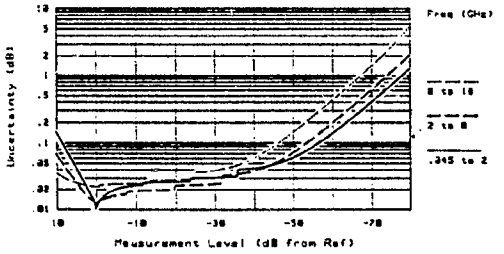

Magnitude

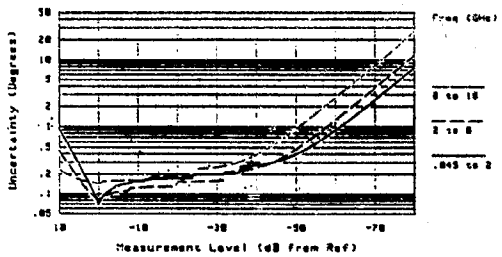

Phase[6]

Measurement port characteristics

The following specifications show the residual system uncertainties after accuracy enhancement using full two-port error correction with the HP 85050B 7 mm Calibration Kit. Environmental temperature is 23 ± 3°C.

	Frequency range		
	.045-2 GHz	2-8 GHz	8-18 GHz
Directivity	52 dB	52 dB	52 dB
Source match	48 dB	44 dB	41 dB
Load match	52 dB	52 dB	52 dB
Reflection tracking	±.003 dB	±.016 dB	±.047 dB
Transmission tracking	±.004 dB	±.005 dB	±.013 dB
Crosstalk[7]	118 dB	114 dB	107 dB

Figure C.2: System performance of HP 8510B/8515A S-paramter test set [101].

For devices with 3.5 mm connectors

Measurement uncertainty

The following graphs show total worst case uncertainty for the HP 8510T system after accuracy enhancement using full two-port error correction with the HP 85052B 3.5 mm Calibration Kit. This includes the residual systematic errors, as well as the system dynamic accuracy, noise, and 3.5 mm connector repeatability[3]. Specific points on the graphs are verified by measuring the devices in the HP 85053B Verification Kit.

Reflection measurements[4]

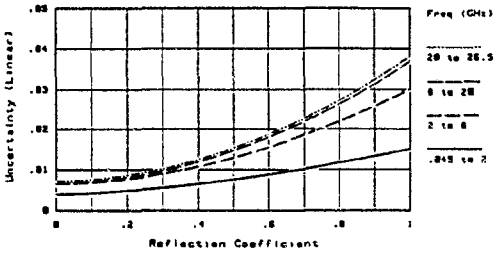

Magnitude

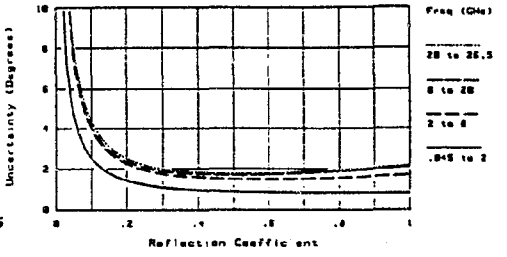

Phase[6]

Transmission measurements[5]

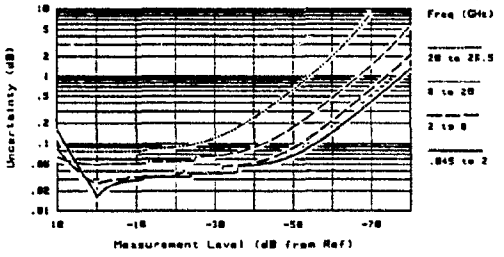

Magnitude

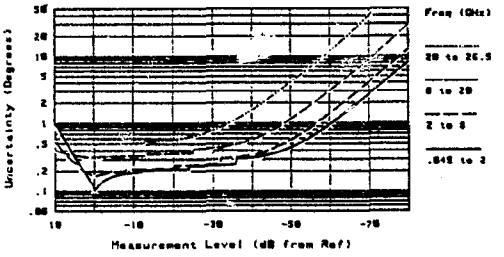

Phase[6]

Measurement port characteristics

The following specifications show the residual system uncertainties after accuracy enhancement using full two-port error correction with the HP 85052B 3.5 mm Calibration Kit. Environmental temperature is 23 ± 3°C.

	Frequency range			
	.045-2 GHz	2-8 GHz	8-20 GHz	20-26.5 GHz
Directivity	48 dB	44 dB	44 dB	44 dB
Source match	40 dB	33 dB	31 dB	31 dB
Load match	48 dB	44 dB	44 dB	44 dB
Reflection tracking	±.003 dB	±.003 dB	±.006 dB	±.006 dB
Transmission tracking	±.009 dB	±.017 dB	±.038 dB	±.06 dB
Crosstalk[7]	118 dB	114 dB	107 dB	94 dB

[1]System performance is shown for a number of HP 8510 configurations. For other configurations, contact your local HP sales representative.
[2]Limited by compression level and system noise floor. Noise floor is measured with full two-port error correction.
[3]Stepped sweep mode with 1024 averages. Cable stability and system drift are not included.
[4]The graphs shown for reflection measurement uncertainty apply to a one-port device.
[5]The graphs for transmission measurements assume a well-matched device ($S_{11}=S_{22}=0$).
[6]Phase detector accuracy is better than ±0.02 degrees, useful for measurements where only phase changes.
[7]Does not include noise.

Figure C.3: System performance of HP 8510B/8515A S-paramter test set [101].

C.2 Phase Stable Cables

Phase stable cables are necessary because the phase must be measured with great accuracy and the phase should not change if the receiving antenna is rotated for cross-polarized transmission coefficient measurements (See Section 7.3.2). An HP 11610B cable of length 1 m is connected to the transmitting antenna and a Sucoflex 104A (Huber+Suhner AG) cable of length 3 m is connected to the receiving antenna.

C.3 Maury Microwave Coax-to-Waveguide converters (Model P209D2)

The waveguide ports are connected to the waveguide flanges of the horn lens antennas. The reflection coefficients of the coax to waveguide converters were measured and are shown in Figure C.4.

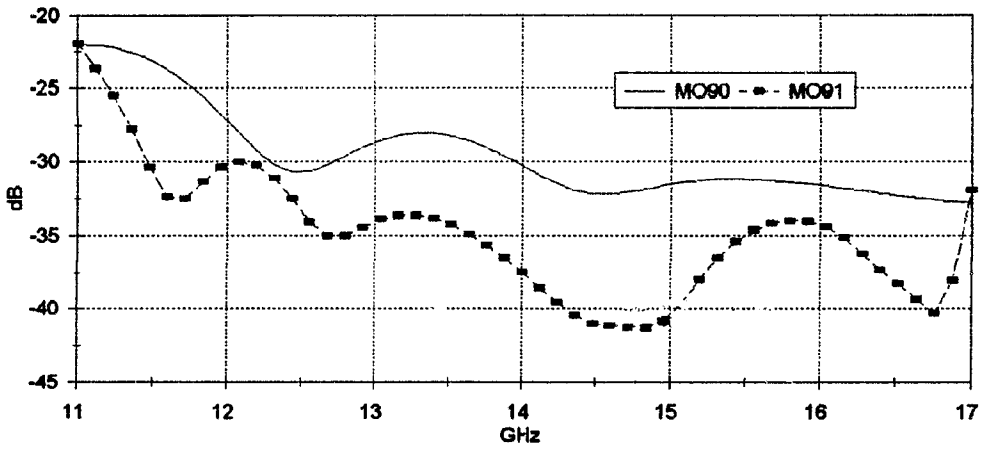

Figure C.4: Reflection coefficients of the Maury Microwave coax to waveguide converters.

C.4 Alpha Industries Series 857 Horn Lens Antennas

The catalogue order description is 857012Ku-1/UG541 (Linear Mode). The conical horn is fed with a rectangular Ku-band waveguide.

The radiation characteristics of the antennas are discussed in detail in Chapter 5. The reflection coefficient of the antennas were measured and are shown in Figure C.5. The measured radiation patterns received from the supplier are shown in Figures C.6 and C.7.

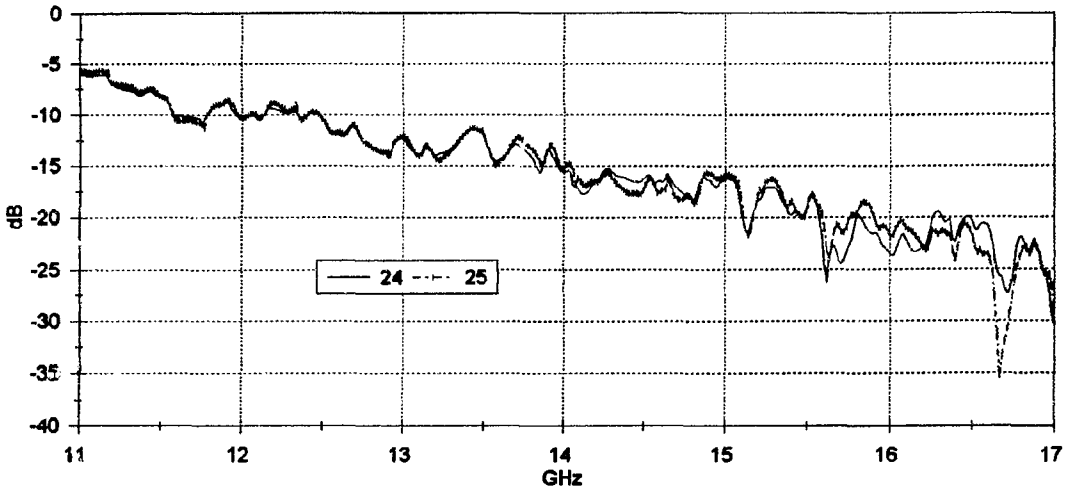

Figure C.5: Reflection coefficients of the two antennas with Maury Microwave coax-to-waveguide converters.

C.5 Alignment of the Antennas

The mechanical configuration of the measurement bench was described in Section 4.2. The bench was designed so that the antennas can be aligned accurately. The alignment was done using the following steps:

1. The lenses of both antennas were taken off.
2. Thin cotton string was then placed over each aperture to form a cross exactly in the middle i.e. on the bore sight axis of each antenna.
3. A thin metal plate, with a small hole in the middle, was placed over the flange of the antenna so that the hole was on the bore sight axis of the antenna.
4. The antennas were then lined up by placing the two crosses and the two holes of the antennas on exactly the same axis along the length of the table.
5. The antennas were then moved along the rails and the previous step repeated at several positions to make sure that the axis of the antennas is parallel to the rails in both the vertical and the horizontal direction.

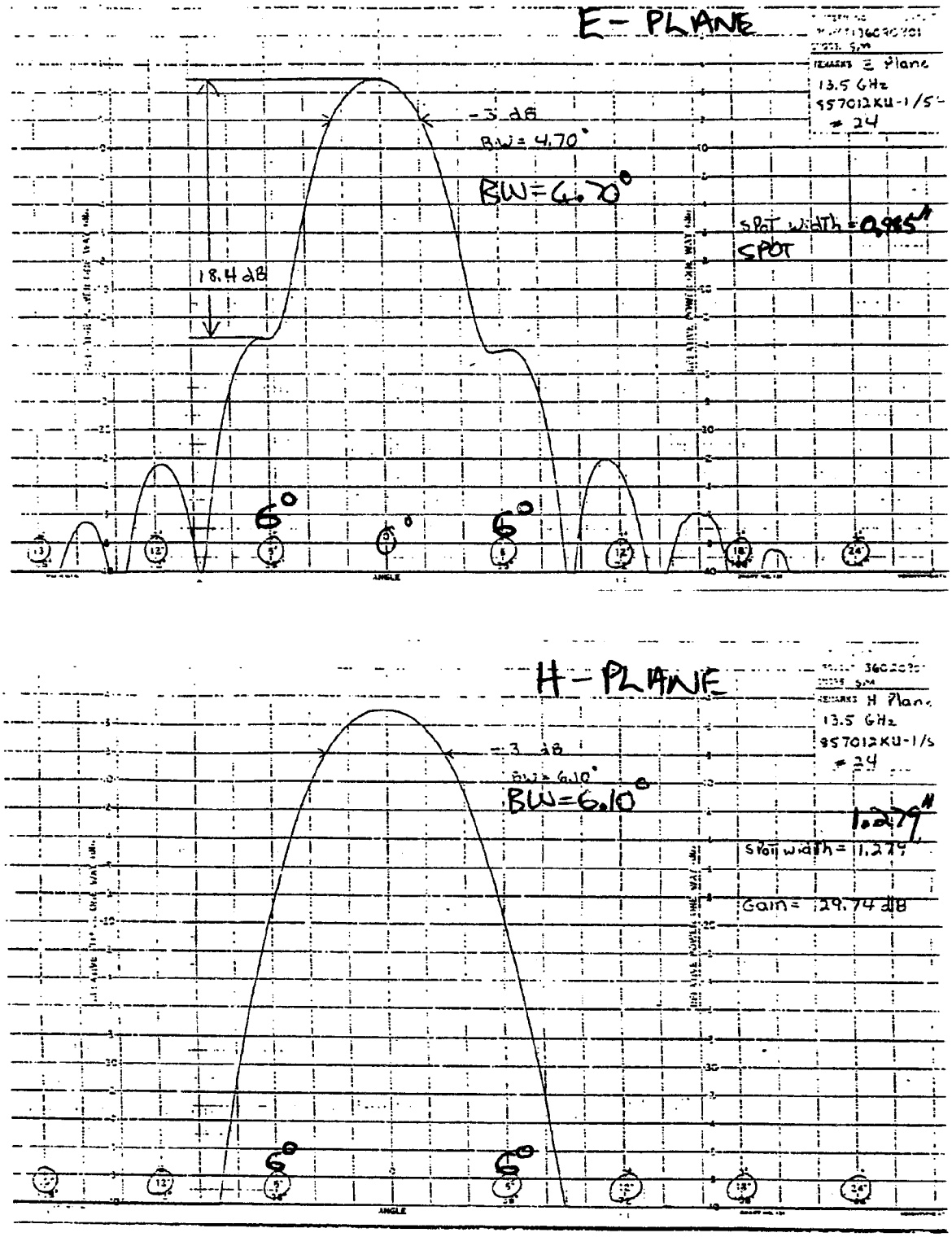

Figure C.6: Measured (by supplier) radiation pattern of antenna no.24: E- and H-plane.

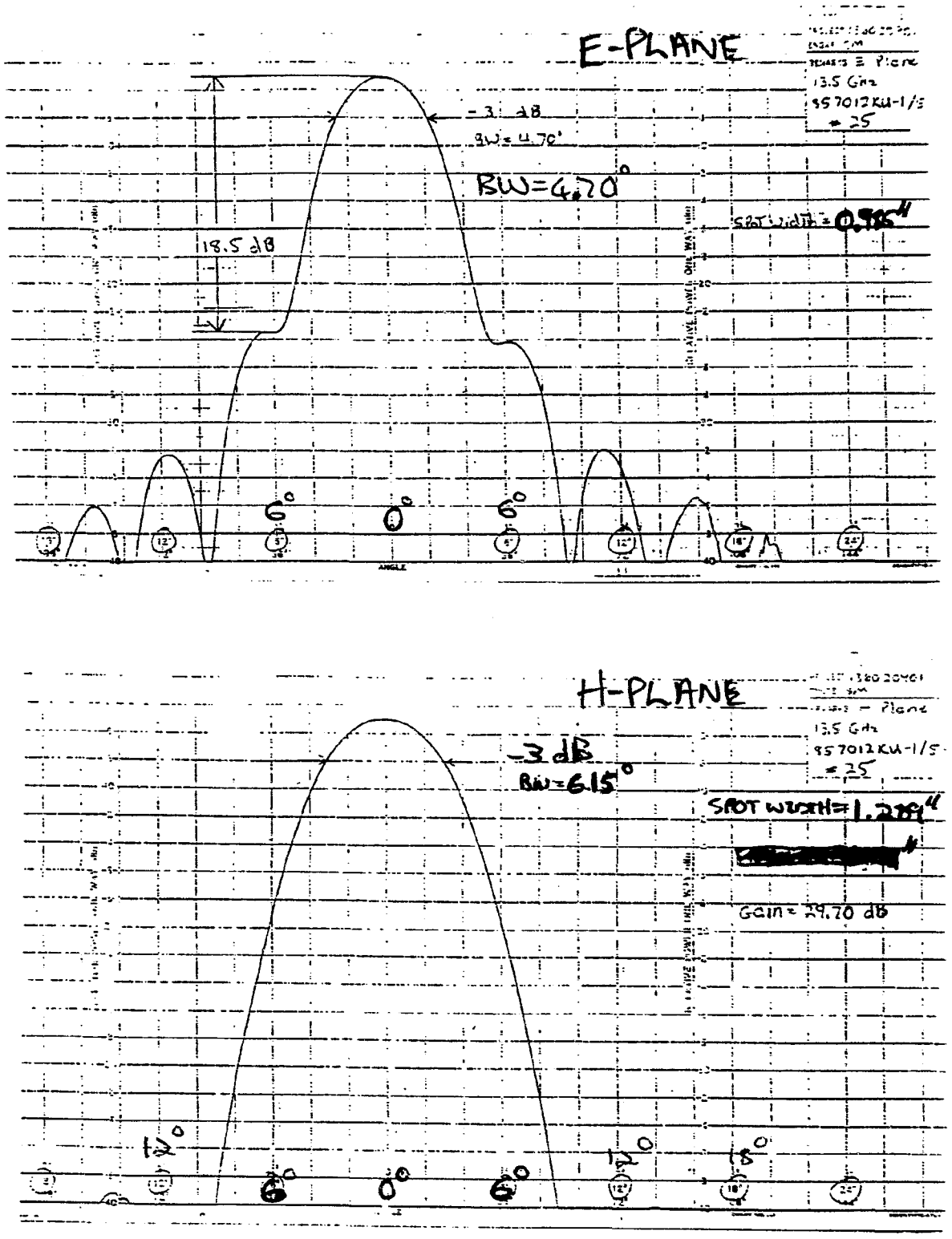

Figure C.7: Measured (by supplier) radiation pattern of antenna no.25: E- and H-plane.

Appendix D

Determining the Calibration Coefficients from the Standard Measurements

The equations used to determine the error coefficients from the measurements of the calibration standards are given below.

The measured reflection coefficient S_{11M} in Figure 6.1 is,

$$S_{11M} = E_{DF} + \frac{S_{11A}E_{RF}}{1 - E_{SF}S_{11A}}. \tag{D.1}$$

Three complex measurements are needed to solve the three error coefficients E_{DF}, E_{SF} and E_{RF}. All measurements of S_{11} during calibration and after calibration are done with microwave absorbing material behind the focal plane of the transmitting antenna, covering the receiving antenna as shown in Figure D.1.

D.1 Load, Short and Offset Short (L2S)

The three standards used are:

Measured S_{11M}	Standard	S_{11A}
M_1	Load	$S_1 = 0$
M_2	Short ($l_2 = 0$)	$S_2 = -1e^0$
M_3	Offset Short ($l_3 = \lambda/4$)	$S_3 = -1e^{i2\beta l_3}$

Inserting the ideal reflection coefficients of the standards (S_1, S_2, S_3) in (D.1) and solving the three resulting equations for the calibration coefficients yields:

$$E_{DF} = M_1, \tag{D.2}$$

$$E_{RF} = \frac{(S_2 - S_3)(M_1 - M_3)(M_1 - M_2)}{S_2S_3(M_3 - M_2)}, \tag{D.3}$$

$$E_{SF} = \frac{S_3(M_2 - M_1) - S_2(M_3 - M_1)}{S_2S_3(M_3 - M_2)}. \quad \text{(D.4)}$$

D.2 Short and Two Offset Short (3S)

The three standards used are:

Measured S_{11M}	Standard	S_{11A}
M_1	Short ($l_1 = 0$)	$S_1 = -1e^0$
M_2	Offset Short ($l_2 = \lambda/6$)	$S_2 = -1e^{i2\beta l_2}$
M_3	Offset Short ($l_3 = 2\lambda/6$)	$S_3 = -1e^{i2\beta l_3}$

Inserting the ideal reflection coefficients of the standards (S_1, S_2, S_3) in (D.1) and solving the three resulting equations for the calibration coefficients yields:

$$E_{RF} = \frac{(M_2 - M_1)(M_3 - M_1)(M_3 - M_2)(S_2 - S_1)(S_3 - S_1)(S_3 - S_2)}{[S_1S_2(M_2 - M_1) + S_1S_3(M_1 - M_3) + S_2S_3(M_3 - M_2)]^2}, \quad \text{(D.5)}$$

$$E_{SF} = \frac{S_1(M_2 - M_3) + S_2(M_3 - M_1) + S_3(M_1 - M_2)}{[S_1S_2(M_2 - M_1) + S_1S_3(M_1 - M_3) + S_2S_3(M_3 - M_2)]}, \quad \text{(D.6)}$$

$$E_{DF} = M_1 - \frac{S_1E_{RF}}{1 - E_{SF}S_1}. \quad \text{(D.7)}$$

D.3 Free-Space Calibration

Because of dispersion in the focal region of the lens antennas, the wavelength in the equations above should be the elongated wavelength, $\lambda = \Lambda\lambda_0$, with Λ a frequency independent dispersion factor.

Initially it was believed that the dispersion factor is $\Lambda = 1.0275$ (7C-Gated) in Figure 5.16 and all the calibrations in the thesis were done with this value. However it was later decided (Section 5.4) that the value as obtained after free-space calibration and time domain gating (FS-Gated) in Figure 5.16, $\Lambda = 1.045$ is more accurate.

The time delay for the offset standards are specified as,

$$t_d = l/\nu, \quad \text{(D.8)}$$

with $\nu = \Lambda c$ the propagation velocity of the wave in the focal region and l the separation between the offset standard and the calibration plane.

The offset delay times for the offset shorts are summarized in Table D.1.

Calibration	Standard	Offset Length mm	Delay Time ps
L2S	Offset Short ($l_3 = \lambda/4$)	5.7	18.504089
3S	Offset Short ($l_2 = \lambda/6$)	3.8	12.336059
3S	Offset Short ($l_3 = 2\lambda/6$)	7.6	24.672119
3C	Offset Short ($l_1 = -\lambda/6$)	-3.8	-12.336059
3C	Offset Short ($l_3 = +\lambda/6$)	+3.8	+12.336059

Table D.1: Specified time delay for the offset calibration standards. With $\lambda = \Lambda\lambda_0$, the wavelength in the focal region. For all the measurements reported in this thesis $\Lambda = 1.0275$ was used.

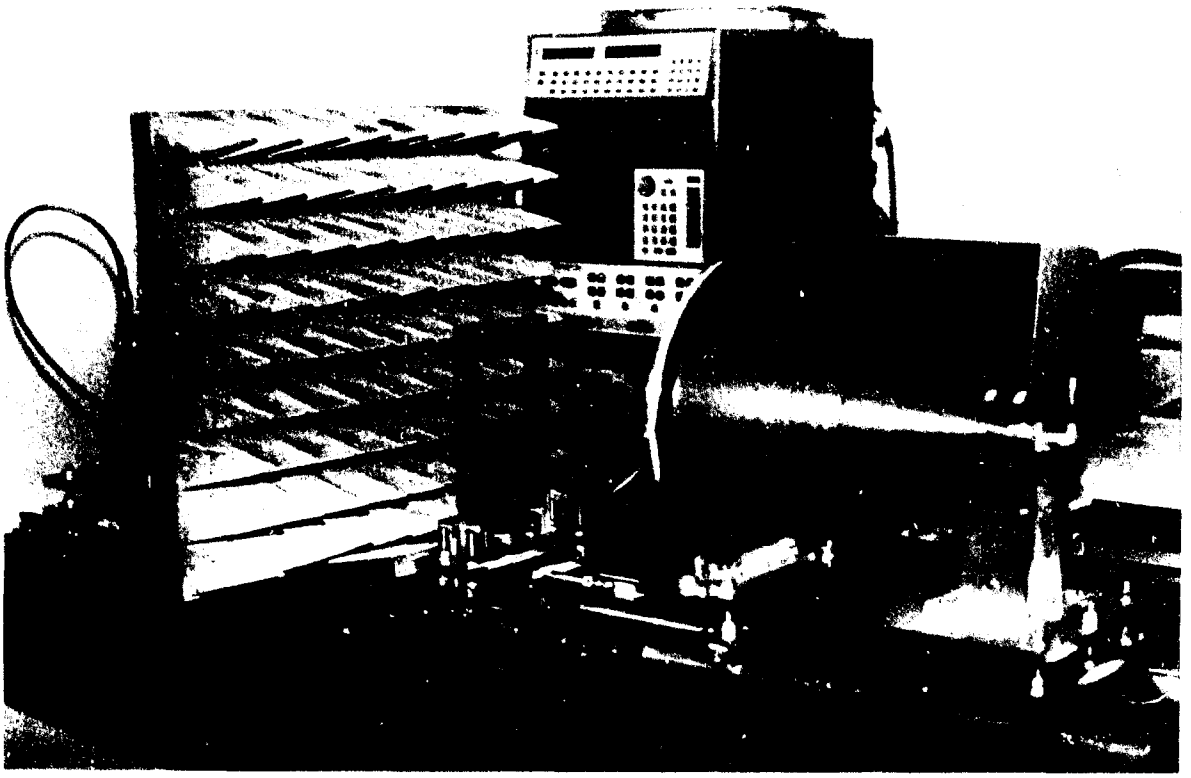

Load standard: $S_{11A} = 0$

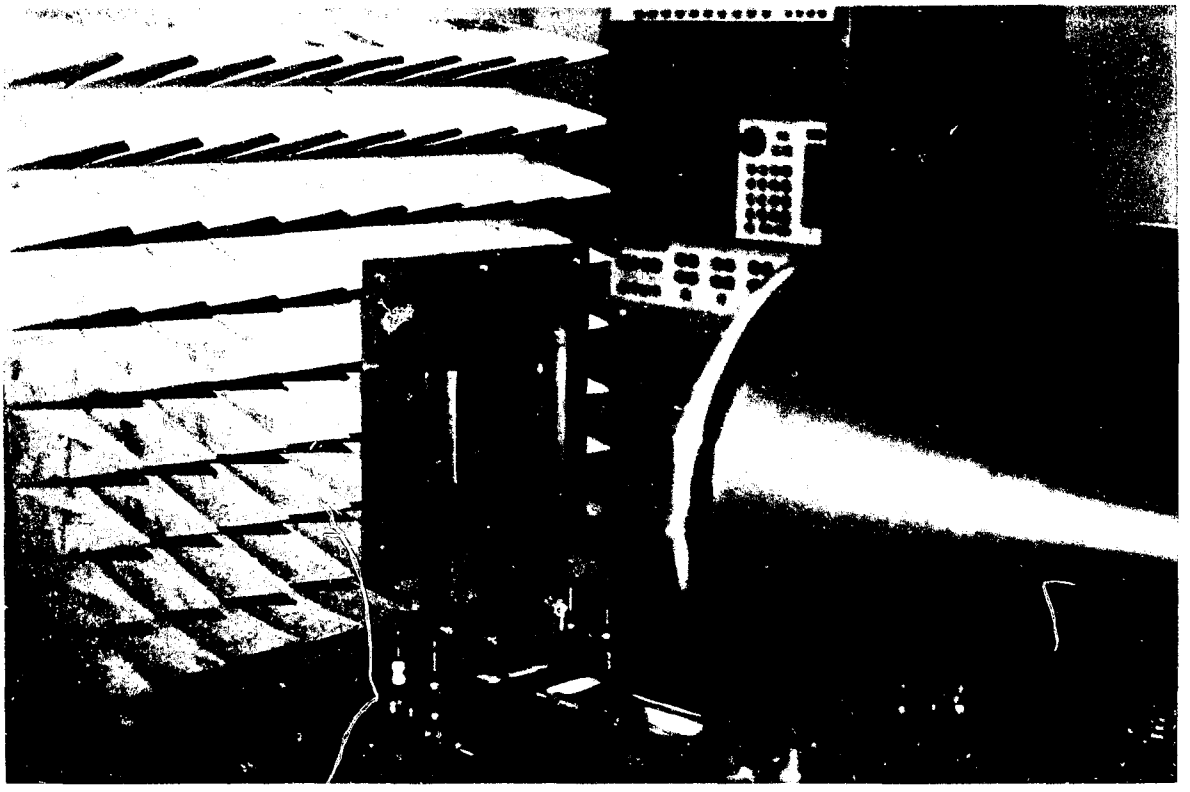

Short standard: $S_{11A} = -1e^{jk(2z)}$

Figure D.1: Configuration for the Load and the Short standard measurements.

Appendix E

Partial Differential Equations of Complex Parameters

The determination of the partial differentials $\frac{\partial \nu'}{\partial |S|}$ and $\frac{\partial \nu'}{\partial \angle S}$ from $\frac{\partial \nu}{\partial S}$, assuming that $\nu = \nu' + i\nu''$ is a complex, analytic function of $S = |S|e^{i\angle S}$.

To get $\frac{\partial \nu'}{\partial |S|}$ from $\frac{\partial \nu}{\partial S}$:

$$\begin{aligned} \frac{\partial \nu'}{\partial |S|} &= \mathrm{Re}\left(\frac{\partial \nu}{\partial |S|}\right) \\ &= \mathrm{Re}\left(\frac{\partial \nu}{\partial S}\,\frac{\partial S}{\partial |S|}\right) \end{aligned} \tag{E.1}$$

and with

$$\begin{aligned} \frac{\partial S}{\partial |S|} &= \frac{\partial |S| e^{i\angle S}}{\partial |S|} \\ &= e^{i\angle S} \end{aligned} \tag{E.2}$$

follows,

$$\frac{\partial \nu'}{\partial |S|} = \mathrm{Re}\left(\frac{\partial \nu}{\partial S} e^{i\angle S}\right). \tag{E.3}$$

The same rule applies for the imaginary part, with Im instead of Re in the equation above.

To get $\frac{\partial \nu'}{\partial \angle S}$ from $\frac{\partial \nu}{\partial S}$:

$$\begin{aligned} \frac{\partial \nu'}{\partial \angle S} &= \mathrm{Re}\left(\frac{\partial \nu}{\partial \angle S}\right) \\ &= \mathrm{Re}\left(\frac{\partial \nu}{\partial S}\,\frac{\partial S}{\partial \angle S}\right) \end{aligned} \tag{E.4}$$

and with

$$\begin{aligned} \frac{\partial S}{\partial \angle S} &= \frac{\partial |S| e^{i\angle S}}{\partial \angle S} \\ &= iS \end{aligned} \tag{E.5}$$

follows,

$$\frac{\partial \nu'}{\partial \angle S} = \mathrm{Re}\left(\frac{\partial \nu}{\partial S}\ iS\right). \tag{E.6}$$

The same rule applies for the imaginary part, with Im instead of Re in the equation above.

These results are in agreement with the formally derived expressions for the derivative of an analytic complex function in terms of the partial derivatives of its real and imaginary parts with respect to polar coordinates [118, Eqns.(2) and (4), p.48]

Appendix F

Measured Results

The measured results are presented in the following order:

Section	Helix	Name	Description	Thickness (mm)
F.1.1	**Blank Host**	PU	Polyurethane	7.03
F.1.2		QS	Quartz-Silicone	7.07
F.1.3		S	Silicone	7.0
F.2.1	**Nickel Chrome**	50LH-PU	50/cc LH in PU	6.64
F.2.2		50LH-QS	50/cc LH in QS	6.88
F.2.3		50RAC-QS	(25LH and 25RH)/cc in QS	6.88
F.2.4		100RH-QS	100/cc RH in QS	6.9
F.2.5		220RH-S	220/cc RH in S	6.7
F.3.1	**Tungsten**	Tu-LD	Polyurethane, Low density	6.6
F.3.2		Tu-HD	Paraffin Wax, High density	8.3

The constitutive parameters are in the Post-Jaggard formalism. (See Appendix A.) The measured values for permittivity ($\epsilon = \epsilon_r\epsilon_0$) and permeability ($\mu = \mu_r\mu_0$) are presented in their normalized form (ϵ_r and μ_r). The chirality parameter ξ is not normalized. The definitions "rotation" and "ellipticity" of the polarization ellipse are defined in Appendix G.

RAC is the abbreviation used to describe racemic media, i.e. media in which the left-handed and right-handed helices are mixed and of the same concentration in the sample.

F.1 Host Media

F.1.1 Polyurethane (PU)

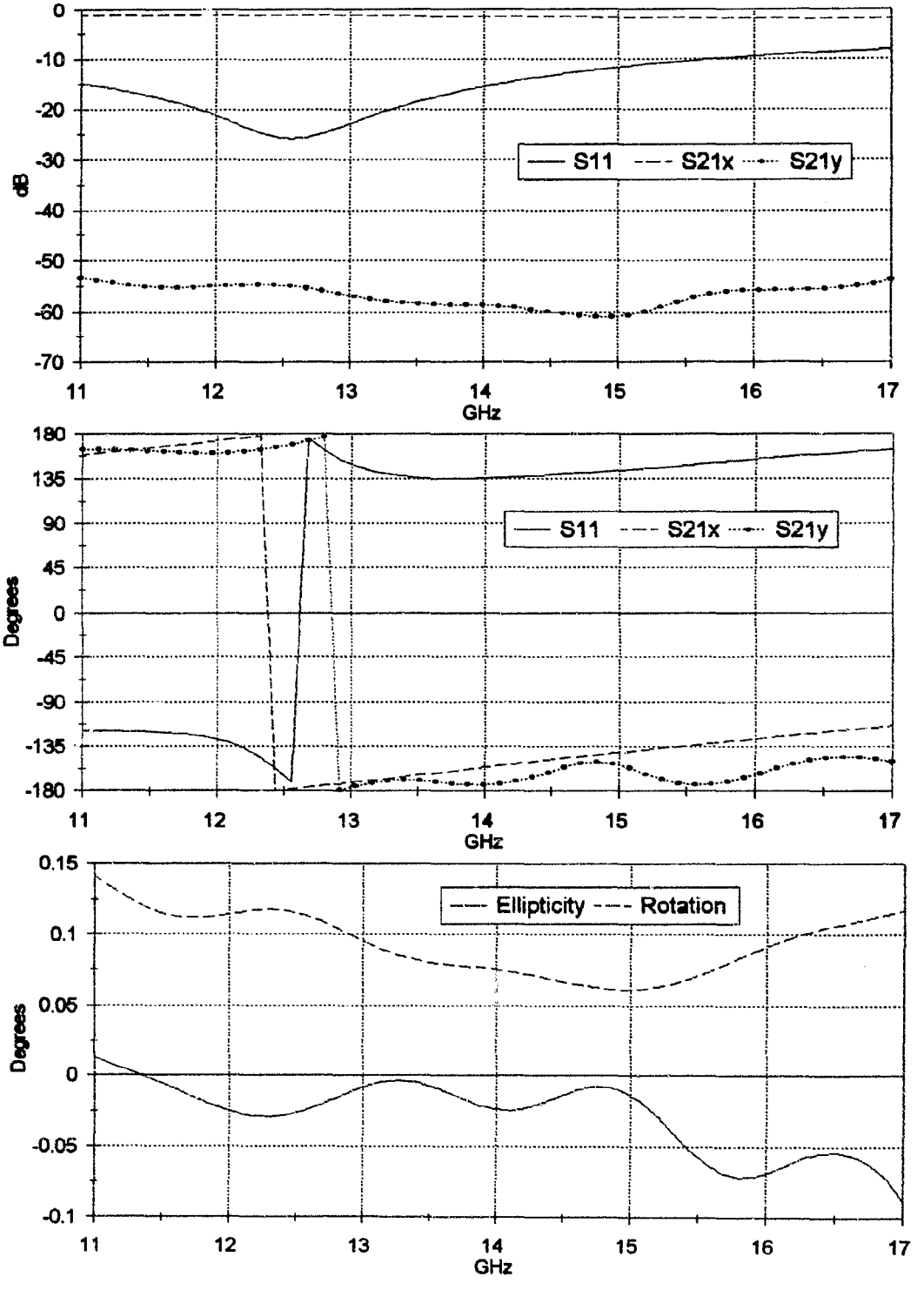

Figure F.1: PU: S-Parameters and polarization ellipse.

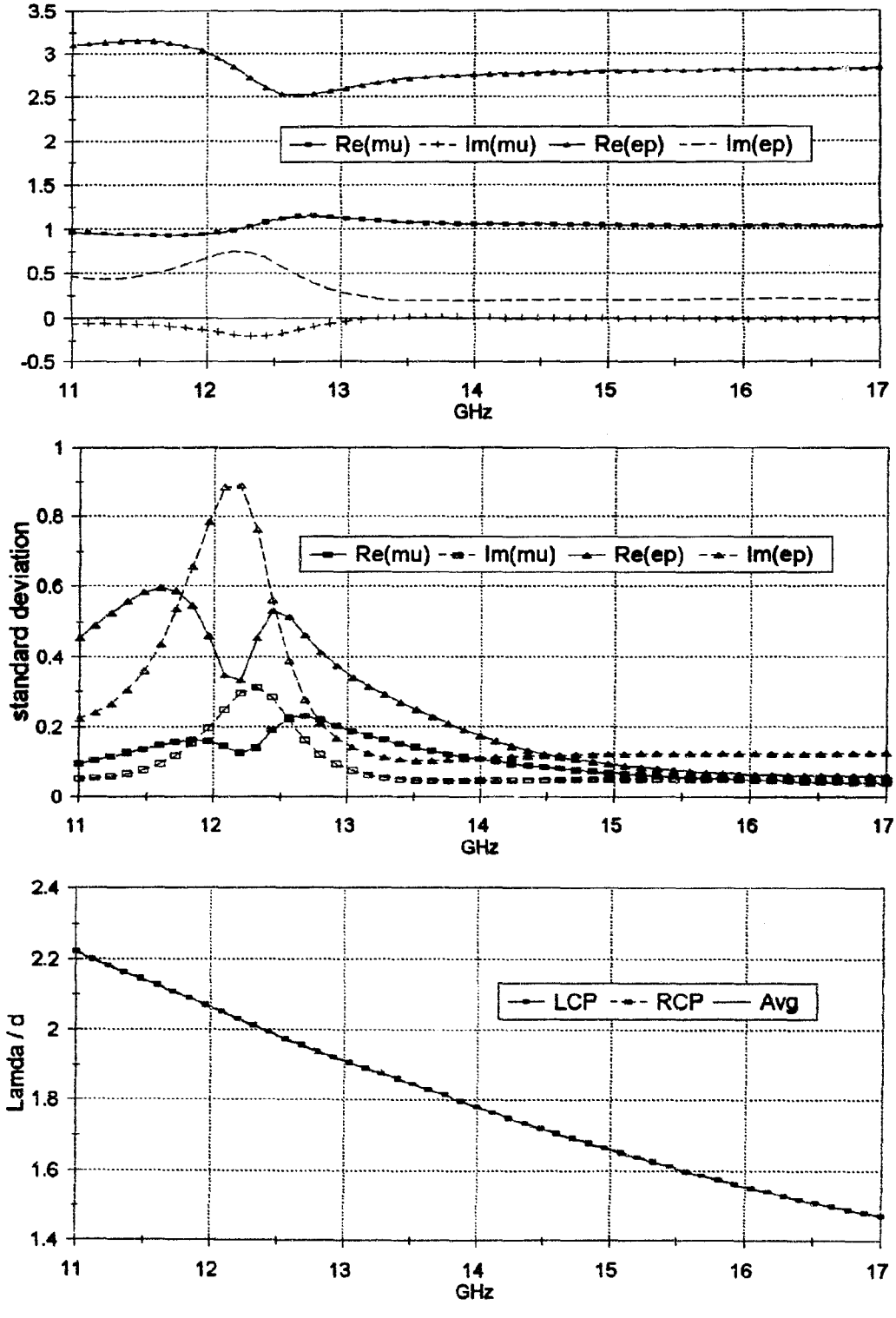

Figure F.2: PU: Constitutive parameters (μ, ϵ), standard deviation and wavelength.

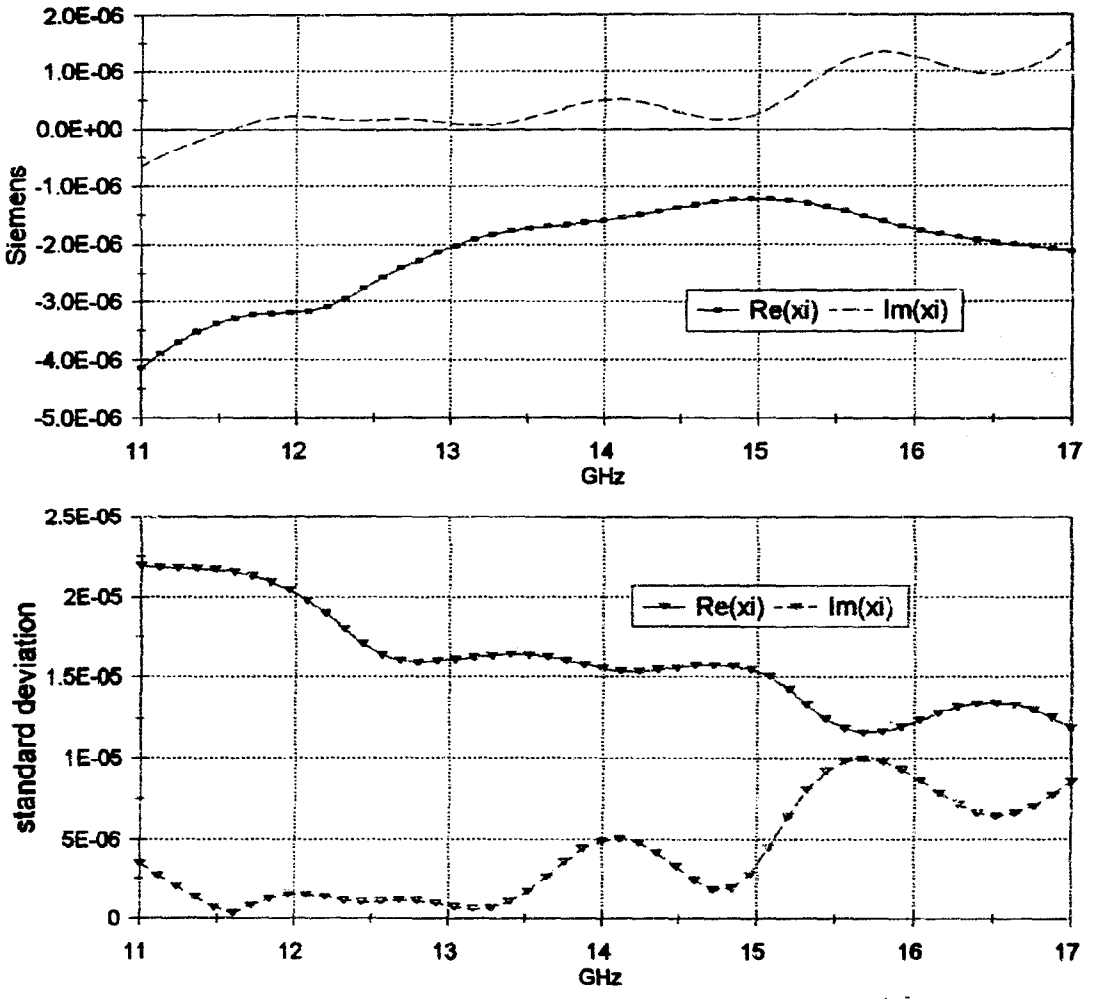

Figure F.3: PU: Chirality parameter and its standard deviation.

F.1.2 Quartz-Silicone (QS)

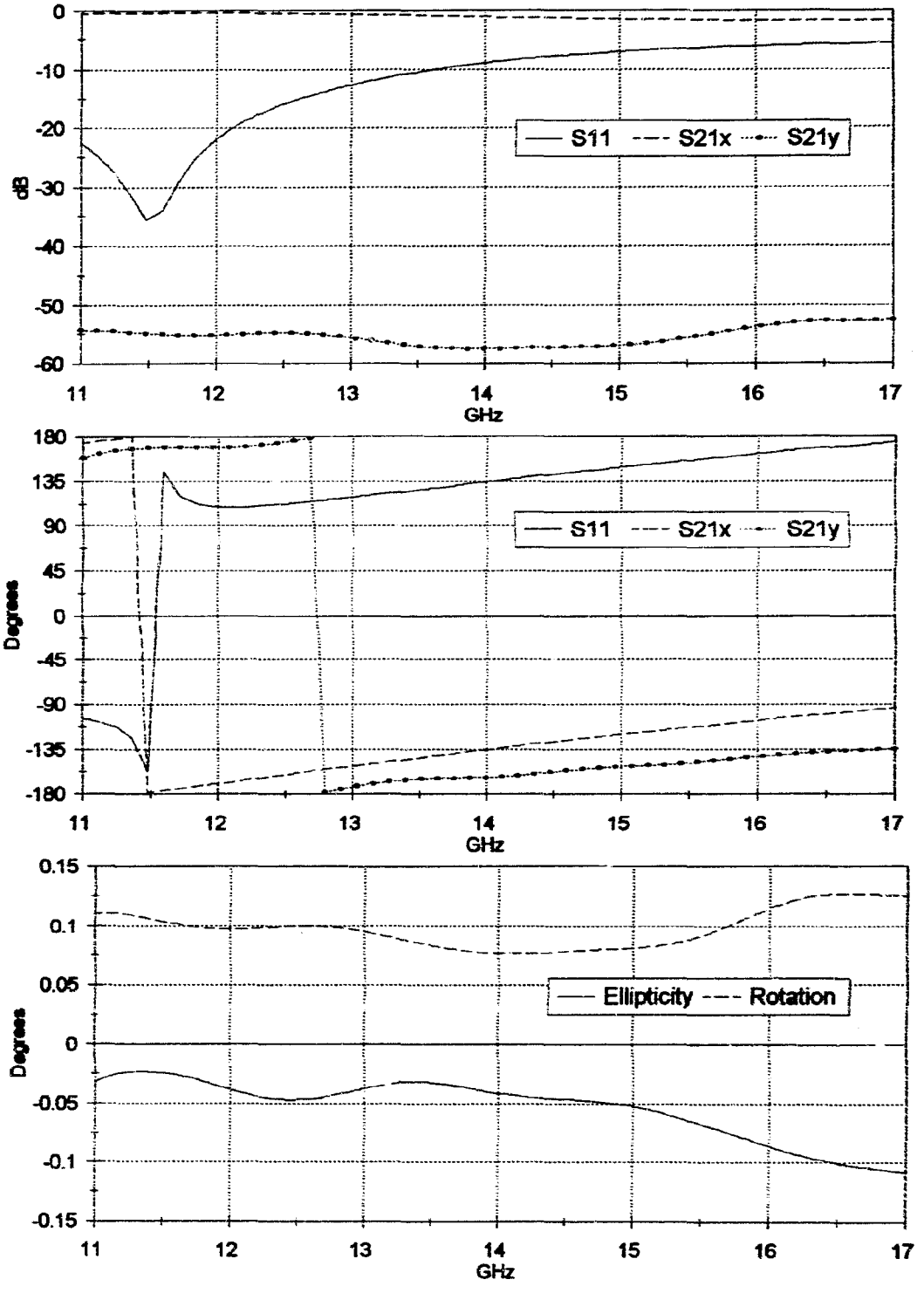

Figure F.4: QS: S-Parameters and polarization ellipse.

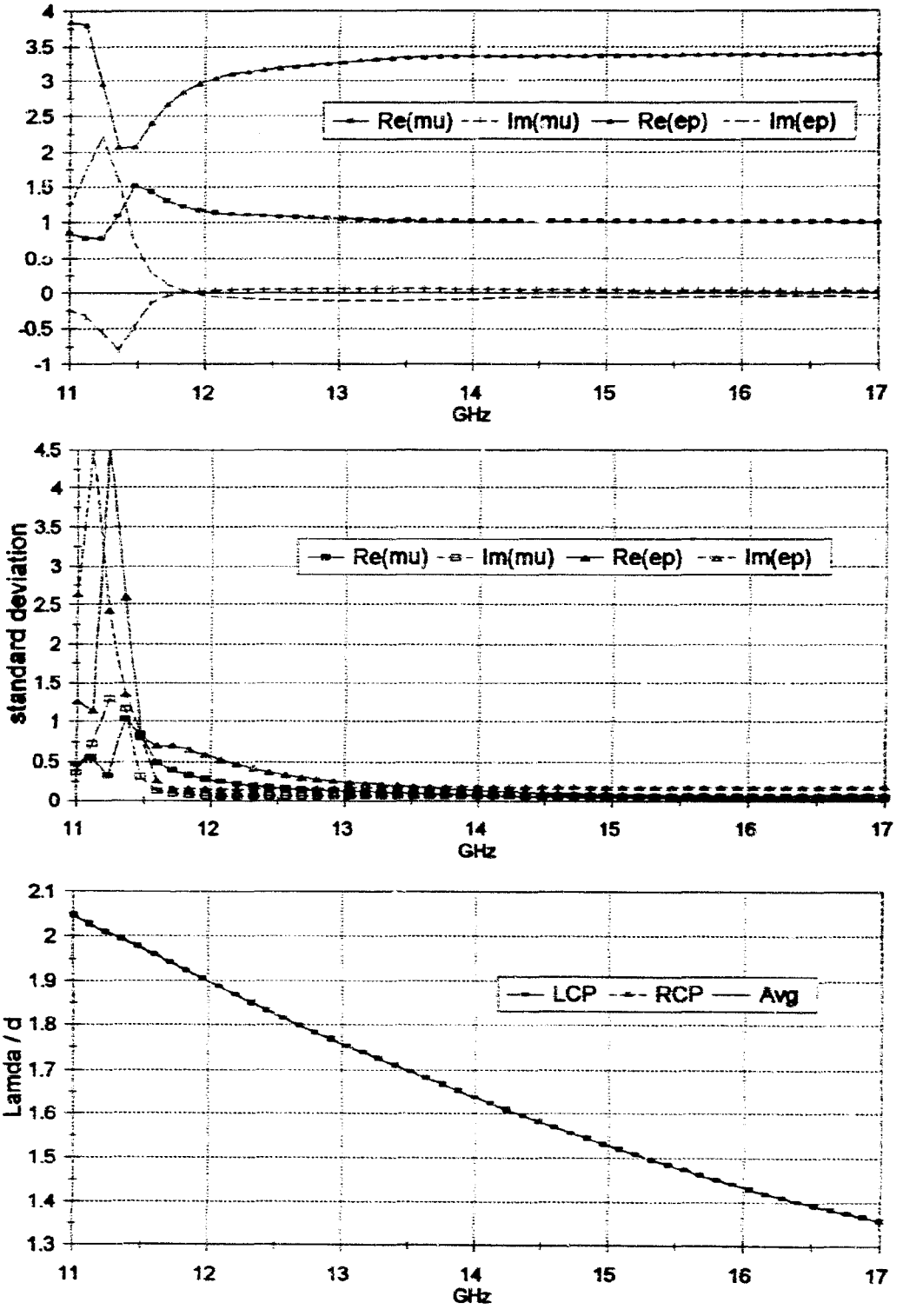

Figure F.5: QS: Constitutive parameters (μ, ϵ), standard deviation and wavelength.

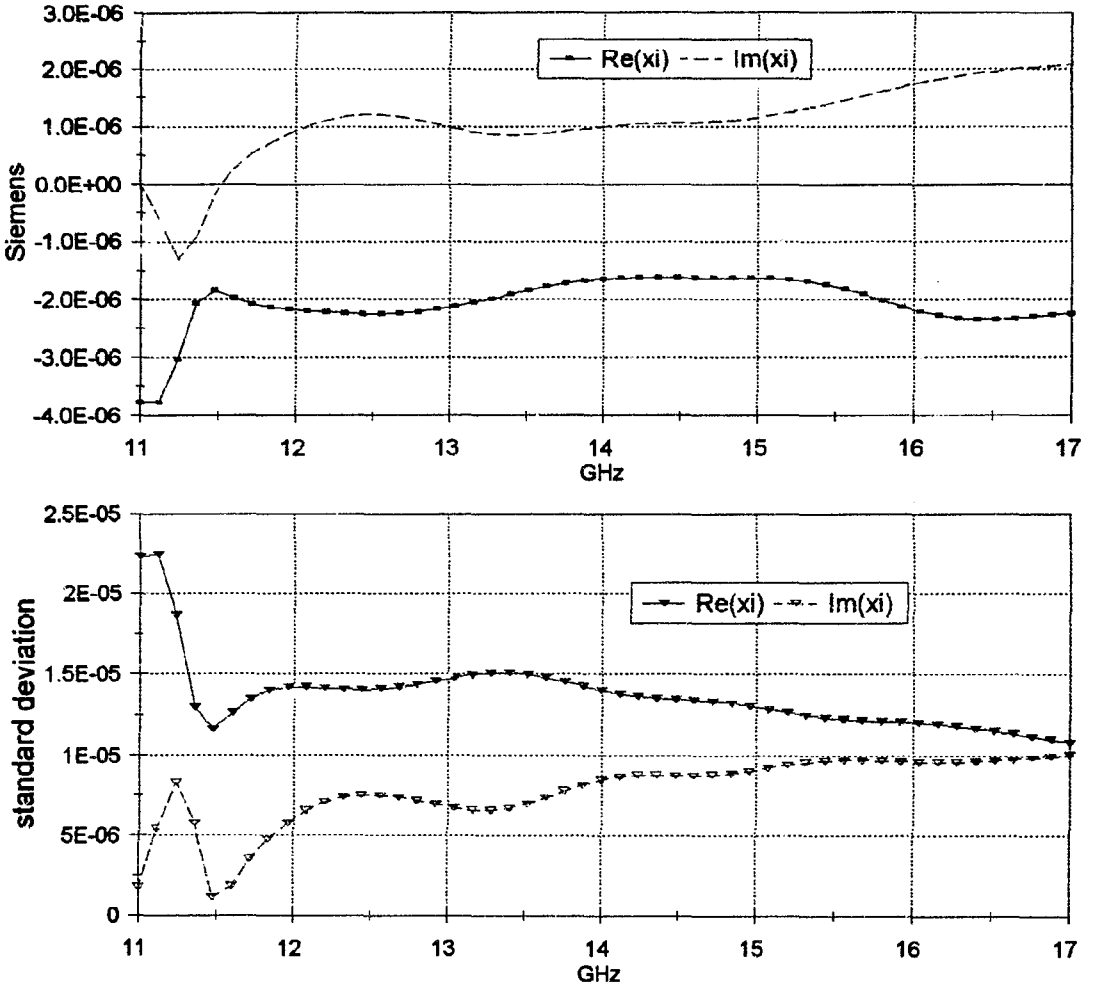

Figure F.6: QS: Chirality parameter and its standard deviation.

F.1.3 Silicone (S)

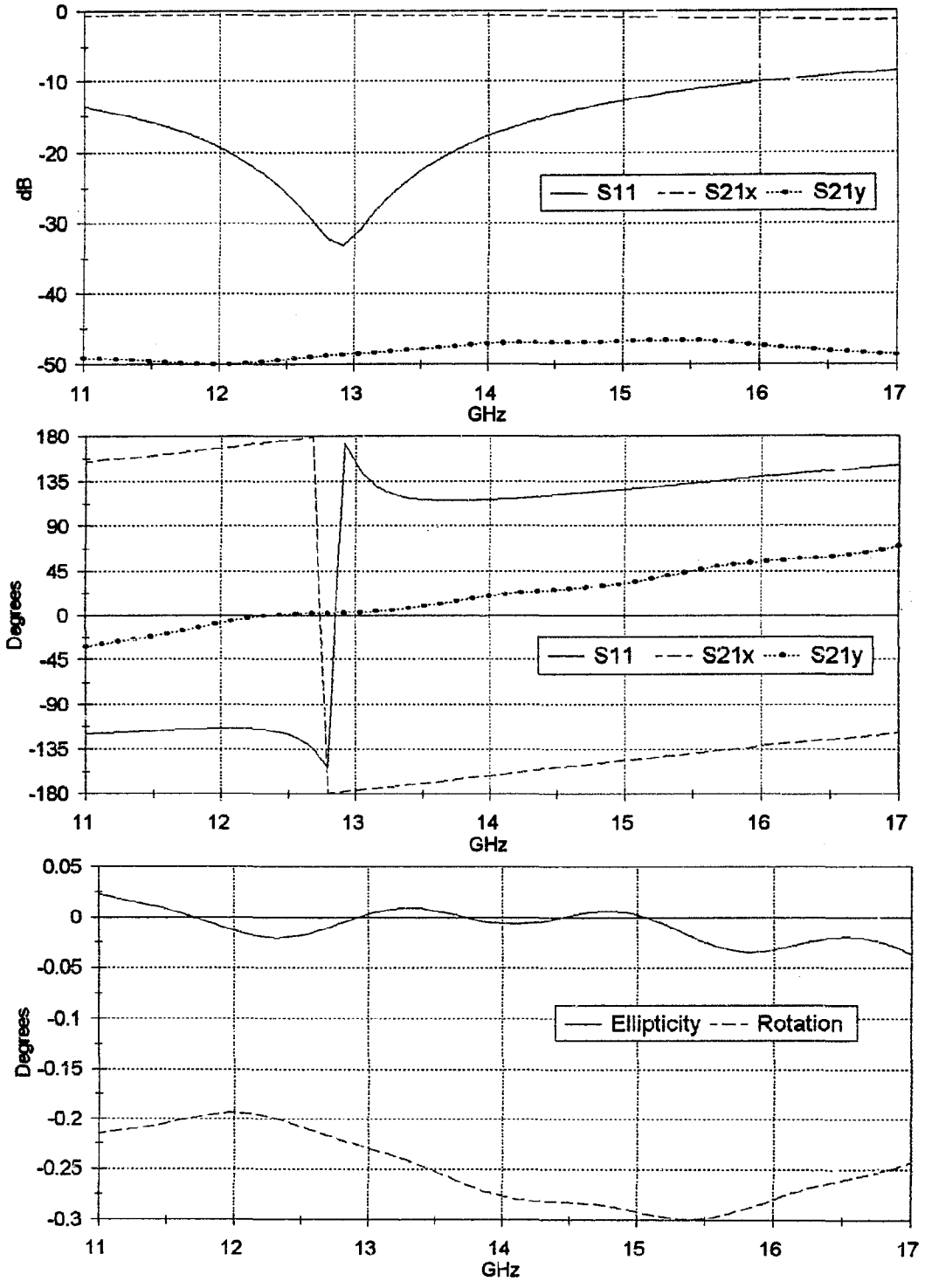

Figure F.7: S: S-Parameters and polarization ellipse.

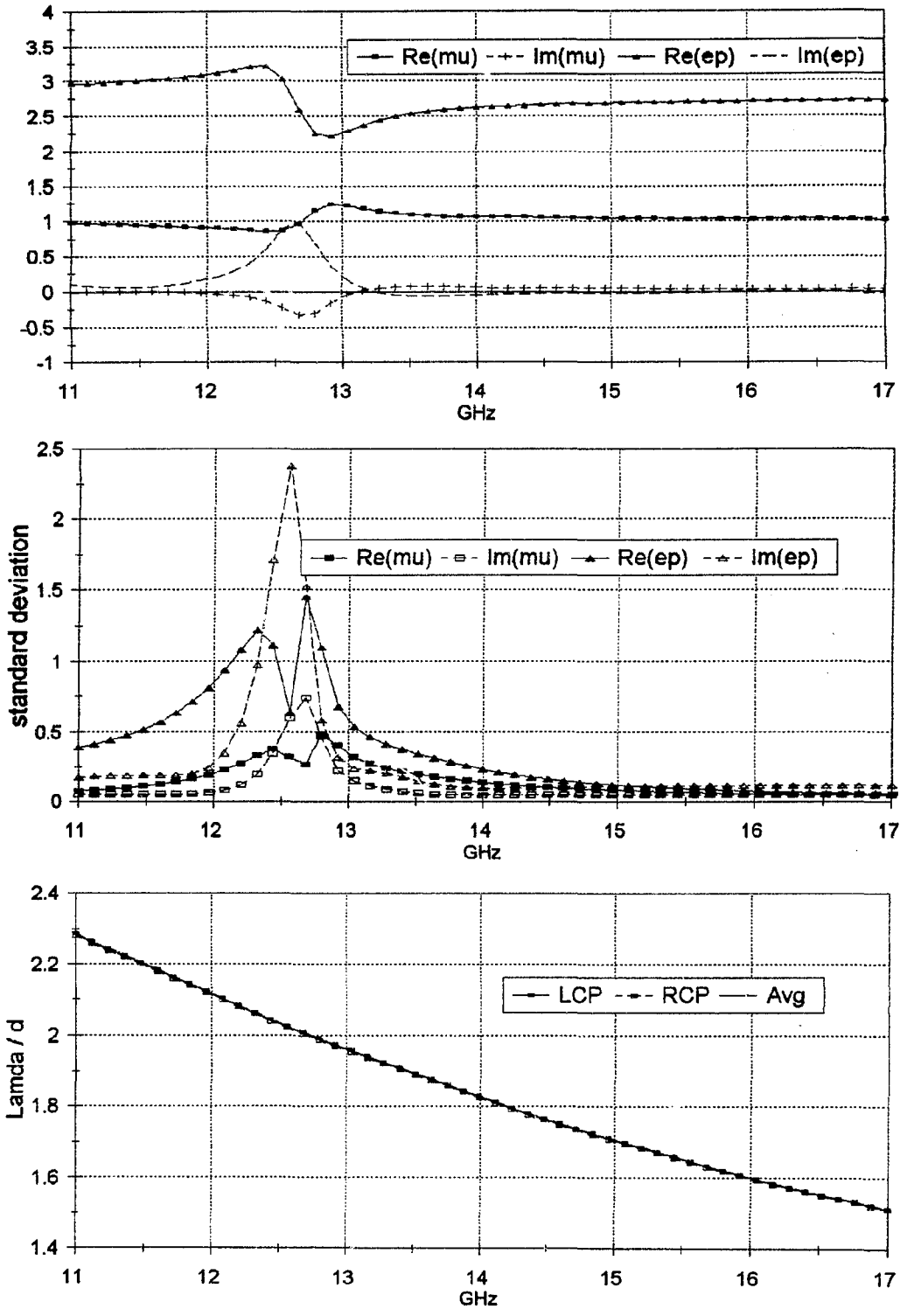

Figure F.8: S: Constitutive parameters (μ, ϵ), standard deviation and wavelength.

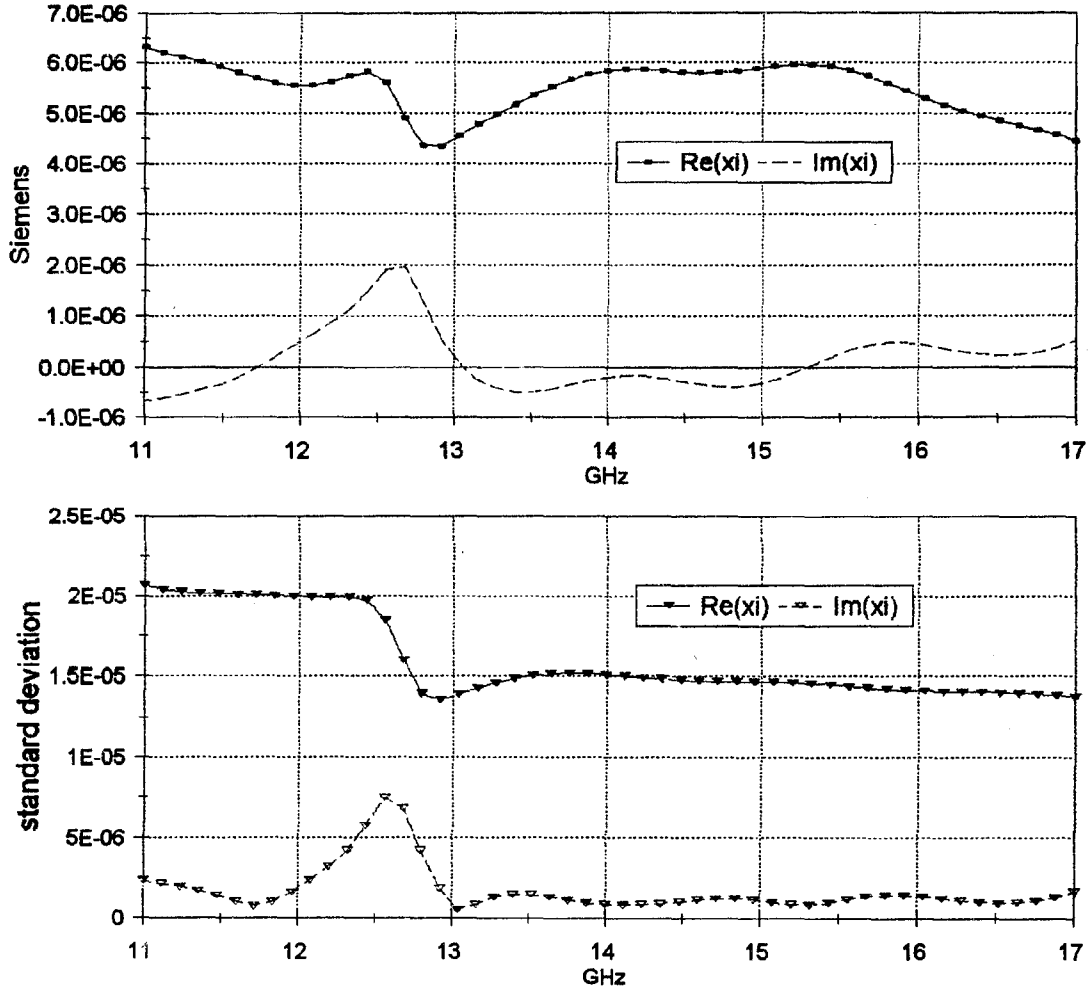

Figure F.9: S: Chirality parameter and its standard deviation.

F.2 Nickel-Chrome

F.2.1 50LH-PU: 50LH/cc in Polyurethane

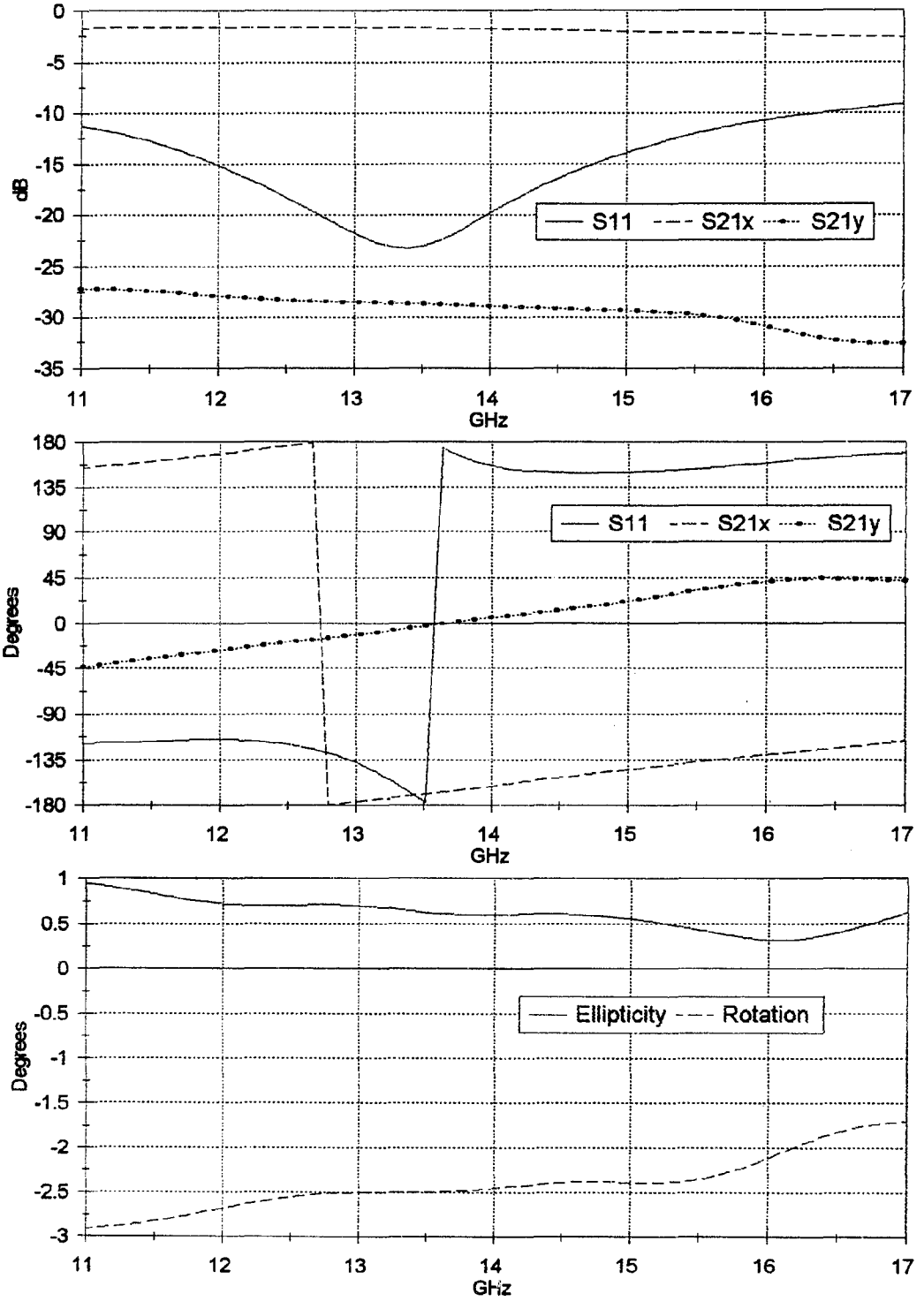

Figure F.10: 50LH-PU: S-Parameters and polarization ellipse.

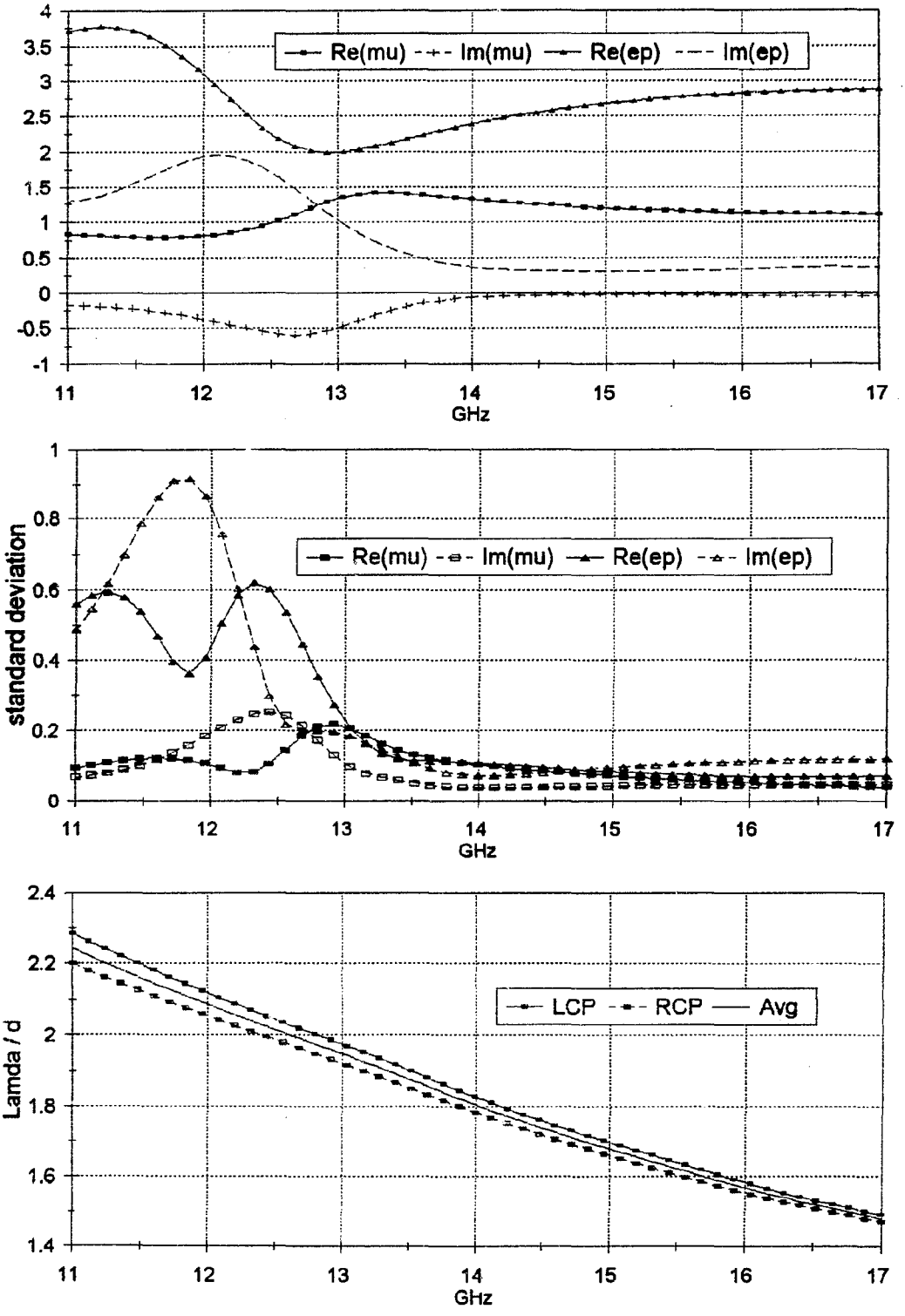

Figure F.11: 50LH-PU: Constitutive parameters (μ, ϵ), standard deviation and wavelength.

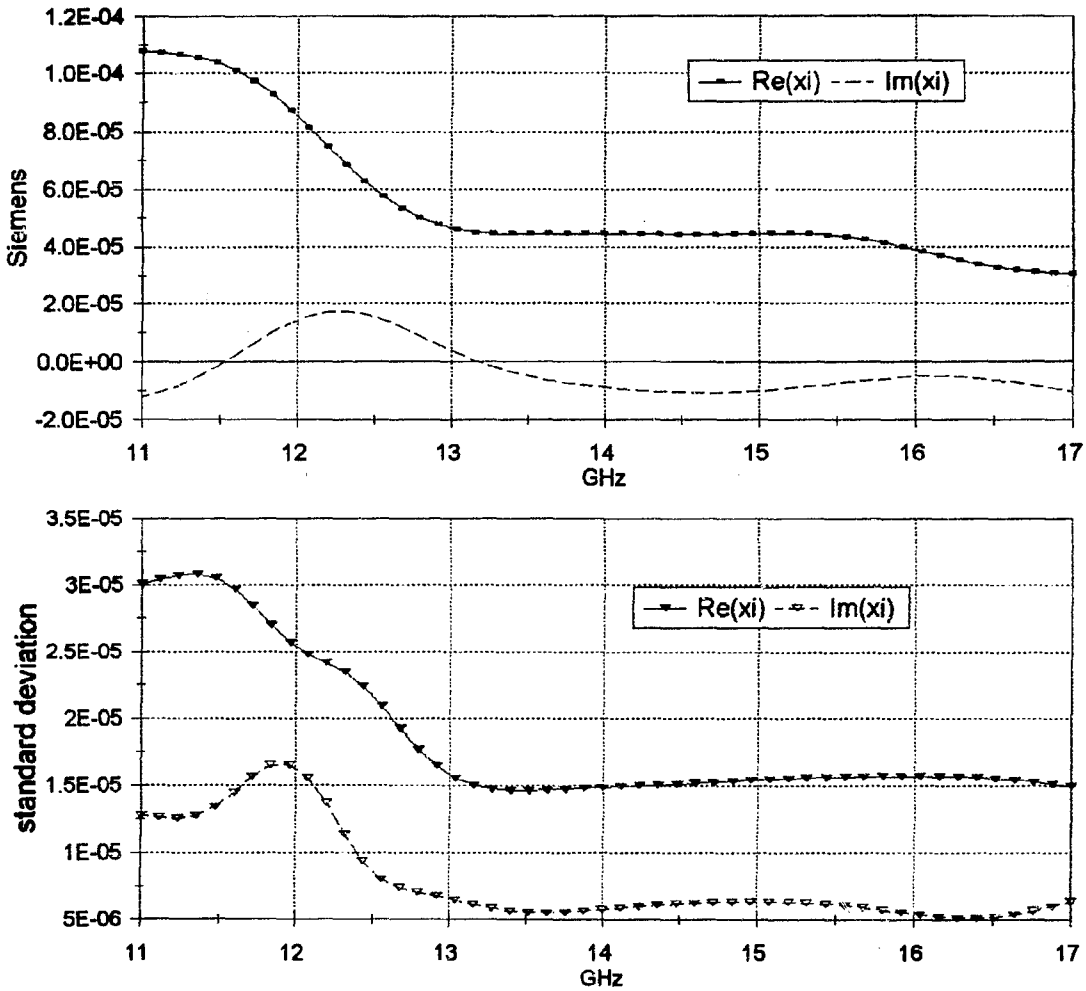

Figure F.12: 50LH-PU: Chirality parameter and its standard deviation.

F.2.2 50LH-QS: 50LH/cc in Quartz-Silicone

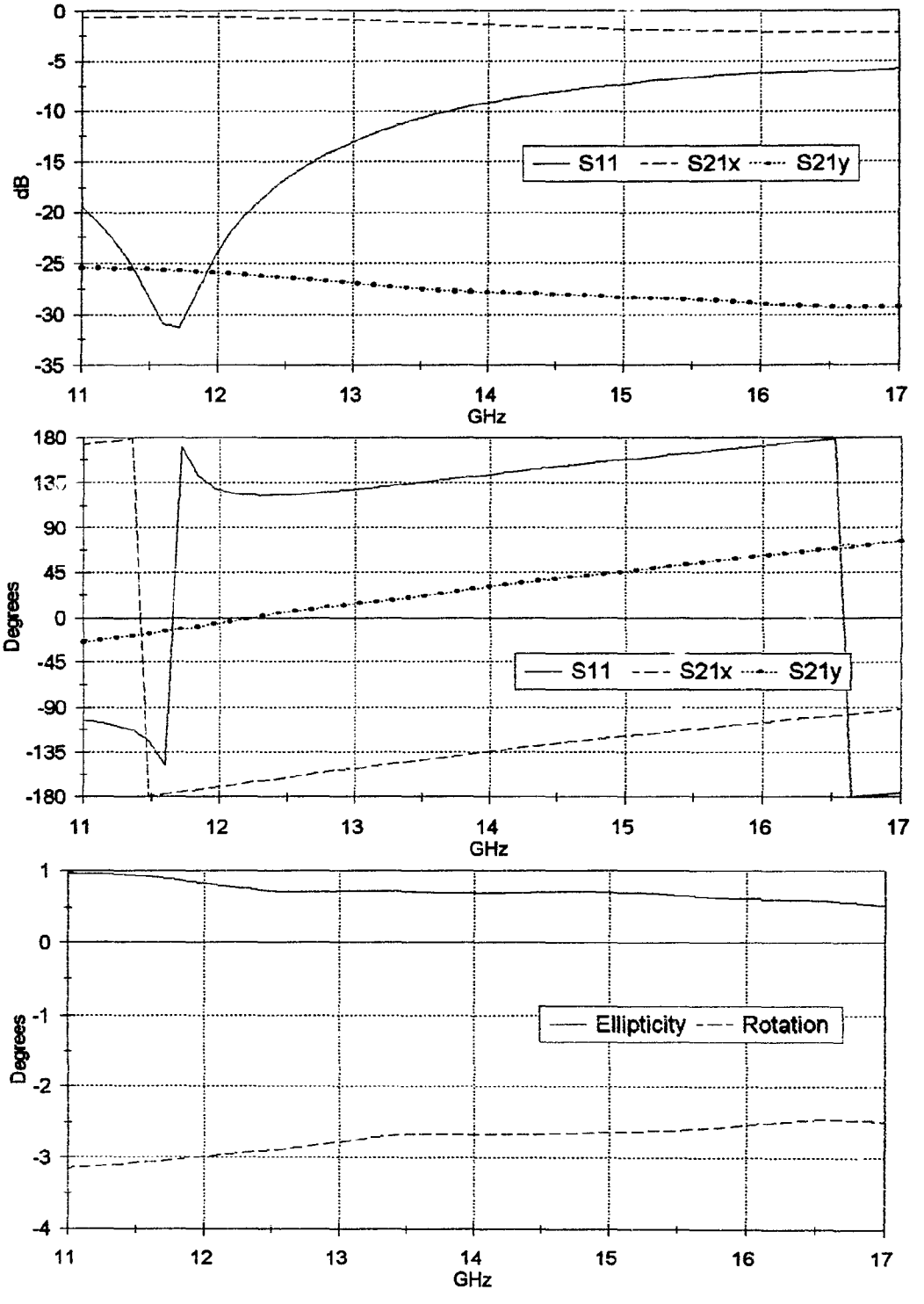

Figure F.13: 50LH-QS: S-Parameters and polarization ellipse.

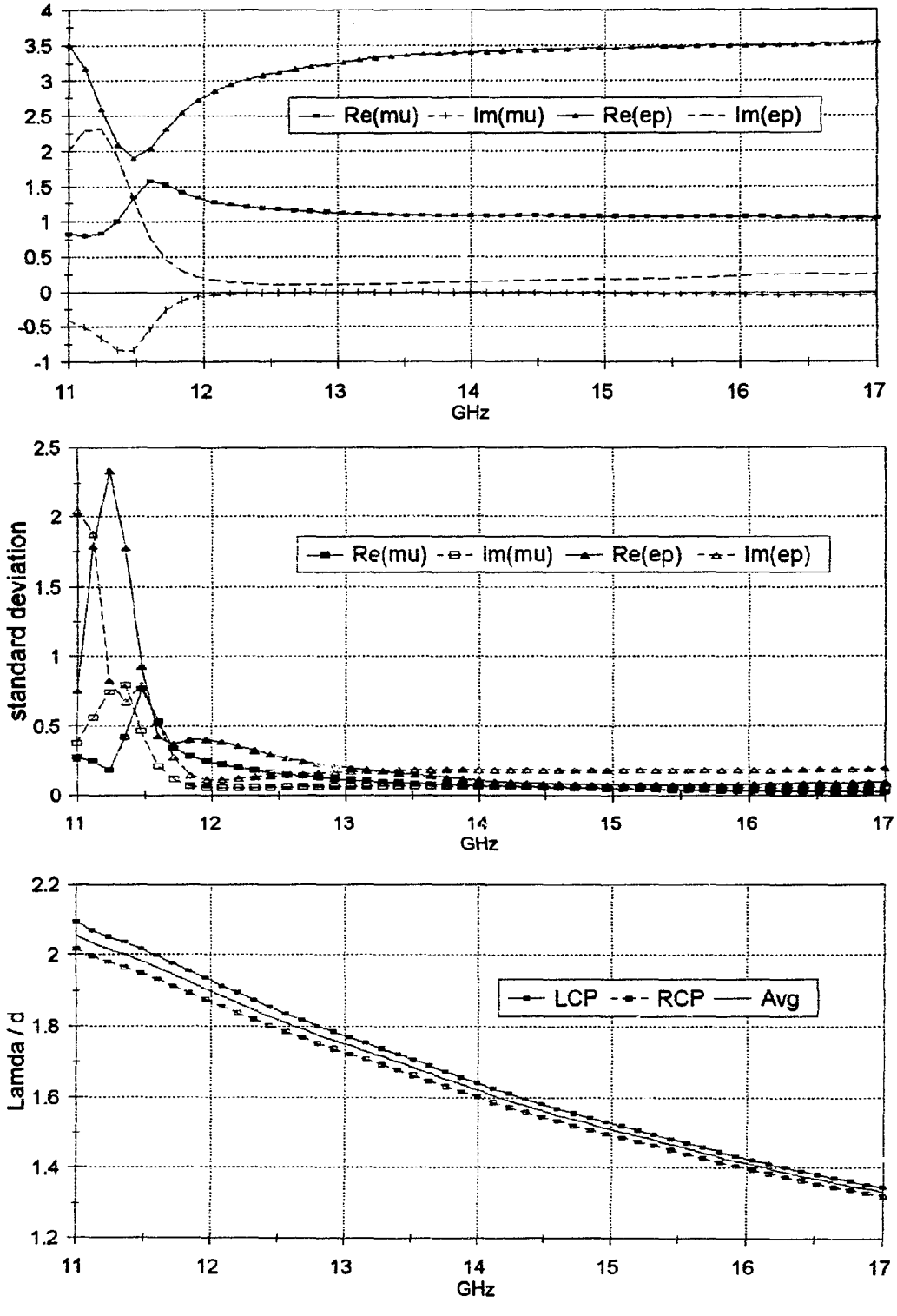

Figure F.14: 50LH-QS: Constitutive parameters (μ, ϵ), standard deviation and wavelength.

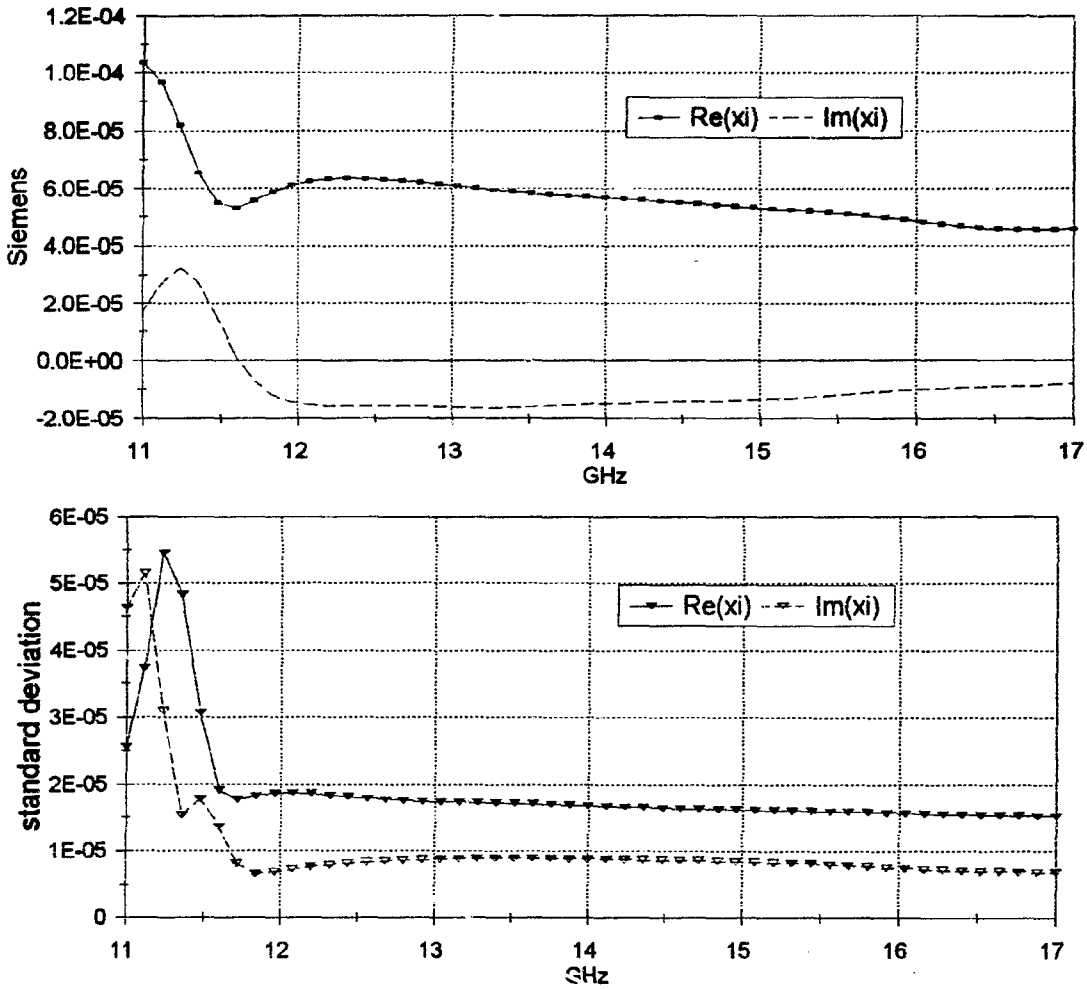

Figure F.15: 50LH-QS: Chirality parameter and its standard deviation.

F.2.3 50RAC-QS: Racemic (25LH and 25RH)/cc in Quartz-Silicone

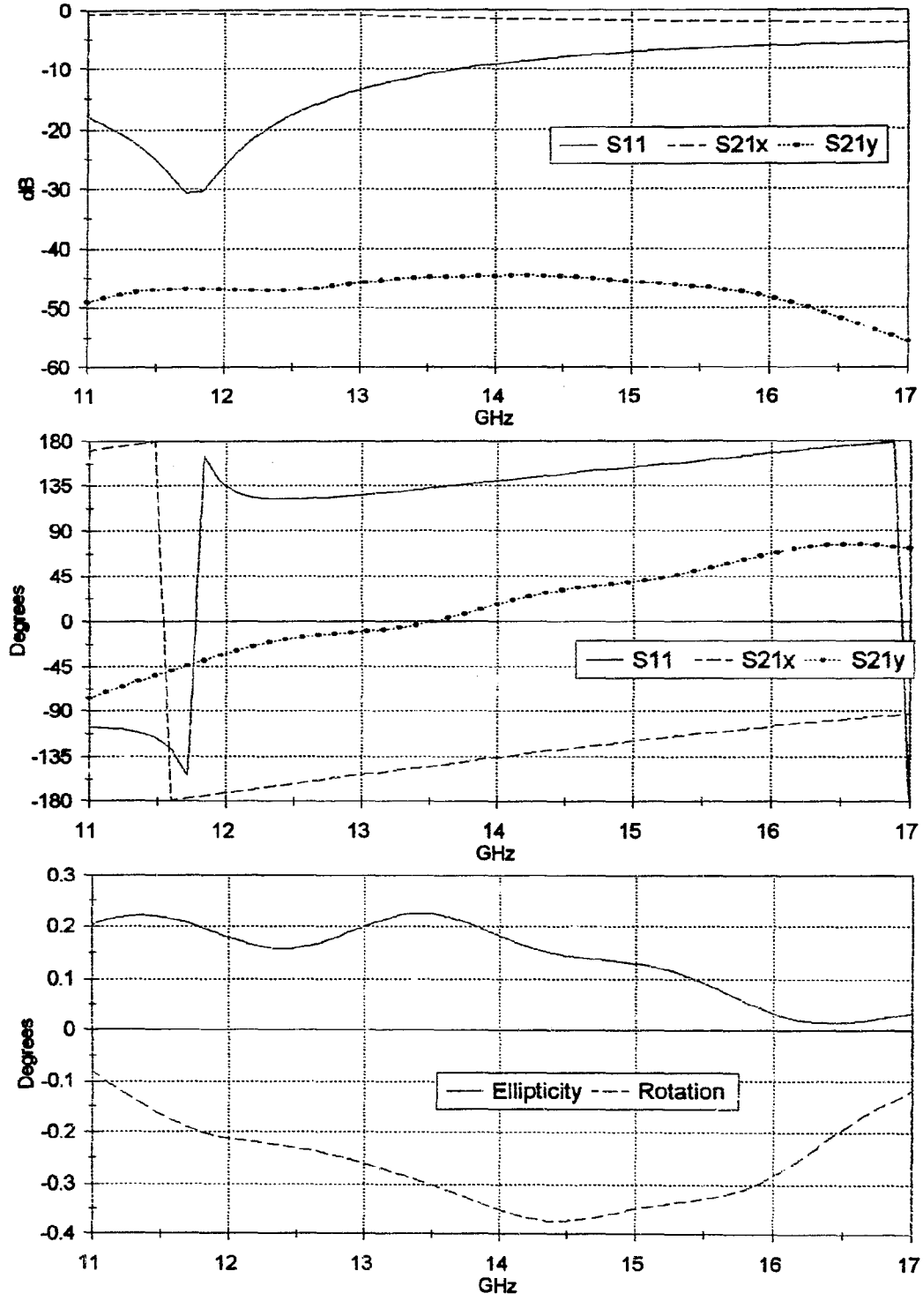

Figure F.16: 50RAC-QS: S-Parameters and polarization ellipse.

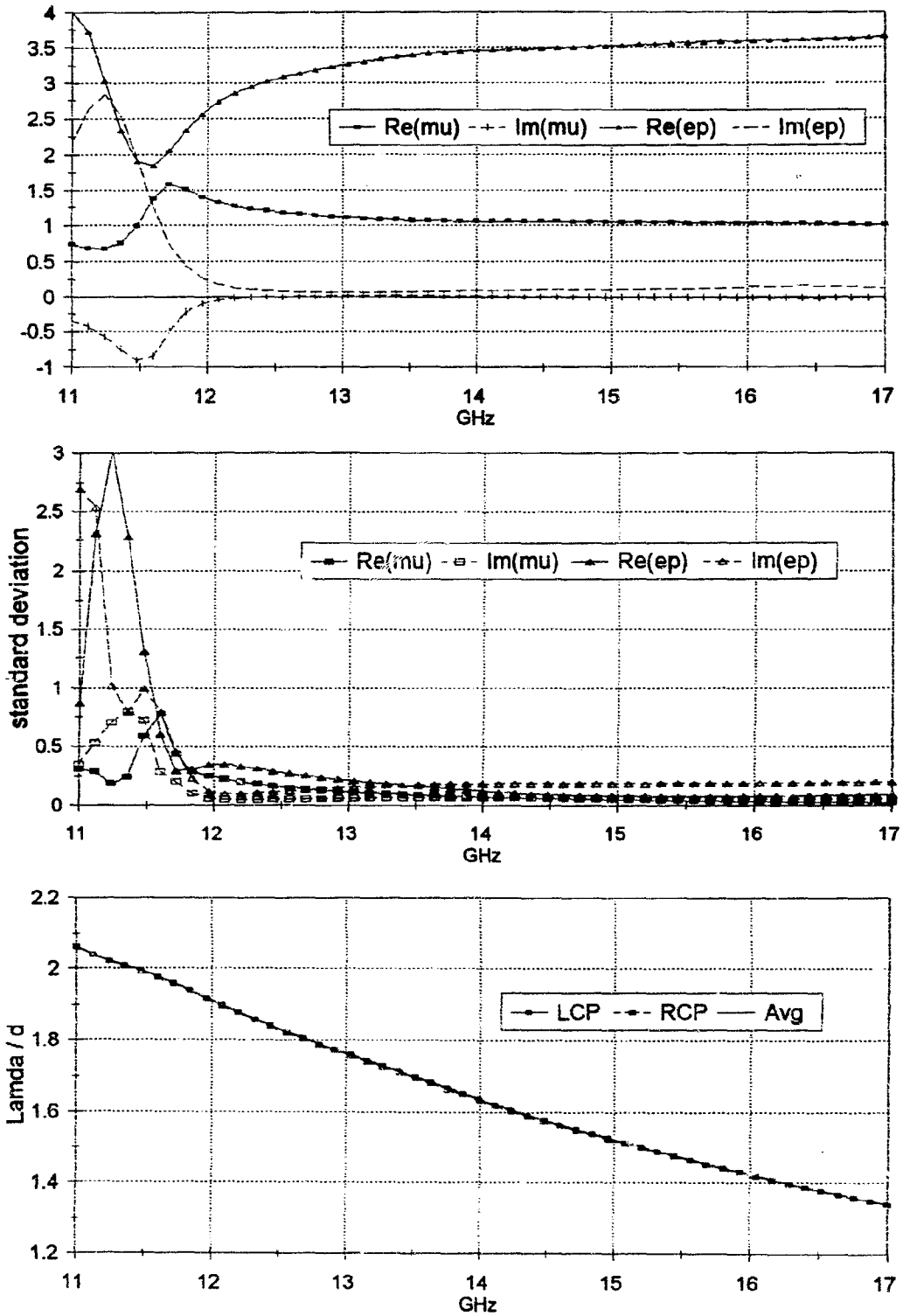

Figure F.17: 50RAC-QS: Constitutive parameters (μ, ϵ), standard deviation and wavelength.

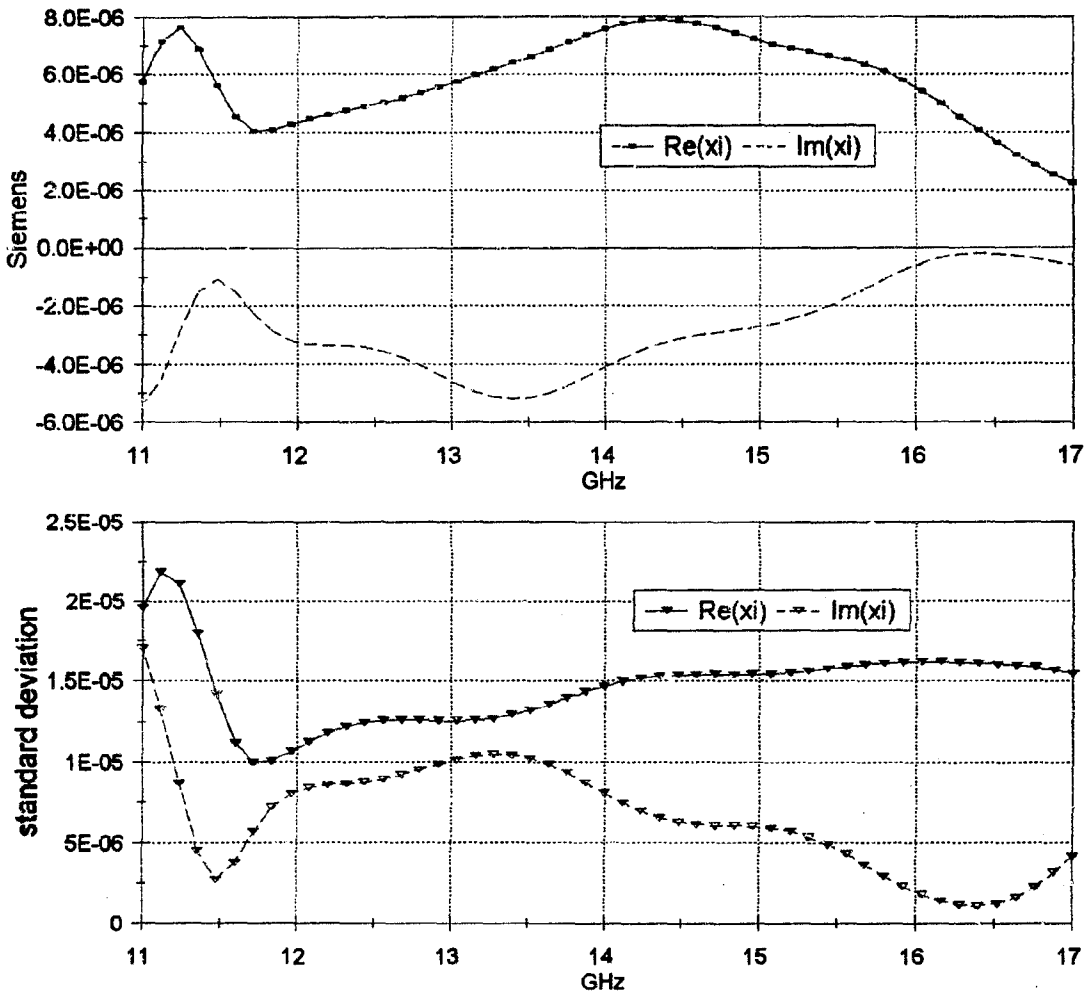

Figure F.18: 50RAC-QS: Chirality parameter and its standard deviation.

F.2.4 100RH-QS: 100RH/cc in Quartz-Silicone

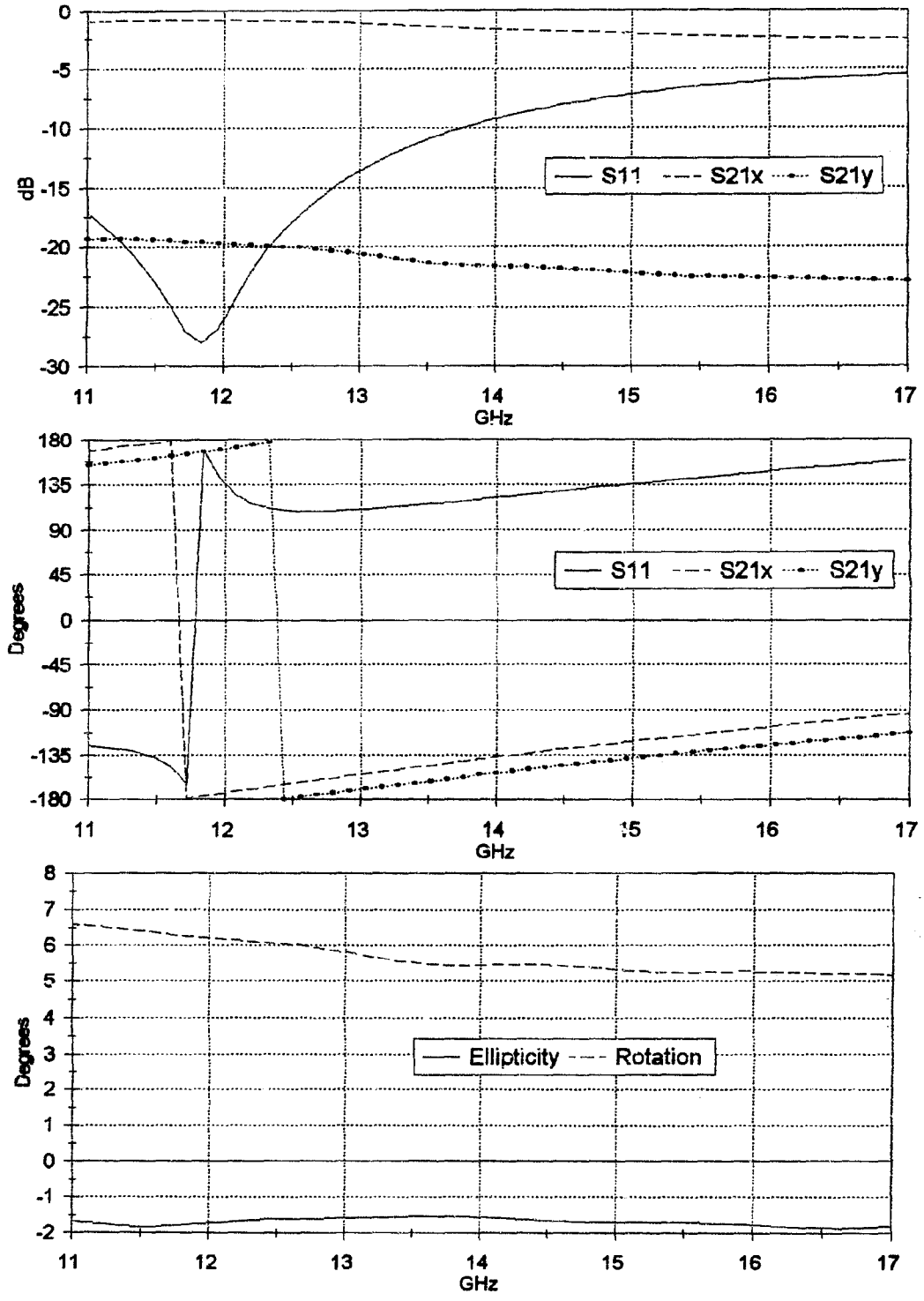

Figure F.19: 100RH-QS: S-Parameters and polarization ellipse.

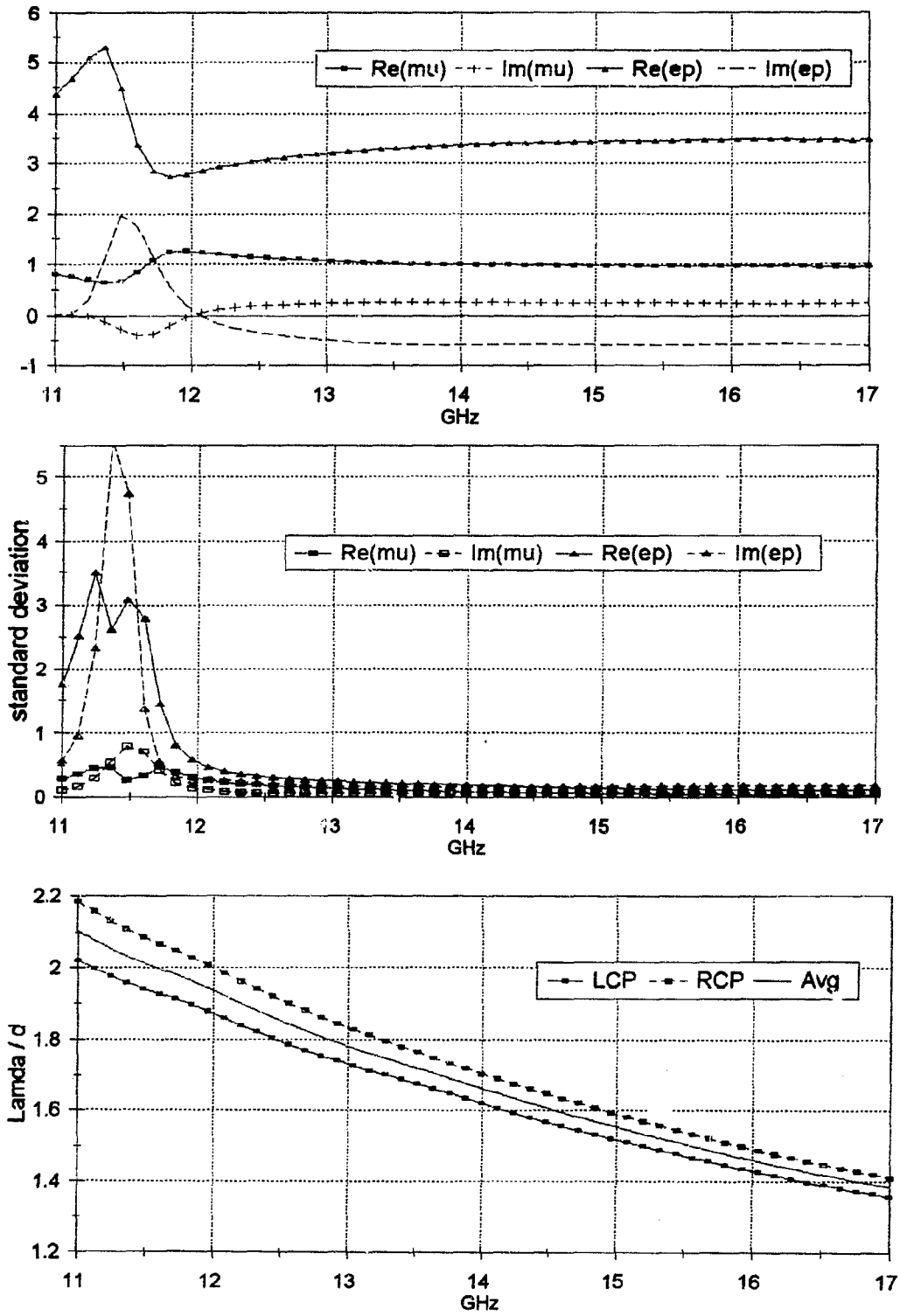

Figure F.20: 100RH-QS: Constitutive parameters (μ, ϵ), standard deviation and wavelength.

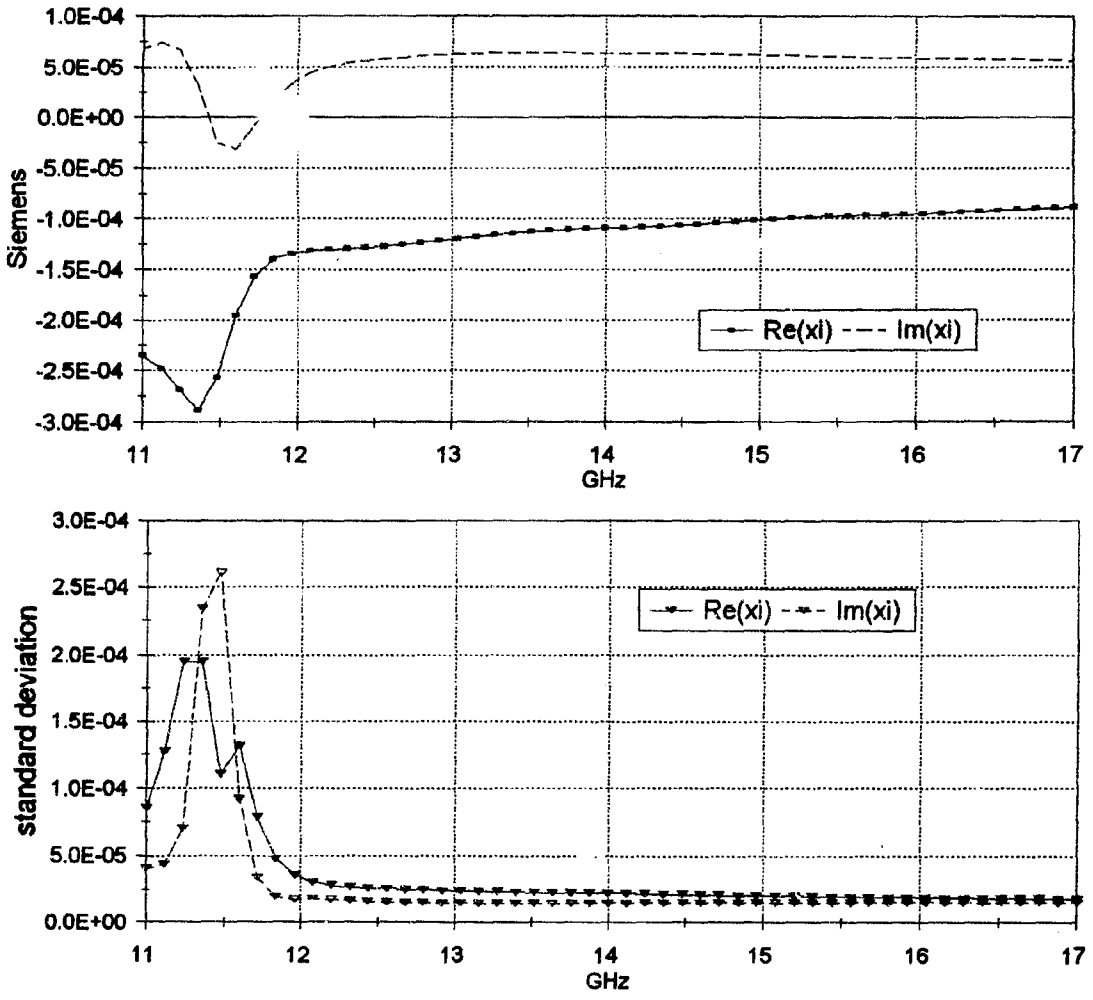

Figure F.21: 100RH-QS: Chirality parameter and its standard deviation.

F.2.5 220RH-S: 220RH/cc in Silicone

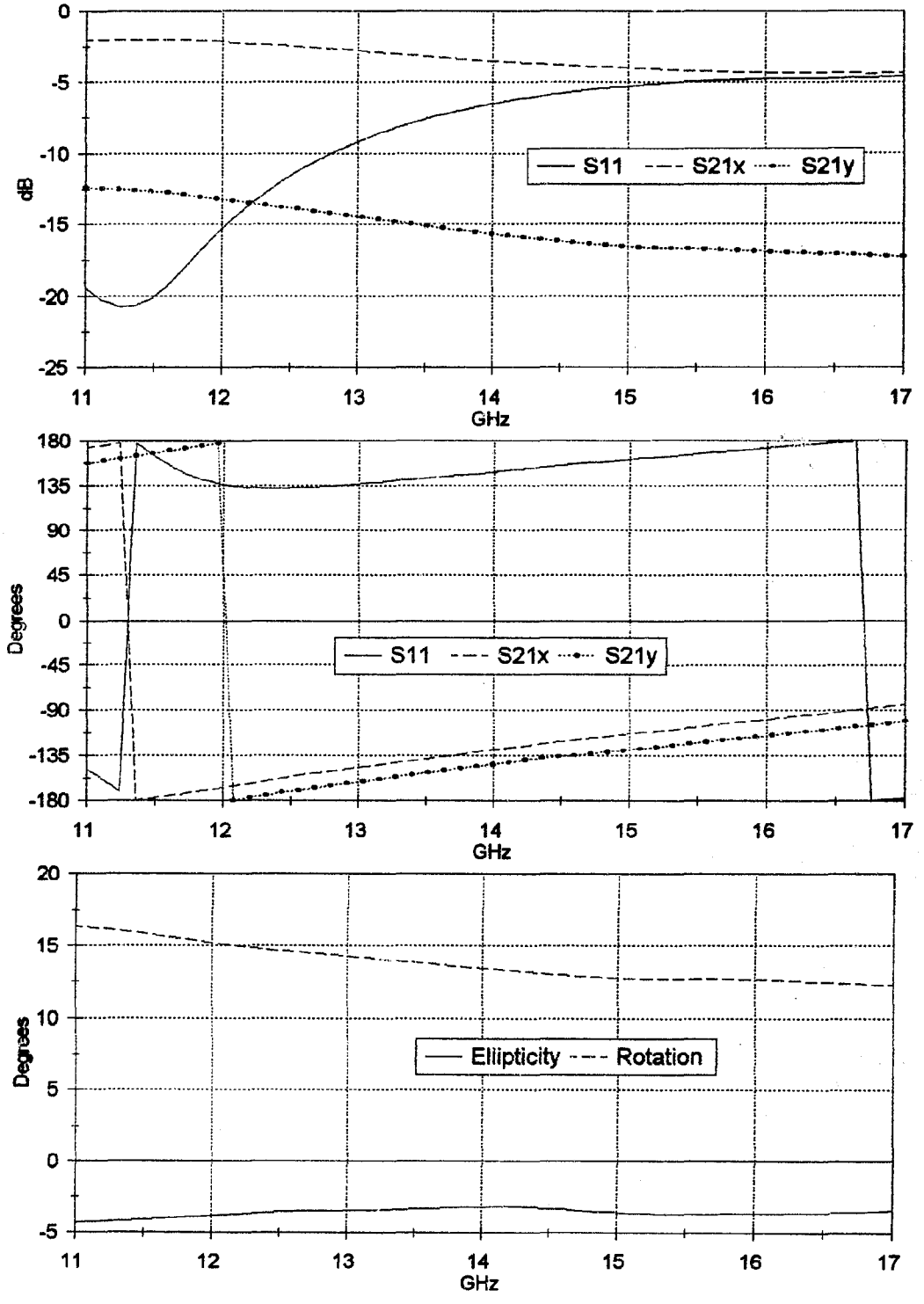

Figure F.22: 220RH-S: S-Parameters and polarization ellipse.

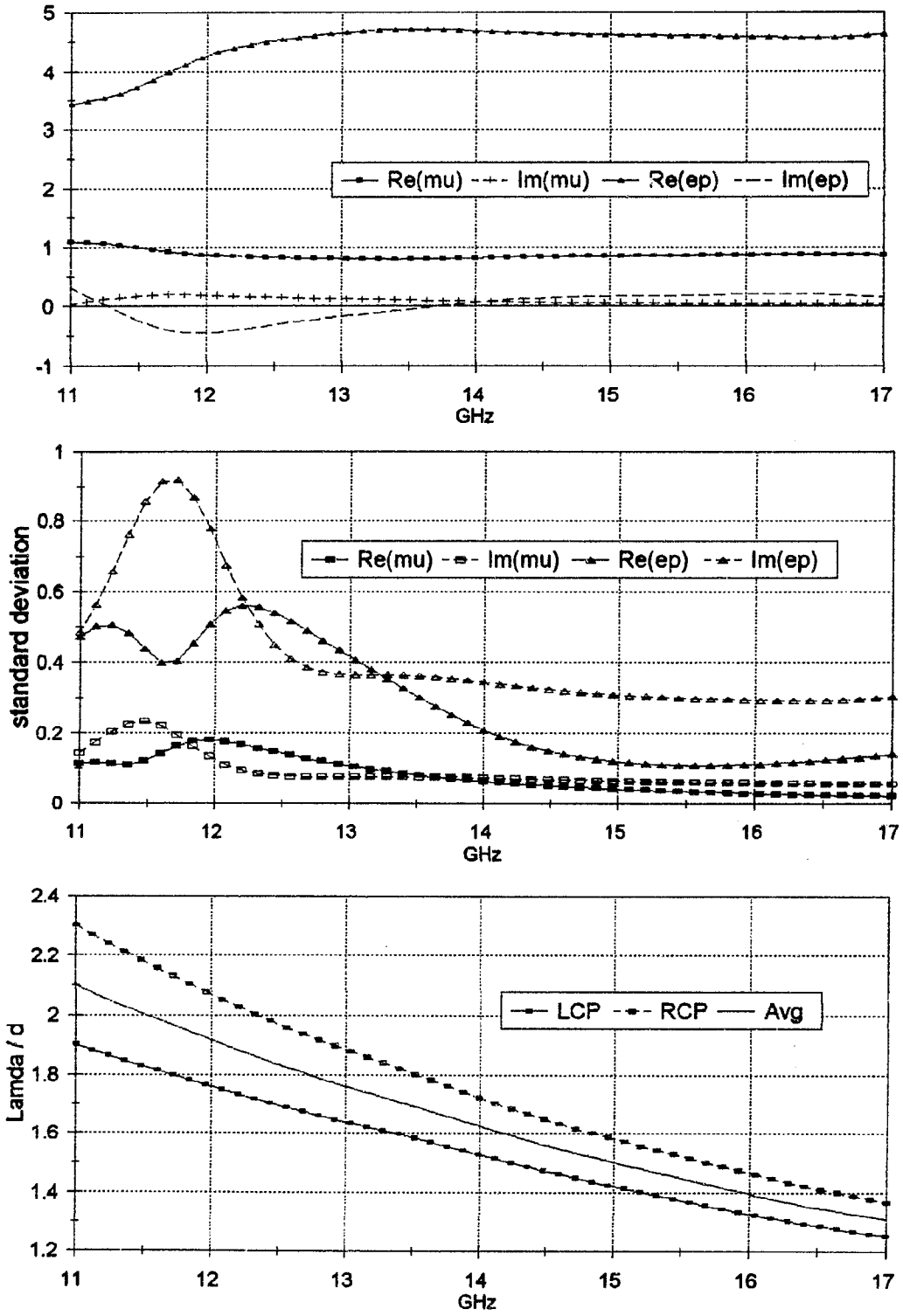

Figure F.23: 220RH-S: Constitutive parameters (μ, ϵ), standard deviation and wavelength.

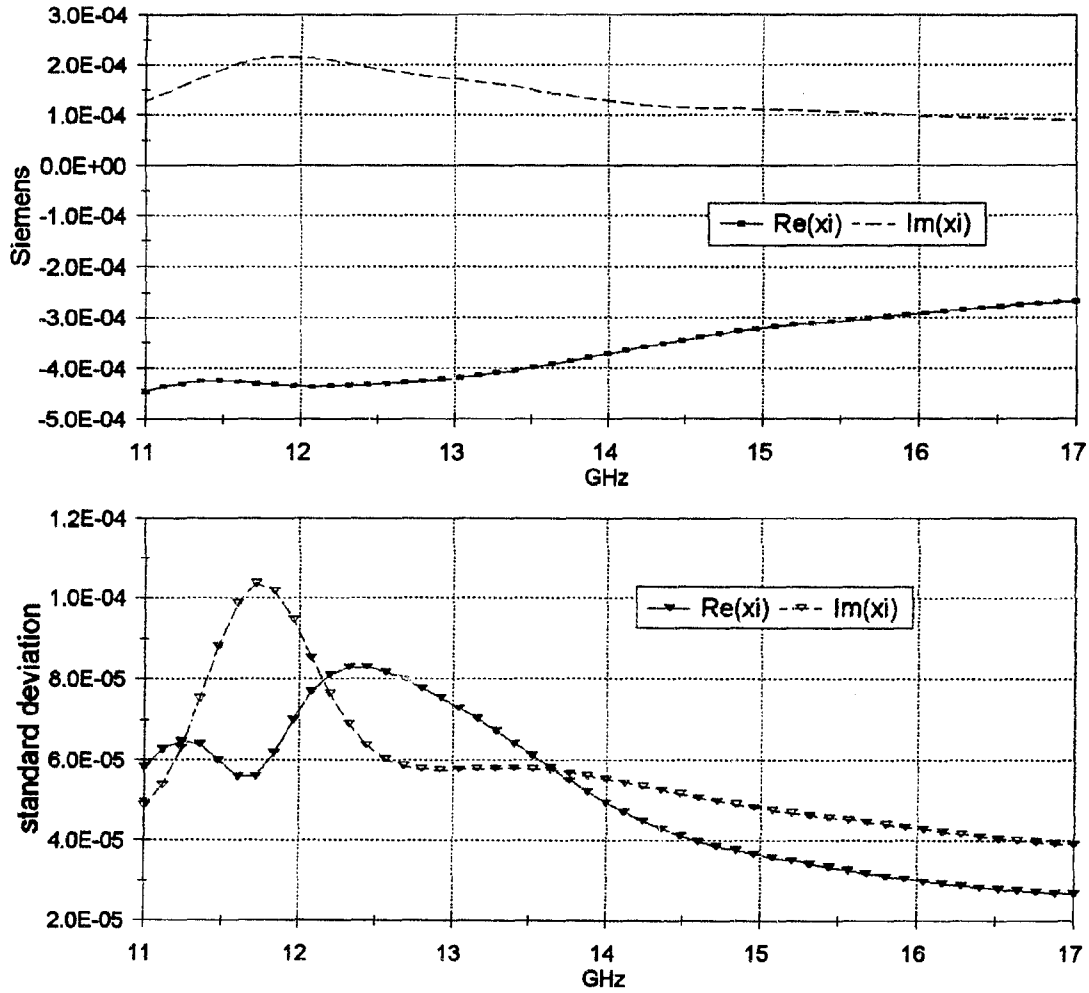

Figure F.24: 220RH-S: Chirality parameter and its standard deviation.

F.2.6 Comparison of results if S_{21y} is measured directly and if the receiver is not rotated through 90 degrees

It is not necessary to rotate the receiver through 90 degrees to measure the cross-polarized component of the transmitted wave S_{21y}. It can also be done by rotating the receiving antenna through an arbitrary angle ϕ and measuring $S_{21\phi}$. The cross-polarized component can then be calculated from S_{21x} and $S_{21\phi}$ using the following equation [48, 65],

$$S_{21y} = \frac{S_{21\phi} - S_{21x}\cos\phi}{\sin\phi}. \tag{F.1}$$

The results for $\phi = 90°$ and for $\phi = 60°$ are compared in Figure F.25. In general it can be concluded that the results obtained from the two methods are the same. Note that the values for $\phi = 90°$ are from an average of two measurements and the results for $\phi = 60°$ was obtained from only one measurement that was done at a later stage and it can therefore not be guaranteed that exactly the same spot was measured. The difference between S_{21y} obtained from the two methods was approximately 0.5 dB and the difference between S_{11} for the two measurements was approximately 2 dB at 11.4 GHz. The larger difference between the constitutive parameters at the lower frequencies are probably caused by the difference in S_{11} where the accuracy of the measurements are expected to be less in this region because of the halfwave effect. An extensive study to compare the accuracy of the two methods has not been done. The optimum angle through which the receiving antenna must be rotated for maximum accuracy should also be determined. This optimum angle should depend on the rotation characteristics of the sample that is being measured.

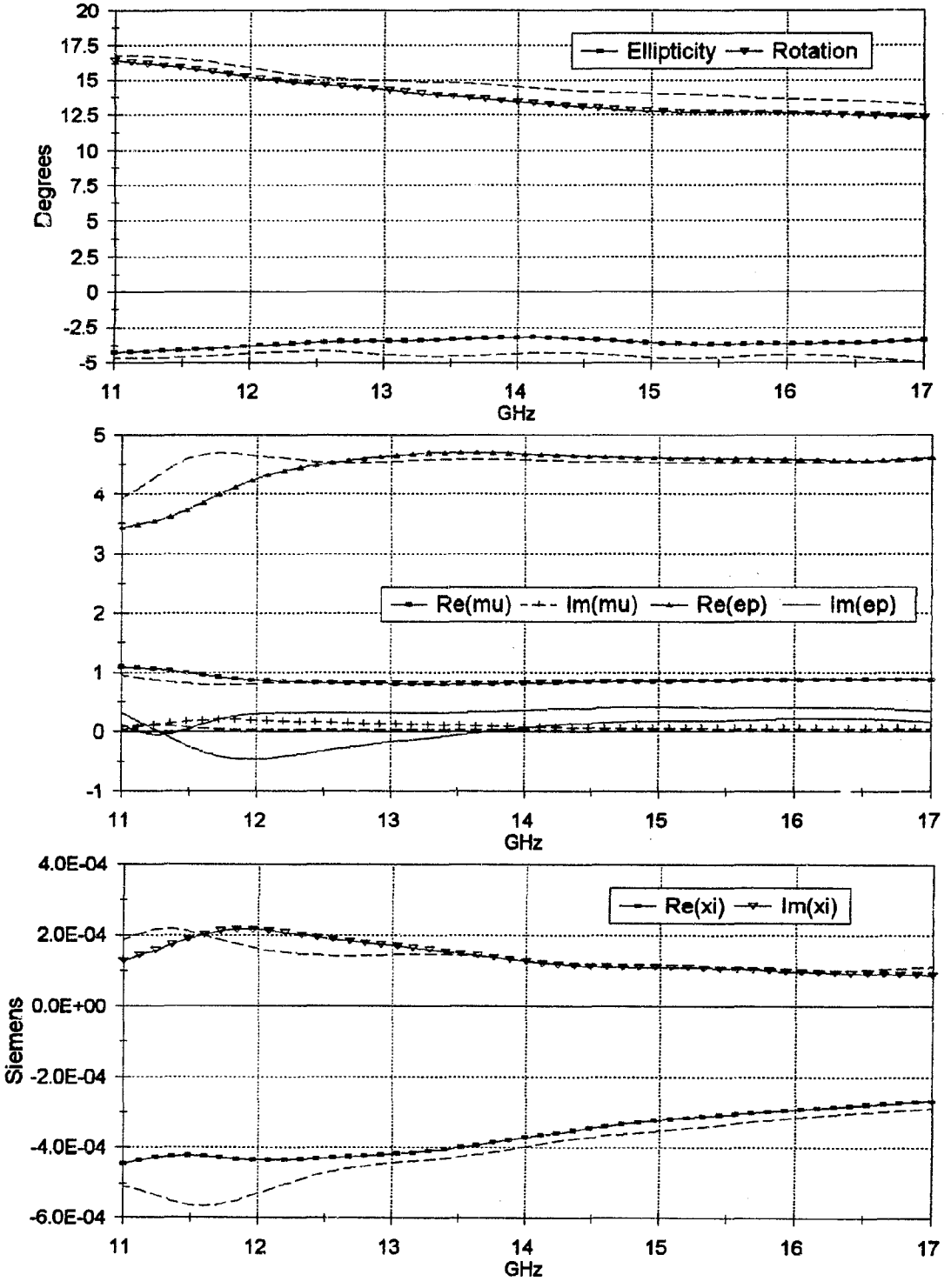

Figure F.25: Comparison of results after S_{21y} was measured by rotating the receiver only $\phi = 60°$ and then using Equation F.1. The unmarked dashed lines are the results from $\phi = 60°$.

F.3 Tungsten

F.3.1 Tu-LD: Low Density in Polyurethane.

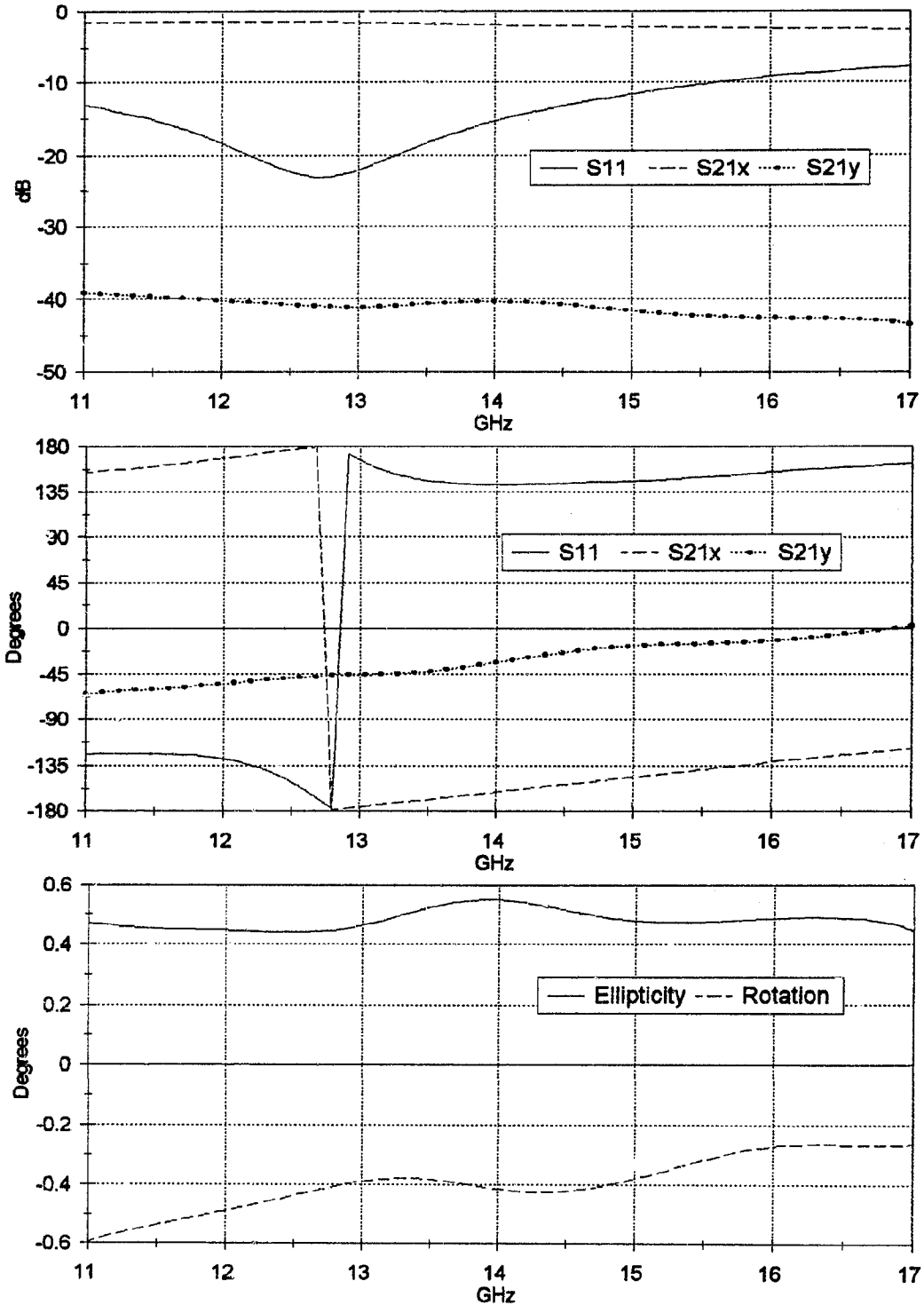

Figure F.26: Tu-LD: S-Parameters and polarization ellipse.

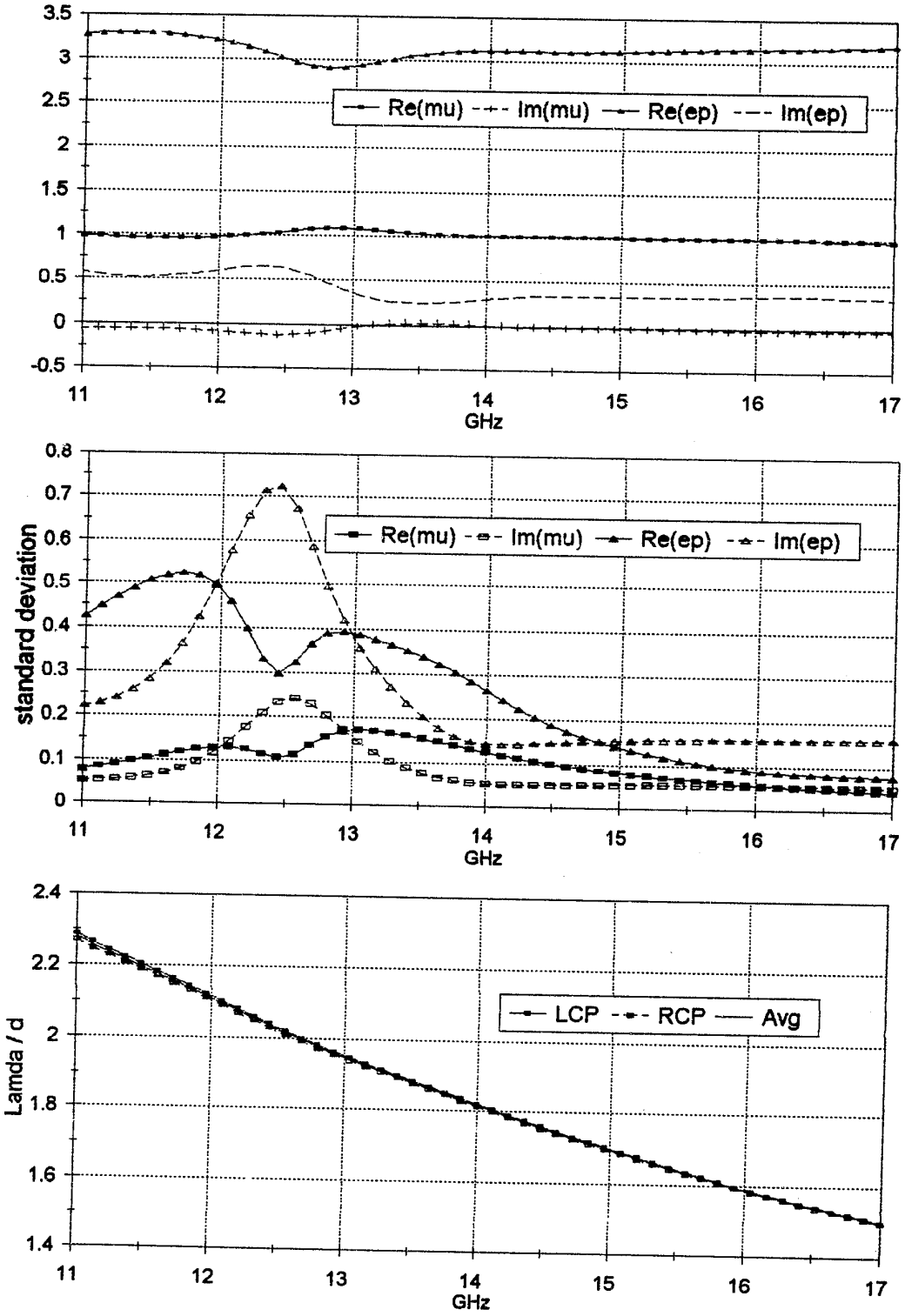

Figure F.27: Tu-LD: Constitutive parameters (μ, ϵ), standard deviation and wavelength.

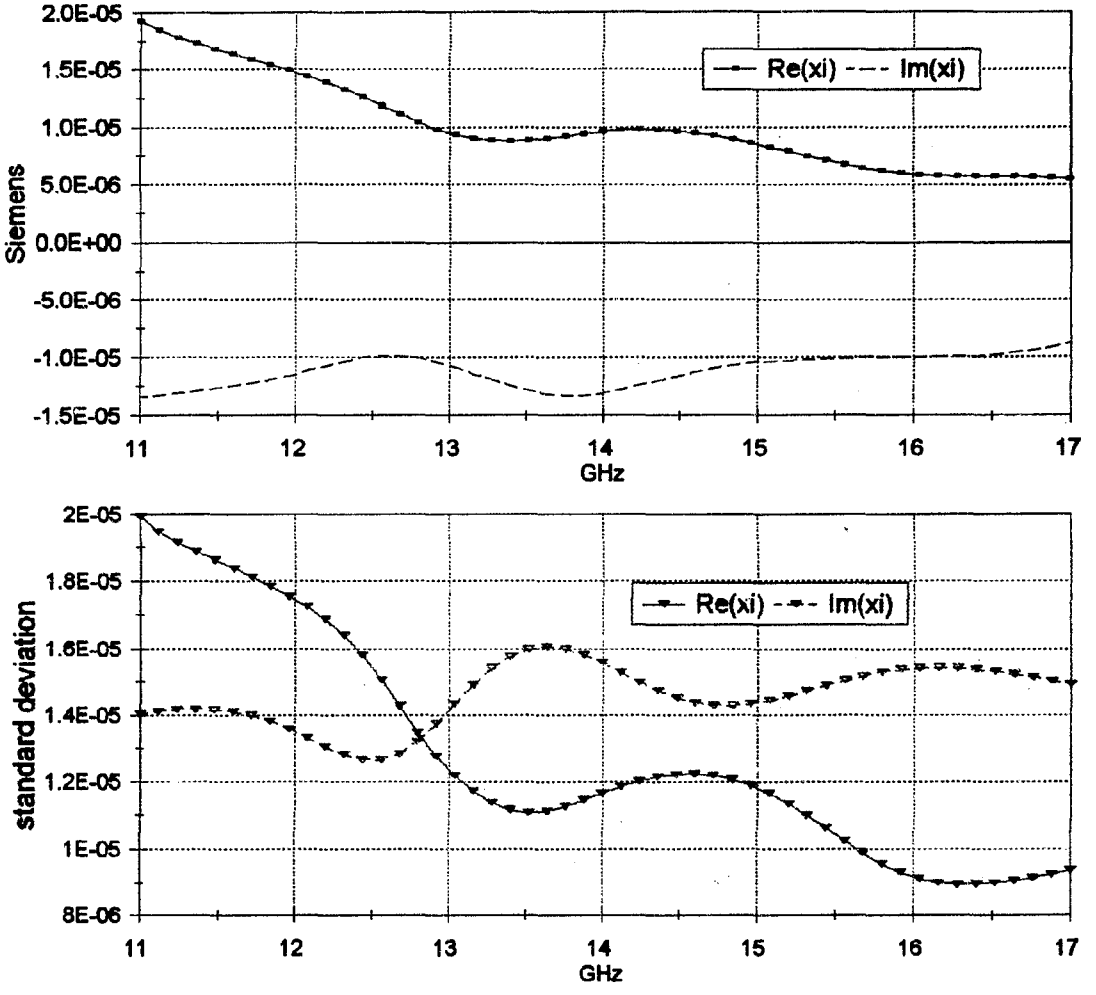

Figure F.28: Tu-LD: Chirality parameter and its standard deviation.

F.3.2 Tu-HD: High Density in Polyurethane.

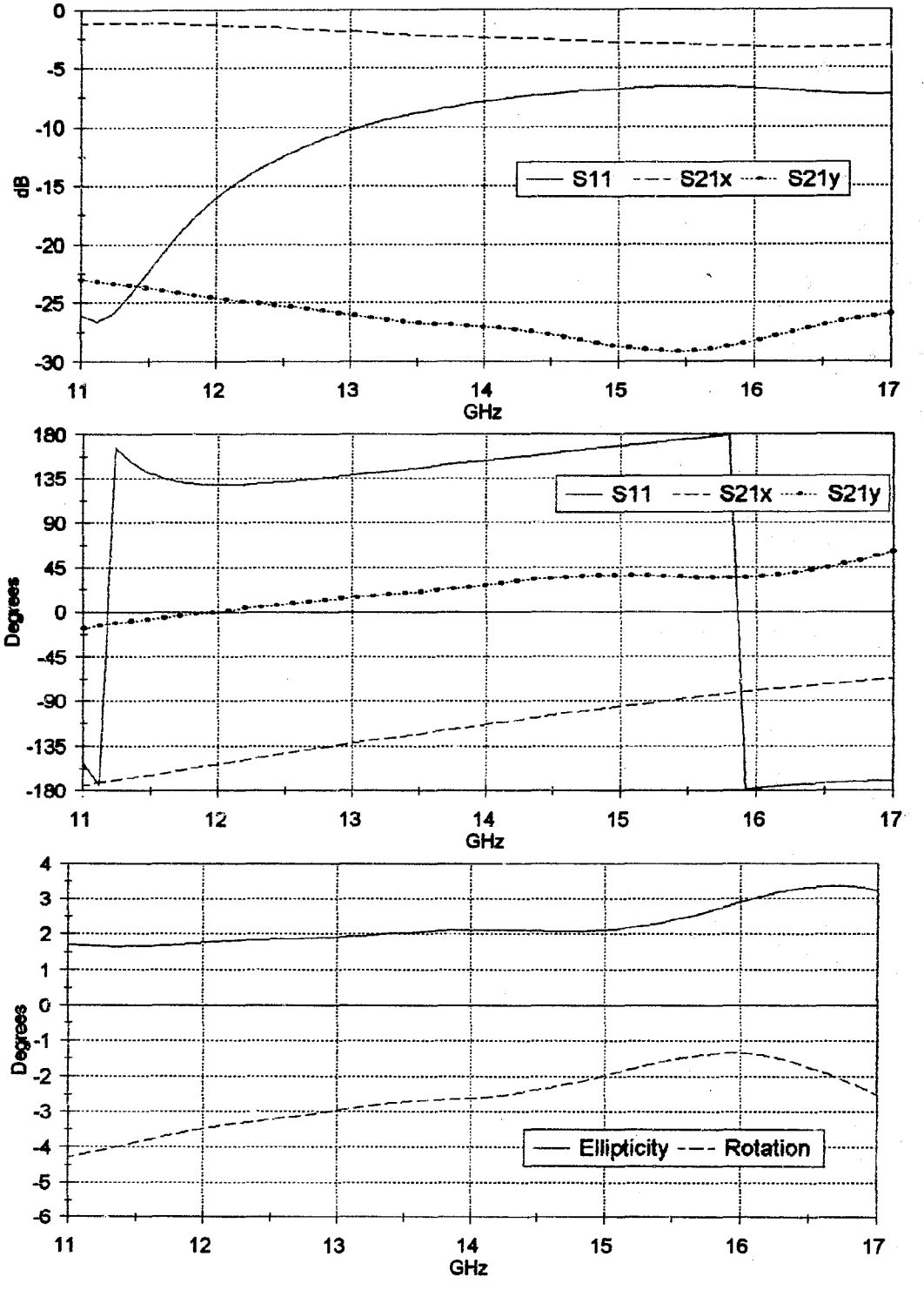

Figure F.29: Tu-HD: S-Parameters and polarization ellipse.

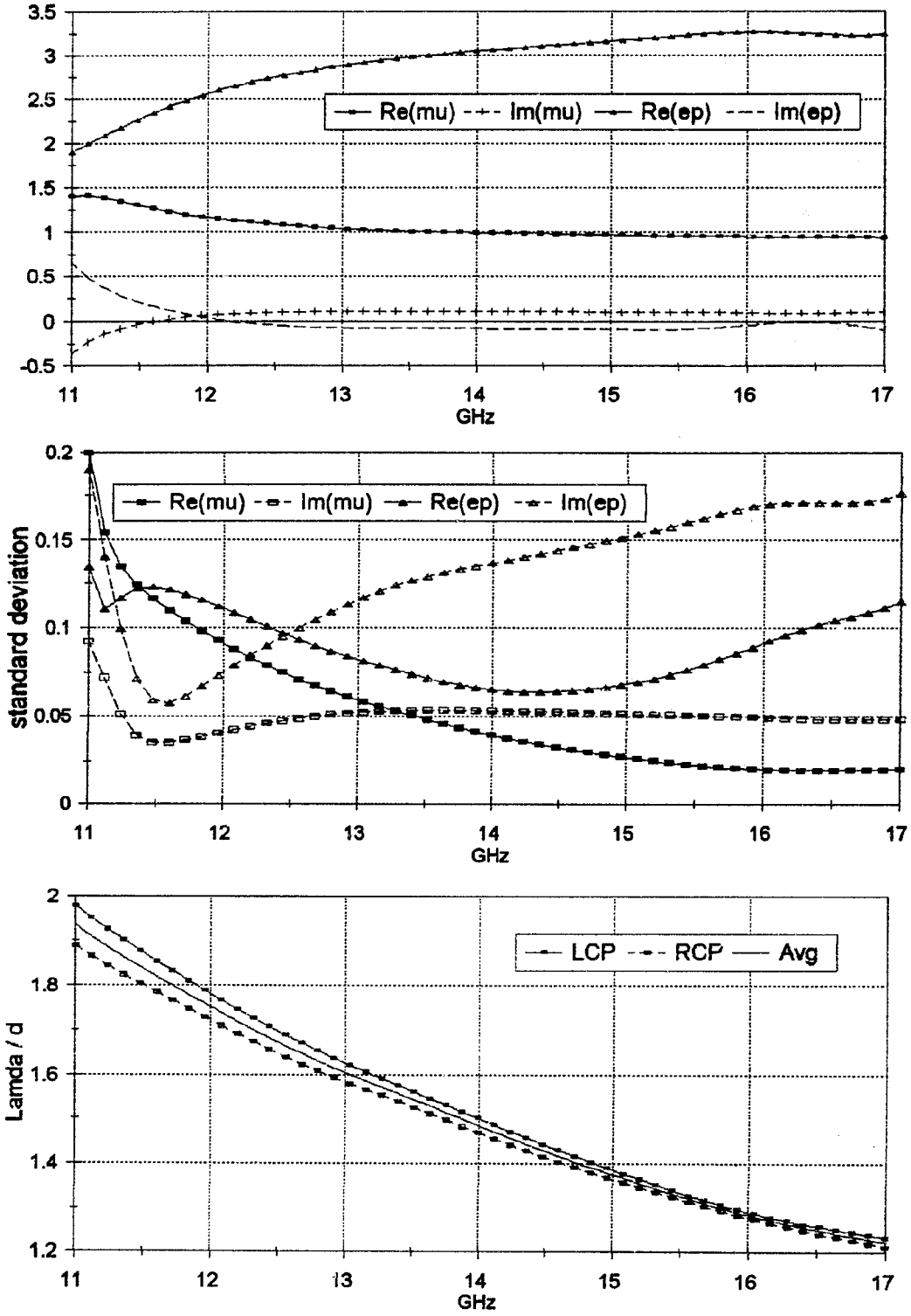

Figure F.30: Tu-HD: Constitutive parameters (μ, ϵ), standard deviation and wavelength.

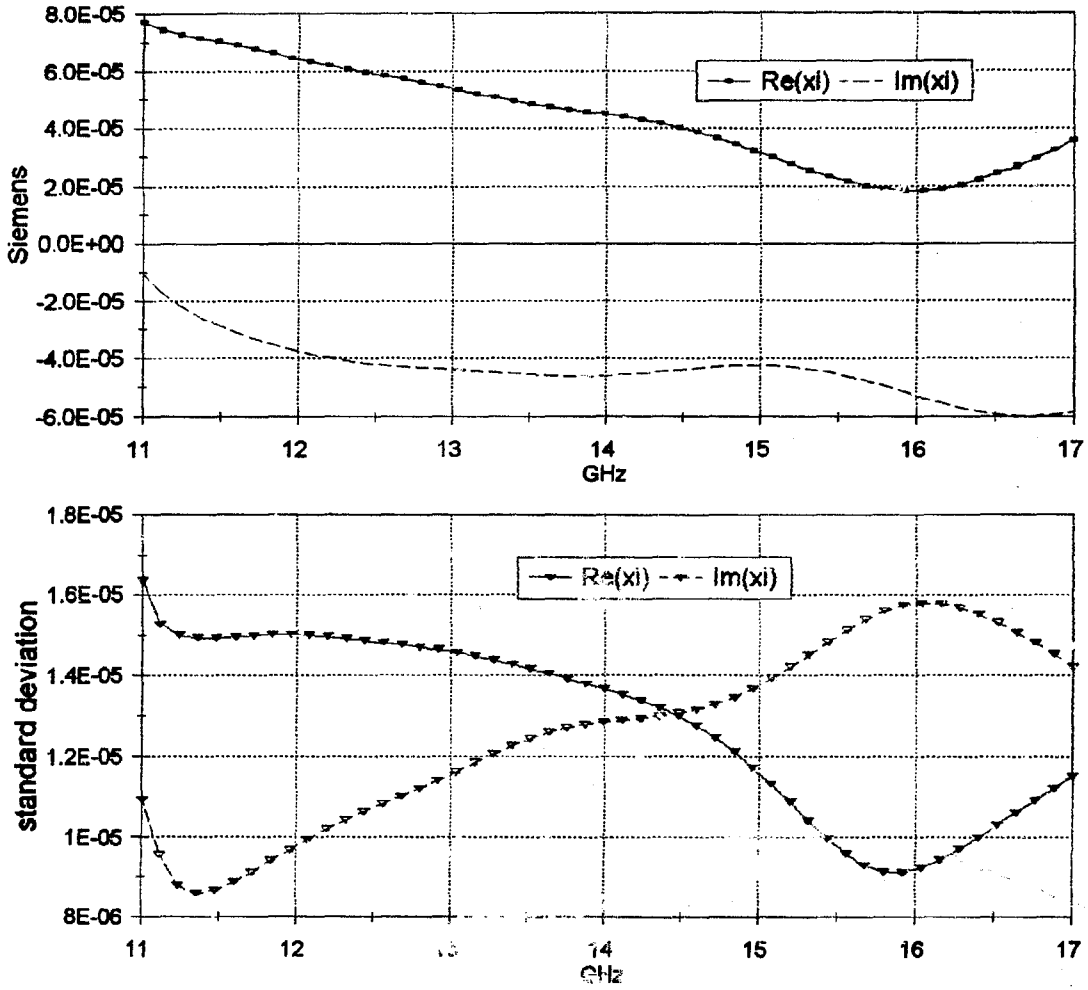

Figure F.31: Tu-HD: Chirality parameter and its standard deviation.

Appendix G

Polarization

G.1 Polarization Ellipse

The definitions used to describe the polarization state of the transmitted wave are summarized below [119, 120]. The electric field can be represented by two orthogonal components,

$$\vec{E} = E_x\hat{x} + E_y\hat{y} \tag{G.1}$$

where,

$$E_x = E_1 e^{-i(\omega t - kz)} \tag{G.2}$$

$$E_y = E_2 e^{-i(\omega t - kz - \delta)}. \tag{G.3}$$

with E_1 and E_2 real, and δ = the difference in phase between the two components. The polarization ellipse is shown in Figure G.1. The ratio between the major and minor

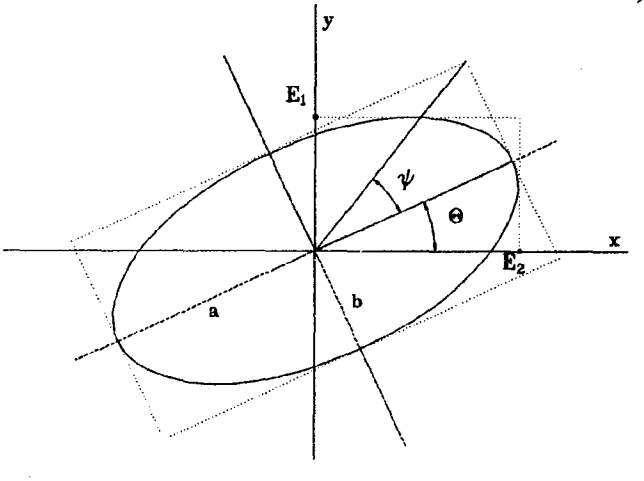

Figure G.1: Relation of amplitudes E_1 and E_2 to the ellipticity angle ψ and the tilt or rotation angle θ.

axis of the ellipse is the axial ratio ($AR = a/b$),

$$\text{(circular polarization)} \quad 1 \leq AR \leq \infty \quad \text{(linear polarization)}.$$

The Stokes parameters for a completely polarized wave are,

$$I = S = \frac{1}{\eta}(E_1^2 + E_2^2), \tag{G.4}$$

$$Q = \frac{1}{\eta}(E_1^2 - E_2^2) = S(\cos 2\psi \ \cos 2\theta), \tag{G.5}$$

$$U = \frac{2}{\eta} E_1 E_2 \cos\delta = S(\cos 2\psi \ \sin 2\theta), \tag{G.6}$$

$$V = \frac{2}{\eta} E_1 E_2 \sin\delta = S(\sin 2\psi). \tag{G.7}$$

The ellipticity angle, ψ, can be determined from,

$$\psi = \tan^{-1}(\pm\frac{1}{AR}) \qquad (LCP \ -45^\circ \leq \chi \leq 45^\circ \ \ RCP) \tag{G.8}$$

$$= \frac{1}{2}\sin^{-1}(\frac{V}{S}). \tag{G.9}$$

The tilt (or rotation) angle, θ, can be determined from,

$$\theta = \frac{1}{2}\tan^{-1}(\frac{U}{Q}). \qquad 0^\circ \leq \theta \leq 180^\circ \tag{G.10}$$

G.2 Circular Polarization

A right hand circularly polarized wave (RCP) will be defined as follows for the $e^{-i\omega t}$ harmonic time convention.

$$\vec{E} = (\hat{x} + i\hat{y})E_0 e^{-i(\omega t - kz)}. \tag{G.11}$$

At a fixed position ($z = 0$) the point of the vector will rotate clockwise with time for an observer looking in the propagation direction of the the wave (i.e. in the $\hat{z}$ direction).

For a fixed time ($t = 0$) the point of the vector will form a spiral along the z-axis. The point of the vector will move in an counterclockwise direction for an observer looking along the z-axis in the direction of propagation.

Glossary of Symbols and Notation

A list of special symbols and notations often used in this thesis are shown here together with the page of appearance.

Expression	Description	page
A	Absorption coefficient of chiral slabs	132
AR	Axial Ratio of polarization ellipse	193
a	Radius of aperture of lens antenna	39
$(A)_B$	Notation used to for partial derivative term $\frac{\partial A}{\partial B}$	91
$\mathbf{B}$	Magnetic flux density (Weber/m^2 or Tesla)	7
β	(a) Drude-Born-Fedorov chirality parameter (meter)	139
	(b) Real part of wavenumber, $\beta = \frac{2\pi}{\lambda}$	36
c	Wave velocity in free space, 2.997×10^8 m/s	61
$\mathbf{D}$	Electric displacement (Coulombs/m^2)	7
d	Thickness of the sample	8
$\mathbf{E}$	Electric field strength (Volts/m)	7
E_{DF}	Directivity in calibration error model	51
E_{LF}	Load Match	51
E_{RF}	Reflection Tracking	51
E_{SF}	Source Match	51
E_{TF}	Transmission Frequency Response	51
ϵ	Permittivity (F/m)	7
FS	Free Space Calibration	36
f	Focal distance	39
f_c	Cutoff frequency	45
Γ	Reflection coefficient from semi-infinite chiral medium	11
$\mathbf{H}$	Magnetic field strength (Amperes/m)	7
i	The symbol used to denote the imaginary number $\sqrt{-1}$	7
$\mathrm{Im}(x)$	Imaginary part of the complex parameter x	194
k	Wavenumber $k = \omega\sqrt{\mu\epsilon}$	8
k_r, k_l	Wavenumber of RCP and LCP waves	8,140
κ	Sihvola–Lindell chirality parameter (dimensionless)	139
L	Focused beam depth	43
L2S	FS Calibration: Load and 2 Shorts	53
l	Physical offset distance (meter)	61

Expression	Description	page
λ	Wavelength	36
λ_{av}	Average wavelength of RCP and LCP: $\lambda_{av} = \frac{1}{2}(\lambda_r + \lambda_l)$	95
Λ	Elongation (or dispersion) factor $\lambda = \Lambda\, \lambda_0$	60
μ	Permeability (H/m)	7
n	Integer $n = 0, 1, 2, 3$	39,142
ν	Propagation velocity of wave	61
η_c	Intrinsic impedance of a chiral medium	8,140
P	Sensitivity of reflection coefficient	53
P_r, P_l	Propagation factors for the RCP and LCP waves	9
Q	Quality factor of calibration procedure	53
RCP, LCP	Right and Left Circularly Polarized	8
Re(x)	Real part of the complex parameter x	131,194
ρ	Reflection coefficient from chiral Dallenbach layer	128
ρ_0	Reflection coefficient between free space and a semi-infinite chiral medium	128
S_{11}	Reflection coefficient	8
S_{21x}	Co-polarized transmission coefficient	8
S_{21y}	Cross-polarized transmission coefficient	9
$\mathcal{S}^{\nu}_{\Psi}$	Sensitivity of ν to a small change in Ψ	89
σ	Standard Deviation	91
t_d	Offset Delay: $t_d = l/\nu$ (seconds)	61
$e^{-i\omega t}$	Harmonic time convention	7
θ	Rotation angle of the polarization ellipse	9,194
ω	Denotes 2π times the time harmonic frequency, f	7
w, w_0	Gaussian beam radius (waist), and minimum beam radius	40
ψ	Ellipticity of polarization ellipse	194
$\hat{\mathbf{x}}$, $\hat{\mathbf{y}}$, $\hat{\mathbf{z}}$	Unit vectors in Cartesian coordinate system	9
ξ	Post-Jaggard chirality parameter (Siemens)	7
$\nabla\times$	Curl of a vector quantity	8
$\frac{\partial f(x)}{\partial x}$	Partial derivative	90
$\times$	Cross product of two vector quantities	8
*	Complex conjugate.	131,194
3S, 3C	FS Calibration: 3 Shorts	53
7C	7 mm Calibration (Hewlett Packard standard)	36

Bibliography

[1] N. Engheta and D. L. Jaggard, "Electromagnetic chirality and its applications," *IEEE Antennas and Propagation Society Newsletter*, pp. 6–12, October 1988.

[2] S. Bassiri, C. H. Papas, and N. Engheta, "Electromagnetic wave propagation through a dielectric-chiral interface and through a chiral slab," *J. Opt. Soc. Am. A*, vol. 5, pp. 1450–1459, September 1988.

[3] J. Galloway, "Helix through the looking glass," *New Scientist*, pp. 242–245, 27 January 1983.

[4] R. A. Hegstrom and D. K. Kondepundi, "The handedness of the universe," *Scientific American*, pp. 98–105, January 1990.

[5] V. A. Avetisov, V. I. Goldanskii, and V. V. Kuz'min, "Handedness, origin of life and evolution," *Physics Today*, pp. 33–41, July 1991.

[6] M. Gardner, *The Ambidextrous Universe: Mirror Asymmetry and Time Reversed Worlds.* Charles Scribner's Sons, Second revised and updated edition, 1979.

[7] A. Lakhtakia, V. K. Varadan, and V. V. Varadan, *Time-Harmonic Electromagnetic Fields in Chiral Media.* Lecture Notes in Physics, Springer-Verlag, 1989.

[8] J. Applequist, "Optical activity: Biot's bequest," *American Scientist*, vol. 75, pp. 59–68, January-February 1987.

[9] L. D. Barron, *Molecular Light Scattering and Optical Activity.* University Press, Cambridge, 1982.

[10] R. Ro, V. V. Varadan, and V. K. Varadan, "Electromagnetic activity and absorption in microwave chiral composites," *IEE Proceedings-H*, vol. 139, pp. 441–448, October 1992.

[11] N. Engheta, "Introduction to the "Special Issue on Wave Interactions with Chiral and Complex Media"," *Journal of Electromagnetic Waves and Applications*, vol. 6, no. 5/6, 1992.

[12] M. P. Silverman and T. C. Black, "Experimental method to detect chiral asymmetry in specular light scattering from a naturally opically active medium," *Physics Letters A*, vol. 126, pp. 171–176, December 1987.

[13] M. P. Silverman, N. Ritchie, G. M. Cushman, and B. Fisher, "Experimental configurations using optically phase modulation to measure chiral asymmetries in light specularly reflected from naturally gyrotropic medium," *J. Opt. Soc. Am.* vol. 5, pp. 1852–1862, November 1988.

[14] K. L. Lindman, "Über eine durch ein isotropes System von spiralförmigen Resonatoren erzeugte Rotationspolarisation der elektromagnetischen Wellen," *Annalen der Physik*, vol. 63, no. 4, pp. 621–644, 1920.

[15] K. L. Lindman, "Über die durch ein aktives Raumgitter erzeugte Rotationspolarisation der elektromagnetischen Wellen," *Annalen der Physik*, vol. 69, no. 4, pp. 270–284, 1922.

[16] I. V. Lindell, A. H. Sihvola, and J. Kurkijärvi, "Karl F. Lindman: The last Hertzian, and a harbinger of electromagnetic chirality," *Antennas and Propagation Magazine*, vol. 34, pp. 24–30, June 1992.

[17] I. Tinoco and M. P. Freeman, "The optical activity of oriented copper helices. I. Experimental," *J.Chem.Phys*, vol. 61, pp. 1196–1200, September 1957.

[18] M. H. Winkler, "An experimental investigation of some models for optical activity," *J. Phys. Chem*, vol. 60, pp. 1656–1659, December 1956.

[19] M. H. Umari, V. V. Varadan, and V. K. Varadan, "Rotation and dichroism associated with microwave propagation in chiral composite samples," *Radio Science*, vol. 26, pp. 1327–1334, September 1991.

[20] T. Guire, V. V. Varadan, and V. K. Varadan, "Influence of chirality on the reflection of EM waves by planar dielectric slabs," *IEEE Transactions on Electromagnetic Compatibility*, vol. EMC-32, pp. 300–303, November 1990.

[21] R. D. Hollinger, V. V. Varadan, D. K. Ghodgaonkar, and V. K. Varadan, "Experimental characterization of isotropic chiral composites in circular waveguides," *Radio Science*, vol. 27, pp. 161–168, March 1992.

[22] N. Engheta and P. Pelet, "Modes in chirowaveguides," *Optics Letters*, vol. 14, pp. 593–595, June 1989.

[23] M. I. Oksanen, P. K. Koivisto, and I. V. Lindell, "Dispersion curves and fields for a chiral slab waveguide," *IEE Proceedings-H*, vol. 138, pp. 327–334, August 1991.

[24] P. Pelet and N. Engheta, "Modal analysis for rectangular chirowaveguides with metallic walls using the finite-difference method," *Journal of Electromagnetic Waves and Applications*, vol. 6, no. 9, pp. 1277–1285, 1992.

[25] T. C. K. Rao, "Radiation characteristics of a circular waveguide containing a chiral medium," *IEE Proceedings-H*, vol. 139, pp. 1–6, February 1992.

[26] R. D. Hollinger, V. V. Varadan, and V. K. Varadan, "Eigenmodes in a circular waveguide containing an isotropic chiral material," *Radio Science*, vol. 26, pp. 1335–1344, September-October 1991.

[27] A. H. Sihvola and I. V. Lindell, "Bi-isotropic constitutive relations," *Microwave and Optical Technology Letters*, vol. 4, pp. 295–297, July 1991.

[28] I. V. Lindell, S. A. Tretyakov, and M. I. Oksanen, "Conductor-backed Tellegen slab as twist polarizer," *Electronics Letters*, vol. 28, pp. 281–282, January 1992.

[29] W. Yin and P. Li, "The theory of multilayered spherical chirodome," *Microwave and Optical Technology Letters*, vol. 6, pp. 179–182, March 1993.

[30] H. Cory and I. Rosenhouse, "Minimization of reflection coefficient at feed of radome-covered reflector antenna by chiral device," *Electronics Letters*, vol. 27, pp. 2345–2347, December 1991.

[31] W. Yin and P. Li, "The focal points of radially stratified spherical chirolenses," *Microwave and Optical Technology Letters*, vol. 6, pp. 561–564, July 1993.

[32] N. Engheta and P. Pelet, "Reduction of surface waves in chirostrip antennas," *Electronics Letters*, vol. 27, pp. 5–6, January 1991.

[33] P. Pelet and N. Engheta, "Chirostrip antenna: Line source problem," *Journal of Electromagnetic Waves and Applications*, vol. 6, no. 5/6, pp. 771–793, 1992.

[34] D. Pozar, "Microstrip antennas and arrays on chiral substrates," *IEEE Trans. Antennas Propagat*, vol. 40, pp. 1260–1263, October 1992.

[35] W. Yin and W. Wang, "Analyzing the radiated characteristics of a two-layered chirostrip dipole antenna using the dyadic Green's function," *Microwave and Optical Technology Letters*, vol. 6, pp. 221–223, March 1993.

[36] V. K. Varadan, V. K. Varadan, and A. Lakhtakia, "On the possibility of designing anti-reflection coatings using chiral composites," *Journal of Wave-Material Interaction*, vol. 2, pp. 71–81, January 1987.

[37] D. L. Jaggard and N. Engheta, "Chirosorb^{TM} as an invisible medium," *Electronic Letters*, vol. 25, pp. 173–174, February 1989.

[38] J. C. Monzon, D. L. Jaggard, and N. Engheta, "Comments and reply on Chirosorb^{TM} as an invisible medium," *Electronics Letters*, vol. 25, pp. 1060–1061, August 1989.

[39] D. L. Jaggard, N. Engheta, and J. Liu, "Chiroshield: a Salisbury/Dallenbach shield alternative.," *Electronic Letters*, vol. 26, pp. 1332–1333, June 1990. Correction: Vol.27, p.547, 1991.

[40] J. C. Liu and D. L. Jaggard, "Chiral layers on planar surfaces," *Journal of Electromagnetic Waves and Applications*, vol. 6, no. 5/6, pp. 651–667, 1992.

[41] D. L. Jaggard and J. C. Liu, "Chiral layers on curved surfaces," *Journal of Electromagnetic Waves and Applications*, vol. 6, no. 5/6, pp. 669–694, 1992.

[42] D. Jaggard, J. Liu, and X. Sun, "Spherical chiroshield," *Electronics Letters*, vol. 27, pp. 77–79, January 1991.

[43] L. Arnaut and L. Davis, "Power reflection and absorption for lossy chiral media," in *Proceedings of "Bianisotropics'93"* (A. Sihvola, S. Tretyakov, and I. Semchenko, eds.), (University of Gomel, Byelarus), December 1993.

[44] W. Yin and P. Li, "Effects of chirality admittance on the cutoff wavelength of propagating modes in a chiral coaxial line," *Microwave and Optical Technology Letters*, vol. 6, pp. 381–382, May 1993.

[45] C. F. Bohren, R. Luebbers, H. S. Langdon, and F. Hunsberger, "Microwave-absorbing chiral composites: Is chirality essential or accidental?," *Applied Optics*, vol. 31, pp. 6403–6407, October 1992.

[46] R. Luebbers, H. S. Langdon, F. Hunsberger, C. F. Bohren, and S. Yoshikawa, "Calculation and measurement of the effective chirality parameter of a composite chiral material over a wide frequency band," in *Private communication, was submitted to IEEE AP-S, December 1992*, November 1993.

[47] A. J. Bahr and K. R. Clausing, "An approximate model for artificial chiral material," *Private communication*, December 1993.

[48] R. Ro, *Determination of the electromagnetic properties of chiral composites, using normal incidence measurements.* PhD thesis, The Pensylvania State University, The Graduate School, Department of Engineering Science and Mechanics, August 1991.

[49] A. Timmerman, J. Dauwen, M. van Craenendonck, and H. Pues, "Microwave chiral absorbers: Some experimental results," in *Proceedings of PIERS 91*, (Cambridge, Massachusetts, USA), p. 297, July 1991.

[50] F. Guerin, M. Labeyrie, and P. Guillon, "Experimental aspects of microwave chirality research," in *Proceedings of "Bianisotropics'93"* (A. Sihvola, S. Tretyakov, and I. Semchenko, eds.), (University of Gomel, Byelarus), December 1993.

[51] H. Pues, J. Dauwen, A. Timmerman, and M. van Craenendonck, "Chiral Absorber," UK Patent Application 9113993.1, Grace N.V., June 1991.

[52] H. Pues, J. Dauwen, A. Timmerman, and M. van Craenendonck, "Chiral Absorbing Structure," European Patent Application 92305547.9, Grace N.V., June 1992.

[53] D. L. Jaggard, A. R. Mickelson, and C. H. Papas, "On electromagnetic waves in chiral media," *Appl. Phys*, vol. 18, pp. 211–216, 1979.

[54] J. C. Monzon, "Radiation and scattering in homogeneous general biisotropic regions," *IEEE Trans. Antennas Propagat*, vol. 38, pp. 227–235, February 1990.

[55] R. E. Raab and J. H. Cloete, "An eigenvalue theory of circular birefringence and dichroism in a non-magnetic chiral medium," *Journal of Electromagnetic Waves and Applications*, vol. 8, pp. 1073–1089, August 1994.

[56] D. L. Jaggard, X. Sun, and N. Engheta, "Canonical sources and duality in chiral media," *IEEE Trans. Antennas Propagat*, vol. AP-36, pp. 1007–1013, July 1988.

[57] N. Engheta, D. L. Jaggard, and M. W. Kowarz, "Electromagnetic waves in Faraday chiral media," *IEEE Trans. Antennas Propagat*, vol. AP-40, pp. 367–374, April 1992.

[58] W. B. Weir, "Automatic measurement of complex dielectric constant and permeability at microwave frequencies," *Proceedings of the IEEE*, vol. 62, pp. 33–36, January 1974.

[59] J. H. Cloete and A. G. Smith, "The constitutive parameters of a lossy chiral slab by inversion of plane-wave scattering coefficients," *Microwave and Optical Technology Letters*, vol. 5, pp. 303–306, June 1992. Correction: Vol.7, No.1, January 1994, p.42.

[60] A. M. Nicolson and G. F. Ross, "Measurement of the intrinsic properties of materials by time domain methods," *IEEE Trans. Instrumentation and Measurements*, vol. IM-19, pp. 377–382, November 1970.

[61] D. K. Ghodgaonkar, V. V. Varadan, and V. K. Varadan, "Free-space measurement of complex permittivity and complex permeability of magnetic materials at microwave frequencies," *IEEE Trans. Instrumentation and Measurements*, vol. 39, pp. 387–394, April 1990.

[62] J. H. Cloete, "High precision measurement of complex permittivity and permeability at microwave frequencies," in *Proceedings of IEEE/SAIEE AP/MTTS-90 Symposium*, (Lord Charles Hotel, Somerset West, South Africa), pp. 365–372, August 1990.

[63] A. Hujanen, "Measuring electrical, magnetic, and chiral material parameters," in *Proceedings of "Bi-Isotropics'93"* (A. Sihvola, ed.), pp. 43–56, Helsinki University of Technology, Finland, February 1993.

[64] M. Oksanen and A. Hujanen, "Determining chiral parameters from measurements," in *URSI Proceedings of IEEE AP/URSI International Symposium–92*, (Chicago, Illinois, USA), p. 368, July 1992.

[65] M. Oksanen and A. Hujanen, "How to determine chiral material parameters," in *Proceedings of 22Nd European Microwave Conference*, pp. 195–199, Microwave Exhibitions and Publishers, August 1992.

[66] S. Ougier, I. Chenerie, and S. Bolioli, "Measurement method for chiral media," in *Proceedings of 22Nd European Microwave Conference*, pp. 682–687, Microwave Exhibitions and Publishers, August 1992.

[67] S. A. Tretyakov and D. Y. Haliullin, "Free-space techniques for biisotropic media parameter measurement," *Microwave and Optical Technology Letters*, vol. 6, pp. 512–515, June 1993.

[68] A. H. Sihvola and I. V. Lindell, "Using Brewster angle for measuring microwave material parameters of bi-isotropic and chiral media," in *IEEE MTT-S International Microwave Symposium Digest Part 2 (of 3)*, (Albuquerque, New Mexico), pp. 1135–1138, 1992.

[69] S. Tretyakov and A. Viitanen, "Waveguide and resonator perturbation techniques for measuring chirality and non-reciprocity of biisotropic materials," Tech. Rep. 134, Electromagnetics Laboratory, Helsinki University of Technology, February 1993.

[70] V. Semenenko and D. Ryabov, "Microwave effective permeability of conductive helices," in *Proceedings of "Bianisotropics'93"* (A. Sihvola, S. Tretyakov, and I. Semchenko, eds.), (University of Gomel, Byelarus), December 1993.

[71] S. S. Stuchly and M. Matuszewski, "A combined total reflection-transmission method in application to dielectric spectroscopy," *IEEE Trans. Instrumentation and Measurements*, vol. IM–27, pp. 285–288, September 1978.

[72] E. Ni, "An uncertainty analysis for the measurement of intrinsic properties of materials by the combined transmission-reflection method," *IEEE Trans. Instrumentation and Measurements*, vol. 41, pp. 495–499, August 1992.

[73] J. Baker-Jarvis, E. Vanzura, and W. A. Kissick, "Improved technique for determining complex permittivity with the transmission/reflection method," *IEEE Trans. Microwave Theory and Techniques*, vol. 38, pp. 1096–1103, August 1990.

[74] J. Baker-Jarvis, R. G. Geyer, and P. D. Dominich, "A nonlinear least-squares solution with causality constraints applied to transmission line permittivity and permeability determination," *IEEE Trans. Instrumentation and Measurements*, vol. 41, pp. 646–652, October 1992.

[75] L. P. Ligthart, "A fast computational technique for accurate permittivity determination using transmission line methods," *IEEE Trans. Microwave Theory and Techniques*, vol. MTT-31, pp. 249–254, March 1983.

[76] H. E. Bussey, "Measurement of RF properties of materials: A survey," *Proceedings of the IEEE*, vol. 55, pp. 1046–1053, June 1967.

[77] M. Maurens, A. Priou, P. Brunier, S. Aussudre, M. Lopez, and P. Combes, "Free-space microwave measurement technique for composite minerals," *PIER 6: Progress in Electromagnetic Research: Dielectric Properties of Heterogeneous Materials*, pp. 345–385, 1993.

[78] J. Musil and F. Žáček, *Microwave Measurements of Complex Permittivity by Free Space Methods and Their Applications*. Studies in Electrical and Electronic Engineering 22, Elsevier, 1986.

[79] D. K. Ghodgaonkar, V. V. Varadan, and V. K. Varadan, "A free-space method for measurement of dielectric constant and loss tangents at microwave frequencies," *IEEE Trans. Instrumentation and Measurements*, vol. 37, pp. 789–793, June 1989.

[80] V. V. Varadan, R. D. Hollinger, D. G. Ghodgaonkar, and V. V. Varadan, "Free-space broadband measurements of high-temperature, complex dielectric properties at microwave frequencies," *IEEE Trans. Instrumentation and Measurements*, vol. 40, pp. 842–846, October 1991.

[81] A. G. Smith and J. H. Cloete, "A free-space permittivity, permeability, and chirality measurement technique at microwave frequencies," in *Proceedings of IEEE/SAIEE AP/MTTS-92 Symposium*, (University of Natal, Durban, South Africa), pp. 131–136, September 1992.

[82] A. G. Smith, S. Kuehl, and J. H. Cloete, "Experimental characterization of artificial chiral materials at microwave frequencies," in *Proceedings of IEEE/SAIEE AP/MTTS-93 Symposium*, (Kempton Park, Johannesburg, South Africa), pp. 17–1 to 17–8, August 1993.

[83] R. H. Clarke and J. Brown, *Diffraction Theory and Antennas*. Ellis Horwood Series in Electrical and Electronic Engineering, Ellis Horwood Limited, 1980.

[84] J. Botha, *Near-Field Antenna Measurements.* M.Eng, University of Stellenbosch, November 1992.

[85] J. Tuovinen, "Accuracy of a Gaussian beam," *IEEE Trans. Antennas Propagat*, vol. 40, pp. 391–398, April 1992.

[86] H. A. Haus, *Waves and Fields in Optoelectronics.* Prentice-Hall, 1984.

[87] J. Tuovinen, T. M. Hirvonen, and A. V. Räisänen, "Near-field analysis of a thick lens and horn combination: Theory and measurement," *IEEE Trans. Antennas Propagat*, vol. 40, pp. 613–619, June 1992.

[88] S. Ramo, J. Whinnery, and T. van Duzer, *Fields and Waves in Communication Electronics.* John Wiley and Sons, 1984.

[89] Hewlett Packard, *Network Analysis: Specifying calibration standards for the HP8510 network analyzer*, February 1988. Product Note 8510-5A.

[90] Hewlett Packard, *Network Analysis: Applying the HP 8510B TRL calibration for non-coaxial measurements*, October 1987. Product Note 8510-8.

[91] G. F. Engen and C. L. Hoer, ""Thru-Reflect-Line": An improved technique for calibrating the dual six-port automatic network analyzer," *IEEE Trans. Microwave Theory and Techniques*, vol. MTT-27, pp. 987–993, December 1979.

[92] J. K. Hunton, "Analysis of microwave measurement techniques by means of signal flow graphs," *IRE Transactions on Microwave Theory and Techniques*, pp. 206–212, March 1960.

[93] B. Bianco, A. Corano, S. Ridella, and C. Simicich, "Evaluation of errors in calibration procedures for measurements of reflection coefficient," *IEEE Trans. Instrumentation and Measurements*, vol. IM-27, pp. 354–358, December 1978.

[94] J. Ladvánszky, A. Hilt, and I. Csonka, "Reduction of measurement error in Microwave reflectometers by minimum sensitivity calibration," *Electronics Letters*, vol. 29, pp. 1305–1307, July 1993.

[95] F. Smith, B. Chambers, and J. Bennett, "Calibration techniques for free space reflection coefficient measurements," *IEE Proceedings-A*, vol. 139, pp. 247–253, September 1992.

[96] A. Von Hippel, *Dielectric Materials and Applications.* N.Y.: The Technology Press of MIT and John Wiley and Sons, 1954.

[97] H. Haus and J. Melcher, *Electromagnetic Fields and Energy.* Prentice-Hall International, Inc., 1989.

[98] D. R. Gagnon, "Highly sensitive measurements with a lens-focused reflectometer," *IEEE Trans. Microwave Theory and Techniques*, vol. 39, pp. 2237–2240, December 1991.

[99] M. H. Umari, D. K. Godgaonkar, V. V. Varadan, and V. K. Varadan, "A free-space bistatic calibration technique for the measurement of parallel and perpendicular reflection coefficients of planar samples," *IEEE Trans. Instrumentation and Measurements*, vol. 40, pp. 19–24, February 1991.

[100] Hewlett Packard, *Instructor Guide for Basic Network Measurements using HP8510B Network Analyzer System*, January 1988. HP Course Number HP 8510B+24D.

[101] Hewlett Packard, *HP 8510B Network Analyzer 45MHz–100GHz*, May 1987. Technical Data.

[102] Hewlett Packard, *Measuring Dielectric Constant with the HP 8510 Network Analyzer*, May 1986. Product Note 8510-3.

[103] H. W. Bode, *Network Analysis and Feedback Amplifier Design*. New York N.Y.: Van Nostrand, 1951.

[104] A. Breipohl, *Probabilistic Systems Analysis: An Introduction to Probabilistic Models, Decisions, and Applications of Rrandom Processes*. John Wiley and Sons, 1970.

[105] V. K. Varadan and V. V. Varadan, "Chiral polymer coatings for microwave applications," *SPIE*, vol. 1307, pp. 122–128, 1990.

[106] F. Mariotte, D. Gogny, A. Bourgeade, and F. Farail, "Backscattering of thin wire helix: analytical model, numerical study and free space measurement. Application to chiral composite modeling," in *Proceedings of "Bianisotropics'93"* (A. Sihvola, S. Tretyakov, and I. Semchenko, eds.), (University of Gomel, Byelarus), December 1993.

[107] V. V. Varadan, A. Lakhtakia, and V. K. Varadan, "Equivalent dipole moments of helical arrangements of small, isotropic, point-polarizable scatters: Application to chiral polymer design," *Journal of Applied Physics*, vol. 63, pp. 280–284, January 1988.

[108] J. Svigelj, E. Michielssen, and R. Mittra, "Absorption characteristics of periodic arrangements of infinite helices," *Microwave and Guided Wave Letters*, vol. 2, pp. 495–496, December 1992.

[109] F. Mariotte, *Matériaux chiraux à structures hétérogènes: modèlisations et applications*. PhD thesis, L'Universite de Bordeaux I, (This thesis was received too late for a thorough study to be made.), March 1994.

[110] J. Svigelj, E. Michielssen, and R. Mittra, "Numerical study of chiral properties of the wire helix," in *Proceedings of IEEE AP/URSI International Symposium–92*, (Hyatt Regency, Chicago), pp. 695–698, July 1992.

[111] D. Jaggard and N. Engheta, "Novel shielding, reflection and scattering control using chiral materials," United States Patent Application 5,099,242, The Trustees of the University of Pennsylvania, March 1992.

[112] V. Varadan and V. Varadan, "Electromagnetic shielding and absorptive materials," United States Patent Application 4,948,922, The Pennsylvania State University, August 1990.

[113] F. Mariotte, A. Fourrier-Lamer, and S. Zouhdi, "Absorbing polarization shield having planar chiral patterns," European Patent Application FR 91-8104, Commissariat a L'Energie Atomique and Universite Pierre et Marie Curie Paris VI, June 1992.

[114] F. Guerin, "Energy dissipation and absorption in bi-isotropic media," in *Proceedings of "Bianisotropics'93"* (A. Sihvola, S. Tretyakov, and I. Semchenko, eds.), (University of Gomel, Byelarus), December 1993.

[115] A. G. Smith, *Specular Reflection of Uniform Plane Waves by a Lossy Chiral Dallenbach Layer.* M.Eng Thesis, University of Stellenbosch, November 1990.

[116] A. G. Smith and J. H. Cloete, "Specular reflection of uniform plane waves by a lossy chiral Dallenbach layer," in *Proceedings of IEEE/SAIEE AP/MTTS-90 Symposium*, (Lord Charles Hotel, Somerset West, South Africa), pp. 99–104, August 1990.

[117] A. Fernandez and A. Valenzuela, "General solution for single-layer electromagnetic-wave asorber," *Electronics Letters*, vol. 21, pp. 20–21, January 1985.

[118] R. V. Churchill and J. W. Brown, *Complex Variables and Applications.* McGraw-Hill Book Company, fourth ed., 1984.

[119] J. A. Kong, *Electromagnetic Wave Theory.* John Wiley and Sons, 1986.

[120] J. D. Kraus, *Electromagnetics.* McGraw-Hill Book Company, second ed., 1984.